Energy level alignment at organic semiconductor interfaces

Héctor Vázquez Melis

Junio de 2006

Memoria presentada para optar al grado de Doctor en Ciencias Físicas por la Universidad Autónoma de Madrid

DIRECTOR: Fernando Flores Sintas

Contents

Agradecimientos

La memoria de la tesis es la punta del iceberg. Detrás hay muchos días de trabajo, resultados válidos y otros erróneos, propuestas para cálculos que han tenido éxito e intentos fallidos, días de satisfacción y otros de desesperación y ganas de dejar la tesis... la piedra de Sísifo. Pero todo se acaba. Hasta la tesis. Con todo, al hacer balance, es sin duda positivo. Ha estado bien.

En estos años, he tratado con gente cuyo apoyo debo ahora agradecer. El primero es, claro, mi director de tesis, Fernando Flores. Su energía inagotable, su gran experiencia y su *instinto* para la física son impresionantes. También están, por supuesto, mis compañeros de departamento, sin los cuales todo esto hubiera sido mucho más aburrido: Pavel (¡y Adri y la pequeña Ella!), Miguel, Yannick, César, Ramiro, Laura, Sebas, Jose Manuel, Pablo (a quien debo agradecer además su apoyo con gcluster *back in the days*), Isa, Pilar, Blanca... la lista es infinita. Mención aparte merecen mis compañeros de despacho, past and present, Quique, Diego y Antonio, por esas carcajadas que alguna vez se han oído en el despacho. De la 'sexta planta' tengo que agradecer el apoyo y la plena disposición a discutir cualquier tema científico (y no científico). A Jose, Rubén, Jaime y Kike les he tratado un poco más. Y tampoco me puedo olvidar de Quique y David, compañeros de carrera y en la ciencia.

Fuera de la universidad, tengo que nombrar a Vishal, Galiana, Gracia, Juan... por la amistad, las risas y el house de calidad. Y un beso muy grande para Mar, que siempre significará mucho para mí.

Y por supuesto a mis padres, por su amor y apoyo incondicionales.

On the academic side, I must sincerely thank Prof. Sydney and Prue Davison for their warm hospitality and surface physics discussions in Waterloo, when all this was starting.

It is a pleasure to thank Prof. Antoine Kahn and his group for the excellent atmosphere I found during my stay at Princeton, and for valuable scientific discussions and collaboration.

¡¡¡A todos vosotros, muchas gracias y un gran, sincero y fuerte abrazooo!!!

Héctor

Junio de 2006.

Resumen

La presente tesis trata del alineamiento de niveles en interfases de semiconductores orgánicos. Este es un tema de gran interés, tanto tecnológico como fundamental, ya que el campo de los materiales orgánicos está en auge y no se entiende del todo desde el punto de vista teórico.

La tesis comienza con una Introducción, en la que se describen cuestiones generales del campo de los semiconductores orgánicos: estos materiales están formados por agregados de moléculas bien diferenciadas que interaccionan débilmente, de manera que se preserva la estructura electrónica de las moléculas que conforman el semiconductor, en los que abundan los enlaces aromáticos π. Esto tiene consecuencias importantes en cuanto al crecimiento de estos materiales y la formación de interfases, ya que la interacción tan débil da lugar a materiales flexibles y/o transparentes, lo que abre un nuevo campo tecnológico. Ya han aparecido dispositivos electrónicos basados en semiconductores orgánicos, y la creciente presencia de estos materiales en artículos científicos y comunicaciones a congresos indica que se trata de un campo en auge. Tras esta discusión, se plantean de manera general las características y problemas de los semiconductores orgánicos: la interacción débil entre las moléculas que conforman el material da lugar a que las excitaciones de carga estén localizadas en gran parte en cada molécula. Esto tiene consecuencias importantes, ya que los gaps ópticos y de transporte difieren de forma significativa y, en particular, ninguno de ellos está bien descrito por los métodos de primeros principios basados en la Teoría del Funcional de la Densidad (DFT). A continuación, se expone la importancia de las interfases, tanto desde un punto de vista fundamental como tecnológico, ya que la eficiencia de los dispositivos electróni-

cos está limitada en último término por el transporte electrónico a través de las interfases. Tras destacar la importancia del alineamiento de niveles en interfases metal/orgánico y orgánico/orgánico, se hace una breve descripción de las técnicas experimentales más usuales, con las que se comparan los resultados teóricos obtenidos en la tesis.

El siguiente capítulo describe las diferentes maneras en las que se calcula, usándo métodos de primeros principios basados en DFT, la estructura electrónica de moléculas pequeñas basadas en carbono, y la de moléculas grandes con enlaces π resonantes. Se describen en primer lugar los fundamentos básicos de DFT, comparando entre la aproximación más común al canje y correlación (LDA) y un método desarrollado por el grupo basado en los números de ocupación. Usando estas dos aproximaciones y distintas bases de orbitales localizados, se calcula la estructura electrónica de estas moléculas, comparando y discutiendo los resultados. Una parte importante de este capítulo está dedicado a resolver el problema de la determinación del gap de la molécula, que DFT subestima de forma notable. El valor del gap es de gran importancia para nuestro trabajo, ya que determina la posición de los niveles moleculares. La parte final de este capítulo describe el trabajo realizado en la línea de desarrollar un método para el cálculo de los gaps de forma adecuada: se describe en detalle este método comparando con resultados nuestra aproximación con cálculos exactos. Tras comprobar el buen acuerdo y la validez del método, se describe en detalle su aplicación a las distintas moléculas orgánicas que son consideradas en esta tesis.

El capítulo 3 introduce nuestro modelo para el alineamiento de niveles en interfases metal/orgánico. Tras describir el trabajo teórico previo existente en el campo, se describe nuestro modelo, comenzando por una introducción histórica del modelo IDIS en interfases de semiconductores inorgánicos, en el que nuestro método está basado. Posteriormente, se introducen los problemas esenciales del alineamiento de niveles en interfases: la regla de Schottky-Mott, la formación de dipolos y barreras Schottky, y el anclaje del nivel de Fermi en el gap del semiconductor. Tras evaluar la situación en el campo de las interfases metal/orgánico, donde no se entiende de forma satisfactoria lo observado experimentalmente, se describe en detalle nuestro modelo, que es aplicable en el límite de interacción débil. Como prototipo de metal poco reactivo, se toma oro. En nuestro modelo, la magnitd más importante es el Nivel de Neutralidad de carga (Charge Neutral-

ity Level, CNL). Este nivel se puede calcular a partir de la estructura electrónica del metal y del material orgánico aislados, y de la interacción entre ellos. Esta interacción tiene como resultado ensanchar los niveles moleculares, dando lugar a ua densidad de estados continua, con valores no despreciables en el gap del semiconductor. La integral de esta densidad de estados inducida hasta la carga del semiconductor aislado da lugar a la posición del CNL. Se calculan de esta manera los valores del Nivel de neutralidad de Carga, así como las propiedades de interfase con oro para distintos materiales orgánicos: PTCDA, PTCBI, CBP, CuPc y Pentaceno. En el cálculo del CNL es esencial tener en cuenta la corección de los niveles introducida en el capítulo anterior, así como los efectos de la polarización en la interfase. El alineamiento de niveles en estas interfases depende de la posición relativa del Nivel de Neutralidad de Carga y de la función de trabajo del metal, así como del apantallamiento en la interfase. Este apantallamiento viene descrito por un parámetro S, que es calculado teóricamente y hallado en buen acuerdo en valores experimentales. A partir del parámetro S, la posición del CNL, y usando la función de trabajo medida experimentalmente, se calculan los dipolos inducidos, barreras Schottky y la posición del nivel de Fermi. La comparación de estos resultados con los valores experimentales da un buen acuerdo. Es importante resaltar que los resultados teóricos dependen sobre todo del valor del Nivel de Neutralidad de Carga, y débilmente de los demás parámetros. Esto hace que los resultados teóricos sean muy robustos y casi independientes de los principales supuestos en nuestro modelo: que las moléculas se depositan planas sobre la superficie y la distancia metal-orgánico, que es considerada un parámetro externo.

A la luz del buen acuerdo obtenido para las interfases metal/orgánico con interacción débil, en el capítulo 4 el modelo se extiende a heterouniones de semiconductores orgánicos. Estas presentan una interacción débil, por lo que la aplicación de nuestro modelo está justificada. De acuerdo con nuestro modelo, el alineamiento de niveles en estas interfases está regido por el alineamiento parcial de los Niveles de Neutralidad de Carga de ambos materiales orgánicos. La diferencia inicial entre ambas cantidades determina en qué dirección la carga va a ser transferida. La diferencia final de niveles depende de la inicial y del apantallamiento en la interfase: este viene descrito por un parámetro S similar al de las uniones metal/orgánico. Este parámetro es estimado (ya que no ha sido medido experimentalmente) de diferentes maneras, que concuerdan entre sí. Es importante señalar que el apantallamiento en las heterouniones de materiales orgánicos es bastante débil, ya que

encontramos S $\sim$ 0.6, a diferencia de los semiconductores inorgánicos, donde el apantallamiento es mucho mayor, lo que da lugar a diferencias finales significativas en los CNLs. La aplicación de nuestro modelo a diversas heterouniones da lugar a dipolos que están en buen acuerdo con los rsultados experimentales. Al mismo tiempo, nuestro modelo permite entender, de manera global, el alineamiento de niveles en heterouniones de materiales orgánicos: experimentalmente, se observa que en la mayoría de las interfases se alinean los niveles de vacío, mientras que en determinados casos hay dipolos muy grandes. Hasta ahora no existía una explicación; nuestro modelo, sin embargo, permite por primera vez entender este comportamiento de una manera global e intuitiva. Nuestro análisis ha sido usado para entender la transitividad en interfases de materiales orgánicos, ya que se encuentra que la regla de transitividad casi se cumple, y que son las pequeñas diferencias en el apantallamiento de las distintas interfases las que 'rompen' la transitividad. Finalmente, se ha extendido el modelo para analizar heterouniones de semiconductores orgánicos, en los que uno de ellos está dopado. Los dipolos y el anclaje del nivel de Fermi que aparecen al dopar son interpretados dentro de nuestro enfoque como una variación del Nivel de Neutralidad de Carga que se produce al dopar el material, y cuyo alineamiento parcial con el CNL del otro material da lugar al comportamiento observado.

En resumen, esta tesis presenta un modelo para el alineamiento de niveles en interfases de semiconductores orgánicos en el régimen de interacción débil. El modelo, que se basa en el alineamiento parcial del Nivel de Neutralidad de Carga del material orgánico con la función de trabajo (en las interfases metal/orgánico), o con el CNL del otro material (en heterouniones) da lugar a resultados que están en buen acuerdo cualitativo y cuantitativo con lo observado experimentalmente. Además, nuestro modelo permite, por primera vez, entender de una forma unificada el comportamiento de estas interfases.

Physics is like sex. Sure, it may give some practical results, but that's not why we do it.

(Richard Feynman)

Friends, Romans, countrymen, lend me your ears;
.....
I come not to steal away your hearts.

(William Shakespeare (Julius Caesar))

CHAPTER 1

Introduction

Before I speak, I have something important to say.

(Grouch Marx)

1.1. Organic materials

Over the last decade, the interest of the scientific and technological communities in organic materials has significantly increased. This rise, evident in the number of publications, patents, conference contributions, as well as in the appearance of new organic-based electronic devices, has made the field which could be generally termed *Organic electronics* the focus of considerable scientific and technological research [Shen01b, Dimitrakopoulos01, Forrest04].

At the core of this success is, on the technological side, the promise of a new generation of ultralow-cost, lightweight and flexible organic-based electronic devices [Forrest04]. High-efficiency light-emitting devices, thin-film transistors and photovoltaic cells, all of which are made of organic materials (Fig. 1.1), are already in commercial production [Vaeth03, Gundlach97, Shtein02, Peumans01, Granström98, Peumans03,Shaheen01], and it seems a wide range of organic-based electronic 'gadgets' (flexible screens that can be rolled, flexible electronic circuits, ultraflat colour displays (Fig. 1.2), and other devices yet unthought of) will become ubiquitous due to their low cost and new functionalities.

On the more scientific or academic side, this flourishing of organic materials has been made possible by the mastery of surface science techniques, on the experimental aspect, and, on a theoretical level, the possibility of a proper theoretical description, largely due to Density-Functional Theory methods. These theoretical methods, despite their limitations, have enabled an understanding of increasingly larger and more complex systems, with the ultimate goal, possibly in the intermediate future, of biological molecules.

Two broad classes of organic materials can be identified: conjugated polymers and small-weight organic molecules [Salaneck01]. While differences in their electronic and optical properties have been pointed out, the main distinction lies in their preparation and deposition.

The relative ease with which the organic material is deposited is the key to the low cost of fabrication of these organic-based devices: thermal sublimation in vacuum is the most common means for small-weight organic molecules, while polymers are generally solution-processed, applied on the entire wafer by spray-on methods similar to ink-jet printing, using shadow masks to achieve pixellation, later removing the solvent by evaporation. In other cases, direct printing using stamps or rollers (Figs. 1.3,1.4) is used [Forrest04]. In any case, an important difference appears with traditional (*i.e.* silicon-based) electronics. This is the ease with

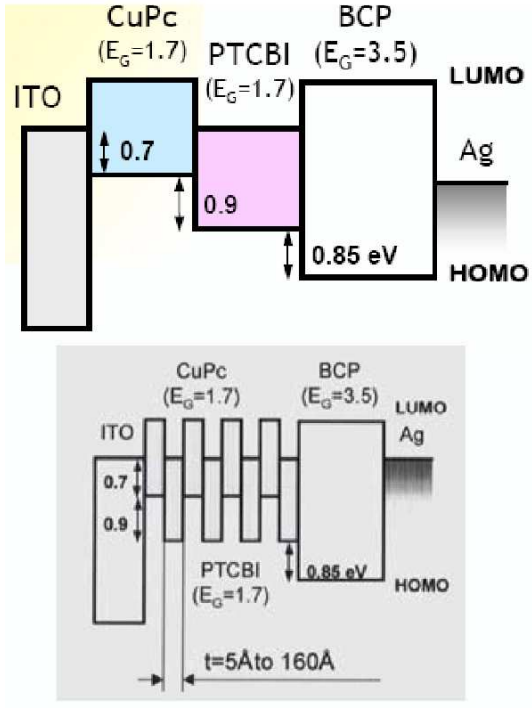

Figure 1.1.: Stacked layers of organic materials in multilayer photodetectors and photovoltaic diodes. Figures from [Peumans00a, Peumans00b].

which organic materials can be grown and deposited on a variety of substrates, as opposed to the arduous task of inorganic semiconductors, with the difficulties that arise from strain, defects or lattice matching[1]. In contrast, organic materials are in general free of many of these problems, so that the possibility of depositing virtually any organic material on almost any substrate opens the way to an unlimited number of possibilities. Thus, the desired material can be chosen almost entirely for its functionality (for instance, its optical or conducting properties), without having to take into consideration the stringent conditions usual in inorganic semiconductors. In addition, many of these electronic and optical properties can be tuned by modifications in the chemical structure. Organic materials, therefore, open the way for the fabrication of devices in which their design is not significantly

[1]For a review of the quasi-epitaxial growth of organic semiconductors on a variety of substrates see [Forrest97].

Figure 1.2.: Present and near future of organic emissive devices: (a) full-colour, 13-inch small-molecular-weight display, manufactured by Sony. The display is only 2 mm thick. (b) Conceptual view of a future organic flexible display, which can be rolled up into a pen-like device, which would contain wireless communication electronics. Images from [Forrest04].

hampered by growth conditions, but are driven purely by the desired functionalities. This somehow compensates for carrier mobilities, which are much smaller in organic materials ($\mu < 10^2$ cm^2 V^{-1} s^{-1} at room temperature for ordered materials [Warta85a, Schön00, Karl99, Warta85b, Karl89, Forrest84]) than is typical for inorganic semiconductors ($\mu \sim 10^2$ – 10^4 cm^2 V^{-1} s^{-1} [Sze81]), since transport in organic materials takes place mostly via hopping between neighbouring molecules of polymer chains.

As has been stated [Forrest04], these comparative advantages of organic materials do not imply that they are likely to replace traditional silicon-based electronics, but will rather fill the *niches* that are not currently accessible with inorganic semiconductors.

1.2. Structure of organic semiconductors

Of all organic materials, this work focuses on small-weight organic molecules; for an overview of the role of polymers in organic electronics, the reader is referred

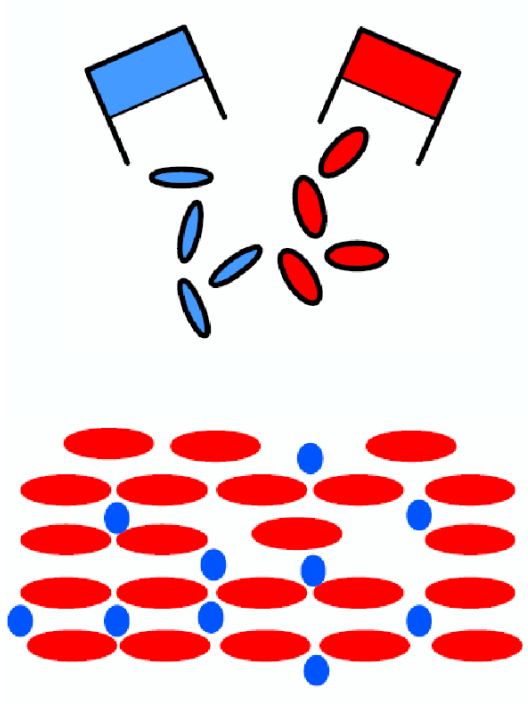

Figure 1.3.: Thermal sublimation in vacuum is the most common means for the deposition of small-weight organic molecules. These can be deposited easily in a variety of substrates.

to [van Hutten01].

An important characteristic of these organic molecules is that they are often flat, π-conjugated molecules, where benzene aromatic rings are abundant. Typically, these molecules contain C, N, O and H, and in some cases metal atoms. In these molecules, there is a strong anisotropy between in-plane σ covalent bonds and the out-of-plane π orbitals (Fig. 1.5). The intermolecular π–π interaction is strongest along the perpendicular (stacking) direction, though much weaker than intramolecular bonds.

The structure of these low-molecular weight organic molecules consists of well-characterized, independent molecules, interacting weakly with one another, where the gas-phase geometrical and electronic structure is preserved when the molecules come together and the organic material is formed.

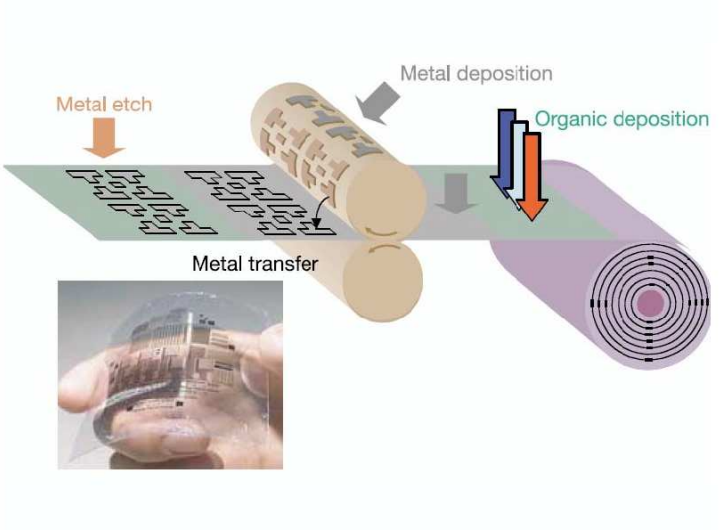

Figure 1.4.: Conceptual diagram of a very low-cost method for manufacturing organic-based devices. On a roll of flexible plastic substrate, the organic material is deposited. The film is then passed between rollers with the desired electrode pattern. The lower picture shows an all-polymer integrated circuit, from Penn. State University. Image from [Forrest04].

Fig. 1.6(a) shows the gas-phase electronic structure of an organic molecule, where occupied and empty molecular states are shown. In particular, the Highest Occupied Molecular Orbital (HOMO) and Lowest Unoccupied Molecular Orbital (LUMO) are important, since they represent the ionization and affinity energies, respectively. The intramolecular forces that hold the molecules together are strong covalent bonds; intermolecular interactions, on the other hand, are weak, usually via van der Waals forces. Given this weak intermolecular interaction, the electronic structure of the organic solid is not significantly disturbed with respect to the gas phase when the molecules are brought together, so that the relevant molecular orbitals, and in particular the HOMO and LUMO, are localized usually on each molecule (Fig. 1.6(b)). The small intermolecular overlap results in bandwidths typically $\lesssim 0.1$ eV [Kao81, Gutmann67]. In the molecular solid, therefore, the HOMO and LUMO (the equivalent of the valence and conduction) bands are thus very narrow. The electronic structure of an organic solid is usually simplified to that shown in Figs. 1.6(c) and (d).

The fact that wavefunctions are localized somewhat complicates the analysis

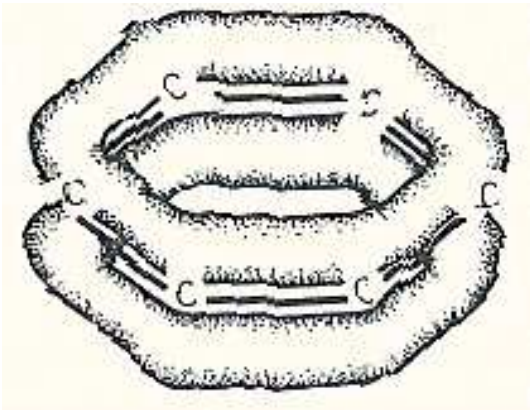

Figure 1.5.: Representation of a π resonant bond in a benzene molecule (Fig. from [Silinsh94]).

from a theoretical point of view, since the delocalized picture of extended wavefunctions usual for inorganic semiconductors breaks down in organic materials. Mechanisms for electronic transport have been argued to be material-dependent [Rajagopal98] and are intermediate between coherent, bandlike transport and disordered hopping between adjacent molecules.

Localization in organic materials is reflected too in charge excitations. These are localized, mostly on single molecules, but extending slightly to neighbouring molecules. As will be discussed, this complicates the understanding of the energy level position, since the localized picture gives rise to strong on-site electron-hole interaction.

The optical and transport gaps differ by several tenths of an eV, and there has been some confusion as to which gap should be used. The difference between them is the exciton binding energy, and it represents the energy needed to 'uncorrelate' the electron-hole pair, which is confined mostly to individual molecules and thus presents a strong Coulomb interaction. Exciton binding energies in organic solids are therefore large, $\sim 0.5 - 1$ eV. This is at variance with inorganic semiconductors, where delocalization of the wavefunctions results in a small interaction between electron and hole.

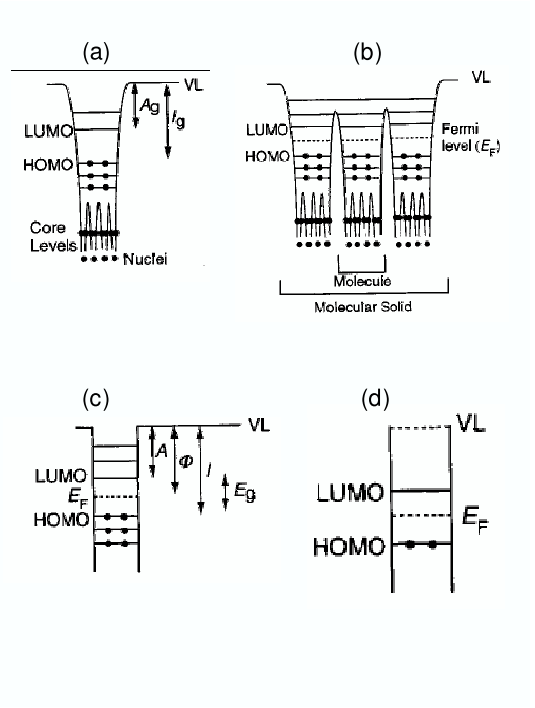

Figure 1.6.: (a) Gas-phase electronic structure of an organic molecule, showing the HOMO, LUMO and gas-phase ionization and affinity levels. (b) Intermolecular interactions are weak at organic solids, and the electronic properties of the individual molecules are preserved. The electronic structure of an organic solid is usually simplified to that shown in (c) or (d). Figures from [Ishii99].

1.3. Interfaces

The above-mentioned structure of organic solids has important consequences for the interfaces of these materials. First, the closed-shell nature of the organic molecules makes it much easier to create these interfaces, since the stringent conditions typical of inorganic semiconductors are not present: there are no such issues such as lattice matching as the molecules are stacked as they are deposited. The weak intermolecular interaction allow for flexibility which eases the structure at the interface. Recombination centers at the interface, associated with broken bonds in inorganic semiconductors, presumably do not exist at organic interfaces. In addition, these interfaces are almost defect-free, again due to the structural flexibility of organic materials which comes from their weak intermolecular interaction. In spite of this,

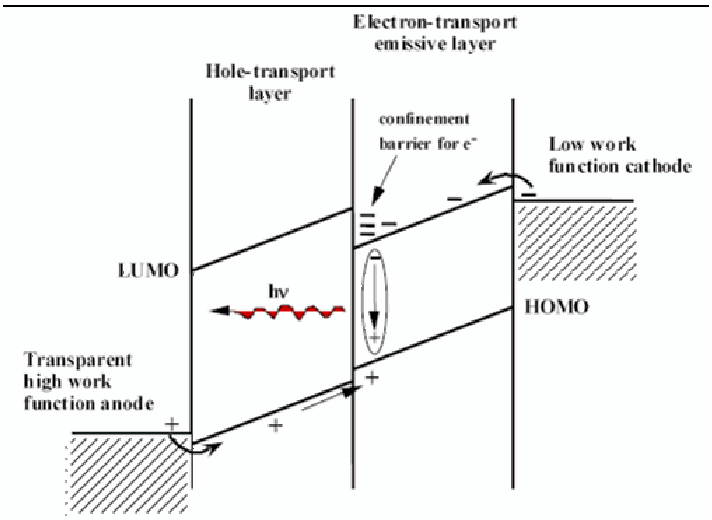

Figure 1.7.: Either from the point of view of basic research or because they limit the performance of devices, the study of interfaces is essential. The figure, showing a schematic energy level diagram of an OLED, highlights the importance of a proper understanding of metal/organic and organic/organic interfaces, the focus of the present work.

interfaces of organic materials with metals exhibit a wide range of reactivities (from weakly-interacting interfaces involving Au as a substrate to highly reactive ones with Mg), while in organic heterojunctions the interaction is very weak.

In turn, the understanding of these interfaces has proved more troublesome. A detailed understanding of the behaviour of organic semiconductor interfaces is necessary, not only for the interest of basic research, but also since the performance of semiconducting devices has been shown to be limited by charge injection at interfaces (Fig. 1.7). From the point of view of basic research, the localization of states and the mechanisms of charge transport, as well as the energy level alignment (which is the focus of this work) are interesting open questions, not completely solved to date. From a more applied or technological perspective, the basic structure of organic-based devices consists of one or more organic layers sandwiched between the electrodes. While all devices must have interfaces with the electrodes, it is usual for optical devices to have several organic layers, each of which is optimized for the transport of electrons or holes, or to enhance recombination and efficient emission or absorption of light. Thus, an understanding of the basic processes taking place at metal/organic and organic/organic interfaces is essential.

Let us first consider metal/organic interfaces. Since the single most important factor that controls charge injection at the interface is the Schottky barrier height, a detailed knowledge of the barrier formation is necessary. In a situation reminiscent of what happened with inorganic (silicon-based) semiconductors, there is the need for an understanding of the basic mechanisms governing the energy level alignment. This will open the way for the control and tailoring of interface properties to the desired needs, rather than having to put up with whatever is found experimentally in the absence of a detailed knowledge.

Consider, for instance, an organic material, characterized by its HOMO and LUMO, and a metal having a work function ϕ_{M_1}. When the interface is formed, an injection barrier ϕ_{B_1} is found (Fig. 1.8). Surprisingly, this barrier is not always the difference between ϕ_{M_1} and the HOMO or LUMO. Moreover, if the same organic material is deposited on another metal, which has a work function different from ϕ_{M_1} by a quantity $\delta\phi_M$, one could naively expect to find a barrier shifted, too, by the same quantity $\delta\phi_M$. However, this is rarely the case. As it turns out, in some cases the Schottky barrier follows the movements of the work function, in others it changes as ϕ_M is varied, though not as much, and in other cases the injection barrier is independent of the value of the metal work function.

The dependence of the Fermi level position (and hence injection barrier) on the metal work function was the subject of intense research in inorganic semiconductors for several decades. The topic, known as **Fermi level pinning**, is now experiencing a similar situation in the organic semiconductor community.

When the interface is formed, charge is in general transferred between metal and semiconductor, so that interface dipoles appear. The interaction between metal and semiconductor can give rise to a DOS in the organic energy gap. This can be originated by several factors such as chemical reaction, defects at the interface, surface rearrangements, the orientation of molecular permanent dipoles. Several mechanisms are, thus, believed to be operating simultaneously at the interface. Large dipoles are observed, the origin of which, such as the pinning of the Fermi level, are not yet fully understood.

When changes in the metal work function are directly reflected in shifts in the Fermi level, the system is said to follow the vacuum level rule. Indeed, this corresponds to the simple alignment of the vacuum levels of both materials[2] (Fig. 1.9(a)).

[2] There is a distinction between the vacuum level 'just outside' a material and the vacuum level at infinity. The former has surface contributions and depends on the particular atomic and electronic structure of the surface, while the latter is invariant and inaccessible experimentally. There has

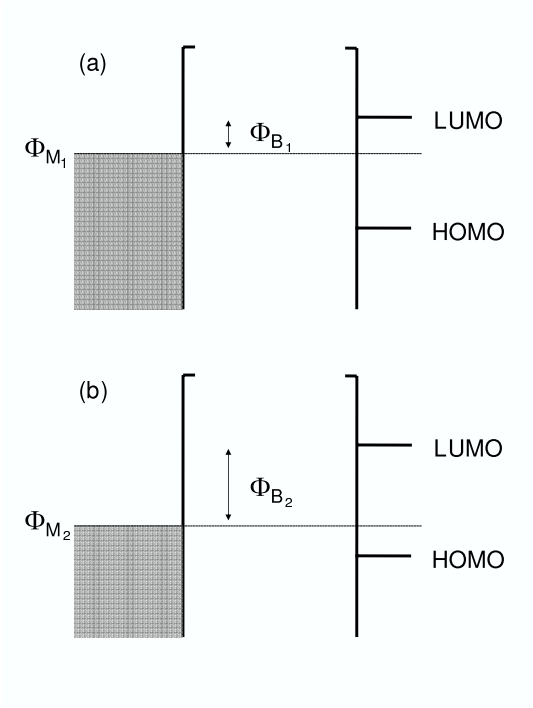

Figure 1.8.: When an organic material is deposited on two different metals, having work functions ϕ_{M_1} and ϕ_{M_2}, the injection barrier ϕ_B (which is not always the difference between the work function and the HOMO or LUMO) sometimes follows this shift in work function, sometimes partially, and in some cases is independent of ϕ_M. Thus, an understanding of the energy level alignment at these interfaces is essential.

Instead, the dipoles that are formed at the interface, due to charge transfer of various origins (such as chemical reaction and gap states) shift the whole spectrum of one of the materials relative to the other one. This results in a pinning of the Fermi level, the degree of which (weaker or stronger) depends on the details of the interface (Fig. 1.9(b)).

At organic heterojunctions, the interaction between both materials is much weaker, and the role of defects is presumably much smaller since metal atoms are much more prone to chemical reaction or interdiffusion, and the interaction between the different closed-shell molecules is of van der Waals type. The structural flexibil-

been some confusion in the literature between both vacuum levels [Ishii99, Cahen03]. For a clear discussion of these concepts, see the excellent papers by H. Ishii *et al.* [Ishii99] and Cahen and Kahn [Cahen03].

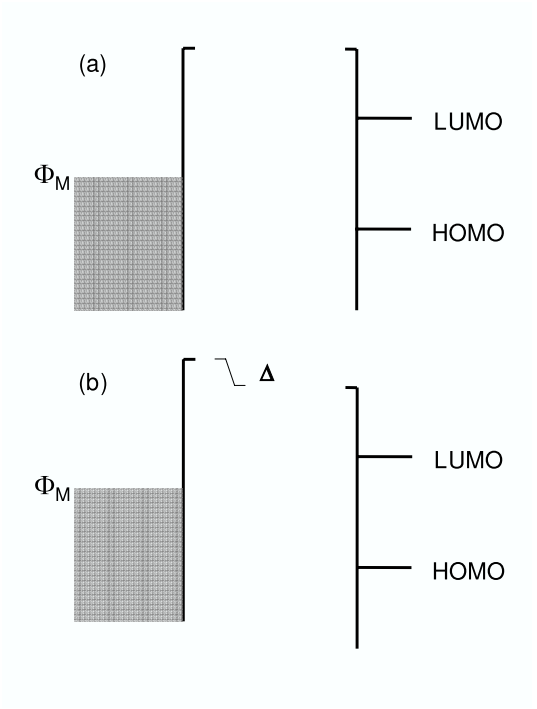

Figure 1.9.: (a) Vacuum level rule, by which the vacuum levels of both materials (in this case a metal and a molecule) directly align when the interface is formed. (b) An interface dipole Δ is formed at the interface, breaking the vacuum alignment rule.

ity of these materials results in non-reactive, weakly-interacting interfaces, almost completely free of defects. At these interfaces, the vacuum level rule is observed in most cases, which is not surprising for such weakly-interacting interfaces. In some particular cases, however, large (up to 0.5 eV) dipoles are observed, the origin of which is not fully understood.

1.4. Overview of experimental techniques

Experimental research has of course been essential in contributing to the understanding of organic semiconductor interfaces. This section presents a brief overview of the two major experimental techniques used to characterize organic interfaces.

1.4.1. Photoemission and Inverse Photoemission Spectroscopies

Large progress has been made experimentally in the study of organic semiconductor interfaces through the use of photoemission techniques. Although a detailed description falls beyond the scope of this thesis, it is nevertheless useful to make a brief overview these experimental techniques. This section is based on W. Gao's PhD thesis [Gao04]. A more detailed discussion can be found elsewhere [Gao04, Salaneck01].

Photoemission and inverse photoemission spectroscopies provide information about the occupied and empty states of the organic material. Since the penetration depth of the radiation used is in the 5 –30 Å, they are surface sensitive techniques.

Ultraviolet photoemission spectroscopy (UPS) involves the use of radiation in the 10 – 100 eV photon energy range, having a photon penetration depth of $\sim$ 5 – 10 Å. It probes the filled states of the material. The sample is irradiated with a photon beam, typically using HeI ($h\nu = 21.22$ eV) and HeII ($h\nu = 40.84$ eV) spectral lines. Valence electrons in the organic material are promoted to empty states and, above a certain threshold, can escape the solid and reach the detector (Fig. 1.10). The energy distribution of the collected electrons thus provides information of the occupied DOS of the sample. It is a convolution of the initial and final densities of states, with the energy dependence of the electronic transition. In addition, there are electrons arriving at the detector after inelastic scattering in the sample, which give rise to a low-energy 'secondary electron background'. However, most of these effects show a weak energy dependence in this range, so that the UPS spectrum can be considered to reflect the occupied DOS. The resolution of UPS is typically $\sim$ 0.1 eV.

X-ray photoemission spectroscopy (XPS) uses higher energy photon beams ($h\nu \geq$ 1000 eV) and is used to measure, following the same guidelines outlined above, core level shifts, from which useful information, notably band bending, can be measured.

A typical UPS spectrum of an organic thin film is shown in Fig. 1.11. The zero of the energy scale is the Fermi level of the film, which coincides with that of the metallic substrate (and with that of the detector, since the latter is electrically connected to the substrate). The lower-energy end of the spectrum shows the sharp onset of photoemission. This corresponds to photons having an energy such that the excited electrons have zero kinetic energy. These electrons are excited to the vacuum level of the organic material. Photon energies lower than this threshold are

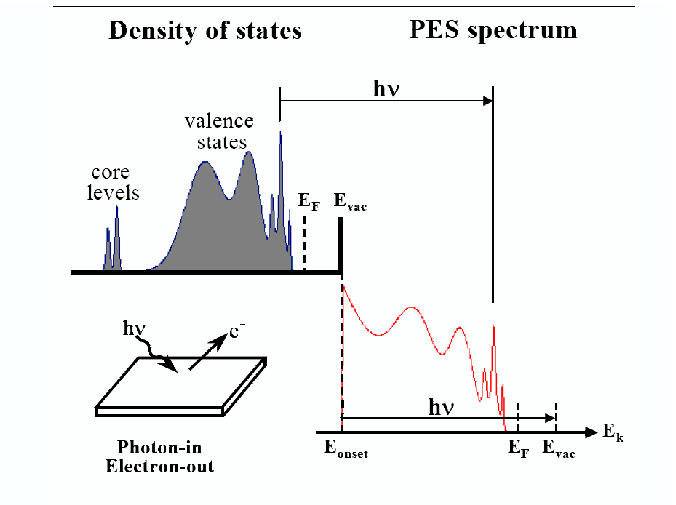

Figure 1.10.: Schematic representation of photoemission experiments: electrons in occupied states are excited by the photons to states above the vacuum level, which reach the detector. The shape of the photoemission spectra resemble the occupied DOS (figure from [Gao04]) .

not enough to promote electrons to escape the solid. Therefore, adding E_{onset} to $h\nu$ gives the position of the vacuum level of the organic material.

Fig. 1.10 also shows low-energy broad features, which are due to secondary electrons. The higher energy spectrum (ie. closer to E_F) shows peaks which represent the valence states of the sample. In particular, the peak closest to the Fermi level corresponds to the organic HOMO. Since these UPS features are broadened in energy, it is common for experimental works to quote the HOMO *onset* or HOMO *edge*. This is defined as the linear extrapolation of the low-energy edge of the peak to the background line of the spectrum. The difference between peak *edges* and *centers* is $\sim$ 0.5 eV [Gao04]. The energy difference between this (center or edge) HOMO peak and the vacuum level is the Ionization Energy (IE) of the material. This is clearly summarized in Fig. 1.11.

Inverse photoemission (IPES) is used to study the empty states of the sample. The sample is irradiated with a beam of low-energy (5 – 20 eV) electrons and the emitted photons are collected (Fig- 1.12). The incident electrons decay into the empty states of the organic material, emitting a photon in this process. The energy of the state into which the electron has decayed is the difference between that of the incident

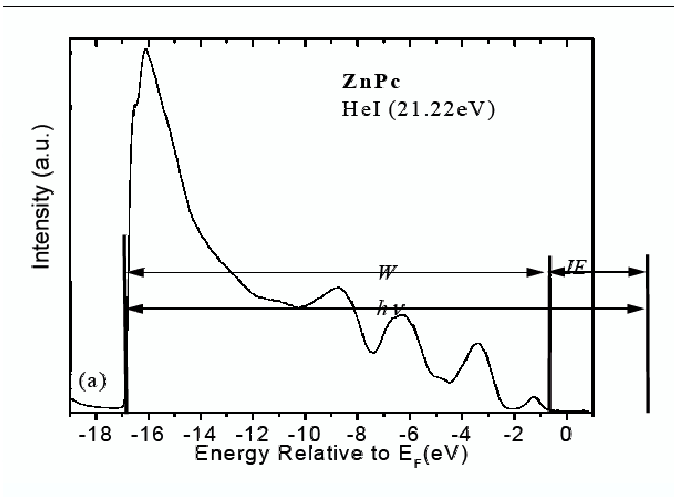

Figure 1.11.: UPS spectrum of a 100 Å ZnPc film. Notice the sharp onset of photoemission at around -17 eV and the molecular peaks at low binding energies (in this case, the center of the HOMO peak is situated at -1.2 eV). The vacuum level is situated an energy $h\nu$ above the photoemission onset. Figure from [Gao04].

electron and detected photon. In this way, the density of unoccupied states of the organic material can be known (in particular, the feature closest to the Fermi level is the LUMO of the organic material). The resolution of IPES is ~ 0.5 eV.

Combined UPS/IPES spectra (Fig. 1.13) are made by aligning the Fermi level (obtained in both cases from the metallic substrate) of both spectra. These are a replica of the density of states of the organic material, and provide valuable information about its electronic structure. An important feature is the transport gap, whose magnitude is essential for the energy level alignment at these interfaces. In this respect, there is an important distinction between the optical and transport gaps. While the former represents a correlated electron-hole pair, in the latter the electron and hole do not interact and thus the value of the transport gap is larger than the optical one. The difference between them is the exciton binding energy, which, due to the localized nature of organic materials, is quite large (0.5 – 1.0 eV), at variance with inorganic semiconductors. This makes the distinction between the optical and transport gaps important, as will be commented below.

The use of photoemission and inverse photoemission techniques to study in-

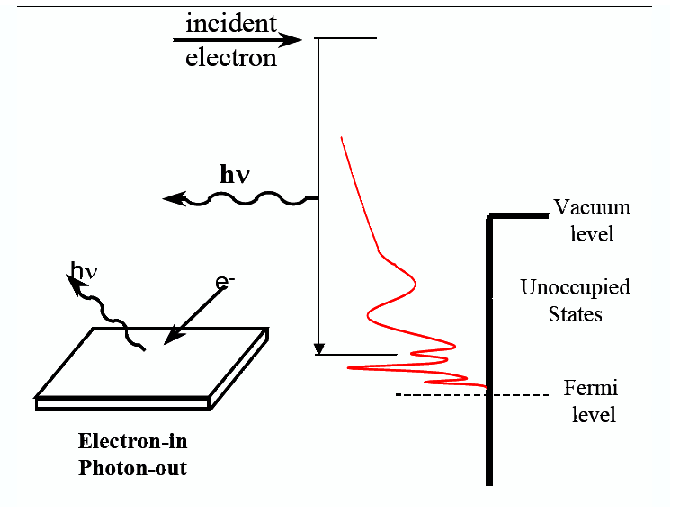

Figure 1.12.: Schematic diagram of inverse photoemission. Low-energy electrons are incident on the sample and populate empty states of the material, emitting a photon. The energy of the empty states is the difference between that of the incident electron and that of the emitted photon (figure from [Gao04]).

terfaces with organic semiconductors, pioneered by the groups of Profs. Seki at Nagoya, Kahn at Princeton, and Salaneck at Linköping, has significantly advanced the field, providing important insight about the energetics of interfaces with organic materials.

1.4.2. Scanning tunneling microscopy (STM)

Since its appearance in 1981 [Binning82b, Binning82a], STM has proved an essential tool in the field of surface science. Based on the quantum phenomenon of tunneling, the STM basically consists of a very sharp tip mounted on a piezoelectric element and an electronics feedback loop that allows for the controlled movement of the tip with atomic precision. The tip is usually metallic, though sometimes alloys or heavily doped semiconducting tips are used. When the tip and the sample are in close proximity (typically 4 – 8 Å) and a small bias is applied, electrons tunnel between tip and sample (see Fig. 1.14). This can be carried out in vacuum, in air, or even in solution. The collected current can be used to extract a wide range of information about the sample. Today, the STM is used to study surface topography, electronic and vibrational properties, surface bonds, magnetic properties, with the

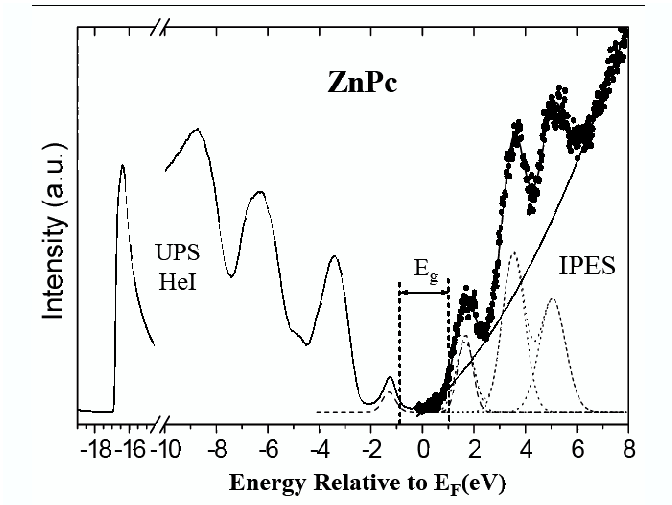

Figure 1.13.: Combined UPS/IPES spectrum of a 100 Å ZnPc film. The spectra are combined by aligning the Fermi level of the metal substrate, measured independently in both cases (from [Gao04]).

possibility of molecular manipulation. The real-space image, in 1983, showing, with atomic resolution, the Si(111) 7x7 reconstruction [Binnig83], earned the recognition of the potential of STM, which resulted in the 1986 Nobel Prize.

The key to the very high resolution, that allows for individual atoms to be probed, lies (apart from the mechanical stability) in the exponential dependence of the tunneling current with the tip-sample distance. However, since the current depends on several other factors, such as the tip and sample DOS, the injection barrier or applied bias, the STM can be used in a variety of ways.

Using the feedback loop, one can maintain a constant current. Since both the tip-sample distance and the local DOS affect the value of the current, both are convoluted and one is almost never (except for clean monoatomic surfaces) measuring the true height. Information about surface topography and adsorbate DOS are obtained. In addition, while keeping the geometry fixed, one can vary the applied voltage and thus perform spectroscopy on the sample (Scanning Tunneling Spectroscopy, STS). The positive (negative) bias images probes the empty (occupied) states of the sample (Fig. 1.15). In semiconductors, this can be used to visualize bonding and antibonding wavefunctions [Hamers96].

STS images are usually represented in terms of dI/dV, or normalized, as a func-

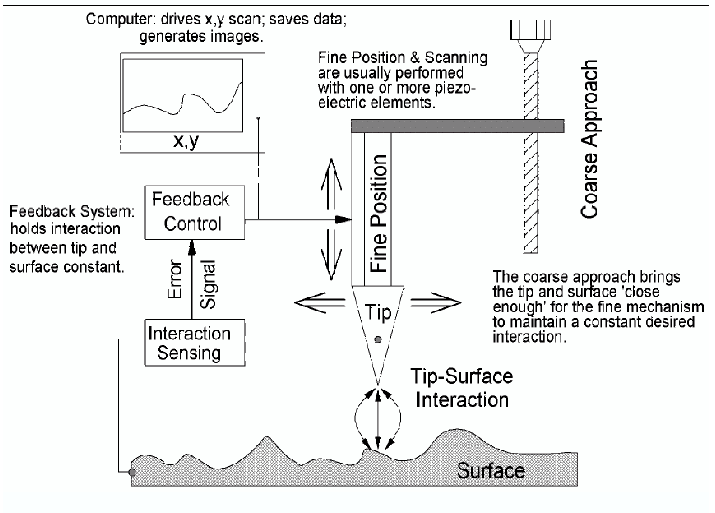

Figure 1.14.: Schematic representation of an STM (from [Hipps05]).

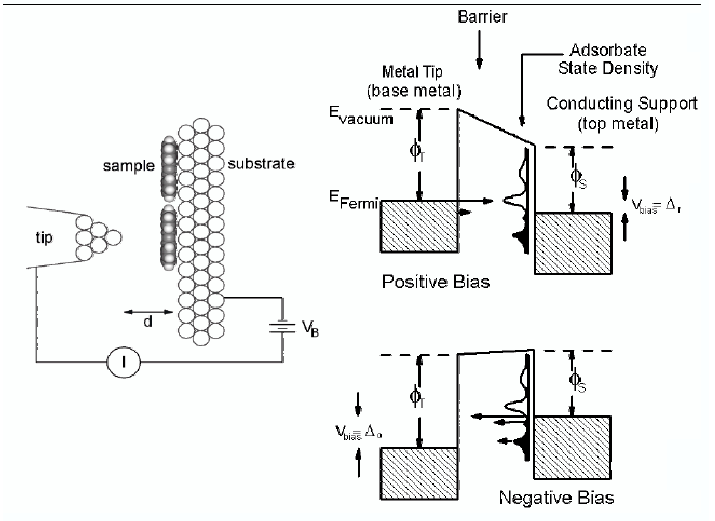

Figure 1.15.: Resonant tunneling through empty (top) and filled (bottom) states of the adsorbate. Figure from [Hipps05].

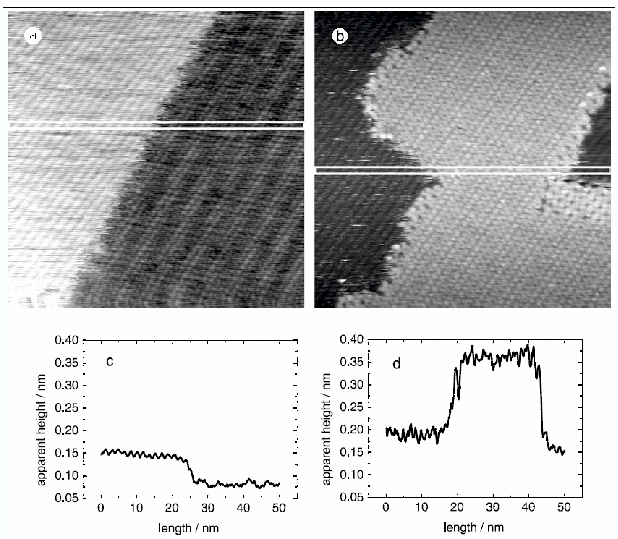

Figure 1.16.: (a) STM constant current image of a molecular island of PTCDA (to the right of the image) on Au(100), showing inverted contrast. (b) STM height image, with normal contrast. (c) and (d) Height profiles of images (a) and (b), respectively. Figure from [Toerker01]

tion of the applied voltage, where the molecular peaks are shown, or as images, mostly with sub-molecular resolution, showing particular molecular orbitals of the adsorbed species, which can be compared to first-principles calculations.

In the case of organic molecules, several examples exist, as are shown below. In the case of weakly-interacting interfaces, submolecular contrast images are seen to agree well with gas-phase calculations.

Fig. 1.16, for instance, shows a constant-current image of a PTCDA island on a Au(100) surface. The bottom figures are the corresponding height profiles. Notice that the figure displays inverted contrast. Because the sample DOS influences the tunneling current, it is not unusual for STM images of organic adsorbates on metal surfaces to exhibit inverted contrast and apparent heights: as C is a poorer conductor than the metallic substrate, the current is lower through the organic material, and the tip approaches the sample in the constant-current mode, resulting in inverted apparent heights. A theoretical analysis of the metallic and organic conductivities is thus necessary for the proper interpretation of the STM data.

Concerning spectroscopy, molecular peaks can be resolved, as seen in Figs. 1.17

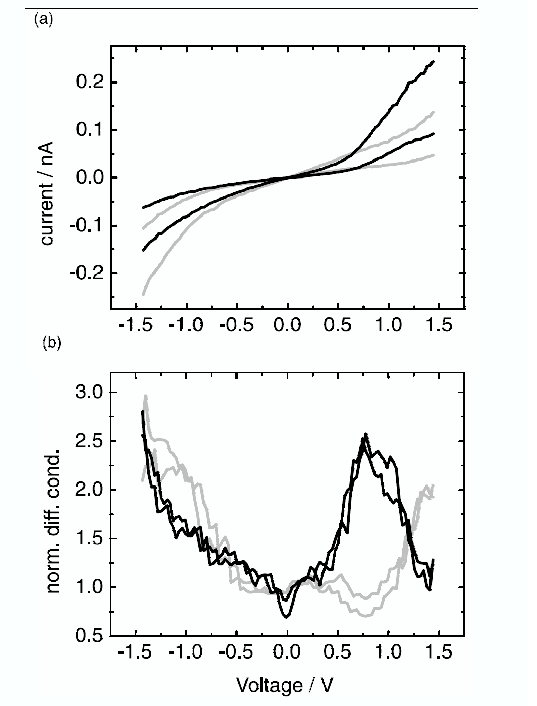

Figure 1.17.: I-V spectroscopy (a) of uncovered gold (grey) and a PTCDA island (black). The bottom figure shows the normalized differential conductivity for the data above, with a clear peak at around 0.8 eV, corresponding to the PTCDA LUMO. Figure from [Toerker01].

and 1.18. In Fig. 1.17, corresponding to PTCDA on Au, a clear peak appears at around 0.8 eV. Since the peak was not observed for the bare metal, it is ascribed to the molecular LUMO. Fig. 1.18(a) shows both the HOMO and LUMO peaks for 1 (bottom) and 2 – 3 MLs of PTCDA on Au. Notice that the transport gap is shown. The peak positions are consistent with each other, though the LUMO position (at 1.3 – 1.45 eV) is slightly different to that reported in the previous figure. STM figures for the HOMO and LUMO, corresponding to charge-density plots, are shown. Since the Au/PTCDA interface is weakly interacting, as will be discussed below, these are similar to the ones obtained from gas-phase theoretical calculations. Finally, Fig. 1.18(b) shows, again, the HOMO and LUMO positions for HBC deposited on Au.

Thus, a wealth of useful information can be obtained from STM studies of organic materials on various substrates.

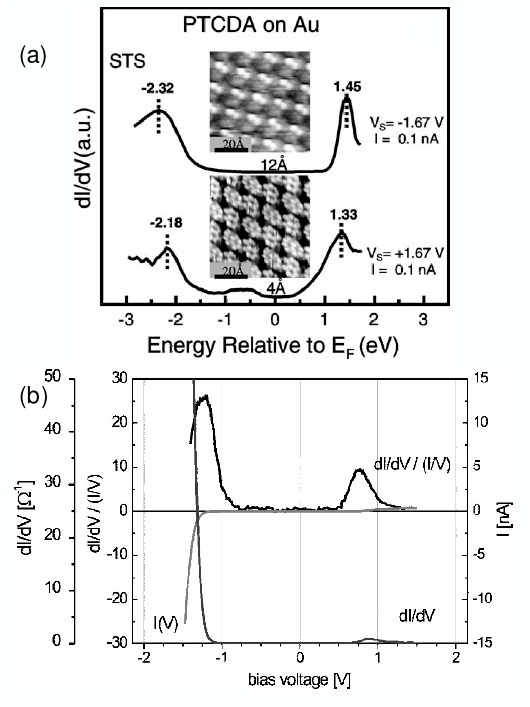

Figure 1.18.: (a) dI/dV spectra of filled and empty states for 1 ML (bottom) and 2 – 3 MLs (top) of PTCDA on Au, showing HOMO and LUMO peaks. The corresponding STM images of the film are shown ([Tsiper02]). (b)Differential conductivity dI/dV and normalized dI/dV for 2 – 3 MLs of Hexa-peri-hexabenzocoronene ($C_{42}H_{18}$, HBC) on Au(111). Notice the peaks at $\sim$ -1.2 eV and $\sim$ 0.8 eV, corresponding to the HBC HOMO and LUMO. Figure from [Proehl01].

1.5. This work

Despite the importance of experimental techniques in the study of organic interfaces, as outlined above, a proper theoretical understanding is needed in order to have a coherent, quantitative analysis of the energy level alignment at these interfaces. The theoretical work presented here is intended to be a step int his direction.

In this work, we have focused on weakly-interacting organic semiconductor interfaces. While the importance of other factors, such as defects and chemical reaction are obviously important, our aim is in fact the **opposite**: free of the complexity of these effects, which can complicate and obscure the understanding of these interfaces, the study of unreactive, 'ideal' interfaces can unveil the basic mechanisms which govern the energy level alignment.

Our approach for the study of these interfaces is based on the concepts of **induced DOS** and **Charge Neutrality Level (CNL)**. When the metal and the organic semiconductor, or both organic materials, are brought together, the interaction between them gives rise to a rearrangement of the organic electronic structure, where a DOS is induced in the former energy gap. By integrating this continuum DOS up to the charge of the isolated molecule, the position of the CNL is determined. Our results show that the energy level alignment at weakly-interacting interfaces can be understood in terms of the tendency of the CNL and the metal work function (in the case metal/organic interfaces) or the CNLs of both materials (at organic heterojunctions) to align.

We have studied the energy level alignment at interfaces containing the following organic materials (see Fig. 4.13): 3,4,9,10-perylenetetracarboxylic dianhydride (PTCDA), 3,4,9,10-perylenetetracarboxylic bisbenzimidazole (PTCBI), 4,4',N,N'- dicarbazolyl biphenyl (CBP), copper phthalocyanine (CuPc), Pentacene, N,N'-diphenyl-N,N'- bis(1-naphthyl)-1,1'- biphenyl-4,4'-diamine (α-NPD), bathocuproine (BCP), tris-(8-hydroxyquinoline) aluminium (Alq_3) and tetrafluorotetracyanoquinodimethane (F_4-TCNQ).

The outline of this thesis is as follows: in the next Chapter, our theoretical method, based on Density Functional Theory (DFT), is described. The advantages and shortcoming are discussed, with emphasis on the well-known underestimation of the energy gap, characteristic of DFT. Since the value of the gap is of great importance in the energy level alignment, a way of correcting this deficiency is presented. The

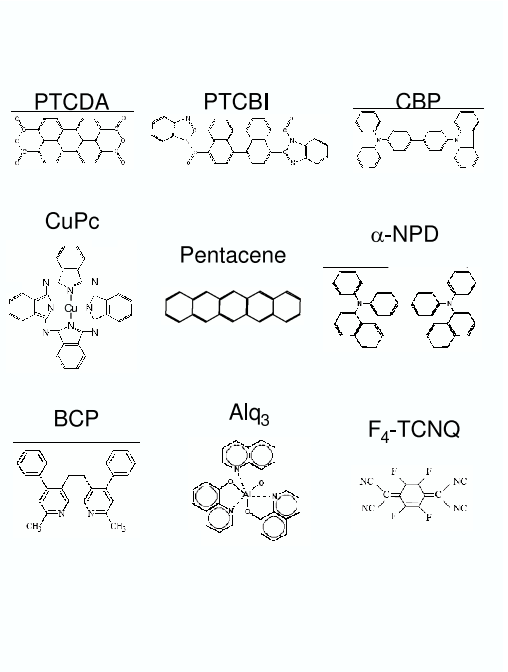

Figure 1.19.: Chemical structure of the organic materials studied in this work.

electronic structure of several organic molecules, ranging from small to large, π-conjugated molecules is presented and discussed.

Chapter 3 deals with metal/organic interfaces. After a brief review of existing mechanisms which have been proposed to operate, our model for non-reactive metal/organic interfaces is presented. Gold is chosen as a typical unreactive metal. From the electronic structure of Au and that of the organic molecules (calculated in the previous chapter), the model for the energy level alignment at these interfaces in terms of the induced DOS, the CNL and interface screening is discussed. Induced dipoles and injection barriers are calculated and compared with experimental results.

In Chapter 4, our model is extended to describe organic/organic interfaces. Since the interaction at these systems is weak, our model is successfully applied to analyze the molecular level offset at organic heterojunctions. Where previous theories had not been able to rationalize the behaviour of these interfaces, our model pro-

vides a simple, yet general explanation, in terms of the partial alignment of the CNLs. The model is then extended to several organic/organic interfaces, where one of the materials is p-doped. The puzzling appearance of large interface dipoles upon doping is explained within our model in terms of a shift in the CNL with doping.

The final Chapter contains some open questions which are treated in an intentionally speculative manner, as well as some concluding remarks about our model, whose strength and appeal lie in being simple and intuitive, while at the same time general and predictive.

CHAPTER 2

Density-functional theory

Oh, I could spend my life having this conversation - look - please try to understand before one of us dies.

(John Cleese)

Don't worry, I know almost exactly what I'm doing.

(Woody Allen)

2.1. Introduction to Density Functional Theory

Since the pioneering work of Hohenberg and Kohn [Hohenberg64] and Kohn and Sham [Kohn65], Density Functional Theory (DFT) has become a standard, powerful technique in theoretical solid-state and condensed-matter physics [Kohn99, Jones89]. In 1998, the Nobel Prize in Chemistry was awarded to Walter Kohn, one of the founding fathers of DFT , and to John Pople, for his work in the implementation of DFT in the famous computational package *Gaussian* [Frisch].

The success of DFT partly stems from the considerable simplification it possesses over traditional wavefunction-based methods, such as Hartree-Fock or Configuration Interaction schemes. Hartree-Fock calculations can be performed on large molecules but electronic correlation, an important ingredient, is not included. Configuration Interaction schemes, on the other hand, include correlation, but fail as they are impossible to implement in practice, when faced with the problem of solving a system with N $\sim$ 100 – 200 electrons, as is the case of the organic molecules considered in this work, due to the enormous complexity of solving the Schrödinger equation (expressed here in atomic units)

$$\sum_i [-\frac{1}{2}\nabla_i^2 \; - \sum_\alpha \frac{Z_\alpha}{|\vec{r}_i - \vec{R}_\alpha|} \; + \sum_{j \neq i} \frac{1}{|\vec{r}_i - \vec{r}_j|}] \; \Psi(\vec{r_1}, \vec{r_2}, ...\vec{r_N}) = E \; \Psi(\vec{r_1}, \vec{r_2}, ...\vec{r_N}) \qquad (2.1)$$

One has no hope of solving an equation like 2.1: as is well known, a wavefunction with 3N variables is unmanageable except in rather small systems. Moreover, the description of the electron-electron interaction, regardless of the number of particles in the system, is a challenge in itself.

The way DFT deals with these problems will be briefly described, focusing on the methods used to calculate exchange correlation energies and the electronic structure of several organic molecules.

2.2. Hohenberg-Kohn theorems

The theoretical foundations of DFT are rooted in a classic paper by Hohenberg and Kohn [Hohenberg64]. This work states that the electronic ground-state density ρ of an interacting N-electron system under an external potential $V^{ext}(\vec{r})$ uniquely determines the Hamiltonian, and thus the energy and other observables of the system.

In addition, the energy functional corresponding to the Hamiltonian of the sys-

tem yields the minimum energy (i.e. the ground-state energy) when the electron density ρ corresponds to the ground-state density, ρ_0.

The ground-state energy, E_0 is therefore a functional of the density of the N-electron system, but E_0 is only obtained when the true ground-state density, ρ_0 is used. A trial density, ρ, yields an upper bound for the ground-state energy, so that the energy functional can be variationally minimized with respect to the density to obtain, at least in principle, the ground-state result.

The N-electron problem is thus reduced to the apparently simpler problem of determining the ground-state density, ρ_0, reducing the initial wavefunction problem of 3N dimensions ($\vec{r}_1$, $\vec{r}_2$, ... $\vec{r}_N$ in the many-body wavefunction Ψ) to one of only 3 ($\vec{r}$ in $\rho(\vec{r})$). However, the exact ground-state density is only obtained, as we have seen, from the *exact* energy functional, and this unfortunately remains unknown.

The energy functional, nevertheless, can be expressed in terms of its different (kinetic, electron-electron and due to the external potential) contributions and one can write, in general terms,

$$E_0[\rho] = T[\rho] + E_{ee}[\rho] + E_{ext}[\rho] \tag{2.2}$$

2.3. The Kohn-Sham equations

The Kohn-Sham (KS) equations [Kohn65] provided a major thrust to DFT by providing a practical method in which the ideas of Hohenberg and Kohn could be implemented.

The key to Kohn-Sham's approach is the statement that, for any interacting N-electron system, an auxiliary **non-interacting** one can be found which yields the same (ground-state) density. To see this, it is useful to separate the 'classical' part of the Coulomb interaction from the 'quantum' one and write

$$E[\rho] = T[\rho] + E_{ext}[\rho] + E_H[\rho] + E_{xc}[\rho] \tag{2.3}$$

where

$$E_{ext}[\rho] = \int V_{ext}(\vec{r})\rho(\vec{r})\ d\vec{r} \tag{2.4}$$

and

$$E_H[\rho] = \frac{1}{2}\ \int \frac{\rho(\vec{r})\rho(\vec{r}')}{|\vec{r}-\vec{r}'|}\ d\vec{r}d\vec{r}' \tag{2.5}$$

E_H is the 'classical' or Hartree contribution, and represents the interaction be-

tween the charge densities $\rho(\vec{r})$ and $\rho(\vec{r}')$ without any quantum effects, such as exchange or correlation, which are included in $E_{xc}[\rho]$, to which we will come later.

Kohn-Sham's approach is to compute the kinetic energy for the auxiliary system, which has the same density as the interacting one. Since the kinetic energy, at variance with exchange and correlation contributions, is known, it is calculated accurately. The exchange and correlation are, too, computed for the non-interacting auxiliary system. The density can thus be written as

$$\rho_{KS}(\vec{r}) = \sum_{i=1}^{N} |\psi_i|^2 \tag{2.6}$$

where ψ_i are the one-particle eigenfunctions of the non-interacting auxiliary system. We therefore have

$$E[\rho_{KS}] = T[\rho_{KS}] + E_{ext}[\rho_{KS}] + E_H[\rho_{KS}] + E_{xc}[\rho_{KS}] \tag{2.7}$$

By variationally minimizing the equation 2.7 with respect to the trial density $\rho_{KS}(\vec{r})$, it can be shown that the non-interacting particles of the auxiliary system must obey the following Schrödinger equation[1]:

$$[-\frac{1}{2}\nabla_i^2 + V_{ext}(\vec{r}) + V_H(\vec{r}) + V_{xc}(\vec{r})]\ \psi_i(\vec{r}) = \epsilon_i\ \psi_i(\vec{r}) \tag{2.8}$$

In this way, the (irresolvable) problem of the interacting N electrons has been substituted by a self-consistent problem of N non-interacting particles moving under the effective potential

$$V_{eff}(\vec{r}) = V_{ext}(\vec{r}) + V_H(\vec{r}) + V_{xc}(\vec{r}), \tag{2.9}$$

where V_{ext} is the external potential, and V_H and V_{xc} are given by

$$V_H(\vec{r}) = \frac{\delta E_H[\rho(\vec{r})]}{\delta\rho(\vec{r})} = \int \frac{\rho(\vec{r}')}{|\vec{r} - \vec{r}'|}\ d\vec{r}' \tag{2.10}$$

[1] It may seem ironical that DFT, which originally devised the density-based approach as an alternative to solving the many-body Schrödinger equation 2.1 ends up faced with another Schrödinger equation such as 2.8. However, the important difference is that equation 2.1 is a many-body irresolvable equation, whereas the one proposed by the Kohn-Sham scheme can be tackled with methods which we now describe.

$$V_{xc}(\vec{r}) = \frac{\delta E_{xc}[\rho(\vec{r})]}{\delta \rho(\vec{r})} \tag{2.11}$$

Within the Kohn-Sham approach, the energy of the system E_{KS} is given by [Kohn65]

$$E[\rho(\vec{r})] = \sum_{i=1}^{N} \epsilon_i - \frac{1}{2} \int V_H(\vec{r}) \rho(\vec{r})\ d\vec{r} + E_{xc}[\rho(\vec{r})] - \int V_{xc}(\vec{r}) \rho(\vec{r})\ d\vec{r} \tag{2.12}$$

It is important to mention that the kinetic energy of the non-interacting particles is not equal to the 'true' kinetic of the interacting electron system. The Kohn-Sham approach is to compute the kinetic energy of the **non-interacting** system and to include the remainder in the exchange-correlation functional. In this way, the Kohn-Sham exchange-correlation energy not only contains quantum-mechanical contributions (exchange and correlation, and possibly self-interaction correction), but also a part of the kinetic energy of the **interacting** system that is not accounted for in the non-interacting picture.

Unfortunately, the exact expression of the exchange-correlation functional is unknown. The central goal in DFT has been, and still is, to find better and better approximations to E_{xc} and V_{xc}.

2.3.1. LDA approximation

The Local-Density Approximation (LDA) [Kohn65, Jones89] consists in assuming that the exchange-correlation energy per electron, $\epsilon_{xc}(\vec{r})$ equals that of a uniform electron gas of the same density $\rho(\vec{r})$. As its name implies, the LDA approximation is **local**: the exchange-correlation energy on each point depends only on the electronic density at that point rather than on the density on all points, so that we have $\epsilon_{xc}(\vec{r})$ and not $\epsilon_{xc}[\rho(\vec{r})]$. We therefore have

$$E_{xc}^{LDA}[\rho(\vec{r})] = \int \epsilon_{xc}(\vec{r}) \rho(\vec{r})\ d\vec{r} \tag{2.13}$$

$$V_{xc}^{LDA} = \epsilon_{xc}(\vec{r}) + \frac{d\epsilon_{xc}(\vec{r})}{d\rho}\ \rho(\vec{r}) \tag{2.14}$$

This implies using, at each point, the equations for a uniform electron gas having that same density. Since the electronic density in real systems is far from uniform, LDA implies quite a simplification, since it neglects the density at points other than

$\vec{r}$, and just considers the value there. Thus, the model is quite a drastic idealization of the rapidly-varying atomic potentials which electrons in metals experience. The reason for invoking the uniform electron gas is that it is the only electron system for which the exact exchange-correlation functional is known. Nevertheless, such an apparently crude approximation made in LDA works surprisingly well and has been used extensively to obtain, with a reasonable degree of accuracy, many electronic properties of atoms, molecules and solids [Jones89, Kohn99].

Nonetheless, it is known that LDA is notable for several characteristic shortcomings. Weak bonds, such as Hydrogen and van der Waals bonds, are poorly described by LDA and, more generally, by DFT. In these weak bonds, the electronic density is small, whereas DFT and LDA are appropriate for stronger bonds where $\rho(\vec{r})$ is higher. Even with very large basis sets, LDA overestimates bond lengths in molecules and solids by $\sim$ 3% [Pou01]. In solids, the compressibility modulus is generally larger than experiment. Moreover, exchange-correlation energy is overestimated in molecules and solids, in some cases by as much as 100% [Oszwaldowski03]. In magnetic systems, in some cases the ground state does not have the appropriate (for instance, ferromagnetic) properties.

2.3.2. GGA approximation

As an extension of the LDA approximation, the Generalized Gradient Approximation (GGA) calculates the exchange-correlation energy as a function f of both the density and its gradient:

$$E_{xc}^{GGA}[\rho(\vec{r})] = \int f[\rho(\vec{r}), \nabla\rho(\vec{r})]\, d(\vec{r}) \tag{2.15}$$

It is a local approximation since it depends on these values at the point $\vec{r}$. The gradient takes into account inhomogeneities in the electron density.

GGA improves on most of the deficiencies of LDA, especially exchange-correlation energies. Bond lengths are mostly unaffected, except for Hydrogen or van der Waals bonds, which are improved. Binding energies are improved too in molecules and solids.

Though not systematic, the improvements of GGA can be understood since it provides a better description of the electron density, taking into account the rapidly-varying potential (and thus density) around atomic nuclei.

The GGA approximation, already proposed in the original Hohenberg-Kohn pa-

per [Hohenberg64], suggests a series expansion of the exchange-correlation functional in powers of the gradient around the uniform density, $\rho(\vec{r})$. However, promising as it seems, this approach fails to produce better and better results when applied to molecules [Koch00], since this series violates certain physical properties[2], thus losing essential features which apparently any successful exchange-correlation functional must possess.

2.3.3. Other functionals

Besides LDA and GGA, many other exchange-correlation functionals have been developed [Koch00]. Some approaches, like the Optimized Effective Potential or Optimized Potential Method [Ullrich95, Sharp53], use as a fundamental quantity not the density, but the Kohn-Sham orbitals. In general terms, this allows a better self-interaction correction at the expense of computational complexity.

Another 'school' has been to use empirical or semiempirical approaches, where the driving force has not been physical intuition as much as better agreement with a given set of experimental data. These 'hybrid' functionals have experienced great success, notably the B3LYP functional [Stephens94]. In general, they contain several contributions, such as exact exchange, and exchange and correlation gradient-corrected expressions, the relative amounts of which are determined by a fit to a large set of experimental results (heats of formation, ionization affinity energies, total energies, etc., of different chemical compounds).

2.4. Orbital Occupancy

The Orbital Occupancy approach is an equivalent formulation of DFT [Pou00], which uses a localized basis set, and considers as the fundamental quantity not the density $\rho(\vec{r})$ but the set of occupations $\{n_i\}$ in the ground state (GS) of the local orbitals $\{\phi_i\}$. The different energy functionals are written in terms of the set $\{n_i\}$, where $n_i = \sum_k^{occ} |\langle\phi_i|\psi_k\rangle|^2$, where ψ_k are the eigenfunctions. It can be shown [Pou00] that this formulation is equivalent to the traditional DFT approach.

Conventional DFT approaches based on $\rho(\vec{r})$ generally use plane waves as the

[2]Such as the Fermi and Coulomb sum rules, or requiring the Fermi hole to be negative for any $(\vec{r_1}, \vec{r_2})$.

basis set [Payne92]:

$$\varphi(\vec{r}) = \frac{1}{V}\sum_i e^{i\vec{k}\vec{r}} \tag{2.16}$$

The Orbital Occupancy method, on the other hand, uses local orbitals as the basis set. These local orbitals are typically the atomic orbitals $\chi(\vec{r})$ of the atoms of the system. Because the atomic basis set is not orthogonal, we follow Löwdin's transformation [Lödin50] and write

$$\phi_i(\vec{r}) = \sum_j (S^{-1/2})_{ij}\ \chi_j(\vec{r}), \tag{2.17}$$

where S is the overlap matrix, with $S_{ij} = < \chi_i | \chi_j >$.

The Löwdin functions $\{\phi_i\}$ form an orthogonal basis set. In the Orbital Occupancy approach, it is useful to work in second quantization [Kittel87], making use of the creation and annihilation operators ($\hat{c}_i^+$, $\hat{c}_i$) in orthogonal states i. The orbital occupancies $\{n_{i\alpha\sigma}\}$ are given by the expectation value of the number operator ($\hat{n}_{i\alpha\sigma} = \hat{c}^+_{i\alpha\sigma}\hat{c}_{i\alpha\sigma}$) in the ground state:

$$n_{i\alpha\sigma} = \langle GS|\hat{n}_{i\alpha\sigma}|GS\rangle \tag{2.18}$$

Typically, the index i refers to the site (i.e. to the atom), α labels an orbitals (an s, p or d orbital of atom i, for example) and σ is the spin (up or down) state.

The general Hamiltonian

$$\hat{H} = -\sum_i \frac{1}{2}\nabla^2\ -\ \sum_{i\alpha}\frac{Z_\alpha}{|\vec{r}_i - \vec{R}_\alpha|}\ +\frac{1}{2}\sum_{i,j\neq i}\frac{1}{|\vec{r}_i - \vec{r}'_j|} \tag{2.19}$$

can be rewritten in second quantization as

$$\hat{H} = \sum_{i\sigma}\left(\epsilon_i + V_{ii}^{psp}\right)\hat{n}_{i\sigma}\ +\ \sum_{\substack{i,j\neq i\\ \sigma}}\left(t_{ij} + V_{ij}^{psp}\right)\hat{c}^+_{i\sigma}\hat{c}_{j\sigma}\ +\ \sum_{\substack{ijkl\\ \sigma\sigma'}} O_{lk}^{ij}\ \hat{c}^+_{i\sigma}\hat{c}^+_{j\sigma'}\hat{c}_{k\sigma'}\hat{c}_{l\sigma} \tag{2.20}$$

where

$$\epsilon_i = \int \phi_i^*(\vec{r}) \left[-\frac{1}{2}\nabla^2 + \sum_\alpha \frac{Z_\alpha}{|\vec{r} - \vec{R}_\alpha|} \right] \phi_i(\vec{r}) \, d\vec{r} \tag{2.21}$$

$$t_{ij} = \int \phi_i^*(\vec{r}) \left[-\frac{1}{2}\nabla^2 + \sum_\alpha \frac{Z_\alpha}{|\vec{r} - \vec{R}_\alpha|} \right] \phi_j(\vec{r}) \, d\vec{r} \tag{2.22}$$

$$O_{lk}^{ij} = \int \phi_i^*(\vec{r}) \phi_j^*(\vec{r}') \, \frac{1}{|\vec{r} - \vec{r}'|} \, \phi_k(\vec{r}') \phi_l(\vec{r}) \, d\vec{r} d\vec{r}' \tag{2.23}$$

$$\tag{2.24}$$

In equation 2.20, V^{psp} is the pseudopotential: it describes the effect of the core electrons on the valence ones [Pou01]. This allows the core electrons to be excluded from the calculations, thereby simplifying the problem, since it reduces the size of the Hamiltonian matrix, such that the index i in equations 2.21 only runs over the valence electrons of the system.

Equation 2.20 is the complete Hamiltonian of the system; in particular, ϵ_i and t_{ij} are one-body terms, whereas O_{lk}^{ij} are the many-body terms, describing the full electron-electron interaction. Equation 2.20 can be simplified by considering all the combinations O_{lk}^{ij} and retaining in the Hamiltonian the most important contributions. These are:

$$\begin{aligned}
\hat{H} \;=\; & \sum_{i\alpha\sigma} \left(\epsilon_{i\alpha} \;+\; V_{i\alpha,i\alpha}^{psp} \right) \hat{n}_{i\alpha\sigma} \;+\; \sum_{\substack{i\alpha\sigma, j\beta\sigma \\ j\beta \neq i\alpha}} \left(t_{i\alpha,j\beta} + V_{i\alpha,j\beta}^{psp} \right) \hat{c}_{i\alpha\sigma}^{+} \hat{c}_{j\beta\sigma} + \\
& + \;\; \frac{1}{2} \sum_{\substack{i\alpha\sigma, i\beta\sigma' \\ i\beta\sigma' \neq i\alpha\sigma}} U_{i\alpha,i\beta} \; \hat{c}_{i\alpha\sigma}^{+} \hat{c}_{i\beta\sigma'}^{+} \hat{c}_{i\beta\sigma'} \hat{c}_{i\alpha\sigma} \;+\; \frac{1}{2} \sum_{\substack{i\alpha\sigma, i\beta\sigma' \\ i\beta\sigma' \neq i\alpha\sigma}} U_{i\alpha,i\beta}^{x} \; \hat{c}_{i\alpha\sigma}^{+} \hat{c}_{i\beta\sigma'}^{+} \hat{c}_{i\alpha\sigma'} \hat{c}_{i\beta\sigma} + \\
& + \;\; \frac{1}{2} \sum_{\substack{i\alpha\sigma, j\beta\sigma' \\ j \neq i}} J_{i\alpha,j\beta} \; \hat{c}_{i\alpha\sigma}^{+} \hat{c}_{j\beta\sigma'}^{+} \hat{c}_{j\beta\sigma'} \hat{c}_{i\alpha\sigma} + \frac{1}{2} \sum_{\substack{i\alpha\sigma, j\beta\sigma' \\ j \neq i}} J_{i\alpha,j\beta}^{x} \; \hat{c}_{i\alpha\sigma}^{+} \hat{c}_{j\beta\sigma'}^{+} \hat{c}_{i\alpha\sigma'} \hat{c}_{j\beta\sigma} + \\
& + \sum_{\substack{i\alpha\sigma, j\beta\sigma, \\ k\gamma\sigma' \\ j\beta \neq i\alpha \\ k\gamma\sigma' \neq i\alpha\sigma, j\beta\sigma}} h_{k\gamma,i\alpha j\beta} \; \hat{c}_{k\gamma\sigma'}^{+} \hat{c}_{i\alpha\sigma}^{+} \hat{c}_{j\beta\sigma} \hat{c}_{k\gamma\sigma'} \;+ \sum_{\substack{i\alpha\sigma, j\beta\sigma, \\ k\gamma\sigma' \\ j\beta \neq i\alpha \\ k\gamma\sigma' \neq i\alpha\sigma, j\beta\sigma}} h_{k\gamma,i\alpha j\beta}^{x} \; \hat{c}_{k\gamma\sigma}^{+} \hat{c}_{i\alpha\sigma'}^{+} \hat{c}_{k\gamma\sigma'} \hat{c}_{j\beta\sigma} + \\
& + \;\; \frac{1}{2} \sum_{\substack{i\alpha\sigma, j\beta\sigma \\ k\gamma\sigma', l\delta\sigma' \\ all \;\; diff.}}^{NN} O_{l\gamma k\delta}^{i\alpha j\beta} \; \hat{c}_{i\alpha\sigma}^{+} \hat{c}_{j\beta\sigma}^{+} \hat{c}_{k\gamma\sigma'} \hat{c}_{l\delta\sigma'}
\end{aligned} \tag{2.25}$$

where index i refers to a particular site (atom), α to an atomic orbital of this atom, and σ labels the spin state.

These contributions are

$$U_{i\alpha} = \int |\phi_{i\alpha}(\vec{r})|^2 \frac{1}{|\vec{r}_i - \vec{r}'_j|} |\phi_{i\alpha}(\vec{r}')|^2 \, d\vec{r}d\vec{r}' \tag{2.26}$$

$$U^x_{i\alpha} = \int \phi^*_{i\alpha}(\vec{r})\phi^*_{i\beta} \frac{1}{|\vec{r}_i - \vec{r}'_j|} \phi_{i\alpha}(\vec{r}')\phi_{i\beta}(\vec{r}) \, d\vec{r}d\vec{r}' \tag{2.27}$$

$$J_{i\alpha j\beta} = \int |\phi_{i\alpha}(\vec{r})|^2 \frac{1}{|\vec{r} - \vec{r}'|} |\phi_{j\beta}(\vec{r}')|^2 \, d\vec{r}d\vec{r}' \tag{2.28}$$

$$J^x_{i\alpha j\beta} = \int \phi^*_{i\alpha}(\vec{r})\phi^*_{j\beta}(\vec{r}') \frac{1}{|\vec{r} - \vec{r}'|} \phi_{i\alpha}(\vec{r'})\phi_{j\beta}(\vec{r}) \, d\vec{r}d\vec{r}' \tag{2.29}$$

$$h_{k\gamma,i\alpha j\beta} = \int |\phi_{k\gamma}(\vec{r})|^2 \frac{1}{|\vec{r} - \vec{r}'|} \phi_{i\alpha}(\vec{r}')\phi_{j\beta}(\vec{r}') \, d\vec{r}d\vec{r}' \tag{2.30}$$

$$h^x_{k\gamma,i\alpha j\beta} = \int \phi^*_{k\gamma}(\vec{r})\phi^*_{i\alpha}(\vec{r}) \frac{1}{|\vec{r} - \vec{r}'|} \phi_{j\beta}(\vec{r}')\phi_{k\gamma}(\vec{r}') \, d\vec{r}d\vec{r}' \tag{2.31}$$

These daunting equations represent the most important contributions to the electron-electron interaction: the first two, $U_{i\alpha}$ and $J_{i\alpha j\beta}$ are the usual Coulomb terms for two charge densities at atoms and sites $i\alpha$ and $i\alpha, j\beta$, respectively. $h_{k,ij}$ describes the hopping term between orbitals i and j, induced by the electron density at site k. The terms U^x_i, J^x_{ij} and $h^x_{k,ij}$ are exchange terms, only between electrons of the same spin, that correct the appropriate (U_i, J_{ij} or $h_{k,ij}$) interactions. Finally, notice that the four-center interactions O^{ij}_{kl} extend only to nearest-neighbour atoms.

Hamiltonian 2.25 is expressed in terms of creation and destruction **operators**, whereas the Orbital Occupancy functionals are expressed in terms of the occupation **numbers** $n_{i\alpha\sigma}$, which are the expectation values of these operators in the ground state. The Hartree and exchange contributions are obtained by averaging the operators $\hat{c}^+_i \hat{c}^+_j \hat{c}_k \hat{c}_l$ in equation 2.25. The contraction of the first and fourth operators, and second and third, leads to Hartree terms, while that of the first and third, and second and fourth, leads to exchange contributions, except for the terms with the 'x' superscript, where the opposite occurs.

2.5. Hartree, exchange and correlation functionals

The Hartree energy, E^H, determined by appropriately averaging the creation and destruction operators in Hamiltonian 2.25, is

$$\begin{aligned} E^H &= \sum_{i\alpha\sigma} \left(\epsilon_{i\alpha} + V^{psp}_{i\alpha,i\alpha}\right) n_{i\alpha\sigma} + \sum_{\substack{i\alpha\sigma,j\beta\sigma \\ j\beta\neq i\alpha}} \left(t_{i\alpha,j\beta} + V^{psp}_{i\alpha,j\beta}\right) n_{i\alpha\sigma,j\beta\sigma} + \\ &+ \frac{1}{2} \sum_{\substack{i\alpha\sigma,i\beta\sigma' \\ i\beta\sigma'\neq i\alpha\sigma}} U_{i\alpha,i\beta}\; n_{i\alpha\sigma} n_{i\beta\sigma'} + \frac{1}{2} \sum_{\substack{i\alpha\sigma,i\beta\sigma' \\ i\beta\sigma'\neq i\alpha\sigma}} U^x_{i\alpha,i\beta}\; n_{i\alpha\sigma,i\beta\sigma}\; n_{i\beta\sigma',i\alpha\sigma'} + \\ &+ \frac{1}{2} \sum_{\substack{i\alpha\sigma,j\beta\sigma' \\ j\neq i}} J_{i\alpha,j\beta}\; n_{i\alpha\sigma} n_{j\beta\sigma'} + \frac{1}{2} \sum_{\substack{i\alpha\sigma,j\beta\sigma' \\ j\neq i}} J^x_{i\alpha,j\beta}\; n_{i\alpha\sigma,j\beta\sigma}\; n_{j\beta\sigma',i\alpha\sigma'} + \\ &+ \sum_{\substack{i\alpha\sigma,j\beta\sigma, \\ k\gamma\sigma' \\ j\beta\neq i\alpha}} h_{k\gamma,i\alpha j\beta}\; n_{k\gamma\sigma'} n_{i\alpha\sigma,j\beta\sigma} + \sum_{\substack{i\alpha\sigma,j\beta\sigma, \\ k\gamma\sigma' \\ j\beta\neq i\alpha}} h^x_{k\gamma,i\alpha j\beta} n_{k\gamma\sigma,j\beta\sigma} n_{i\alpha\sigma,k\gamma\sigma'} + \\ &+ \frac{1}{2} \sum_{\substack{i\alpha\sigma,j\beta\sigma \\ k\gamma\sigma',l\delta\sigma' \\ all\ diff.}}^{NN} O^{i\alpha j\beta}_{l\gamma\ k\delta}\; n_{i\alpha\sigma,l\delta\sigma} n_{j\beta\sigma',k\gamma\sigma'} \end{aligned} \tag{2.32}$$

where the last term O^{ij}_{kl} is included in mean field and are small ($< 1\%$) in the case of the molecules which have been studied.

Notice that in this formulation, self-interaction corrections, so troublesome in conventional DFT, are automatically taken into account, since self-interaction terms in 2.32 are appropriately corrected by the corresponding terms in 2.33.

The exchange energy derived from Hamiltonian 2.25, obtained by contracting the

creation and destruction operators, is given by

$$\begin{aligned} E^x &= -\frac{1}{2}\sum_{i\alpha\sigma} U_{i\alpha,i\alpha}\; n_{i\alpha\sigma}n_{i\alpha\sigma} - \frac{1}{2}\sum_{i\alpha\sigma,i\beta\sigma} U_{i\alpha,\beta}\; n_{i\alpha\sigma,i\beta\sigma}n_{i\beta\sigma,i\alpha\sigma} - \frac{1}{2}\sum_{i\alpha\sigma,\beta\sigma} U^x_{i\alpha,i\beta}\; n_{i\alpha\sigma}n_{i\beta\sigma} - \\ &- \frac{1}{2}\sum_{i\alpha\sigma,j\beta\sigma} J_{i\alpha,j\beta}\; n_{i\alpha\sigma,j\beta\sigma}n_{j\beta\sigma,i\alpha\sigma} - \frac{1}{2}\sum_{i\alpha\sigma,j\beta\sigma} J^x_{i\alpha,j\beta}\; n_{i\alpha\sigma}n_{j\beta\sigma} - \\ &- \sum_{i\alpha\sigma,j\beta\sigma}[h_{i\alpha,i\alpha j\beta}\; n_{i\alpha\sigma}n_{i\alpha\sigma,j\beta\sigma} + h_{j\beta,i\alpha j\beta}\; n_{j\beta\sigma}n_{i\alpha\sigma,j\beta\sigma}] - \sum_{\substack{i\alpha\sigma,j\beta\sigma,\\ k\gamma\sigma',\\ j\beta\neq i\alpha}} h_{k\gamma,i\alpha j\beta}\; n_{i\alpha\sigma,k\gamma\sigma}n_{k\gamma\sigma,j\beta\sigma} - \\ &- \sum_{i\alpha\sigma,j\beta\sigma}[h^x_{i\alpha,i\alpha j\beta}\; n_{i\alpha\sigma}n_{i\alpha\sigma,j\beta\sigma} + h^x_{j\beta,i\alpha j\beta}\; n_{j\beta\sigma}n_{i\alpha\sigma,j\beta\sigma}] - \sum_{\substack{i\alpha\sigma,j\beta\sigma,\\ k\gamma\sigma',\\ j\beta\neq i\alpha}} h^x_{k\gamma,i\alpha j\beta}\; n_{k\gamma\sigma}n_{i\alpha\sigma,j\beta\sigma} - \\ &- \frac{1}{2}\sum_{\substack{i\alpha\sigma,j\beta\sigma\\ k\gamma\sigma,l\delta\sigma}} O^{i\alpha j\beta}_{l\delta\;\; k\gamma}\; n_{i\alpha\sigma,l\delta\sigma}n_{j\beta\sigma,k\gamma\sigma} \end{aligned} \tag{2.33}$$

Many contributions of equation 2.33, such as the first term and those in square brackets, are self-interaction correction terms, as mentioned above. This energy can be further simplified by making use of the sum rule [Pou00]

$$\sum_{j\beta\neq i\alpha} n_{i\alpha\sigma,j\beta\sigma}n_{j\beta\sigma,i\alpha\sigma} = n_{i\alpha\sigma}\;(1 - n_{i\alpha\sigma}) \tag{2.34}$$

and introducing an effective interaction J^{eff} between the charge $n_{i\alpha\sigma}$ and its hole 1 - $n_{i\alpha\sigma}$ through

$$\begin{aligned} -\frac{1}{2}\sum_{i\alpha\sigma,i\beta\sigma} U_{i\alpha,i\beta}\;\; n_{i\alpha\sigma,i\beta\sigma}n_{i\beta\sigma,i\alpha\sigma} - \frac{1}{2}\sum_{\substack{i\alpha\sigma,j\beta\sigma\\ (j\neq i)}} J_{i\alpha,j\beta}\; n_{i\alpha\sigma,j\beta\sigma}n_{j\beta\sigma,i\alpha\sigma} = \\ = \quad -\frac{1}{2}\sum_{i\alpha\sigma} J^{eff}_{i\alpha\sigma}\; n_{i\alpha\sigma}(1 - n_{i\alpha\sigma}) \end{aligned} \tag{2.35}$$

If the fraction $n_{i\alpha\sigma}$ is located at the site $i\alpha\sigma$, then the remainder up to the total hole of 1 must be found outside. Here, $J^{eff}_{i\alpha\sigma}$ is the effective Coulomb interaction between the electron density at site i, $n_{i\alpha\sigma}$, and its exchange hole, with the intraatomic ($n_{i\alpha\sigma}$) and extraatomic (1 - $n_{i\alpha\sigma}$) holes appropriately weighted. The extraatomic hole is delocalized typically over the nearest-neighbors.

We introduce intraatomic exchange effects by the appropriate modification of the interactions: if we consider that a fraction x of the exchange hole is intraatomic

(located on other orbitals of the same atom), this is accounted for, with a similar decrease of the extraatomic hole. The exchange contribution now reads:

$$U\ x\ n_{i\alpha\sigma}\ (1-n_{i\alpha\sigma}) + (1-x)\ J\ n_{i\alpha\sigma}\ (1-n_{i\alpha\sigma}) \tag{2.36}$$

This intraatomic exchange hole has been shown to be important for the molecules studied.

The exchange energy 2.33 can thus be written as

$$\begin{aligned} E^x = \ & -\ \frac{1}{2}\sum_{i\alpha\sigma}\Big[U_{i\alpha}\ n_{i\alpha\sigma} + J^{eff}_{i\alpha}\ (1-n_{i\alpha\sigma})\Big] n_{i\alpha\sigma} - \frac{1}{2}\sum_{i\alpha\sigma,i\beta\sigma} U^x_{i\alpha,i\beta}\ n_{i\alpha\sigma}n_{i\beta\sigma} - \\ & -\ \frac{1}{2}\sum_{i\alpha\sigma,j\beta\sigma} J^x_{i\alpha,j\beta}\ n_{i\alpha\sigma}n_{j\beta\sigma} - \sum_{i\alpha\sigma,j\beta\sigma} h^{eff}_{i\alpha,j\beta}\ n_{i\alpha\sigma,j\beta\sigma} - \\ & -\ \sum_{\substack{i\alpha\sigma,j\beta\sigma,\\ k\gamma\sigma}} h^x_{i\alpha,j\beta k\gamma}\ n_{i\alpha\sigma}n_{j\beta\sigma,k\gamma\sigma} - \frac{1}{2}\sum_{\substack{i\alpha\sigma,j\beta\sigma\\ k\gamma\sigma,l\delta\sigma}} O^{i\alpha j\beta}_{l\delta\ k\gamma}\ n_{i\alpha\sigma,l\delta\sigma}n_{j\beta\sigma,k\gamma\sigma} \end{aligned} \tag{2.37}$$

The correlation energy can be included by considering that the exchange (now exchange-correlation) hole is modified, in such way that it is not localized on the neighbours, but that a fraction $f_{i\alpha\sigma}$ ($0 < f_{i\alpha\sigma} < 1$) of the hole is transferred to site $i\alpha\sigma$. Thus, the correlation energy can be written as

$$E^c[n_{i\alpha\sigma}] = -\frac{1}{2}\sum_{i\alpha\sigma} f_{i\alpha\sigma}(U_{i\alpha} - J^{eff}_{i\alpha\sigma})\ n_{i\alpha\sigma}(1-n_{i\alpha\sigma}) \tag{2.38}$$

The Hartree, exchange and correlation functionals are given in terms of the orbital occupancies by equations 2.32, 2.37 and 2.38.

The derivative of the Hartree and exchange-correlation energies with respect to the occupation numbers yields the corresponding potentials:

$$\begin{aligned} V^H_{i\alpha\sigma}[n_{i\alpha\sigma}] &= \frac{\partial E_H}{\partial n_{i\alpha\sigma}} \\ V^{xc}_{i\alpha\sigma}[n_{i\alpha\sigma}] &= \frac{\partial E_{xc}}{\partial n_{i\alpha\sigma}} \end{aligned} \tag{2.39}$$

With these potentials, the full Hamiltonian 2.25 is reduced to an effective one-

particle Hamiltonian:

$$\hat{H}^{eff} = \sum_{i\alpha\sigma} (\widetilde{\epsilon}_{i\alpha\sigma} + V^H_{i\alpha\sigma} + V^{xc}_{i\alpha\sigma})\ \hat{n}_{i\alpha\sigma}\ +\ \widetilde{T}_{ij}\ \hat{c}^+_{i\alpha\sigma}\hat{c}_{j\alpha\sigma} \tag{2.40}$$

Hamiltonian 2.40 can be solved iteratively. Starting with an initial guess $\{n^{in}_{i\alpha\sigma}\}$, these occupation numbers are used to compute the different terms of 2.40: the values $\epsilon_{i\alpha\sigma}$, T_{ij} and the potentials which simulate the electron-electron interaction, $V^H_{i\alpha\sigma}$ and $V^{xc}_{i\alpha\sigma}$. With these, $\hat{H}^{eff}$ is solved, and the output charges are obtained by summing the weight of the occupied eigenfunctions of $\hat{H}^{eff}$ on the corresponding Löwdin orbitals, $n^{out}_{i\alpha\sigma} = \sum_n^{occ} |\langle\phi_{i\alpha\sigma}|\psi_n\rangle|^2$. These are, in turn, used as inputs for the next iteration, until the $\{n^{in}_{i\alpha\sigma}\}$ equal $\{n^{out}_{i\alpha\sigma}\}$ to within a (small) tolerance, whereby self-consistency is achieved.

The ground-state energy of Hamiltonian 2.40 is given by

$$\begin{aligned} E[\{n_{i\sigma}\}] &= \sum_n^{occ} \epsilon_n + E_H[\{n_{i\sigma}\}] + E_{xc}[\{n_{i\sigma}\}] - \sum_{i\sigma}(V^H_{i\sigma} + V^{xc}_{i\sigma})\ n_{i\sigma} = \\ &= \sum_n^{occ} \epsilon_n - E_H[\{n_{i\sigma}\}] + E_{xc}[\{n_{i\sigma}\}] - \sum_{i\sigma} V^{xc}_{i\sigma}\ n_{i\sigma} \end{aligned} \tag{2.41}$$

2.6. Results for small molecules

We have investigated the accuracy of the above exchange-correlation functional through the study of the electronic structure of several small molecules: CO, CO_2, CH_4, C_2H_4 and Benzene (C_6H_6), as well as in PTCDA (discussed later). The electronic spectrum, as well as binding, exchange-correlation energies and bonding distances are calculated and compared to other theoretical approaches and experimental results.

This method, which uses the Orbital Occupancy approach, is implemented using Slater-type orbitals, and is therefore referred to as LCAO-OO. Details of the method and its implementation in several computational codes have been described elsewhere [Pou00, Pou01, Pou02].

2.6.1. Basis set

For our calculation, a minimal basis set was used. This means using the 2s and 2p orbitals for C and O, and 1s for H (since the molecules under study in this section only contain these atoms). A 'frozen core' approximation has been intro-

duced for the core orbitals (C 1s and O 1s). Although the oscillations of the valence orbitals in the core region are not eliminated, the core electrons are included as a pseudopotential acting on the valence electrons: the diagonal and off-diagonal elements for valence orbitals are modified to include the effect of the core electrons [Pou01, Pou98]. This modification consists on a shift in the diagonal and off-diagonal elements for the valence orbitals. The shifts are calculated by expanding the interactions between the core and valence orbitals in powers of their mutual overlap, and approximating them up to second order. The shifts have contributions coming from electrostatic interaction and repulsion due to the valence-core overlap and hybridization [Pou98] (for clarity the formulas provided here are slightly simplified with respect to the ones used in the actual calculation). The diagonal and off-diagonal shifts are:

$$\Delta V_{vv\sigma} = \sum_c \left[S_{vc}^2 \left(E_{v\sigma}^{at} - E_{c\sigma}^{at} \right) + J_{vc}^{(0)} \left(n_{c\sigma} + n_{c\bar{\sigma}} \right) + J_{vc}^{(0)} S_{vc}^2 n_{c\sigma} - J_{vc}^{X(0)} n_{c\sigma} \right], \quad (2.42)$$

$$\Delta V_{vv'\sigma} = \sum_c \left[S_{vc} S_{v'c} \left(\frac{E_{v\sigma}^{at} + E_{v'\sigma}^{at}}{2} - E_{c\sigma}^{at} \right) + h_{c,vv'}^{(0)} \left(n_{c\sigma} + n_{c\bar{\sigma}} \right) \right] + + \sum_c \left(\frac{J_{vc}^{(0)} + J_{v'c}^{(0)}}{2} S_{vc} S_{v'c} - h_{c,vv'}^{X(0)} \right) n_{c\sigma}. \quad (2.43)$$

Here S_{cv} are overlap matrix elements (c=core, v=val), $E_{v\sigma}^{at}$ $\left(E_{c\sigma}^{at} \right)$ are atomic valence (core) levels, and $J_{vc}^{(0)}$, $h_{c,vv'}^{(0)}$, $h_{c,vv'}^{X(0)}$ are the interactions described previously, but calculated for atomic (non-orthogonal) orbitals. The first term both in (2.42) and (2.43) represents the repulsion due to the overlap and hybridization. The other terms stem from the electrostatic repulsion and exchange interaction of the valence and core electrons.

Even though a minimal basis set is mainly useful in the case of large molecules or bulk crystals, we have nevertheless found it a sufficiently good description for the study of the electronic properties of these molecules. The effect of the basis set will be nevertheless commented on below.

In the LCAO-OO approach, the basis set comprises Slater-type orbitals (STOs). The characteristic of these STOs is that their radial part has an negative exponential term which governs the 'size' or extension of the orbital:

$$STO\ (r) \sim r^l\ e^{-\zeta r} \quad (2.44)$$

Atomic orbitals are described as a linear combination of STOs, where the coefficients for the different atoms are parameterized in the Tables of Clementi and Roetti [Clementi74]. For instance, 2s and 2p orbitals can be given by

$$\begin{aligned} |2s\rangle &= \alpha_1 |STO_1\rangle + \alpha_2 |STO_2\rangle, \\ |2p\rangle &= \alpha_3 |STO_3\rangle \end{aligned} \tag{2.45}$$

or by

$$\begin{aligned} |2s\rangle &= \alpha_1 |STO_1\rangle + \alpha_2 |STO_2\rangle + \alpha_3\rangle |STO_3\rangle + \alpha_4 |STO_4\rangle, \\ |2p\rangle &= \alpha_5 |STO_5\rangle + \alpha_6 |STO_6\rangle \end{aligned} \tag{2.46}$$

Notice that STOs of the correct angular dependence are combined: in the case of equations 2.45, for example, STOs 1 and 2 have s ($l = 0$) symmetry, whereas STO_3 has $l = 1$, as corresponds to the 2p orbital it describes. Note also that half as many STOs are involved in equation 2.45 than in 2.46. The first case is referred to as a single-zeta (sz) basis set, whereas the second is a double-zeta (dz) one. A double-zeta basis set provides a better description of the molecular bonds at the expense of a greater computational cost. We have used both single-zeta and double-zeta basis sets in our calculations, and the results are discussed. Fig. 2.1 shows the atomic single- and double-zeta 2s and 2p orbitals for C.

Since the **atomic** orbitals parameterized by the tables of Clementi and Roetti do not provide the best description of the molecular bonds, we have optimized the (single- or double-zeta) basis for each molecule. This optimization was done by variationally maximizing the binding energy with respect to the Slater (ζ) exponents. More will be said about this procedure below. This basis optimization enables a better description of the molecular bonds.

The atomic orbitals thus described are then subject to a Löwdin transformation (equation 2.17), since they are not orthogonal.

Results for several small molecules are presented. By computing the molecular energy at several distances, the binding energy curve can be obtained, and a bonding distance can be calculated. This is done for several approximations to Hamiltonian 2.40. The molecular binding energy E^b is defined as the difference between the molecular energy and the sum of the individual atomic energies (which sets the zero of the binding energy scale):

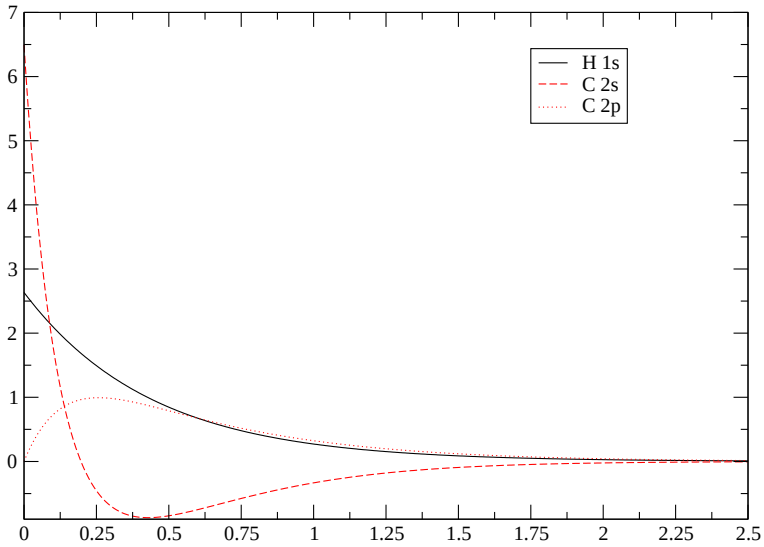

Figure 2.1.: Radial part of the atomic H 1s and C 2s and 2p wavefunctions.

$$E^b = E_{molec} - \sum E_{at} \tag{2.47}$$

The binding energy, the different contributions to it, as well as the electronic structure of several small molecules are presented and discussed below:

2.6.2. CO

The results for the binding energy of CO can be summarized in the following table. The total binding energy (E^b) includes correlation effects, when these are calculated. E^{HF} represents the Hartree-Fock contribution to the binding energy, and E^c is the correlation energy, defined at the difference between E^b and E^{HF}. The equilibrium bonding distance d is also quoted. sz and dz mean single- and double-zeta basis sets, respectively.

The 'experimental' Hartree-Fock energy is calculated using a large basis set, so it can be considered basis-converged. The 'experimental' value for the correlation energy is defined as the difference between the experimental binding energy and the basis-converged Hartree-Fock value.

	-E^b (eV)	-E^{HF} (eV)	E^c (eV)	d Å (au)
CO sz atomic orbitals HF	4.60	4.60	—	1.17 (2.21)
CO sz opt. orbitals HF	5.11	5.11	—	1.17 (2.21)
CO sz opt. orbitals correl.	8.49	5.04	3.58	1.17 (2.21)
CO dz atomic orbitals HF	2.71	2.71	—	1.23 (2.33)
CO dz opt. orbitals HF	3.75	3.75	—	1.17 (2.21)
CO dz opt. orbitals correl.	6.57	2.69	3.23	1.23 (2.33)
Experiment [Clementi90, Lide98]	11.24	7.88	3.36	1.13 (2.14)

Table 2.1.: Total binding energy, Hartree-Fock and correlation energies, and equilibrium bonding distance in Å (in au in parentheses), for different approximations and single- and double-zeta basis sets. Experimental data are taken from Refs. [Clementi90, Lide98].

The results show a rather poor agreement with experiment for CO: Hartree-Fock energies are greatly underestimated, as the use of a minimal basis is critical in yielding such poor results. The agreement in the total binding energies is better, because the correlation energy is well described (it is, in fact, slightly overestimated) in the single- and double-zeta cases, but it is clear that the poor agreement in binding energies comes from the use of a minimal basis, which is crucial in such a small molecule as CO. As for the bonding distance, our method overestimates it by $\sim 6\%$, surely due to the use of a minimal basis. The effect of the basis set will be discussed in Section 2.6.8.

The binding energy curves for the sz and dz cases are shown below.

As for the electronic spectrum, the HOMO is directed along the CO axis, while below it lie two degenerate π orbitals, perpendicular to the molecular axis, as shown in Fig. 2.4. The LUMO is degenerate, of π symmetry, and above it lies the σ antibonding state. The HOMO-LUMO gap varies slightly between the sz and dz cases (6.6 and 6.1 eV respectively).

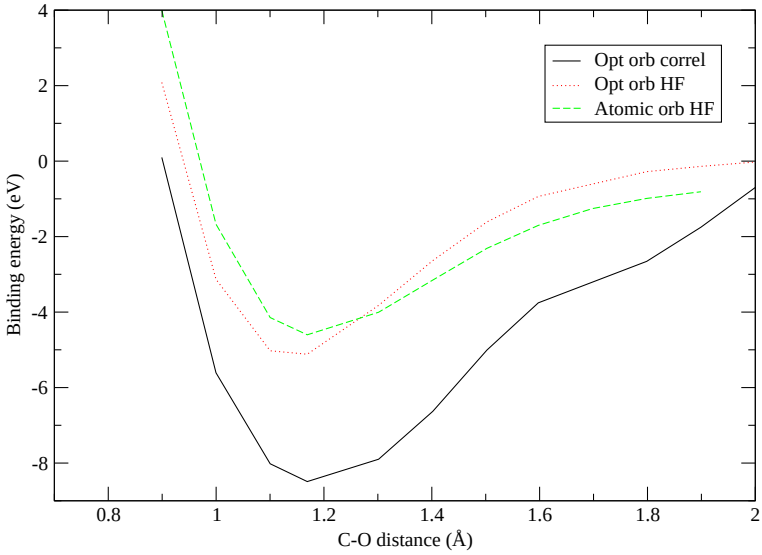

Figure 2.2 ... sis.

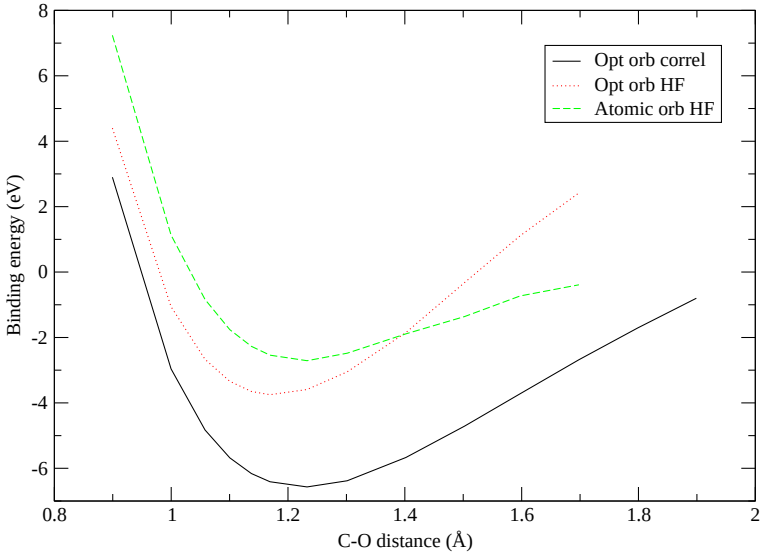

Figure 2.3.: Binding energy as a function of distance for CO using the double-zeta basis.

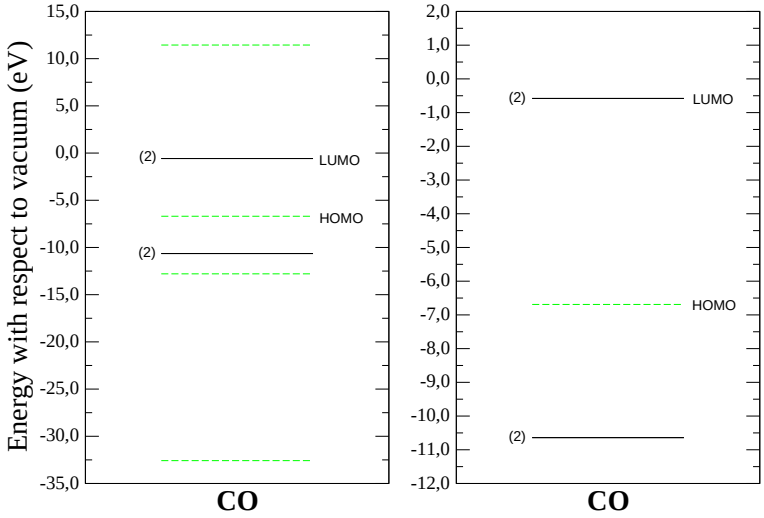

Figure 2.4.: Electronic spectrum of CO (double-zeta basis), including correlation. The left panel shows the full electronic spectrum, while the right panel focuses on the region near the HOMO-LUMO gap. Continuous black (dashed grey) bars represent π (σ) molecular orbitals. Numbers on the left indicate the degeneracy of the states.

2.6.3. CO_2

The data for CO_2 are summarized in Table 2.2 below:

	-E^b (eV)	-E^{HF} (eV)	E^c (eV)	d Å (au)
CO_2 sz atomic orbitals HF	4.03	4.03	—	1.25 (2.36)
CO_2 sz opt. orbitals HF	5.08	5.08	—	1.20 (2.27)
CO_2 sz opt. orbitals correl.	11.50	4.67	6.83	1.25 (2.36)
CO_2 dz atomic orbitals HF	1.11	1.11	—	1.30 (2.46)
CO_2 dz opt. orbitals HF	5.15	5.15	—	1.20 (2.27)
CO_2 dz opt. orbitals correl.	11.02	5.08	5.94	1.25 (2.36)
Experiment [Clementi90, Lide98]	17.08	11.25	5.83	1.16 (2.19)

Table 2.2.: Total binding energy, Hartree-Fock and correlation energies, and equilibrium bonding distance in Å (in au in parentheses), for different approximations and single- and double-zeta basis sets. Experimental data are taken from Refs. [Clementi90, Lide98].

The binding energy curves for the single- and double-zeta cases are plotted in the following figures:

The electronic spectrum is illustrated in Fig, 2.7, where σ orbitals are directed along the molecular axis, and π states are situated in a plane perpendicular to this line. The HOMO is, as in the case of CO, directed along the C=C axis (σ symmetry), while the LUMO is two-fold degenerate and corresponds to the antibonding states of the p_x and p_y orbitals (assuming the C=C axis is along the z direction). The value of the gap is $\sim$ 2.5 eV.

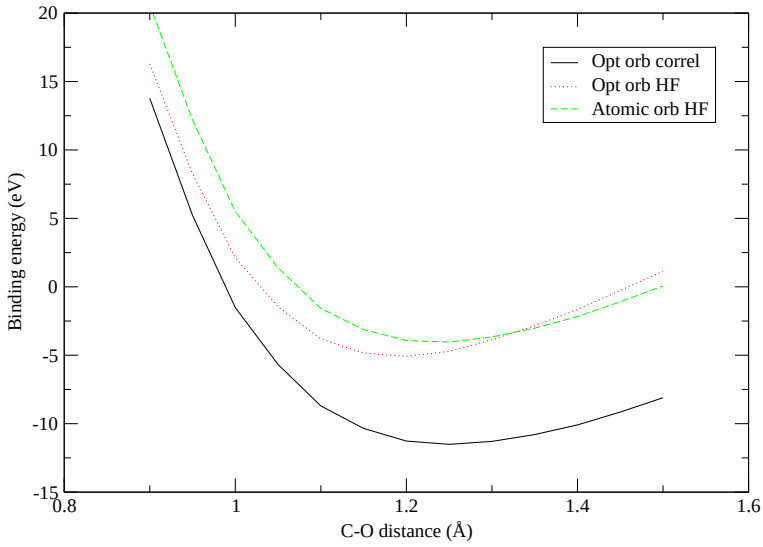

Figure 2.5.: Binding energy as a function of distance for CO_2 using the single-zeta basis.

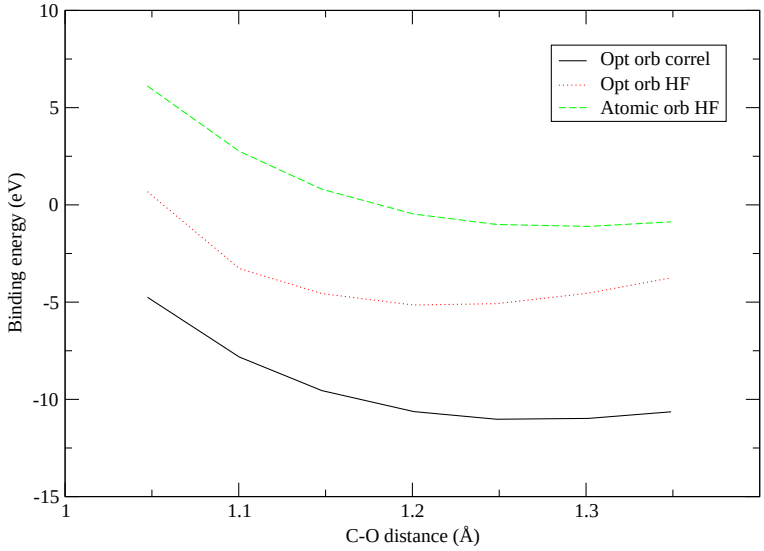

Figure 2.6.: Binding energy as a function of distance for CO_2 using the double-zeta basis.

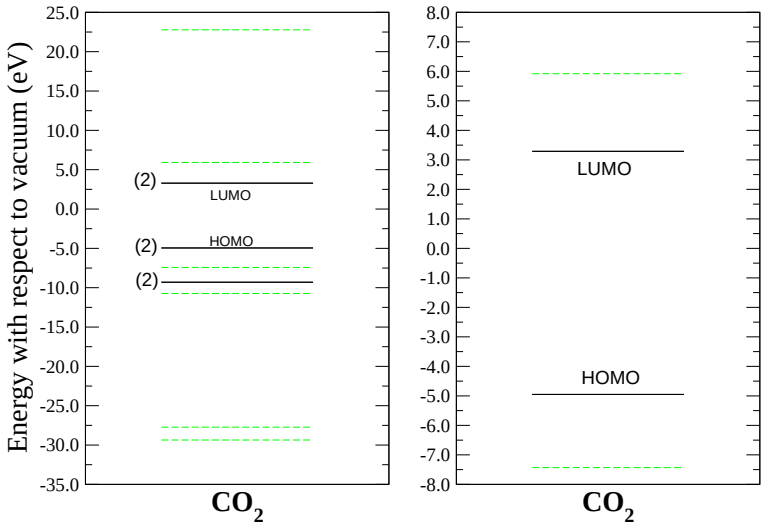

Figure 2.7.: Electronic spectrum of CO_2 (double-zeta basis), including correlation. The left panel shows the full electronic spectrum, while the right panel focuses on the region near the HOMO-LUMO gap. Continuous black (dashed grey) bars represent π (σ) molecular orbitals. Numbers on the left indicate the degeneracy of the states.

2.6.4. CH_4

CH_4 is a tetrahedral molecule where C exhibits sp^3 hybridization. Its binding energy curves for the different approximations are shown below:

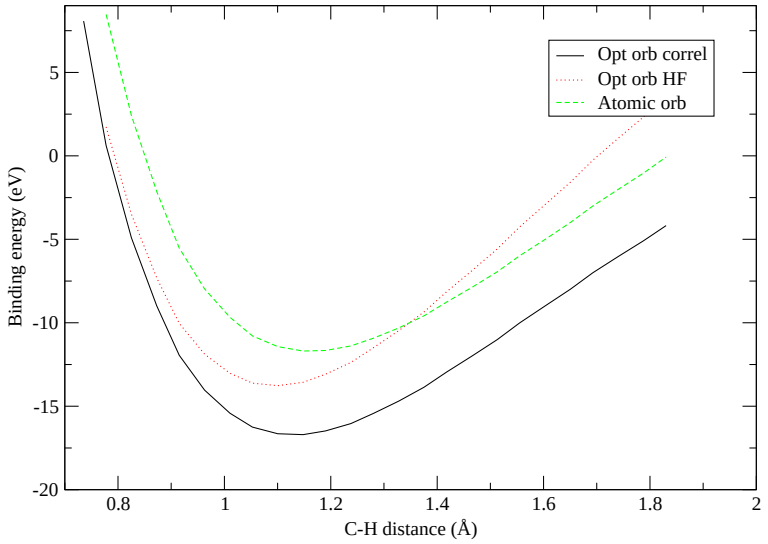

Figure 2.8.: Binding energy as a function of distance for CH_4 using the single-zeta basis.

Notice how the equilibrium C-H distance shortens after orbital optimization. This because the orbitals contract during this relaxation, and this is particularly significant for H 1s, resulting in a shorter C-H bond. Nevertheless, these distances are consistently larger than experimental, which we attribute to our basis set.

The agreement in binding, Hartree-Fock and correlation energies is better than in the previous cases, probably due to a better description of the bonds (again, due to a better basis).

As for the electronic spectrum, it shows a deep bonding state and three sp^3 degenerate hybrids. The empty part of the spectrum corresponds to the (threefold degenerate) hybrid antibonding states and another empty state. In the double-zeta case, the LUMO is not degenerate and the three hybrids are slightly above it. The HOMO-LUMO gap is $\sim$ 16 eV (sz) and $\sim$ 18 eV (dz).

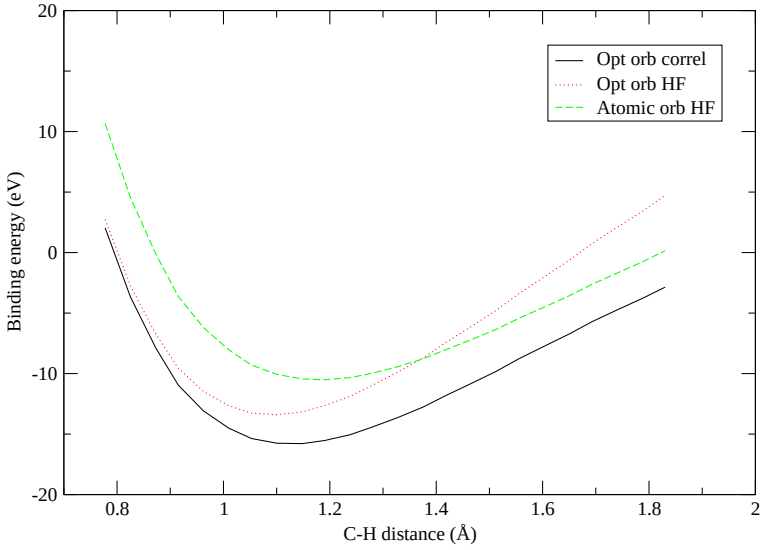

Figure 2.9.: Binding energy as a function of distance for CH_4 using the double-zeta basis.

	-E^b (eV)	-E^{HF} (eV)	E^c (eV)	d Å (au)
CH_4 sz atomic orbitals HF	11.69	11.69	—	1.15 (2.17)
CH_4 sz opt. orbitals HF	13.77	13.77	—	1.10 (2.08)
CH_4 sz opt. orbitals correl.	17.70	13.47	3.23	1.15 (2.17)
CH_4 dz atomic orbitals HF	10.51	10.51	—	1.19 (2.25)
CH_4 dz opt. orbitals HF	13.40	13.40	—	1.10 (2.08)
CH_4 dz opt. orbitals correl.	15.79	13.11	2.68	1.15 (2.17)
Experiment [Clementi90, Lide98]	18.40	14.39	4.01	1.09 (2.06)

Table 2.3.: Total binding energy, Hartree-Fock and correlation energies, and equilibrium bonding distance in Å (in au in parentheses), for different approximations and single- and double-zeta basis sets. Experimental data are taken from Refs. [Clementi90, Lide98].

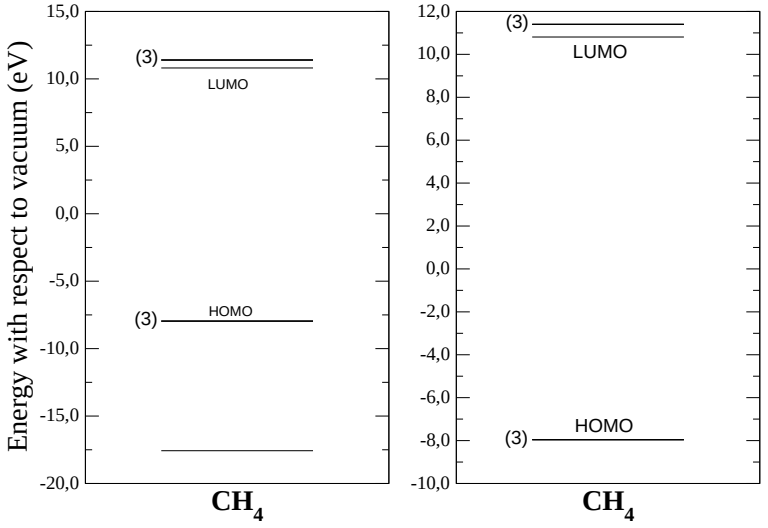

Figure 2.10.: Electronic spectrum of CH_4 (double-zeta basis), including correlation. The left panel shows the full electronic spectrum, while the right panel focuses on the region near the HOMO-LUMO gap. Continuous black (dashed grey) bars represent π (σ) molecular orbitals. Numbers on the left indicate the degeneracy of the states.

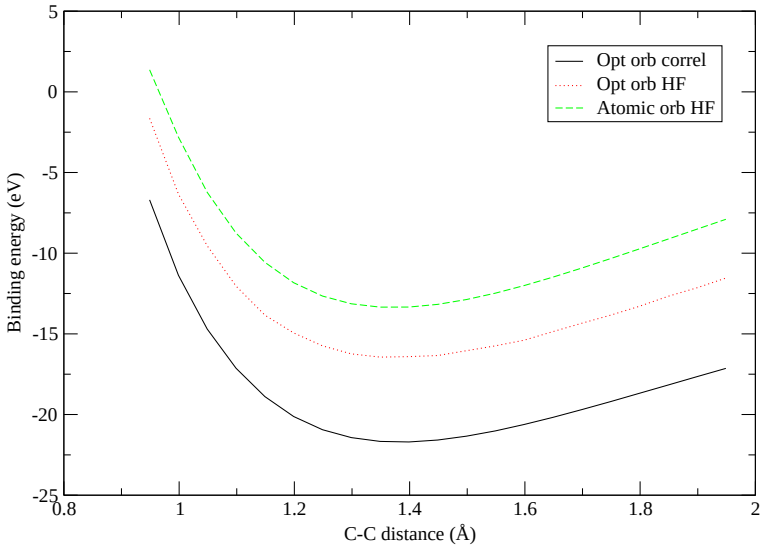

Figure 2.11.: Binding energy as a function of distance for C_2H_4 using the single-zeta basis.

2.6.5. C_2H_4

C_2H_4 is a flat molecule, which has a double C=C bond. Here, C is sp^2 hybridized. The binding energy curves yield bonding distances of 1.35 Å for the C=C bond, and 1.15 Å for the C-H one, for both the sz and dz bases. In our calculations, we have kept the C=C-H angle fixed at the experimental value of 122 degrees.

It can be seen that the agreement in the binding, Hartree-Hock and correlation energies is better than for other molecules, which we attribute to the greater size of the molecule. Notice how the single- and double-zeta values are very similar to each other: this means that the effect of the basis is not so important on the results. The larger the molecule, the more available atomic orbitals in the Hilbert space to describe the molecular bonds, and thus differences between sz and dz results can be expected to be smaller.

The agreement with in the bonding distance is fairly good, with differences similar to other molecules studied.

The spectrum shows the HOMO and LUMO of π character (in the plane perpendicular to the C=C axis), which are the symmetric and antisymmetric combinations

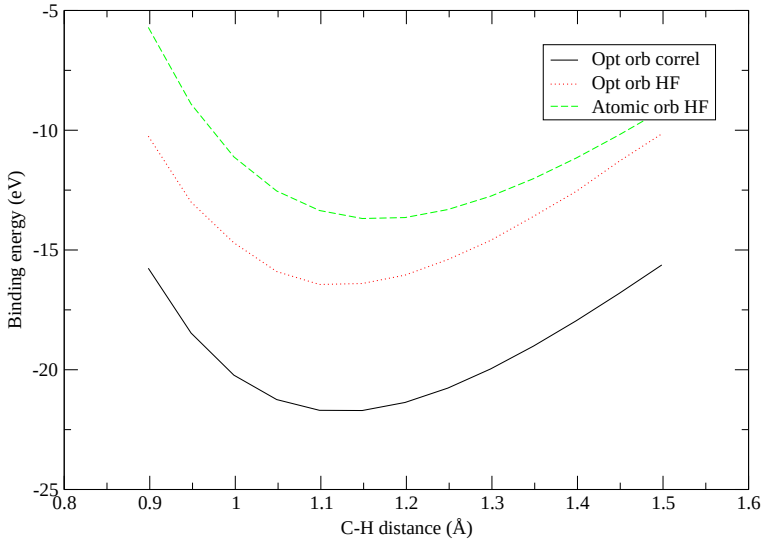

Figure 2.12.: Binding energy as a function of distance for C_2H_4 using the single-zeta basis.

of the out-of-plane atomic orbitals. Since C suffers a sp^2 hybridization, there is only one p orbital left per carbon, which gives rise to the bonding and antibonding π molecular states. The HOMO-1 and LUMO+1 molecular orbitals are directed along the C=C axis. The value of the gap is 7.9 eV for the sz case and 7.1 for the dz basis.

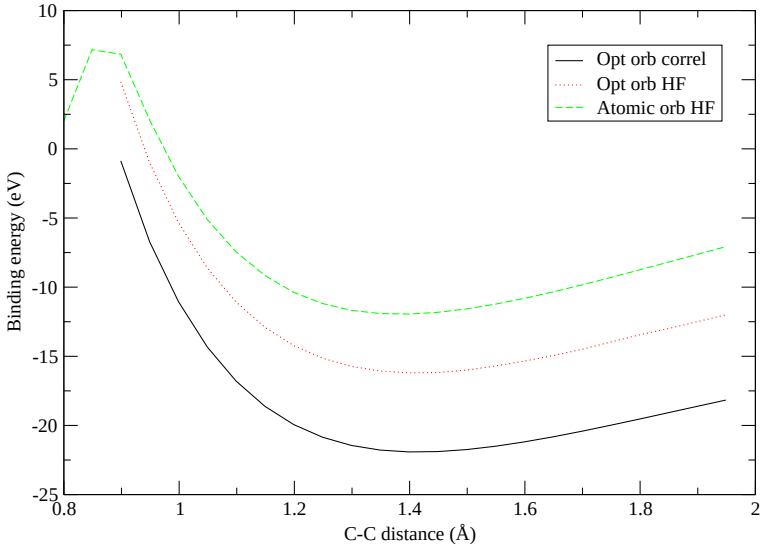

Figure 2.13.: Binding energy as a function of distance for C_2H_4 using the double-zeta basis.

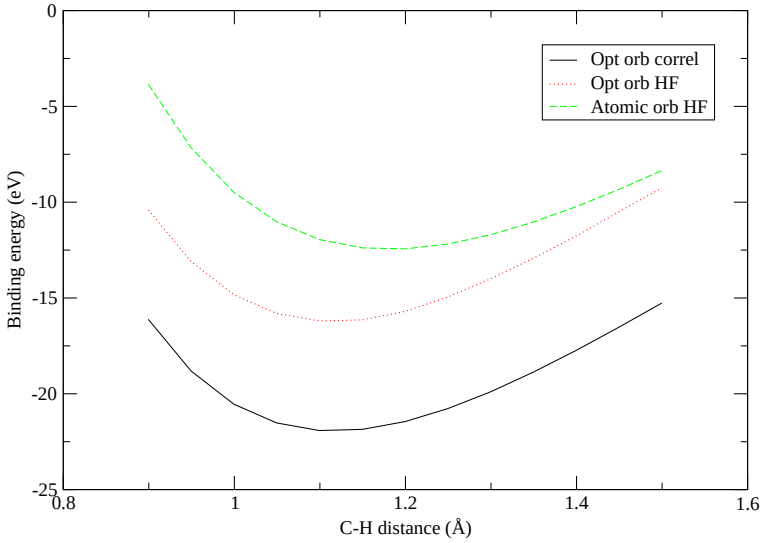

Figure 2.14.: Binding energy as a function of distance for C_2H_4 using the double-zeta basis.

	-E^b (eV)	-E^{HF} (eV)	E^c (eV)	d Å (au)
C_2H_4 sz atomic orbitals HF	13.68	13.68	—	1.35 (2.55) C=C
				1.15 (2.17) C-H
C_2H_4 sz opt. orbitals HF	16.44	16.44	—	1.35 (2.64) C=C
				1.10 (2.08) C-H
C_2H_4 sz opt. orbitals correl.	21.70	16.12	5.58	1.35 (2.55) C=C
				1.10 (2.08) C-H
C_2H_4 dz atomic orbitals HF	12.44	12.44	—	1.40 (2.64) C=C
				1.20 (2.27) C-H
C_2H_4 dz opt. orbitals HF	16.20	16.20	—	1.40 (2.64) C=C
				1.10 (2.08) C-H
C_2H_4 dz opt. orbitals correl.	21.03	16.06	4.97	1.40 (2.64) C=C
				1.10 (2.08) C-H
Experiment [Clementi90, Lide98]	24.65	18.71	5.94	1.34 (2.53) C=C
				1.09 (2.06) C-H

Table 2.4.: Total binding energy, Hartree-Fock and correlation energies, and equilibrium bonding distance in Å (in au in parentheses), for different approximations and single- and double-zeta basis sets. Experimental data are taken from Refs. [Clementi90, Lide98].

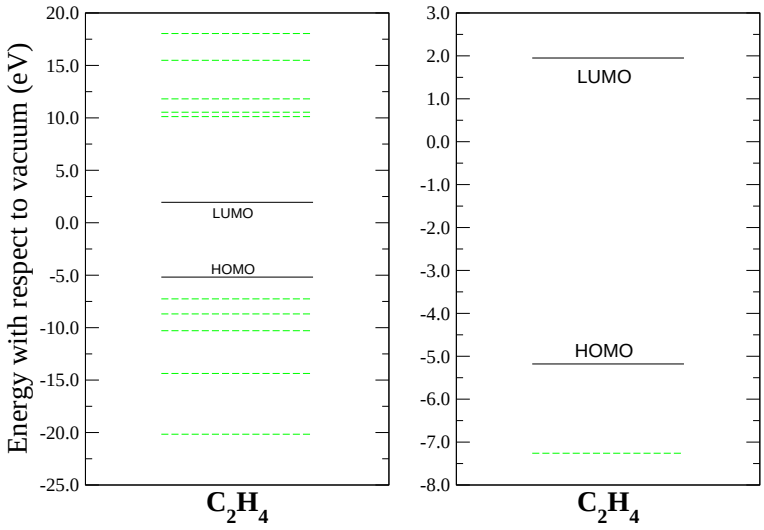

Figure 2.15.: Electronic spectrum of C_2H_4 (double-zeta basis), including correlation. The left panel shows the full electronic spectrum, while the right panel focuses on the region near the HOMO-LUMO gap. Continuous black (dashed grey) bars represent π (σ) molecular orbitals. Numbers on the left indicate the degeneracy of the states.

2.6.6. Benzene

Benzene (C_6H_6) is the 'building block' of the large π-conjugated molecules studied in this thesis. The resonant π bonds, which are characteristic of benzene, result from the combination of the out-of-plane atomic orbitals.

The binding energy curves were calculated by varying the C-C and C-H distances independently. The results are shown in the following figures:

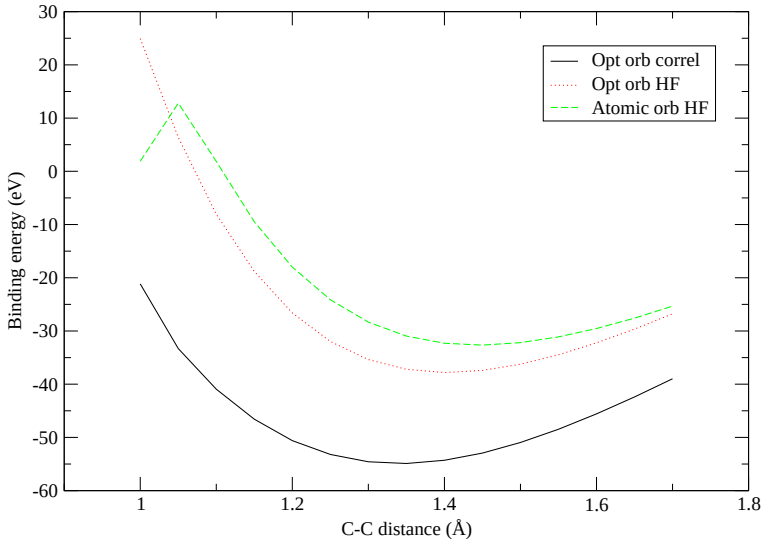

Figure 2.16.: Binding energy as a function of distance for benzene using the single-zeta basis.

where the equilibrium values are shown in Table 2.5:

These results show that, as before, the correlation energy is being overestimated slightly. On the other hand, the Hartree-Fock results for the single- and double-zeta cases are similar, showing, again, that for molecules this size, the dimension of the Hilbert space is large enough to yield little differences between the sz and dz basis sets. The difference of $\sim$ 7–9 eV with the 'experimental' (basis converged) Hartree-Fock value must therefore reflect the error introduced by the use of a minimal basis.

The electronic spectrum of benzene is characterized by the presence of the π molecular orbitals, resulting from the combination of the out-of-plane p_z atomic

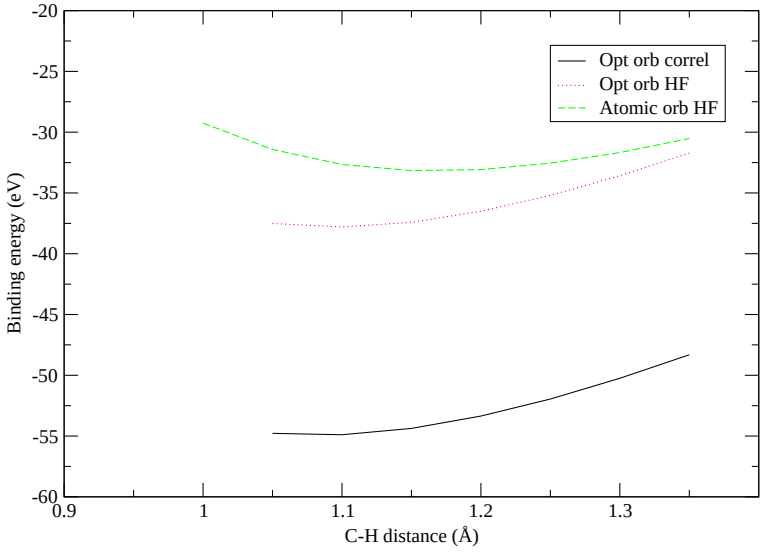

Figure 2.17.: Binding energy as a function of distance for benzene using the single-zeta basis.

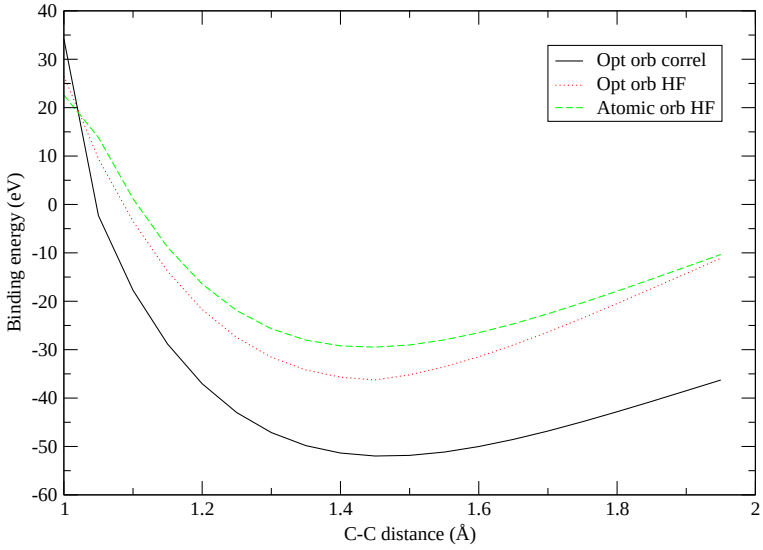

Figure 2.18.: Binding energy as a function of distance for benzene using the double-zeta basis.

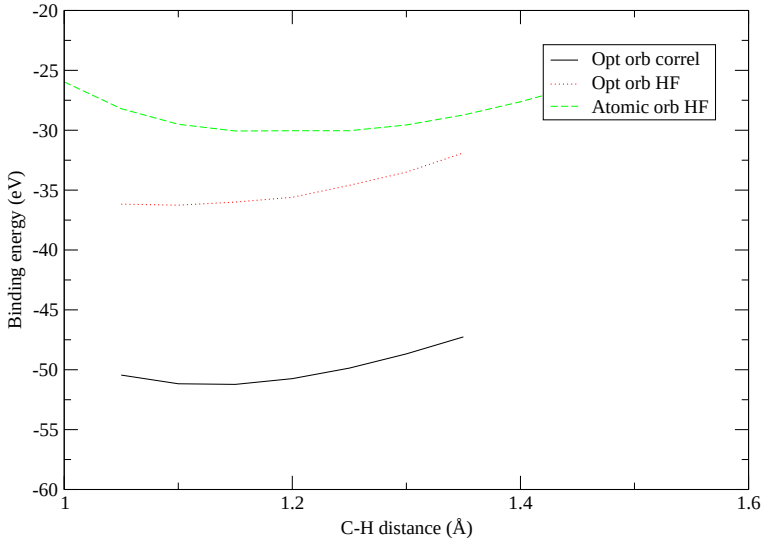

Figure 2.19.: Binding energy as a function of distance for benzene using the double-zeta basis.

orbitals. Its symmetry allows for the determination of the π spectrum by simple arguments. Since there are six C atoms, there are also six π molecular orbitals, three of which will be occupied (or bonding), and the other three empty (antibonding, in the language of quantum chemists). The most bonding molecular orbital results from the symmetric combination of the atomic orbitals (both their amplitude and their sign are the same). The remaining two occupied molecular orbitals are degenerate, as are the first two empty states. The molecular highest in energy (the most antibonding), the combination will be antisymmetric (same amplitudes with alternating signs).

These π states can be determined from a simple symmetry-based phase argument:

$$|MO_N\rangle = \sum e^{\pm i2\pi j\ N/6}\ |j\rangle \tag{2.48}$$

where j runs over the atomic p_z orbitals, and N labels the molecular orbital from the most bonding to the most antibonding: 0 for the most bonding, 1 for the twofold degenerate HOMO, 2 for the twofold degenerate LUMO, and 3 for the most antibonding state. For the twofold-degenerate HOMO and LUMO, in each case the choice of a plus or minus sign for the degenerate states leads to orthogonal

	-E^b (eV)	-E^{HF} (eV)	E^c (eV)	d Å (au)
Benzene sz atomic orbitals HF	33.15	33.15	—	1.45 (2.74) C=C 1.15 (2.17) C-H
Benzene sz opt. orbitals HF	37.80	37.80	—	1.45 (2.74) C=C 1.10 (2.08) C-H
Benzene sz opt. orbitals correl.	54.89	38.61	16.28	1.45 (2.74) C=C 1.10 (2.08) C-H
Benzene dz atomic orbitals HF	30.06	30.06	—	1.45 (2.74) C=C 1.15 (2.17) C-H
Benzene dz opt. orbitals HF	36.26	36.26	—	1.45 (2.74) C=C 1.10 (2.08) C-H
Benzene dz opt. orbitals correl.	51.22	36.12	15.10	1.45 (2.74) C=C 1.15 (2.17) C-H
Experiment [Clementi90, Lide98]	59.67	45.19	14.48	1.40 (2.65) C=C 1.10 (2.07) C-H

Table 2.5.: Total binding energy, Hartree-Fock and correlation energies, and equilibrium bonding distance in Å (in au in parentheses), for different approximations and single- and double-zeta basis sets. Experimental data are taken from Refs. [Clementi90, Lide98].

orbitals.

We thus have the following molecular states (in order of decreasing binding energy):

$$
\begin{aligned}
|\pi_1\rangle &= \sum_j e^{i0\pi j/6}\,|j\rangle \\
|\pi_2\rangle = \sum_j e^{i2\pi j/6}\,|j\rangle \quad &, \quad |\pi_3\rangle = \sum_j e^{-i2\pi j/6}\,|j\rangle \\
|\pi_4\rangle = \sum_j e^{i4\pi j/6}\,|j\rangle \quad &, \quad |\pi_5\rangle = \sum_j e^{-i4\pi j/6}\,|j\rangle \\
|\pi_6\rangle &= \sum_j e^{i6\pi j/6}\,|j\rangle
\end{aligned}
\tag{2.49}
$$

The above molecular states with complex coefficients can be combined to yield

real coefficients. The calculations yield the following π molecular orbitals:

$$\begin{aligned}
|\pi_1\rangle &= 0.41\ |C_1 p_z\rangle + 0.41\ |C_2 p_z\rangle + 0.41\ |C_3 p_z\rangle + \\
&\quad 0.41\ |C_4 p_z\rangle + 0.41\ |C_5 p_z\rangle + 0.41\ |C_6 p_z\rangle \\
|\pi_2\rangle &= -0.50\ |C_1 p_z\rangle - 0.50\ |C_2 p_z\rangle + 0.00\ |C_3 p_z\rangle + \\
&\quad 0.50\ |C_4 p_z\rangle + 0.50\ |C_5 p_z\rangle - 0.00\ |C_6 p_z\rangle \\
|\pi_3\rangle &= -0.29\ |C_1 p_z\rangle + 0.29\ |C_2 p_z\rangle + 0.58\ |C_3 p_z\rangle + \\
&\quad 0.29\ |C_4 p_z\rangle - 0.29\ |C_5 p_z\rangle - 0.58\ |C_6 p_z\rangle \\
|\pi_4\rangle &= 0.29\ |C_1 p_z\rangle + 0.29\ |C_2 p_z\rangle - 0.58\ |C_3 p_z\rangle + \\
&\quad 0.29\ |C_4 p_z\rangle + 0.29\ |C_5 p_z\rangle - 0.58\ |C_6 p_z\rangle \\
|\pi_5\rangle &= 0.50\ |C_1 p_z\rangle - 0.50\ |C_2 p_z\rangle - 0.00\ |C_3 p_z\rangle - \\
&\quad 0.50\ |C_4 p_z\rangle - 0.50\ |C_5 p_z\rangle + 0.00\ |C_6 p_z\rangle \\
|\pi_6\rangle &= 0.41\ |C_1 p_z\rangle - 0.41\ |C_2 p_z\rangle + 0.41\ |C_3 p_z\rangle - \\
&\quad 0.41\ |C_4 p_z\rangle + 0.41\ |C_5 p_z\rangle - 0.41\ |C_6 p_z\rangle
\end{aligned} \tag{2.50}$$

The HOMO and LUMO are these doubly-degenerate π orbitals. In-plane σ molecular orbitals are distributed more or less evenly throughout the spectrum, as shown in Fig. 2.20:

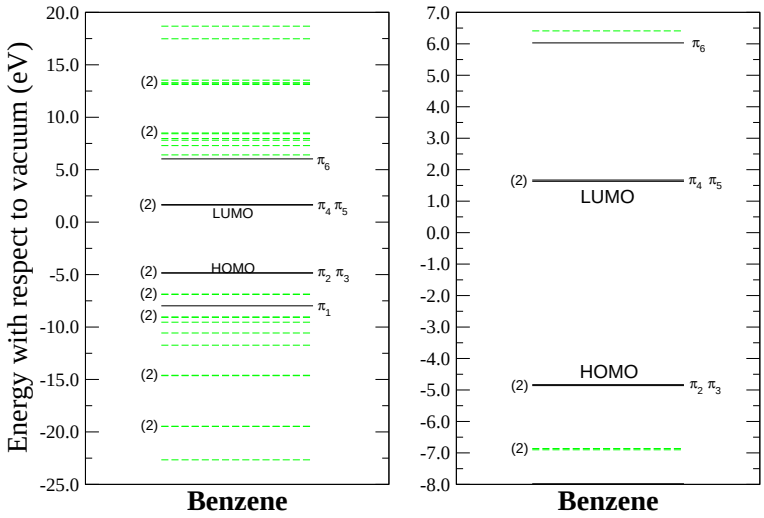

Figure 2.20.: Electronic spectrum of benzene (double-zeta basis), including correlation. The left panel shows the full electronic spectrum, while the right panel focuses on the region near the HOMO-LUMO gap. Continuous black (dashed grey) bars represent π (σ) molecular orbitals. Numbers on the left indicate the degeneracy of the states.

2.6.7. Orbital optimization

Let us comment on the orbital optimization. A binding energy curve is calculated using the atomic (non-optimized) orbitals. At the minimum of this curve, the basis optimization is carried out by allowing the exponents (ζ) of the STOs to relax. After this, the optimized atomic orbitals are then appropriately normalized.

Since the atomic exponents parameterized by the Tables of Clementi and Roetti [Clementi74] are aimed at calculating atomic energies, we find that these exponents increase during the optimization: the orbitals contract, due to the repulsion of neighboring atoms. We quote the values of the exponents before and after orbital optimization:

CO		ζ (initial)	ζ (final)
C (sz)	STO_2 (2s)	1.608330	1.607810
	STO_3 (2p)	1.567880	1.707470
C (dz)	STO_3 (2s)	1.830680	1.853699
	STO_4 (2s)	1.152820	1.165365
	STO_5 (2p)	2.730450	2.759715
	STO_6 (2p)	1.256560	1.515154
O (sz)	STO_2 (2s)	2.245880	2.256232
	STO_3 (2p)	2.226620	2.267472
O (dz)	STO_3 (2s)	2.688010	2.640517
	STO_4 (2s)	1.675430	1.802349
	STO_5 (2p)	3.694450	3.645390
	STO_6 (2p)	1.658640	1.642929

Table 2.6.: Initial and final values during optimization of the exponents ζ of the STOs which describe the atomic orbitals for CO.

As an example, the radial part of the C 2s and 2p orbitals are plotted in Fig. 2.21, before and after optimization in Benzene:

Finally, we give the energy gained during orbital relaxation, which is the difference between the molecular energy before and after the basis is optimized. Note than in some cases, a new equilibrium geometry is obtained, especially in the case of the C-H bonds, which are shortened as the H 1s orbitals contract upon optimization.

CO_2		ζ (initial)	ζ (final)
C (sz)	STO_2 (2s)	1.608330	1.797446
	STO_3 (2p)	1.567880	1.739912
C (dz)	STO_3 (2s)	1.830680	1.866717
	STO_4 (2s)	1.152820	1.906580
	STO_5 (2p)	2.730450	2.685390
	STO_6 (2p)	1.256560	1.611723
O (sz)	STO_2 (2s)	2.245880	2.235957
	STO_3 (2p)	2.226620	2.223287
O (dz)	STO_3 (2s)	2.688010	2.668961
	STO_4 (2s)	1.675430	1.720583
	STO_5 (2p)	3.694450	3.647967
	STO_6 (2p)	1.658640	1.612477

Table 2.7.: Initial and final values during optimization of the exponents ζ of the STOs which describe the atomic orbitals for CO_2.

CH_4		ζ (initial)	ζ (final)
C (sz)	STO_2 (2s)	1.608330	1.733959
	STO_3 (2p)	1.567880	1.733959
C (dz)	STO_3 (2s)	1.830680	1.725421
	STO_4 (2s)	1.152820	1.784318
	STO_5 (2p)	2.730450	2.821490
	STO_6 (2p)	1.256560	1.335275
H (sz)	STO_1 (1s)	1.000000	1.161482
H (dz)	STO_1 (1s)	1.000000	1.267193

Table 2.8.: Initial and final values during optimization of the exponents ζ of the STOs which describe the atomic orbitals for CH_4.

C_2H_4		ζ (initial)	ζ (final)
C (sz)	STO_2 (2s)	1.608330	1.737195
	STO_3 (2p)	1.567880	1.690680
C (dz)	STO_3 (2s)	1.830680	1.746047
	STO_4 (2s)	1.152820	1.807684
	STO_5 (2p)	2.730450	2.768537
	STO_6 (2p)	1.256560	1.337744
H (sz)	STO_1 (1s)	1.000000	1.203352
H (dz)	STO_1 (1s)	1.000000	1.293596

Table 2.9.: Initial and final values during optimization of the exponents ζ of the STOs which describe the atomic orbitals for C_2H_4.

Benzene		ζ (initial)	ζ (final)
C (sz)	STO_2 (2s)	1.608330	1.726761
	STO_3 (2p)	1.567880	1.686754
C (dz)	STO_3 (2s)	1.830680	1.776614
	STO_4 (2s)	1.152820	1.793817
	STO_5 (2p)	2.730450	2.773994
	STO_6 (2p)	1.256560	1.386807
H (sz)	STO_1 (1s)	1.000000	1.204947
H (dz)	STO_1 (1s)	1.000000	1.201832

Table 2.10.: Initial and final values during optimization of the exponents ζ of the STOs which describe the atomic orbitals for benzene.

	ΔE_{molec} (eV)	
	sz	dz
CO	0.45	1.21
CO_2	1.30	4.15
CH_4	2.03	2.89
C_2H_4	2.77	3.77
Benzene	6.21	7.02

Table 2.11.: Molecular energy gain ΔE_{molec} during basis optimization for the different molecules.

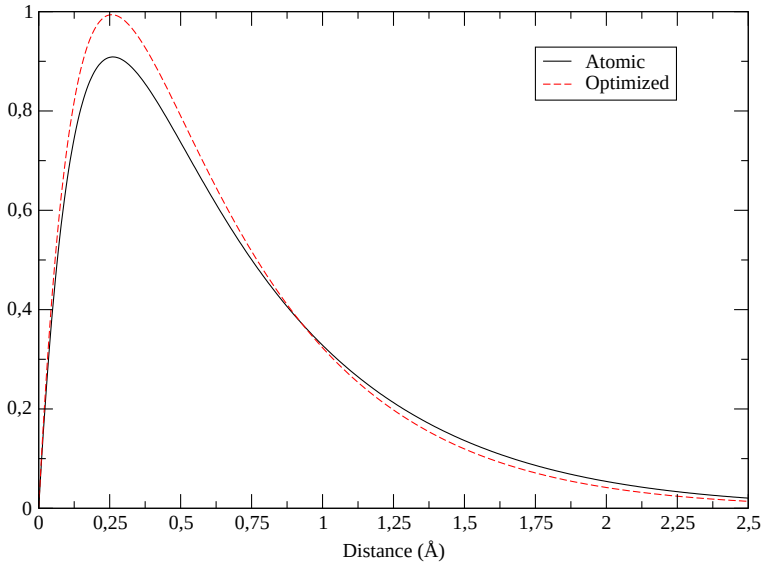

Figure 2.21.: Radial part of C double-zeta 2p orbitals. Notice that, due to orthogonalization with orbitals of neighbouring atoms, the orbital contracts with respect to the atomic (Clementi-Roetti) case.

2.6.8. Some general trends

From the somewhat overwhelming data presented above for the small molecules, several general trends can be observed.

First, notice that the difference in binding energy between the single- and double-zeta cases decreases with the size of the molecule, and the same can be said for E^{HF} and E^{c}. As was mentioned previously, this is due to the fact that the increasing number of atoms provides additional orbitals which increase the dimension of the Hilbert space and thus allow for a better description of the molecular bonds, since the molecular bonds can be described in terms of a larger number of atomic orbitals. Within our minimal basis, the size of benzene is such that doubling the base (in going from the double- to the single-zeta basis) makes little difference, and results for single- and double-zeta bases are thus expected to be increasingly convergent for larger molecules.

Note also that the binding energies obtained using a double-zeta basis are consistently smaller (in magnitude) than those obtained for the single-zeta case. This seems striking, since one would at first expect a better description of the bonds with the larger (dz) basis. To clarify this, we quote again the definition of the molecular binding energy $E^b = E_{molec} - \sum E_{at}$ as the difference between the molecular energy and the sum of the individual atomic energies (which sets the zero of the binding energy scale). Differences between single-zeta and double-zeta basis affect both E_{molec} and E_{at}, while the tabulated values of Clementi and Roetti [Clementi74] are aimed at the description of atomic properties. Notice (Table 2.11) how the energy gained during the basis optimization is consistently larger for the double-zeta case. This suggests that the non-optimized double-zeta orbitals of Clementi and Roetti provide a poorer initial description of the molecule than the single-zeta ones. When the bases are optimized, the double-zeta orbitals change more than the single-zeta ones from their initial values, and a larger molecular energy gain is obtained (note that the 'perfect' initial basis set would yield zero energy gain during the basis optimization). Thus, the only consistent explanation is that going from a single- to a double-zeta basis improves both E_{molec} and E_{at}, but improves the latter **more**, thereby reducing the magnitude of E^b.

This details of the basis set certainly affects this result; for instance allowing for orbitals within a subshell (such as p_x, p_y and p_z) to be described by different STOs, with different exponents ζ would definitely improve the molecular energy. The orbitals along the interatomic axes could then be optimized independently

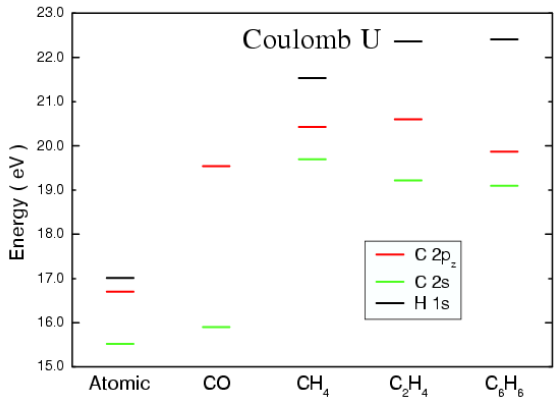

Figure 2.22.: Coulomb U interaction for different orbitals within the different molecules.

from out-of-plane orbitals, for example, and a better description of the molecular bonds would be achieved. In the calculation of E_{at}, the spherical symmetry of the isolated atoms (which certainly does not exist in the molecule) does not pose these problems: in our approach, the same radial function is applied to p_x, p_y and p_z orbitals, which makes no difference in isolated atoms, but averages the in-plane and out-of-plane molecular properties.

In addition, we note that the rather poor agreement with experiment in the bonding distances, with errors of $\sim 5\%$ are affected by our basis optimization, since it was designed to maximize the molecular binding energy, rather than to optimize bond lengths and curvatures around the energy minima.

We mention also that Coulomb interactions within the molecule, such as U_i and J_{ij} are shown to depend on the local chemical environment (practically, the nearest-neighbor atoms) and are thus convergent with increasing size of the molecule. Since our final goal is the study of large π-conjugated molecules, this result is important as it provides a way of easily calculating the interactions within the molecule by approximating them by their values in a cluster which resembles the chemical environment of a particular atom.

Finally, it should be noted that DFT greatly underestimates the HOMO-LUMO gap. Thus the spectra taken here should be taken with care, knowing that the 'true' HOMO-LUMO gap is much greater (in some cases by as much as $\sim$ 200 %). The difference between a correlated and uncorrelated electron-hole pair (optical and transport gap, respectively) was already mentioned briefly. In this respect, it is curious to note that underestimation of the gap by DFT more or less equals the exciton binding energy, such that the DFT gap is roughly equal to the optical gap [Oszwaldowski03]. Thus, while a scheme to compensate for this underestimation of the gap has been developed (see Section 2.8.6), this crude rule of thumb that the DFT gap roughly equals the optical one can serve as a guide. Thus, the results presented in these sections are valid, but one should remember that the gap is greatly underestimated by DFT, and keep it in mind when considering the molecular spectra.

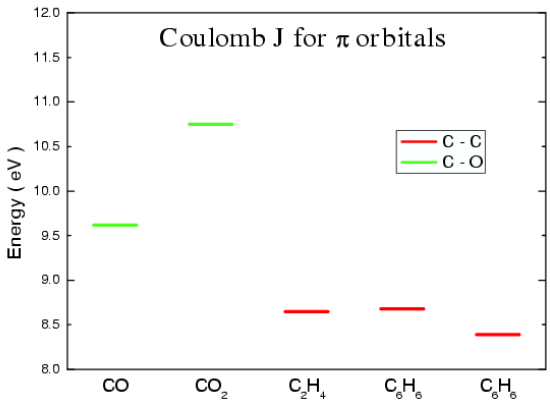

Figure 2.23.: Coulomb nearest-neighbor J integrals for π orbitals for the different molecules.

2.7. *Fireball*

Fireball is a first-principles simulation package. Based on the original ideas by Sankey and Niklewski [Sankey89], it is a fast, efficient computational method which can be used to calculate the electronic structure of clusters, molecules and solids [Demkov95, Lewis01, Jelínek05].

In the present work, *Fireball* has been used to determine the electronic properties of several π-conjugated organic molecules (PTCDA, PTCBI, CBP, CuPc and several polyacenes). *Fireball* allows for molecular dynamics simulations and geometry optimization, which enables the equilibrium geometry of these large molecules to be determined, since they lack the symmetry of the smaller molecules (CO, CO_2, CH_4, C_2H_4 and benzene). In the case of these small molecules, the interatomic distances were fixed and the electronic structure was calculated at that particular geometry. With *Fireball*, on the other hand, the electrostatic forces acting on the atoms are calculated quantum-mechanically; by minimizing these interatomic forces, the equilibrium geometry of the molecules can be determined.

2.7.1. *Fireball* orbitals

Fireball uses a local-orbital basis set. This is composed of atomic-like orbitals, which are numerical wavefunctions obtained by solving the atomic Hamiltonian with the boundary conditions that the orbitals vanish beyond a certain cutoff radius, R_C. Unlike 'real' atomic orbitals, which extend to infinity, the boundary condition at R_C has the effect of simulating the repulsion of neighboring atoms which is found in molecules or solids, which results in a contraction of the orbital, pushing the wavefunction peak closer to the nucleus, thereby increasing its kinetic energy. Thus, these orbitals are slightly excited, hence the (somewhat exaggerated) name *Fireball*. Fireballs have enormous computational advantages, since the overlap matrix between two such orbitals will be strictly zero if they are separated by a distance greater than $R_{C_1} + R_{C_2}$, thereby simplifying the calculation of many interaction terms to point charges if this condition is met.

Thus, while the long-range behavior of the orbitals is poorly described (in contrast, for example, to the STO basis, with its exponential decay), the region around typical bonding distances is equivalent to other basis sets.

For comparison, the radial part of the H 1s, C 2p and O 2p wavefunctions are shown in Fig. 2.24.

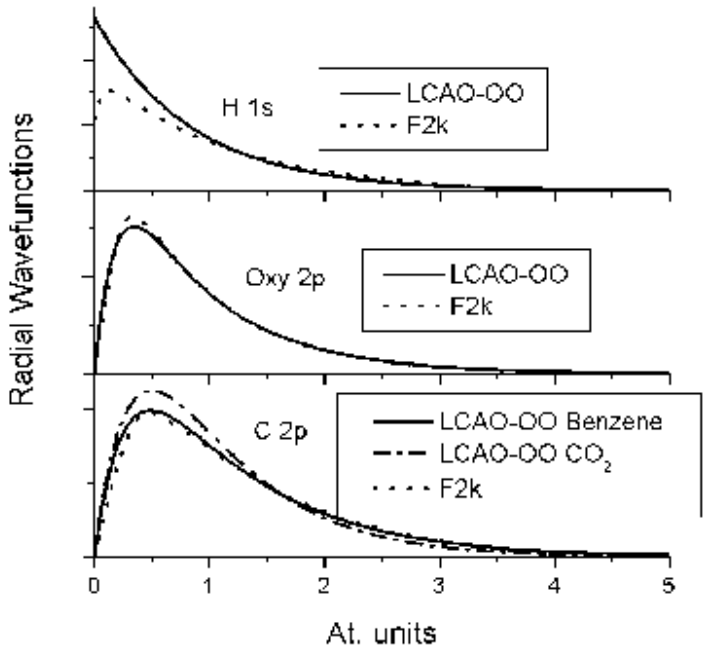

Figure 2.24.: Radial part of the H 1*s*, C 2*p* and O 2*p* orbitals, within the *Fireball* and the LCAO basis sets.

As in the case of the STO basis, the atomic orbitals (the *Fireballs*) are, in general, not orthogonal, so that the Löwdin transformation 2.17 is performed.

2.7.2. Harris functional

The *Fireball* code uses an extension of the Harris functional [Harris85]. This functional provides a simplified way of calculating the Kohn-Sham ground-state energy 2.12 by approximating the electronic density around the sum of the densities of the composing atoms. The greatest advantage is that it uses a trial density, ρ_{Harris}, to compute the Hamiltonian 2.8 and the energy 2.12, but avoids the computationally costly procedure of self-consistency. This functional is equivalent to the Kohn-Sham approach whenever the initial guess ρ_{Harris} equals the self-consistent density ρ_{SC}, and is applicable whenever the density of the system under study does not deviate significantly from the sum of densities of the individual fragments. Weakly-interacting systems are well described within the Harris functional, but in many

cases, where strong, covalent bonds are present (such as in a molecule), the sum of the atomic densities is not a good approximation, and a better description of the electronic density is needed.

Fireball uses the Harris functional while allowing for charge transfer and self-consistency, and can thus be viewed as a self-consistent extension of the Harris functional. In our formalism, in which the orbital occupancies replace the density ρ, this means that the different contributions to the Hamiltonian and thus the molecular energies are calculated from the **input** occupancies $\{n_{ij}^{in}\}$, in the spirit of the Harris functional, rather than the output ones $\{n_{ij}^{out}\}$ as is usual in conventional self-consistent calculations. Then, self-consistency is done on the diagonal elements $\{n_i\}$, rather than with the whole matrix (diagonal and off-diagonal elements), simplifying the procedure. This self-consistency ensures a good description of the charge density.

Fireball considers up to three-center terms in the interaction, all of which are tabulated in a grid for the different atoms considered. During the molecular dynamics simulation or geometry optimization, these interactions are not calculated, but read or interpolated from the tabulated values, saving computational time.

2.8. DFT results for π-conjugated molecules

We now present results for the electronic structure of large π-conjugated molecules ar their equilibrium geometries. A common feature to all molecules, as will be commented on, is the small HOMO-LUMO gap, characteristic of DFT. A way of improving on this deficiency and obtaining a good description of the single-particle gas-phase gap will be described in the following section.

2.8.1. PTCDA

In this case, the molecule was studies using three different approximations: compare *Fireball*-OO, *Fireball*-LDA and LCAO-OO [Oszwaldowski03]. The difference in *Fireball*-LDA and *Fireball*-OO lies in the exchange-correlation functional used: the former uses conventional LDA, while the latter uses the one described by equations 2.39. On the other hand, *Fireball*-OO and LCAO-OO differ in the basis set used (*Fireball* or STO-type orbitals, see Fig. 2.24), and in the description of the core electrons: standard Hamann-type pseudopotentials in the case of *Fireball* and as shifts in the valence-orbital diagonal and hopping terms.

		F2k-LDA	F2k-OO	LCAO-OO	Exp. [Lide98] [Clementi90]
CO		1.255	1.29	1.30	1.13
CH_4		1.17	1.21	1.15	1.09
C_6H_6	C–H	1.17	1.20	1.15	1.10
C_6H_6	C–C	1.41	1.48	1.50	1.40
PTCDA	C=O	1.31	1.39	1.32	1.23
PTCDA	C–O	1.48	1.54	1.48	1.38
PTCDA	C–C	1.49	1.49	1.51	1.47

Table 2.12.: Calculated and experimental equilibrium bond lengths (Å).

The following tables display the equilibrium bond lengths, and binding and correlation energies at the equilibrium and experimental geometries, for PTCDA as well as several small molecules whose bonds resemble those found in PTCDA.

In the case of PTCDA in Table 2.12, no experimental binding distances are available, and the reported values are those of other theoretical calculations.

Table 2.13 compares the results for the binding and correlation energies using the different methods at their equilibrium geometries calculated within each approach. In order to provide a direct comparison of the LDA and OO exchange-correlation approaches, the *Fireball*-OO results for the LDA equilibrium geometries are also given (in parenthesis). As before, the binding energy E^b represents the difference between the molecular energy and the sum of the isolated atoms. The *Fireball* reference energies, the atomic wavefunctions were numerically calculated by solving the atomic problem in the LDA using a large R_C. In the case of LCAO-OO approach, the reference atomic energies are the double-zeta Clementi-Roetti results [Clementi74]. Experimental correlation energies E_C are defined as the difference between the experimental binding energy and a basis-converged Hartree Fock result, quoted in Ref. [Clementi90].

The comparison between *Fireball*-LDA and -OO results leads to an evaluation of the different exchange-correlation functionals. On the other hand, the effect of the basis set is seen by comparing the *Fireball*-OO and LCAO-OO data.

From Table 2.12, our results are systematically larger than the experimental values, which is probably due to the use, in all cases, of a minimal basis set. Even in the case of the energy-optimized LCAO basis, the limitations imposed by a minimal basis result in an inevitably poorer description of the bonds, and the larger than experimental values are attributed to this. The *Fireball*-LDA results yield con-

	CO	CH_4	C_6H_6	PTCDA
E^b (F2k-LDA)	-10.2	-13.3	-51.7	-222.2
E^b (F2k-OO)	-4.6 (-4.5)	-11.0 (-10.9)	-40.8 (-40.0)	-140.5 (-133.2)
E^b (LCAO-OO)	-6.3	-15.8	-52.9	-202.3
Exp.	-11.2	-18.4	-59.7	-235.1(*)
E^c (F2k-OO)	-4.3 (-4.0)	-3.1 (-2.9)	-16.6 (-15.25)	-74.8 (-65.7)
E^c (LCAO-OO)	-3.6	-2.7	-16.9	-73.2
Exp.	-3.4	-4.0	-14.5	—

Table 2.13.: Binding (E^b) and correlation (E^c) energies (eV) at equilibrium geometries.

(*) For lack of information, this is estimated as the sum of bond energies. The sum was calculated using typical bond energies: E(C–C) = E(C–O) = 3.6 eV, E(C–H) = 4.3 eV, (C=C) = E(C=O) = 2.8 eV, from [Pauling60].

sistently smaller bond lengths than their OO counterparts, due to the well-known overestimation of the exchange-correlation energy [Koch00]. On the other hand, the comparison between the *Fireball* and LCAO bases does not seem to have a large effect on bond lengths: the results are quite similar, and in some cases the LCAO bond lengths are slightly larger, though in others it is the other way around.

In Table 2.13, the overestimation of the exchange-correlation by the LDA functional can be clearly seen in the comparison of *Fireball*-LDA and -OO results, since the large differences in binding energy must be largely due to this overestimation. This is particularly acute for CO (where the use of a minimal basis for such a small molecule results in large error percentage-wise, as commented before, and with a strong contribution to correlation from electronegative oxygen), and in PTCDA, where the large size of the molecule results in the addition of small differences in many molecular bonds. Moreover, the fact that the OO correlation energies are larger than experimental even in a minimal basis (where one would not expect to account for all of the correlation energy), leads to the conclusion that the LDA correlation energies are much larger than these, and thus that LDA greatly overestimates E^c in the molecules studied.

Thus, even though the OO exchange-correlation functional presented here within a minimal basis shows some limitations, such as larger bond lengths and in some cases an overestimation of the correlation energy, this error is so large in the case of LDA that this fact in itself justifies the quest for an alternative functional.

Let us now focus on the electronic spectrum of the molecule and, in particular,

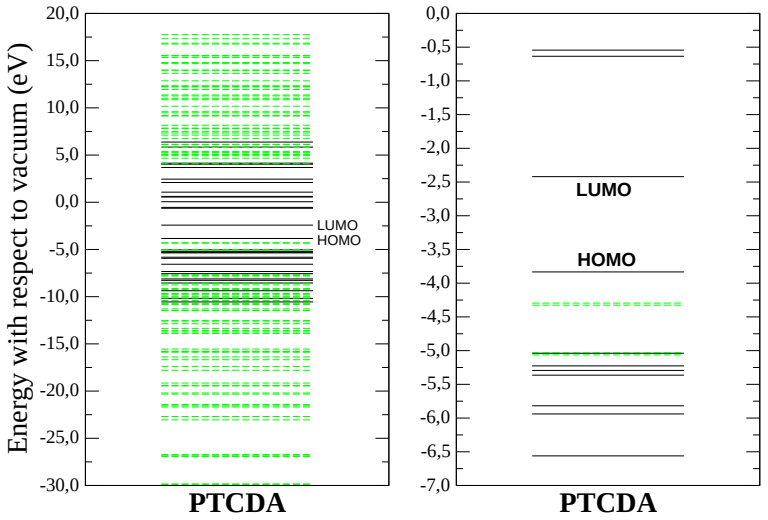

Figure 2.25.: Gas-phase single-molecule spectrum (DFT eigenvalues) for PTCDA: complete electronic spectrum (left) and zoom near the molecular gap (right), showing π (σ) molecular orbitals as continuous black (dashed grey) lines.

the states around the energy gap.

The DFT calculation yields an electronic spectrum as shown in Fig. 2.25 in the -10 – 0 eV range. Notice the Highest Occupied Molecular Orbital (HOMO) at $\sim$ -3.8 eV, and the Lowest Unoccupied Molecular Orbital (LUMO), located at $\sim$ -2.4 eV, yielding a DFT gap of $\sim$ 1.4 eV. This small value, as in the case of the other molecules studied, will be commented on in the following section.

As to the states around the molecular energy gap, the HOMO is of π symmetry, delocalized over the perylene core (the central five benzene rings), with some contribution of the oxygen atoms. Below it lie two pairs of in-plane (σ) doubly-degenerate orbitals, localized on the oxygen atoms, which resemble the oxygen lone pairs. The next molecular state is again of π symmetry, delocalized mostly over the perylene core. Below this lie other occupied states, some of π, some of σ symmetry, which will not be commented on.

The empty part of the spectrum near the gap is characterized by the abundance of π molecular orbitals. The LUMO is delocalized over the whole molecule, with a smaller contribution of the oxygen atoms. Because of the symmetry of the molecule, the HOMO and LUMO have certain symmetry characteristics: the amplitude at the atoms along the x-axis is zero, and they are symmetry or antisymmetric with

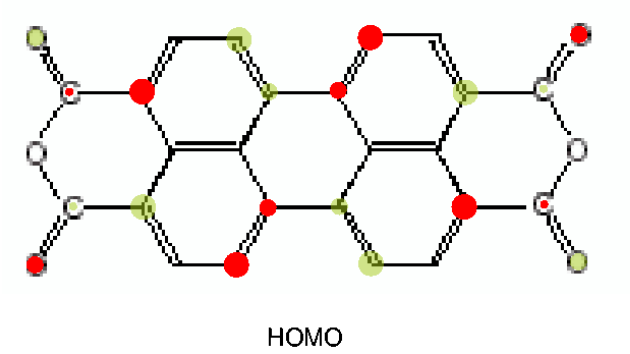

Figure 2.26.: DFT-calculated gas-phase PTCDA HOMO.

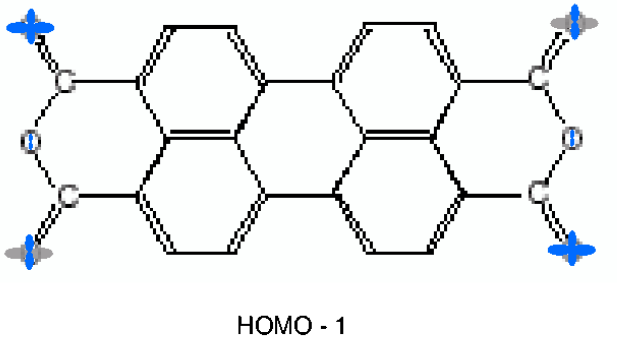

Figure 2.27.: DFT-calculated gas-phase PTCDA HOMO-1.

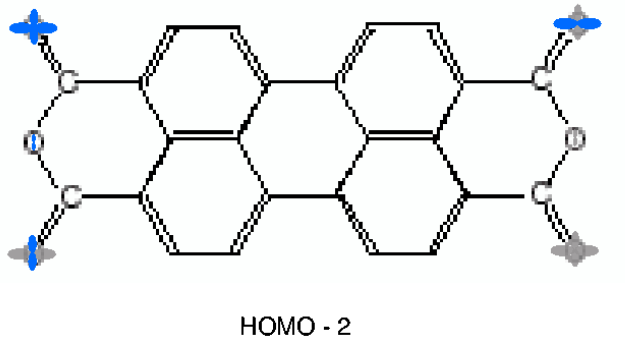

Figure 2.28.: DFT-calculated gas-phase PTCDA HOMO-2.

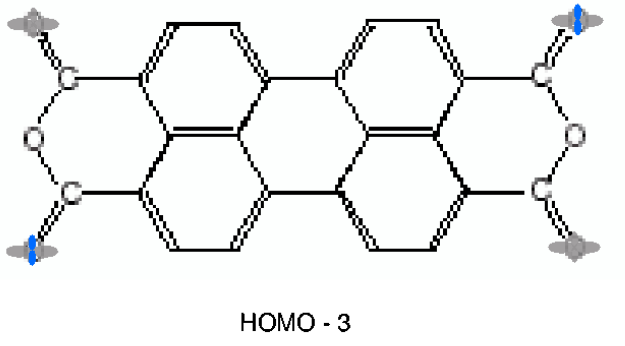

Figure 2.29.: DFT-calculated gas-phase PTCDA HOMO-3.

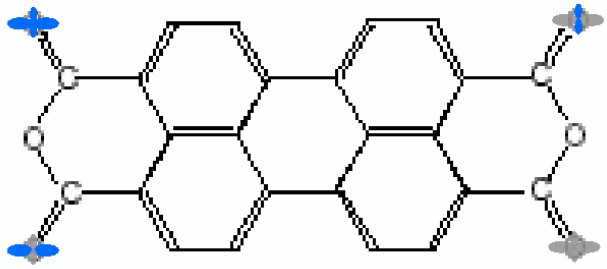

Figure 2.30.: DFT-calculated gas-phase PTCDA HOMO-4.

respect to reflections at the plane bisecting the molecule along the x or y axes. Similar (though not necessarily equal) symmetry characteristics are displayed in other molecular orbitals and other molecules.

The next empty orbitals are also delocalized over the whole molecule, especially the LUMO+1. This delocalization of the HOMO, LUMO and LUMO+1 over the molecule is of course of great importance when it comes to considering molecular transport.

Similar results were obtained for PTCDA with the different approaches, *Fireball*-LDA, *Fireball*-OO and LCAO-OO, with slight differences in the amplitude of the molecular orbitals on each atom, but showing overall agreement with each other. Due to the different approximations, there are differences in the position of the molecular orbitals, resembling more or less shifts in the states, but the overall aspect of the spectrum is preserved [Oszwaldowski03]. For simplicity, however, since *Fireball* allows for the easy determination of the equilibrium geometry, the other molecules were calculated using the *Fireball*-LDA approximation.

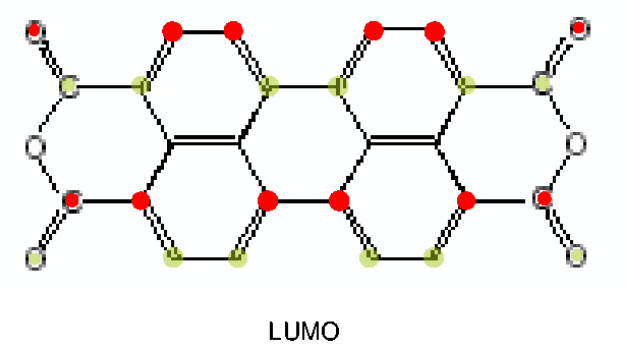

Figure 2.31.: DFT-calculated gas-phase PTCDA LUMO.

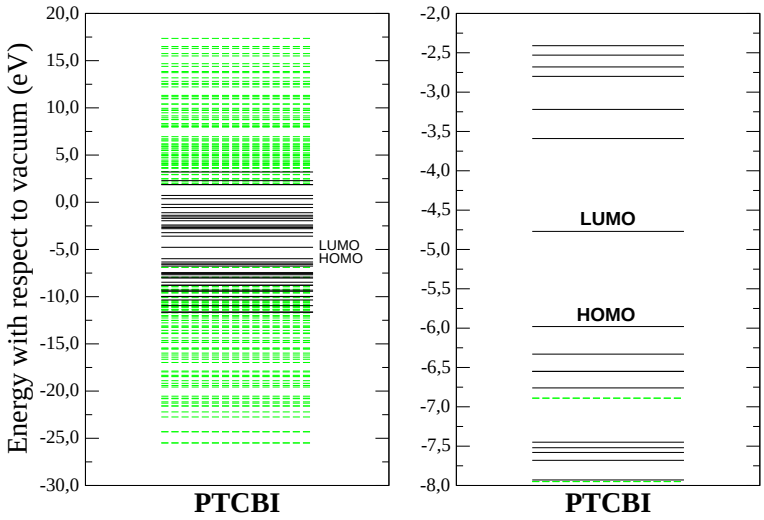

Figure 2.32.: Gas-phase single-molecule spectrum (DFT eigenvalues) for PTCBI: complete electronic spectrum (left) and zoom near the molecular gap (right), showing π (σ) molecular orbitals as continuous black (dashed grey) lines.

2.8.2. PTCBI

The spectrum of PTCBI is shown in Fig. 2.32. The HOMO (-6.0 eV) and LUMO (-4.8 eV) are, again, both of π symmetry, and the LUMO is rather separated from the rest of the other empty orbitals. As in PTCDA, orbitals of this symmetry are more abundant near the gap in the empty part of the spectrum.

Though the HOMO and LUMO are rather delocalized over the molecule, the former has greater weight on the N atoms and radical benzene groups, whereas in the case of the LUMO, the atoms with larger amplitude are mostly those of the perylene core, and the N and O atoms.

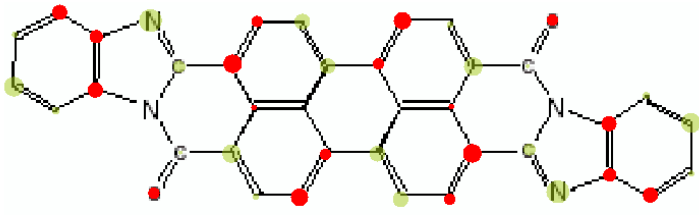

Figure 2.33.: DFT-calculated gas-phase PTCBI HOMO.

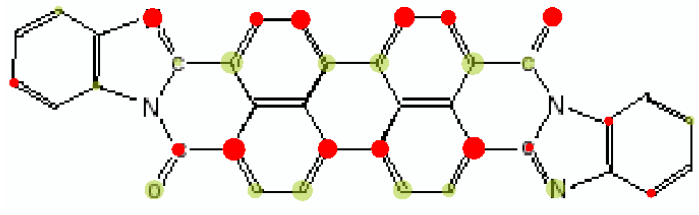

Figure 2.34.: DFT-calculated gas-phase PTCBI LUMO.

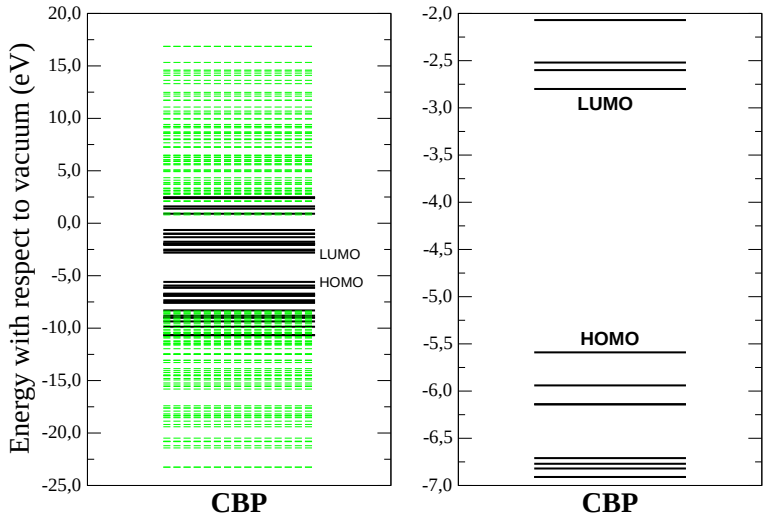

Figure 2.35.: Gas-phase single-molecule spectrum (DFT eigenvalues) for CBP: complete electronic spectrum (left) and zoom near the molecular gap (right), showing π (σ) molecular orbitals as continuous black (dashed grey) lines.

2.8.3. CBP

CBP has a large, clear DFT gap of $\sim$ 2.8 eV (Fig. 2.35). As can be seen, both the HOMO and LUMO have significant weight on most atoms of the molecule, though the HOMO has a large amplitude on the N atoms, and smaller on the other ones. The LUMO, on the other hand, has more weight on the central C atoms and the outside benzene rings, and negligible amplitude on the N. Notice also how the HOMO is antisymmetric and the LUMO is symmetric with respect to the yz plane.

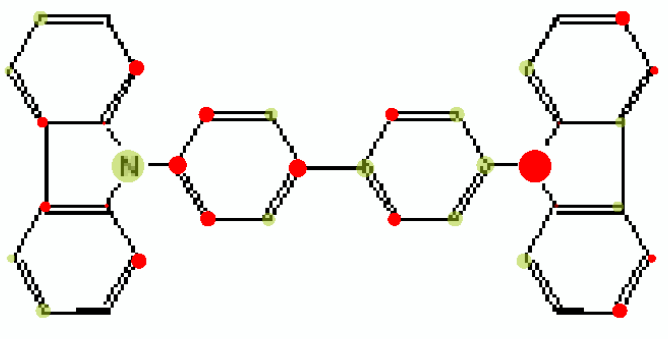

Figure 2.36.: DFT-calculated gas-phase CBP HOMO.

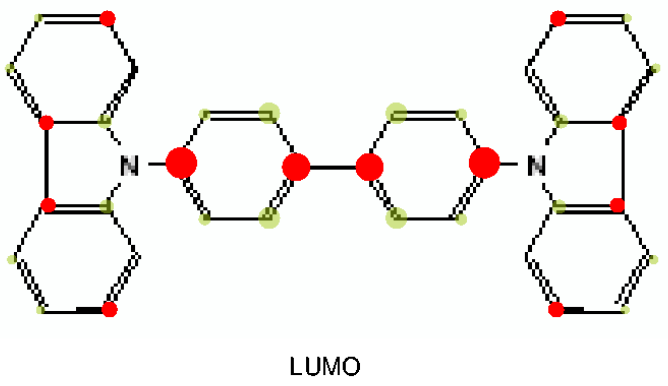

Figure 2.37.: DFT-calculated gas-phase CBP LUMO.

2.8.4. CuPc

In CuPc, a situation arises which DFT calculations are not well-suited to describe properly. The DFT spectrum (Fig. 2.38) shows a separation of around 1 eV between two empty states and a singly-occupied molecular orbital. This singly-occupied state (-4.6 eV) is, at the same time, the DFT HOMO and LUMO, since the next electron will be placed there, in a one-electron picture. Thus, our DFT calculation yields the results that CuPc is gapless. The HOMO (at the same time LUMO) is of in-plane σ symmetry, strongly localized around the Cu atom, while HOMO-1 (-4.9 eV) is of π symmetry. The doubly-degenerate LUMO+1 ($\sim$ 3.6 eV) is of π symmetry. The number of electrons in CuPc is odd, but our calculations are not spin-dependent. Ideally, one would have different (exchange) potentials for electrons of different spin, and two different spectra, one for each spin, would be obtained. Our calculation, however, average over spin occupations, so that the HOMO is singly-occupied with half an electron of up spin and half of down spin. Thus, the position of the HOMO (and, at the same time, LUMO) is not very reliable, since this averaging of occupations over both spin configurations would not occur in the isolated molecule, which means that the position of the HOMO could vary slightly in the spectrum. The position of the energy levels is quite unreliable within DFT, and even more so in the case of the Cu-localized singly-occupied state, where our calculation averages over spin occupations. To correct this, we have developed a scheme to calculate the correct positions of the energy levels, and more about correcting the DFT position of molecular orbitals will be said in Section 2.8.6. Particular attention will be paid to this Cu-related state, since the difference between the position of this orbital when an electron is removed or added (the 'proper' many-body HOMO and LUMO, see eqns. 2.51 in Section 2.8.6) yields the Coulomb U_{eff}, a measure of the electronic repulsion at this state.

The CuPc molecule is gapless since, as stated, the DFT HOMO is singly-occupied, and it can therefore accommodate one more electron. The spectrum yields a separation of $\sim$ 0.3 eV between the HOMO (LUMO) and the next occupied state (HOMO-1), and $\sim$ 1 eV with other empty states. As in other molecules, the presence of π molecular orbitals is more abundant in the empty part of the spectrum.

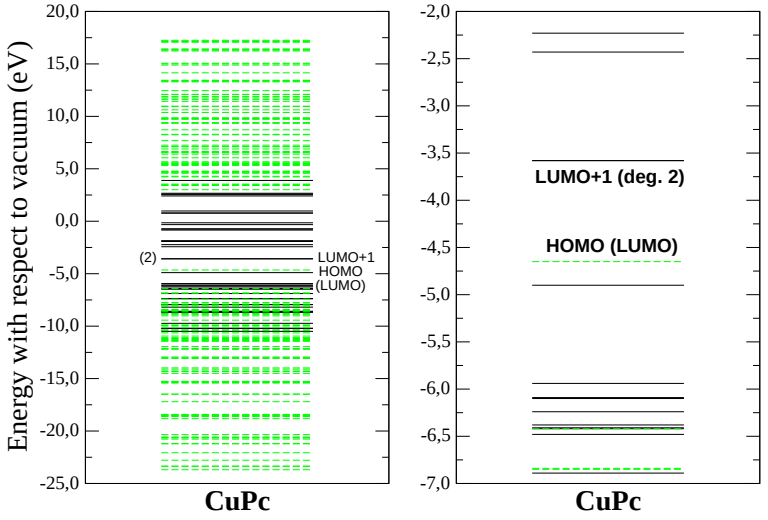

Figure 2.38.: Gas-phase single-molecule spectrum (DFT eigenvalues) for PTCDA: complete electronic spectrum (left) and zoom near the molecular gap (right), showing π (σ) molecular orbitals as continuous black (dashed grey) lines.

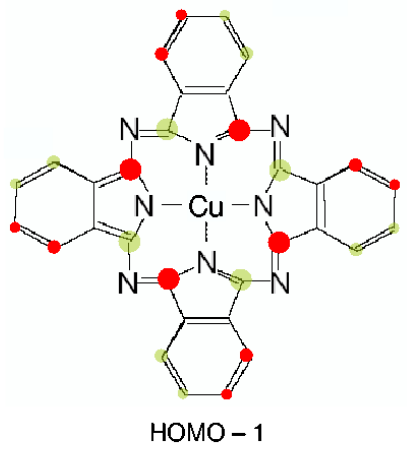

Figure 2.39.: DFT-calculated gas-phase CuPc HOMO-1.

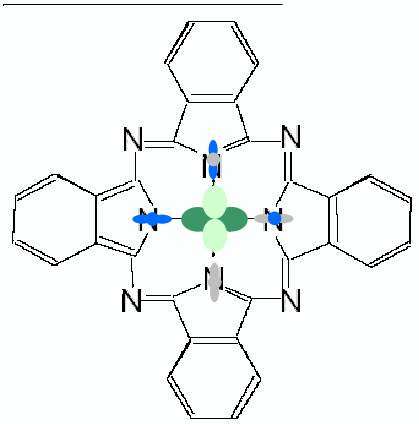

Figure 2.40.: DFT-calculated gas-phase CuPc singly-occupied HOMO (LUMO).

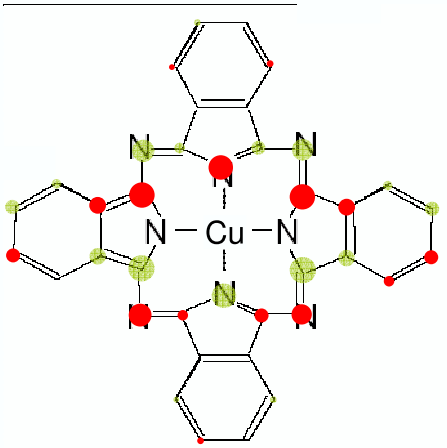

Figure 2.41.: DFT-calculated gas-phase CuPc LUMO+1.

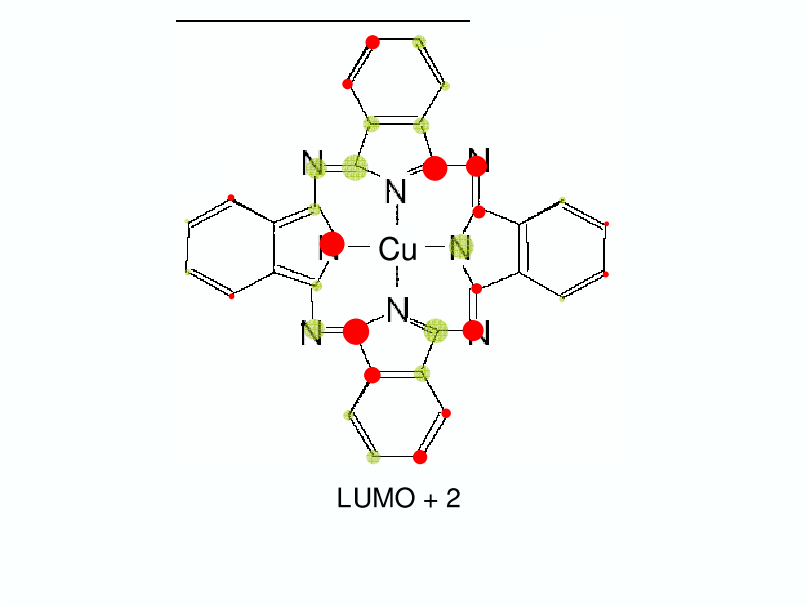

Figure 2.42.: DFT-calculated gas-phase CuPc LUMO+2.

2.8.5. Polyacenes

In the polyacene series, molecules of 3 to 6 benzene rings have been studied and are reported here. The spectrum of these molecules (Fig. 2.44) shows a greater 'packing' of molecular states with increasing number of rings, as more orbitals are added. In all cases, the HOMO and LUMO are separated from other molecular states, and orbitals of π symmetry are abundant around the gap.

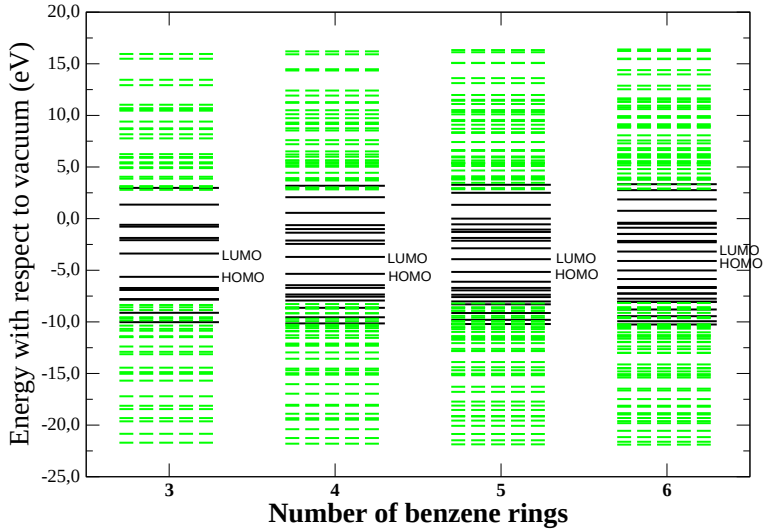

Figure 2.43.: Complete gas-phase single-molecule spectrum (DFT eigenvalues) for different polyacenes (Anthracene to 'Hexacene'), showing π (σ) molecular orbitals as continuous black (dashed grey) lines.

Let us comment on the value of the DFT gap as a function of the number of rings. Fig. 2.45 shows the values for the 3 – 6 ring series, as well as GGA calculations and experimental measurements [Hummer05a], which has been calculated within a slightly different approximation (LCAO-OO instead of *Fireball*-LDA). A striking inverse dependence on the number of benzene rings can be noticed. This dependence has been reported before for the polyacene and oligothiophene series [Hummer05a, Hummer05b, Andrzejak00, Niehaus05], but the reasons why the DFT gap should be almost inversely proportional to the number of rings is not clear. It obviously seems to be related to the quasi-linear geometry of the molecules. If

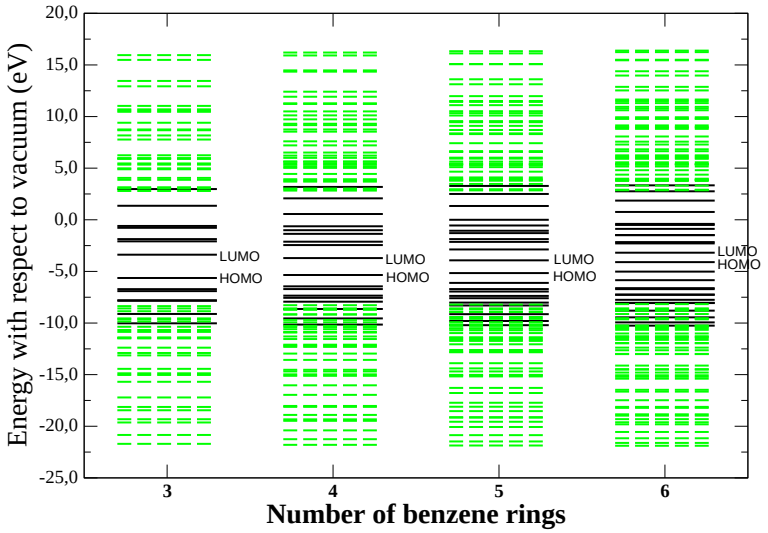

Figure 2.44.: Zoom of the gas-phase single-molecule spectrum (DFT eigenvalues) for different polyacenes (Anthracene to 'Hexacene') near the molecular gap, showing π (σ) molecular orbitals as continuous black (dashed grey) lines.

the position of the LUMO is taken, on a first approximation, as that of the HOMO plus some repulsion terms, related to the Coulomb U and J, and the orbital occupancies, then it is clear that the gap should decrease with increasing number of benzene rings, as this molecular orbitals are more delocalized and these repulsion terms become smaller. It is not clear, however, why they should do so in a way that is close to a 1/n dependence. Given the quasi-liner geometry of the molecules, an analytical model could be devised, though this is beyond the scope of this thesis and therefore left for future work.

It is interesting to extrapolate the results shown in Fig. 2.45 to the case of an infinite number of rings, $n \to \infty$, which corresponds to $1/n \to 0$ in Fig. 2.45. The extrapolation of a linear fit to the data shown for $1/n \to 0$ yield the values -0.45 $\pm$ 0.07 eV and -1.15 $\pm$ 0.03 eV for LDA and GGA cases, respectively, and -0.28 $\pm$ 0.41 eV for the experimental data. This is rather disappointing, since the negative values for the gap are clearly unphysical, while the large error in the case of the experimental data make this extrapolation inconclusive: more experimental data are needed to obtain a fit with less error. Thus, the question of whether polyacenes become metallic or remain semiconducting for an infinite number of rings is not resolved, and the only useful result from these extrapolations seems to be to highlight

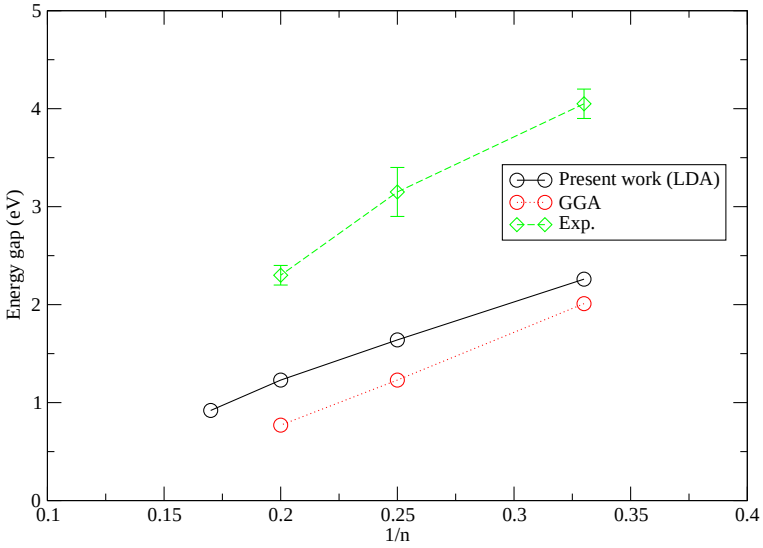

Figure 2.45.: Gas-phase single-molecule DFT (black, continuous), GGA (red, dotted) and experimental (green, dashed) energy gap for different polyacenes.

the deficiencies of DFT in the calculation of the energy gap.

Concerning the HOMO and LUMO of the polyacenes, results for Anthracene, Tetracene, Pentacene and Hexacene are presented.

The larger amplitude of both HOMO and LUMO is found in the central atoms, near the center of the molecule. In addition, carbon atoms which join two benzene rings exhibit a smaller amplitude of both HOMO and LUMO.

Concerning the symmetry of these molecular orbitals, the HOMO of polyacenes with an odd number of benzene rings (Anthracene and Pentacene) are symmetric with respect to the yz plane, whereas those with an even number (Tetracene and Hexacene) are antisymmetric with respect to this plane. The HOMO of all molecules is antisymmetric with respect to the xz plane. The symmetry of the LUMO with respect to the yz plane is the same as the HOMO: molecules with an odd number of benzene rings (Anthracene and Pentacene) are symmetric with respect to the yz plane and those with an even number (Tetracene and Hexacene) are antisymmetric with respect to this plane. But, at variance with the HOMO, the LUMO of all molecules is symmetric with respect to the xz plane.

HOMO

Figure 2.46.: DFT-calculated gas-phase Anthracene HOMO.

LUMO

Figure 2.47.: DFT-calculated gas-phase Anthracene LUMO.

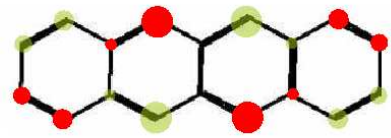

HOMO

Figure 2.48.: DFT-calculated gas-phase Tetracene HOMO.

LUMO

Figure 2.49.: DFT-calculated gas-phase Tetracene LUMO.

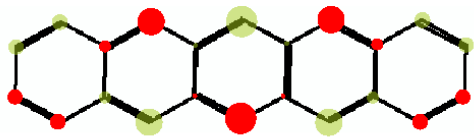

HOMO

Figure 2.50.: DFT-calculated gas-phase Pentacene HOMO.

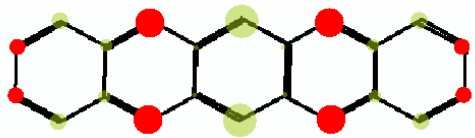

LUMO

Figure 2.51.: DFT-calculated gas-phase Pentacene LUMO.

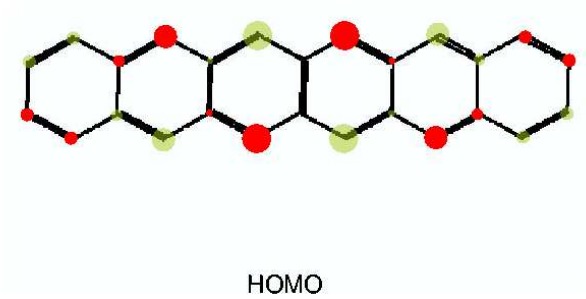

Figure 2.52.: DFT-calculated gas-phase 'Hexacene' HOMO.

Figure 2.53.: DFT-calculated gas-phase 'Hexacene' LUMO.

2.8.6. Koopmans' energy shift

From a theoretical point of view, the problem with DFT methods for organic molecules (and other small molecules) is that the energy eigenvalues do not correctly represent real electrons or hole excitations, making the calculation of the Ionization and Affinity levels more intricate. Since DFT eigenvalues are solutions to a one-electron effective Hamiltonian (equation 2.8), the ground-state spectrum of the N-electron system provides a poor description of the energy levels when an electron or hole are added to the molecule. In order to calculate the transport gap, however, the energy of an uncorrelated electron-hole pair must be computed, and this requires determining the Ionization and Affinity levels of the organic molecule.

To do this, we first recall the definitions of the Ionization (IE) and Affinity (A) energies:

$$\begin{aligned} IE &= E[N] - E[N-1] \\ A &= E[N+1] - E[N] \end{aligned} \tag{2.51}$$

where E[N_i] is the energy of the molecule with N_i = N, N-1 or N+1 electrons.

The transport gap is given by the difference between the two[3]:

$$E^t = IE - A \tag{2.52}$$

We have devised a means of determining IE and A in a simple way which, unlike LDA, does not require the calculation of either E[N+1] or E[N-1]. Instead, it introduces corrections to the energy levels of the E[N] system, using a modification of Koopmans' theorem [Koopmans33],

In our approach [Oszwaldowski03], we approximate the wavefunctions of the 'N+1'th ('N-1'th) electron by the LUMO (HOMO) of the N-electron solution. This implies neglecting electron relaxation effects, which describe how the wavefunctions are modified to accommodate the extra electron or hole. By comparing the amplitudes of the molecular orbitals of Benzene and PTCDA for the N and N$\pm$1 cases, we have verified that only minor changes place (no more than 5%), mainly on the HOMO or LUMO, as expected, and that the molecular orbitals are not significantly disturbed. These electronic relaxation effects are expected to decrease the larger the molecule, as the wavefunctions are more delocalized.

[3] The application of this approach to the optical gap is discussed in Ref. [Oszwaldowski03]

If the aforementioned relaxation effects are neglected, the additional electron (hole) wavefunctions can be described by the LUMO (HOMO) of the N-electron solution . The orbital occupancies $\{n_{i\alpha\sigma}\}$ are modified to describe the electron or hole which is being accommodated in the molecule by:

$$n_{i\alpha\sigma}^{N+1} = n_{i\alpha\sigma}^{N} + \delta n'_{i\alpha\sigma}; \qquad n_{i\alpha\sigma}^{N-1} = n_{i\alpha\sigma}^{N} - \delta n_{i\alpha\sigma} \tag{2.53}$$

where the change in the orbital occupancies are given by

$$\delta n'_{i\alpha\uparrow} = |\langle \phi_{i\alpha} | LUMO_N \rangle|^2; \qquad \delta n_{i\alpha\uparrow} = |\langle \phi_{i\alpha} | HOMO_N \rangle|^2. \tag{2.54}$$

The position of the Ionization and Affinity levels within our approximation is given by

$$\tilde{IE} = -\epsilon_{HOMO}^{N} + \delta IE; \quad \tilde{A} = -\epsilon_{LUMO}^{N} + \delta A \tag{2.55}$$

where the corrections to the HOMO and LUMO of the neutral case can be calculated from

$$\begin{aligned}
\delta IE &= \frac{1}{2} \sum_{i\alpha \neq j\beta} J_{i\alpha j\beta} \delta n_{i\alpha\uparrow} \delta n_{j\beta\uparrow} + \frac{1}{2} \sum_{i\alpha} J_{i\alpha}^{\text{eff}} \delta n_{i\alpha\uparrow}^2 + \frac{1}{2} \sum_{i\alpha} f_{i\alpha} \left(\tilde{U}_i - J_{i\alpha}^{\text{eff}} \right) \delta n_{i\alpha\uparrow}^2 \\
\delta A &= -\frac{1}{2} \sum_{i\alpha \neq j\beta} J_{i\alpha j\beta} \delta n'_{i\alpha\uparrow} \delta n'_{j\beta\uparrow} - \frac{1}{2} \sum_{i\alpha} J_{i\alpha}^{\text{eff}} \delta n'^2_{i\alpha\uparrow} - \frac{1}{2} \sum_{i\alpha} f_{i\alpha} \left(\tilde{U}_i - J_{i\alpha}^{\text{eff}} \right) \delta n'^2_{i\alpha\uparrow}
\end{aligned} \tag{2.56}$$

The term $\delta n_{i\alpha\uparrow}$ corresponds to considering the addition or removal of an electron of a particular (up or down) spin, rather than averaging over both spin configurations.

The terms δIE and δ A, which can be interpreted as self-interaction corrections for the extra hole or electron, give the variation in Hartree and exchange-correlation energy due to the change in the orbital occupancies $\{n_{i\alpha\sigma}\}$.

In the spirit of the theorem by T. Koopmans [Koopmans33], which states that, **in the absence of molecular relaxation**, the ionization energy of the system is given by -ϵ_{HOMO}, we call δIE and δA 'Koopmans energy shifts'.

To asses the validity of our approximation, we calculated the gas-phase IE, A and E^t for Benzene and PTCDA in two ways: from the (exact) definitions (2.51);

Benzene	IE	$-\epsilon^N_{HOMO}+\delta$IE	A	$-\epsilon^N_{LUMO}+\delta$A	E^t_{exact}	$E^t_{Koopmans}$
Fireball-LDA	9.35	—	-2.5	—	11.85	—
Fireball-OO	8.6	8.2 (0.4)	-4.0	-4.6 (0.6)	12.6	12.8 (-0.2)
LCAO-OO	6.6	7.3 (-0.7)	-5.3	-5.7 (0.4)	11.9	13.0 (-1.1)

and from the adaptation of Koopmans theorem described above, using equations (2.55)–(2.56). The results [Oszwaldowski03] are summarized in the tables below (all energies are expressed in eV). For the sake of clarity, we have shown the difference between both approaches in parentheses:

Note that there is no comparison at the LDA level, since this is only possible within the Orbital-Occupancy approximation.

The differences between the *Fireball*-OO and LCAO-OO approaches has already been discussed; here we will comment on the accuracy of the 'Koopmans' approach, by comparing with the exact results.

In Benzene, the differences (shown in parentheses) in IE and A are rather large. Moreover, when calculating E^t, a small difference of 0.2 eV (for the case of *Fireball*-OO) results if these differences cancel each other out, but a very large 1.1 eV error results when they add up in the case of the LCAO-OO data. The rather large errors in the 'Koopmans' calculation of IE and A indicate that the assumption of negligible electronic relaxation is not valid. Why these differences should cancel or not when calculating E^t is unclear. The experimental values for the gas-phase Ionization and Affinity levels of Benzene are -9.24 eV [Lide98] and -1.14 eV [Nenner75], respectively, yielding E^t = 10.38 eV. The IE compares well only with the *Fireball*-LDA results. The discrepancies in IE and A are quite large, and are partly compensated in the calculation of E^t. The comparison with experimental data indicated that our results for the gas-phase transport gap have an accuracy of $\sim$ 1.5 eV. The accuracy of the ´Koopmans' approach is much better for the case of *Fireball*-OO.

PTCDA	IE	$-\epsilon^N_{HOMO}+\delta$IE	A	$-\epsilon^N_{LUMO}+\delta$A	E^t_{exact}	$E^t_{Koopmans}$
Fireball-LDA	7.6	—	2.6	—	5.0	—
Fireball-OO	5.9	6.1 (-0.2)	1.1	1.2 (-0.1)	4.8	4.9 (-0.1)
LCAO-OO	5.9	6.2 (-0.3)	0.4	0.3 (0.1)	5.5	5.9 (-0.4)

The results clearly show an improvement for the case of PTCDA (Table 2.8.6). The 'Koopmans' calculation of IE and A show good agreement with the exact values, with smaller differences than in Benzene. This is attributed to the larger size of the molecule, which results in more extended wavefunctions (in particular, HOMO and LUMO), which reduces the electronic relaxation effects. Since our 'Koopmans' approximation neglects these relaxation effects, it is not surprising to find a better agreement than in a smaller molecule like Benzene.

For PTCDA, the experimental IE is 8.15 eV [Anderson98]. In addition, theoretical values, using a large (6-31G*) basis set and the B3LYP exchange-correlation functional, were reported [Andrzejak00], yielding IE = 7.79 eV and A = 2.59 eV, which give E^t = 5.2 eV. Since this theoretical result can be considered to be basis-converged, the 0.36 eV difference in IE with experiment gives an idea of the typical errors of theoretical calculations. If a similar value is taken for A, then errors in E^t can range from practically zero to $\sim$ 0.7–0.8 eV. Our results show smaller values for IE and A, especially the OO ones, while the *Fireball*-LDA results are quite similar to the reported theoretical values. Within our (*Fireball*-OO or LCAO-OO) approach, however, the comparison between exact and 'Koopmans' energies yields differences which are smaller than in Benzene, and a better agreement in E^t is found.

In summary, we have used a scheme for calculating IE, A and E^t in organic molecules in a simple way. The use of this scheme to calculate IE, A and E^t, through equations (2.55)–(2.56), which implies neglecting electron relaxation effects, was investigated in Benzene and PTCDA. For both molecules, the *Fireball*-OO method was found to produce better agreement with the exact calculation. For both cases, better results were found for PTCDA, where relaxation effects are smaller since the molecular orbitals are more delocalized due to the larger size of the molecule. We have therefore made use of these 'Koopmans energy shifts' to calculate the Ionization and Affinity levels, as well as transport gap, of the organic molecules considered in this thesis.

We can plot the 'Koopmans' energy shifts for each molecular orbital for these materials. The figures show the magnitude and sign of these energy shifts vs. the molecular orbital number. The occupied molecular orbitals have a negative 'Koopmans' energy shift, whereas this is positive for empty states; the result is an increase in the energy gap, as corresponds to a correction to the underestimation coming from DFT. A second characteristic of these results is the similarity between

energy shifts of different orbitals sharing the same symmetry: energy shifts which are roughly the same for all π orbitals, and, to a lesser extent, the same can be said of σ states. This is especially so for π molecular orbitals, and is due to the similarity in the wavefunctions. Finally, it should be mentioned that we believe our correction to the molecular orbital energies (the 'Koopmans' shifts) are more meaningful the closer the states are to the gap: charge excitations in orbitals with very low or high energy, far away from the HOMO or LUMO (such as 'core' molecular orbitals), are not properly described by this approach but these states do not play a significant role in Fermi level pinning. Therefore, a proper treatment of these states is not necessary for our purposes, since they do not affect the DOS induced in the energy gap.

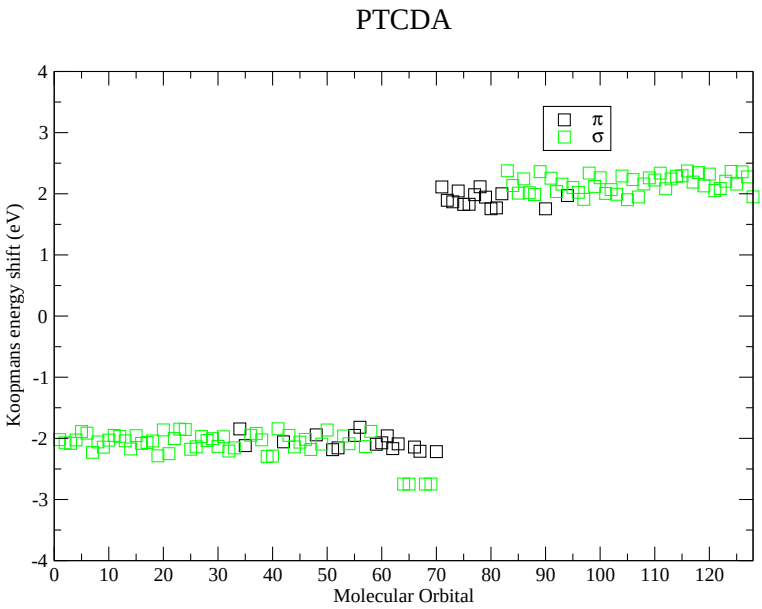

Figure 2.54.: 'Koopmans' correction terms (eV) for the different molecular orbitals.

PTCDA

The results for PTCDA show the 'Koopmans' shift, which acts as a 'scissors' operator, opening the molecular gap. The DFT gap is $\sim$ 1.6 eV, while the calculated value after the 'Koopmans' shift is $\sim$ 5.7 eV. Thus, the Koopmans correction is quite large, of $\sim$ 4.1 eV, as shown in Fig. 2.55.

Concerning the energy corrections ('Koopmans shifts') to the different molecular orbitals, those corresponding to π molecular orbitals (shown in black) are in general larger than those for in-plane σ orbitals (see Fig. 2.54). Notice, however, the four σ occupied molecular orbitals closest to the gap. These correspond to oxygen-related states, similar to dangling bonds, strongly localized around the O atoms. This localization, together with the physical proximity of these oxygen atoms, give rise to large contributions in equations 2.56 which make the ´Koopmans shifts' for these orbitals rather large.

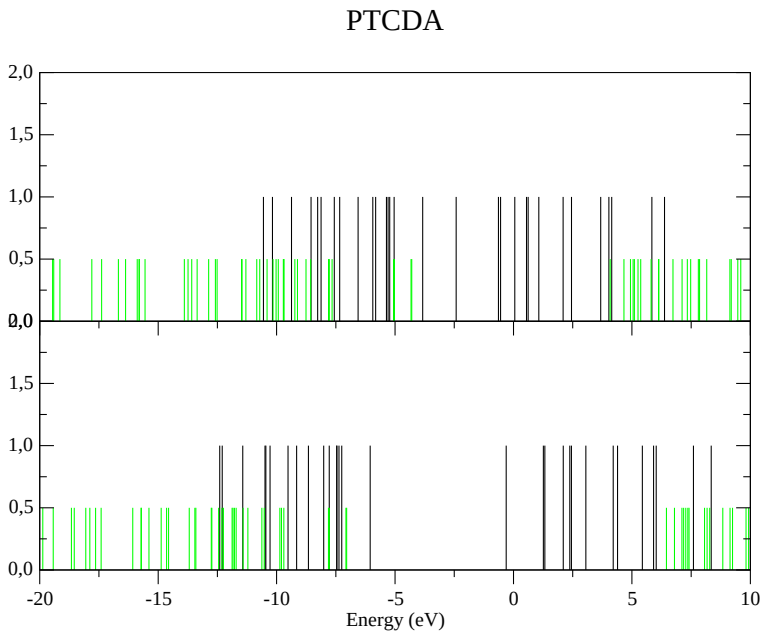

Figure 2.55.: Energy spectrum before (top) and after (bottom) applying the 'Koopmans' energy shift to the DFT spectrum. π (σ) molecular orbitals are shown as long black (short grey). DFT HOMO at -4.0 eV, LUMO at -2.4 eV (top), and 'Koopmans' HOMO at -6.0 eV and LUMO at -0.3 eV (bottom).

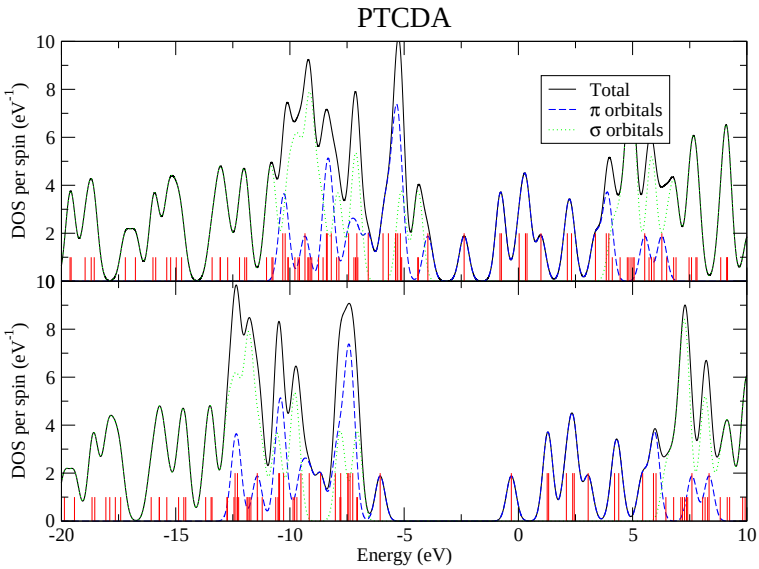

Figure 2.56.: DOS per spin for the DFT spectrum (top) and after applying the 'Koopmans' correction (bottom). The states in Fig. 2.55 have been broadened using a 0.5 eV FWHM Gaussian broadening. The contributions coming from the π and σ molecular orbitals are shown.

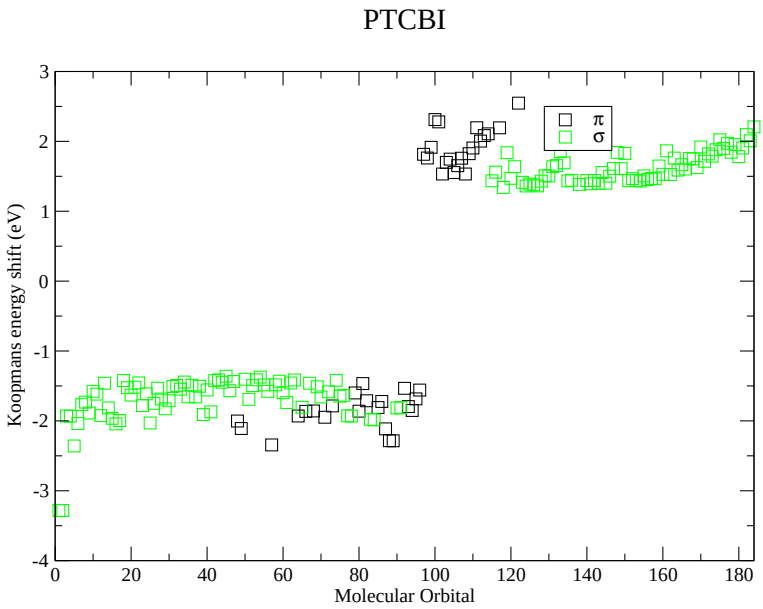

Figure 2.57.: 'Koopmans' correction terms (eV) for the different molecular orbitals.

PTCBI

The results for PTCBI are similar to PTCDA: shifts of around $\sim$ 1.5–2.0 eV for most states, resulting in an increase of the gap of 3–4 eV with respect to the DFT results.

These energy shifts are similar to a scissors operator, shifting the occupied and empty states, increasing the energy gap. This is shown in Fig. 2.58. In particular, notice how the energy gap increases from $\sim$ 1.2 eV in the DFT spectrum to $\sim$ 4.6 eV, as corresponds to a better calculation of the gap, underestimated by DFT.

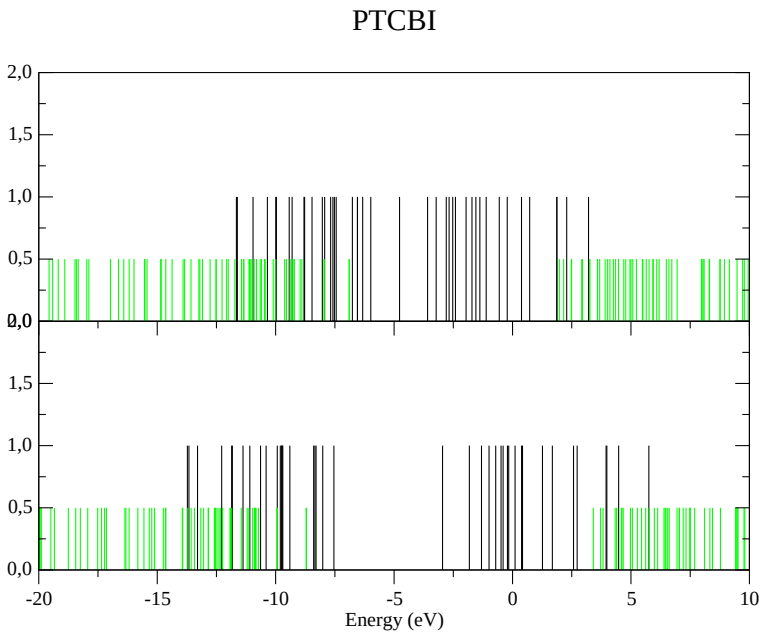

Figure 2.58.: Energy spectrum before (top) and after (bottom) applying the 'Koopmans' energy shift to the DFT spectrum. π (σ) molecular orbitals are shown as long black (short grey). DFT HOMO at -6.0 eV, LUMO at -4.8 eV (top), and 'Koopmans' HOMO at -7.5 eV and LUMO at -3.0 eV (bottom).

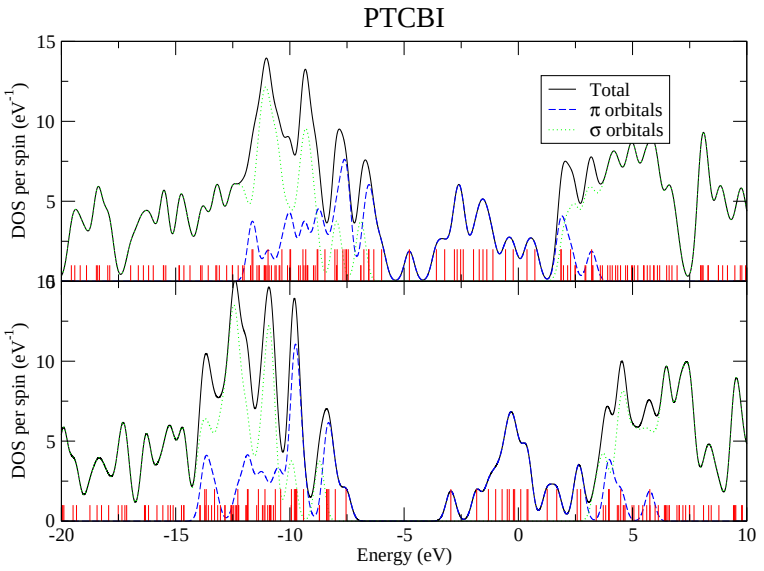

Figure 2.59.: DOS per spin for the DFT spectrum (top) and after applying the 'Koopmans' correction (bottom). The states in Fig. 2.58 have been broadened using a 0.5 eV FWHM Gaussian broadening. The contributions coming from the π and σ molecular orbitals are shown.

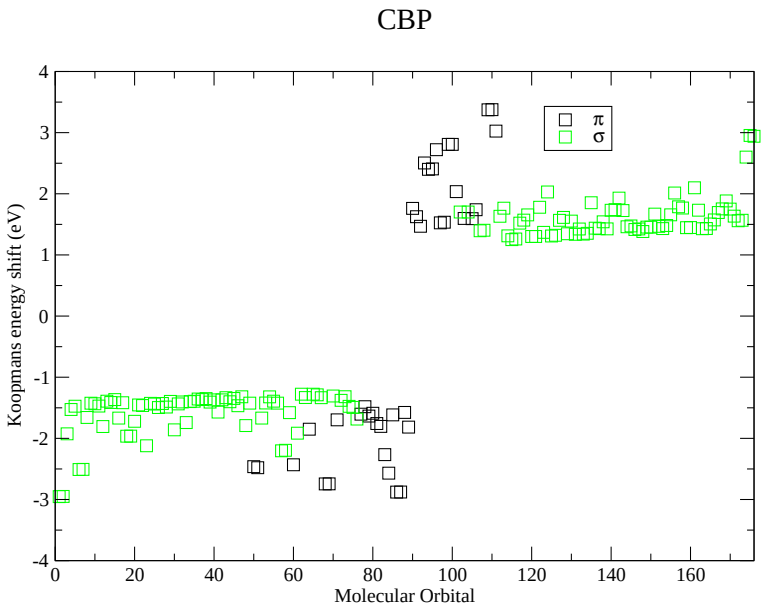

Figure 2.60.: 'Koopmans' correction terms (eV) for the different molecular orbitals.

CBP

For CBP, the results are similar, showing slightly greater energy shifts for some empty and occupied results and the scatter, especially in π orbitals is larger.

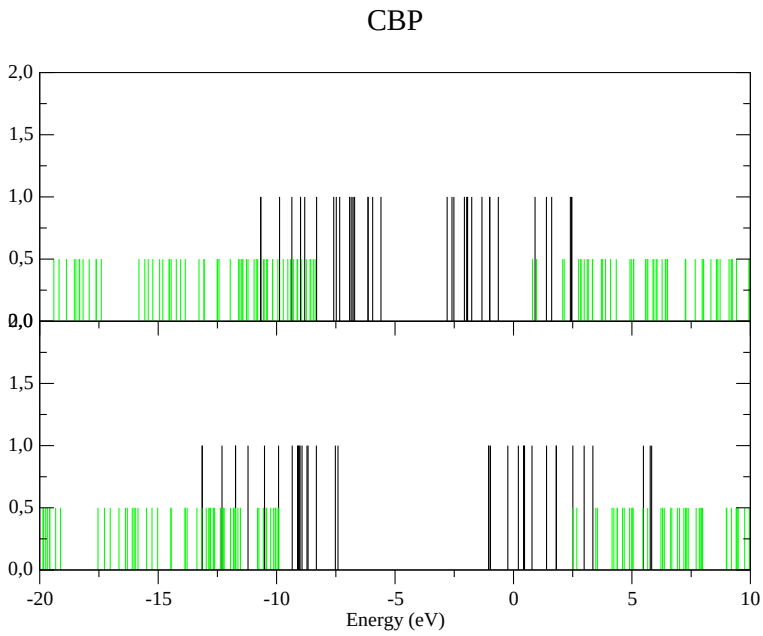

Figure 2.61.: Energy spectrum before (top) and after (bottom) applying the 'Koopmans' energy shift to the DFT spectrum. π (σ) molecular orbitals are shown as long black (short grey). DFT HOMO at -5.6 eV, LUMO at -2.8 eV (top), and 'Koopmans' HOMO at -7.4 eV and LUMO at -1.0 eV (bottom).

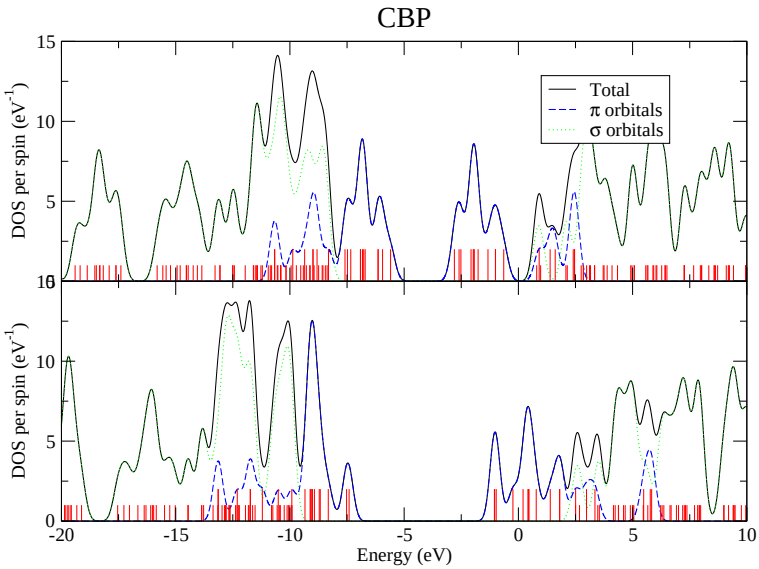

Figure 2.62.: DOS per spin for the DFT spectrum (top) and after applying the 'Koopmans' correction (bottom). The states in Fig. 2.61 have been broadened using a 0.5 eV FWHM Gaussian broadening. The contributions coming from the π and σ molecular orbitals are shown.

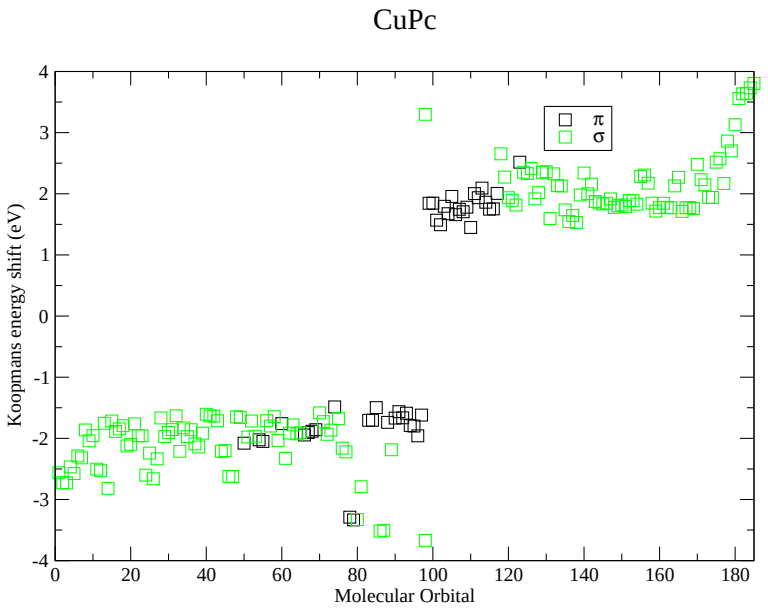

Figure 2.63.: 'Koopmans' correction terms (eV) for the different molecular orbitals.

CuPc

In this case, the differences between π and σ orbitals are much greater, due to the strong interactions at the Cu atoms. Note that the 'Koopmans' shift for π orbitals is 1.6–2.0 eV, while those for Cu-localized σ states are larger: molecular orbitals with a large amplitude in the Cu atom give rise to a large contribution in equation 2.56, resulting in exceptionally large energy shifts. This tends to push those orbitals away from the gap, leaving mainly π molecular orbitals.

In the case of CuPc, the singly-occupied HOMO is, at the same time, the LUMO since in a one-electron picture, the next electron would be 'placed' on this molecular orbital. The CuPc molecule is therefore gapless. Thus, when calculating the Koopmans energy shifts, the HOMO (also LUMO) gives rise to two states: an empty and an occupied one, which correspond to the energy positions of adding or removing an electron to or from this state. This can be seen in Fig. 2.64: the HOMO (also the LUMO) at -4.6 eV, indicated by a short grey bar (top panel) gives rise to two states: one at -8.3 eV and another at -1.3 eV (bottom panel). Since this case is rather intricate, we mention that the DFT HOMO (also LUMO, at -4.6 eV) was first corrected to compensate for the self-interaction introduced in our calculations by averaging the

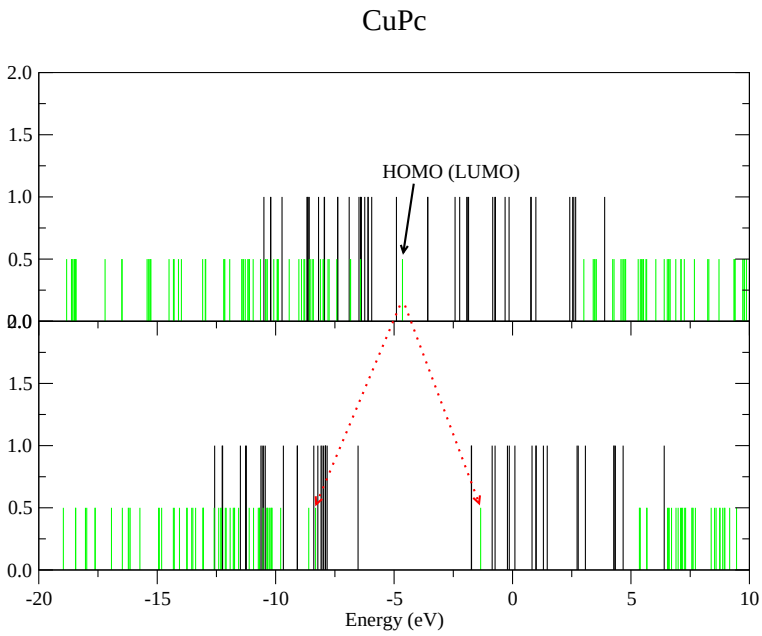

Figure 2.64.: Energy spectrum before (top) and after (bottom) applying the 'Koopmans' energy shift to the DFT spectrum. π (σ) molecular orbitals are shown as long black (short grey). DFT HOMO (also LUMO) at -4.6 eV (top), and 'Koopmans' HOMO at -6.5 eV and LUMO at -1.7 eV (bottom). In the case of CuPc, notice how the Cu-related HOMO (also LUMO) at -4.6 eV (top) gives rise to two states, at -8.3 and -1.3 eV (bottom). Note that each of these states can accommodate one electron **in total** (not per spin).

singly-occupied state over spin occupations, half an electron spin up, half down. This correction is $\sim$ 0.4 eV, and shifts the state towards higher binding energies. From this energy position, the 'Koopmans' shifts which determine the energy positions for the empty and occupied states were determined. The difference between them yields the effective Coulomb repulsion of the Cu-localized state, U_{eff} = 7.0 eV.

This value is interesting since metal phthalocyanines where the metal has an uneven number of electrons can be thought of as (para)magnetic impurities embedded in a matrix of aromatic benzene rings. Kondo-like effects have been observed in these systems [Zhao05] and the Coulomb repulsion is thus of importance (although no estimate for U is given in Ref. [Zhao05] for comparison).

It is worth noting that the 'Koopmans' shift creates a crossing of molecular levels. The HOMO, with its localized nature and large energy shift is pushed deeper in

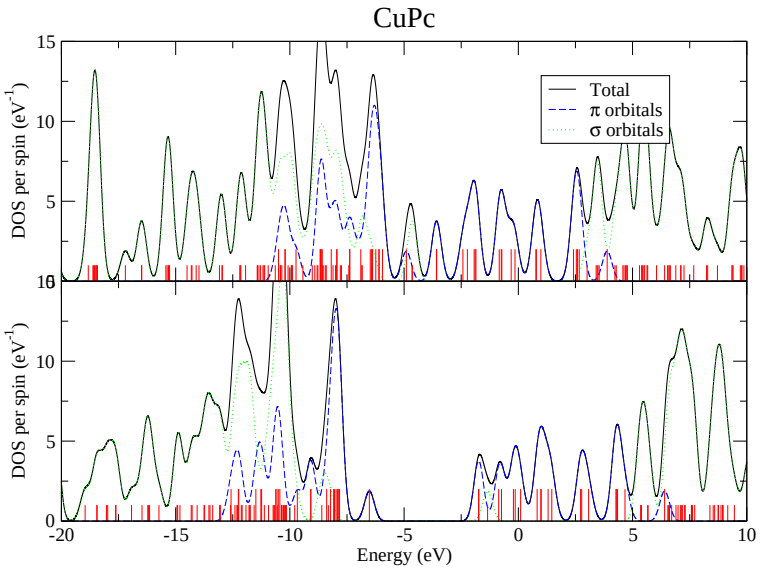

Figure 2.65.: DOS per spin for the DFT spectrum (top) and after applying the 'Koopmans' correction (bottom). The states in Fig. 2.64 have been broadened using a 0.5 eV FWHM Gaussian broadening. The contributions coming from the π and σ molecular orbitals are shown.

energy more than the HOMO-1, of π symmetry, which has a smaller Koopmans shift. The same happens with the LUMO and LUMO+1: the Koopmans shift of both states is such that it gives rise to a crossing of both molecular states. Thus, the application of our modification of Koopmans theorem yields a HOMO which is the HOMO-1 of the DFT calculation, and a LUMO which is the LUMO+1 of the DFT results.

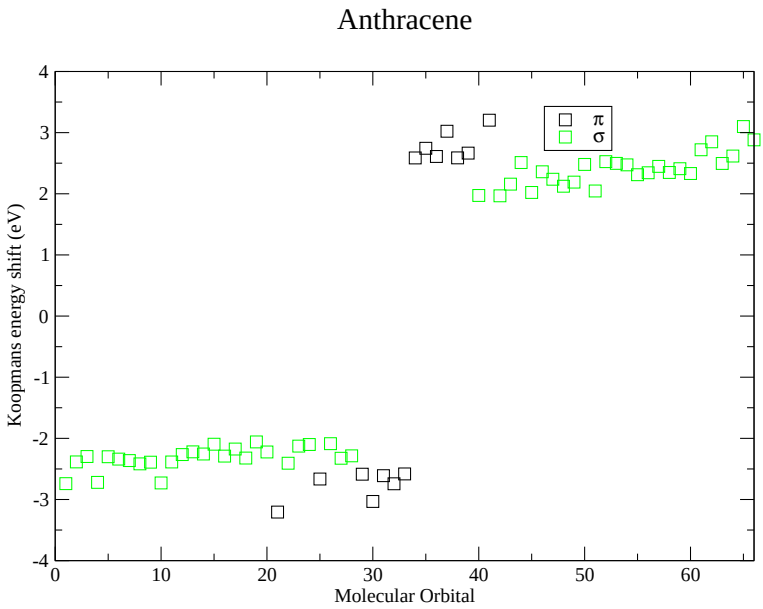

Figure 2.66.: 'Koopmans' correction terms (eV) for the different molecular orbitals.

Polyacenes

The energy shifts for the polyacenes show trends with increasing size of the molecule. The magnitude of these shifts is greater for Anthracene and decreases with the number of benzene rings, as corresponds to greater delocalization of the molecular orbitals and thus energy relaxation values (see Figures 2.66–2.69).

As before, the shift of π orbitals are similar to one another, and those of σ orbitals are normally greater, as they contain intraatomic contributions in equation 2.56.

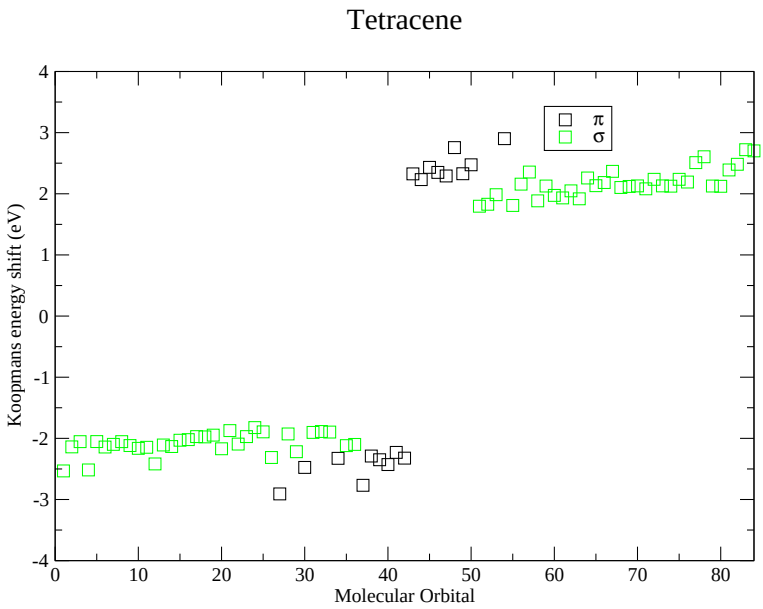

Figure 2.67.: 'Koopmans' correction terms (eV) for the different molecular orbitals.

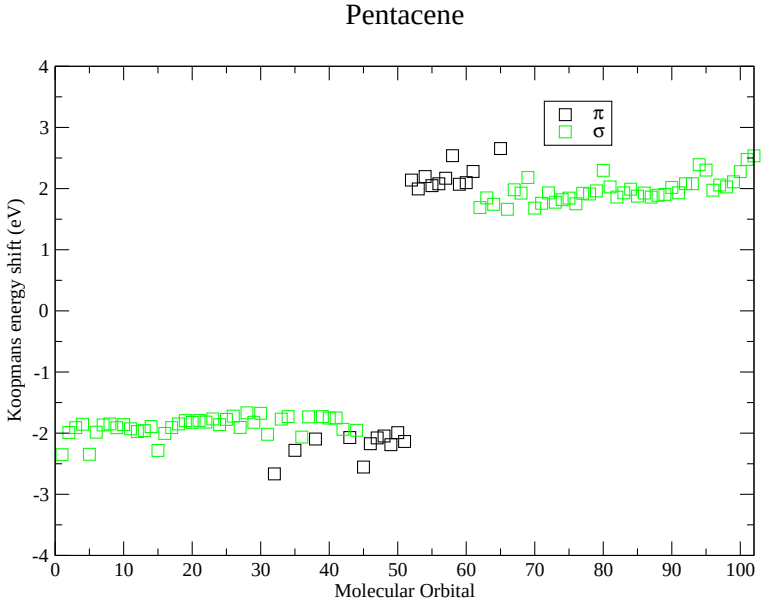

Figure 2.68.: 'Koopmans' correction terms (eV) for the different molecular orbitals.

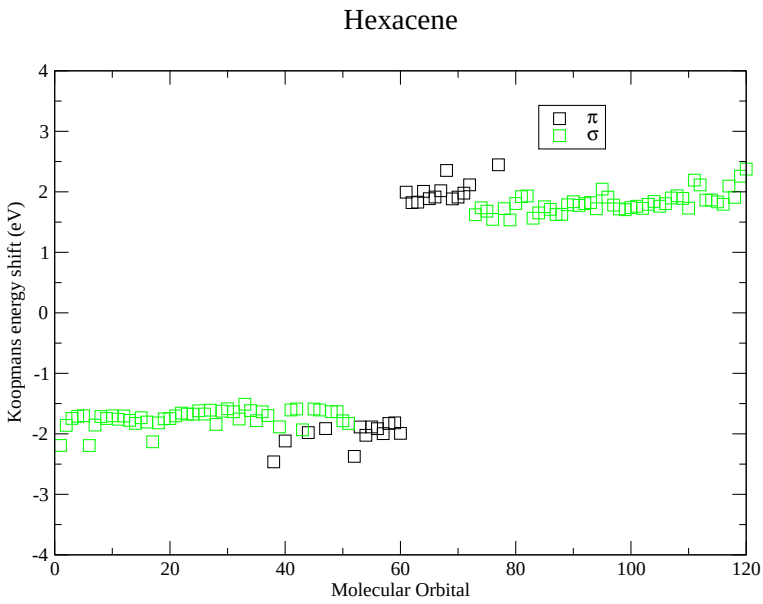

Figure 2.69.: 'Koopmans' correction terms (eV) for the different molecular orbitals.

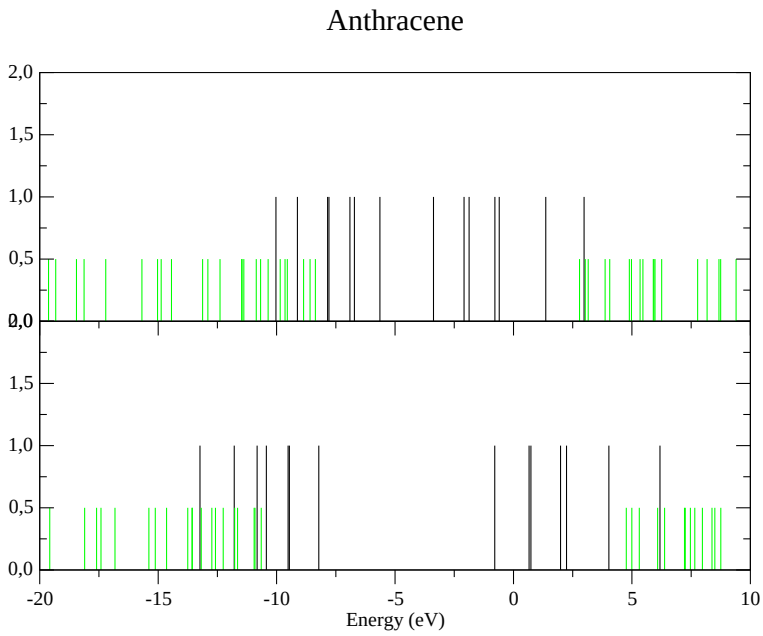

Figure 2.70.: Energy spectrum before (top) and after (bottom) applying the 'Koopmans' energy shift to the DFT spectrum. π (σ) molecular orbitals are shown as long black (short grey). DFT HOMO at -5.6 eV, LUMO at -3.4 eV (top), and 'Koopmans' HOMO at -8.2 eV and LUMO at -0.8 eV (bottom).

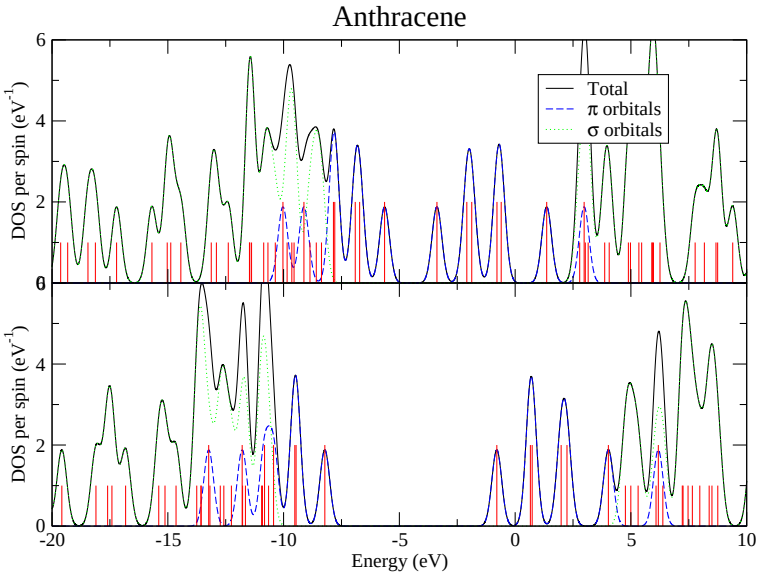

Figure 2.71.: DOS per spin for the DFT spectrum (top) and after applying the 'Koopmans' correction (bottom). The states in Fig. 2.70 have been broadened using a 0.5 eV FWHM Gaussian broadening. The contributions coming from the π and σ molecular orbitals are shown.

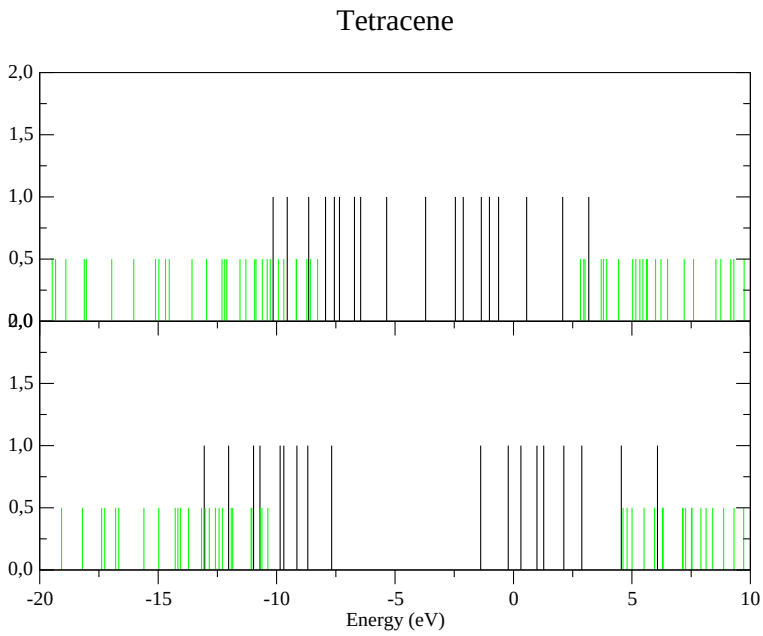

Figure 2.72.: Energy spectrum before (top) and after (bottom) applying the 'Koopmans' energy shift to the DFT spectrum. π (σ) molecular orbitals are shown as long black (short grey). DFT HOMO at -5.4 eV, LUMO at -3.7 eV (top), and 'Koopmans' HOMO at -7.7 eV and LUMO at -1.4 eV (bottom).

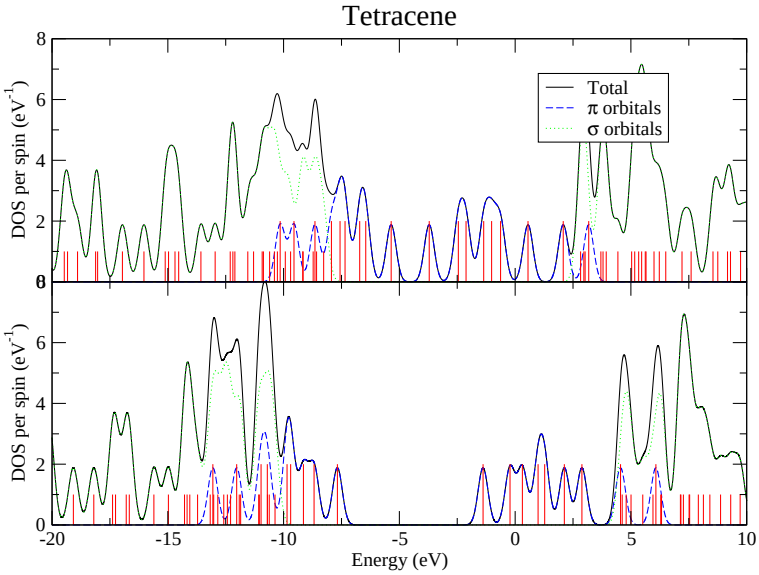

Figure 2.73.: DOS per spin for the DFT spectrum (top) and after applying the 'Koopmans' correction (bottom). The states in Fig. 2.72 have been broadened using a 0.5 eV FWHM Gaussian broadening. The contributions coming from the π and σ molecular orbitals are shown.

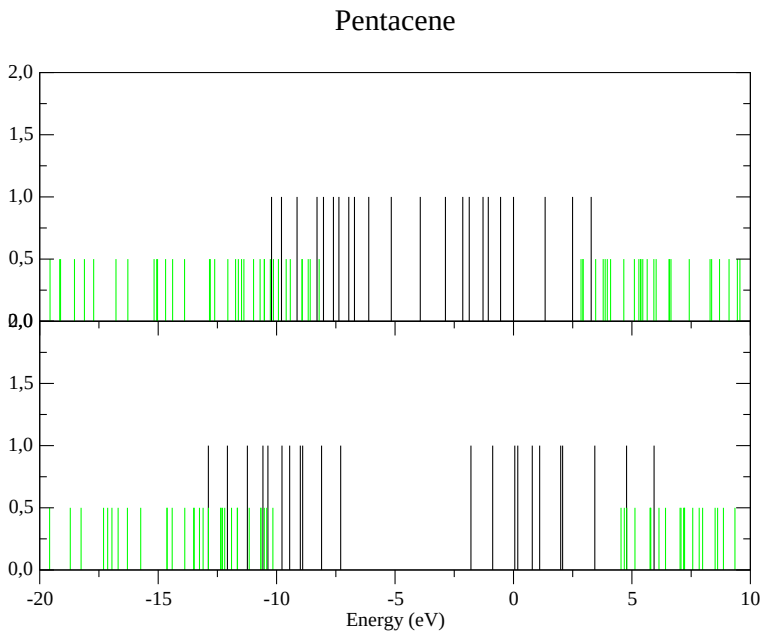

Figure 2.74.: Energy spectrum before (top) and after (bottom) applying the 'Koopmans' energy shift to the DFT spectrum. π (σ) molecular orbitals are shown as long black (short grey). DFT HOMO at -5.2 eV, LUMO at -3.9 eV (top), and 'Koopmans' HOMO at -7.3 eV and LUMO at -1.8 eV (bottom).

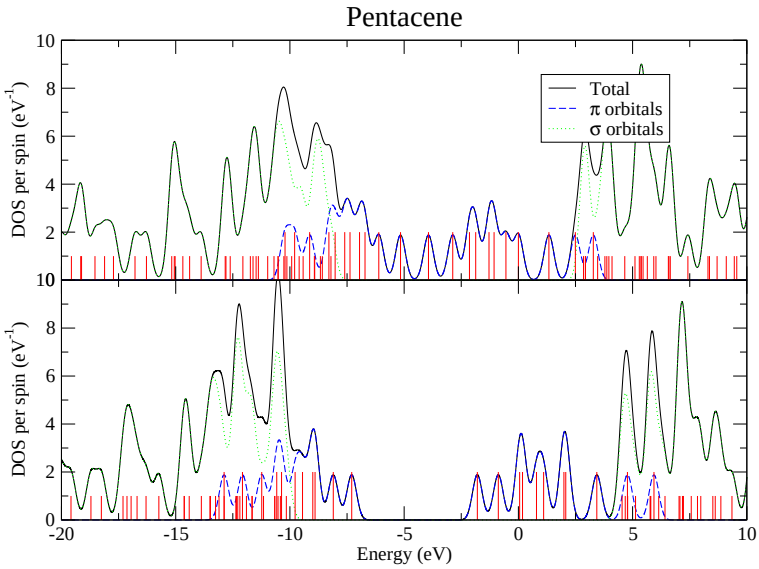

Figure 2.75.: DOS per spin for the DFT spectrum (top) and after applying the 'Koopmans' correction (bottom). The states in Fig. 2.74 have been broadened using a 0.5 eV FWHM Gaussian broadening. The contributions coming from the π and σ molecular orbitals are shown.

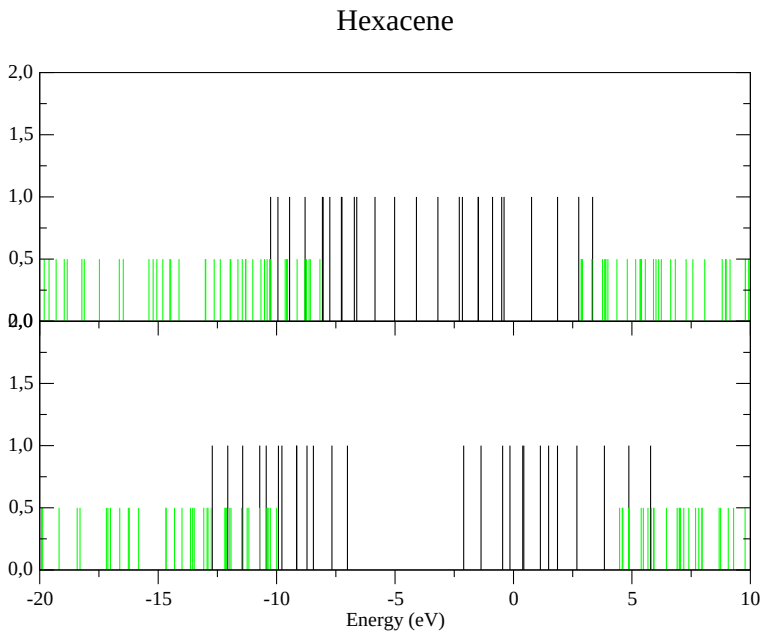

Figure 2.76.: Energy spectrum before (top) and after (bottom) applying the 'Koopmans' energy shift to the DFT spectrum. π (σ) molecular orbitals are shown as long black (short grey). DFT HOMO at -5.0 eV, LUMO at -4.1 eV (top), and 'Koopmans' HOMO at -7.0 eV and LUMO at -2.1 eV (bottom).

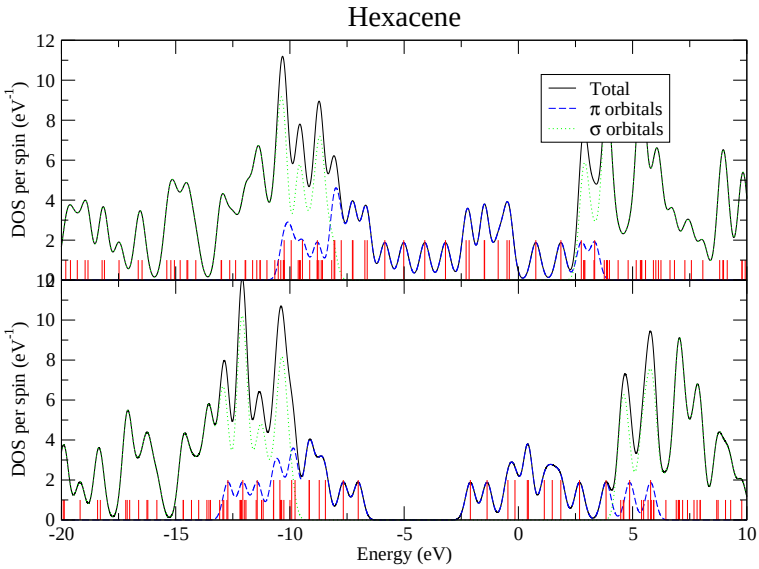

Figure 2.77.: DOS per spin for the DFT spectrum (top) and after applying the 'Koopmans' correction (bottom). The states in Fig. 2.76 have been broadened using a 0.5 eV FWHM Gaussian broadening. The contributions coming from the π and σ molecular orbitals are shown.

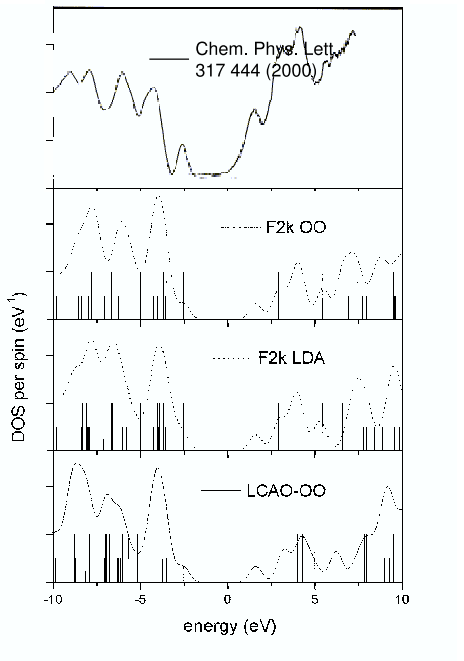

Figure 2.78.: Comparison of experimental photoemission measurements (Ref. [Hill00a]) with the DOS (eV^{-1}, arbitrary units) calculated with the different approximations.

In summary, notice how in the case of all molecules, the underestimation of the energy gap by DFT leads to a bad representation of the energy levels. In particular, for the case of PTCDA, the DOS of our results using the different methods was compared with direct and inverse photoemission experimental measurements of a PTCDA thin film [Hill00a]. Since the molecular levels of the film are broadened by thermal effects and possibly disorder [Hill00a], our calculated peaks were broadened by gaussian functions having a FWHM of 1 eV. Since the transport gap in thin films has a significant contribution from polarization of the surrounding media, not taken into account by our 'Koopmans' approximation, we have fitted, as is done usually since no *ab-initio* method can calculate these terms with sufficient accuracy, the ionization and affinity levels to experiment.

The general shape of the calculated spectra agree well with experiment. The HOMO is best resolved in the LCAO-OO case, while in the case of LDA is it barely discernible from a group of close-lying occupied states. The peaks in the occupied part of the experimental spectrum, which correspond to the presence of several states close in energy, are well reproduced. As for the unoccupied states,the LUMO is well resolved in all cases, in accordance with the experimental spectrum, and other features such as the next two peaks, are well reproduced.

From this good agreement with experiment, we conclude that first-principles methods are an important tool to study the electronic structure and DOS of small-molecule organic materials.

2.9. Conclusions

DFT has been used to investigate the electronic properties of several molecules. First, we have briefly described the fundamentals of DFT-based methods. Second, two different DFT approaches (conventional LDA and the OO method) have been compared and results for small molecules have been presented: the effect of different exchange-correlation functionals and of the basis set used was analyzed, and the electronic structure of these small molecules was presented. Then, the electronic properties of π-conjugated organic molecules is calculated. For this, the *Fireball*-LDA approach was chosen, since the geometrical optimization of these molecules is essential and this code is the only one which enables molecular dynamics and geometry optimization. The position and nature of the electronic levels of these molecules is calculated and discussed, paying special attention to the symmetry of the states around the gap (HOMO and LUMO). Finally, since it is known that DFT underestimates the energy gap, as is seen for the case of the π-conjugated organic molecules studied, a method for correcting this deficiency is presented and discussed. It is shown that, within the limitations of a minimal basis set, or approach, reminiscent of Koopmans' theorem, is a useful and necessary method to calculate the 'true' gas-phase energy gap of localized systems such as the organic molecules analyzed.

The results presented in this chapter are important because they show, in the first place, the prime importance of DFT-based methods in calculating the electronic properties of nanostructures; in this case, of π-conjugated organic molecules and metal surfaces. DFT has become increasingly important and is nowadays an essential and almost standard tool of theoretical solid-state or condensed-matter

physics.

The electronic structure of these π-conjugated molecules is important for our analysis of weakly interacting metal/organic or organic/organic interfaces. The position of the molecular levels, for which our 'Koopmans' approach is relevant, and the nature (symmetry, charge distribution, ...) of the molecular states around the gap is essential for a correct description of the interface properties. Since weakly-interacting interfaces, such as those formed between these molecules and non-reactive metals, or between two different organic materials, preserve the individuality of the molecules, the charge density of the molecules at the interface resemble those of the free molecule. Thus, a detailed knowledge of the electronic structure of the organic molecules is essential.

CHAPTER 3

Metal/organic interfaces

At the moment it's just a Notion, but with a bit of
backing I think I could turn it into Concept,
and then an Idea.

(Woody Allen)

Confidence is what you have
before you understand the problem.

(Woody Allen)

3.1. Introduction to metal/organic interfaces

The field of organic electronics has developed to a point where new devices based on organic materials, such as organic light-emitting diodes, organic thin-film transistors or organic solar cells, have already emerged (see [Forrest04] and references therein). In all cases, metal electrodes are used to inject charge into, and extract charge from, the organic layer(s). Since the process of charge injection determines the performance of the devices, it is essential to understand the basic processes that take place at the metal/organic semiconductor interface.

Central to this issue is the problem of the energy level alignment at the interface: the Schottky barrier is the single most important parameter determining the injection properties [Scott03]. In spite of the theoretical and experimental work carried out over the past decades, the understanding of the Schottky barrier formation at metal/organic interfaces is still far from complete.

Although inorganic semiconductor interfaces offer inspiration for the basic mechanisms, organic semiconductors are amorphous materials, where charges are localized mostly at individual molecules, with strong Coulomb effects. This breaks down the delocalized picture in terms of valence and conduction bands that is used to describe inorganic semiconductors. The formulation of a model describing the energy level alignment at metal/organic interfaces is therefore the focus of ongoing research.

In many cases, dipoles are observed at these interfaces. These act on the energy levels at the interface, shifting the electronic spectrum of the metal and the organic material with respect to each other. The choice of materials at the interface is mostly determined by their electronic structure, so as to match the work function of the anode with the HOMO of the organic material, and/or that of the cathode with the LUMO [Shen04] (see Fig. 3.1). Since the difference between these quantities **when the interface is formed** determines the electron or hole injection barriers, the formation of an interface dipole disrupts these barriers. In some cases [Wan05], the interface dipole actually increases the anode–HOMO offset, contrary to what is desired as it worsens the injection barrier. A detailed understanding of the basic mechanisms operating at metal/organic interfaces is therefore needed.

A brief review of the different models that have been proposed is presented below. Next, we introduce the theoretical approach that we propose, highlighting the complications of determining the energy levels at the interface, and describing a scheme to calculate them. In the following sections, the method for determining the

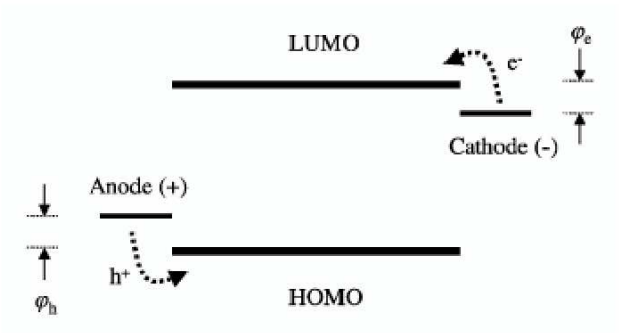

Figure 3.1.: Schematic energy level diagram of a single-layer OLED: the offsets between the molecular HOMO and LUMO and the anode and cathode Fermi levels, respectively, determine the hole and electron injection barriers (from Ref. [Shen04]).

interface electronic structure is described, followed by the results of its application to the interface between Au and several organic materials: PTCDA, PTCBI, CBP, CuPc and Pentacene. The final section contains some concluding remarks.

3.2. Breakdown of vacuum level rule

The simplest model for the energy level alignment at metal/organic interfaces is the vacuum level alignment rule. This consists in simply aligning the vacuum levels of the metal and the organic material, which implies that no dipoles are formed at the interface, so that the position of molecular levels with respect to the metal Fermi level is defined by vacuum level alignment.

The validity of this model for many organic materials was disproved by Narioka *et al.* [Narioka95] using UPS. Independent data by Hill *et al.* [Hill98c] confirmed this conclusion (see Fig. 3.2). While the vacuum level rule was observed in some instances, the formation of large (0.5-1.0 eV) dipoles were measured at several metal/organic interfaces. This is shown in Fig. 3.2: vacuum level alignment or the Schottky-Mott limit is represented as a dashed line. The experimental Fermi level positions, shown in Fig. 3.2, deviate from this limit, and the vertical lines represent

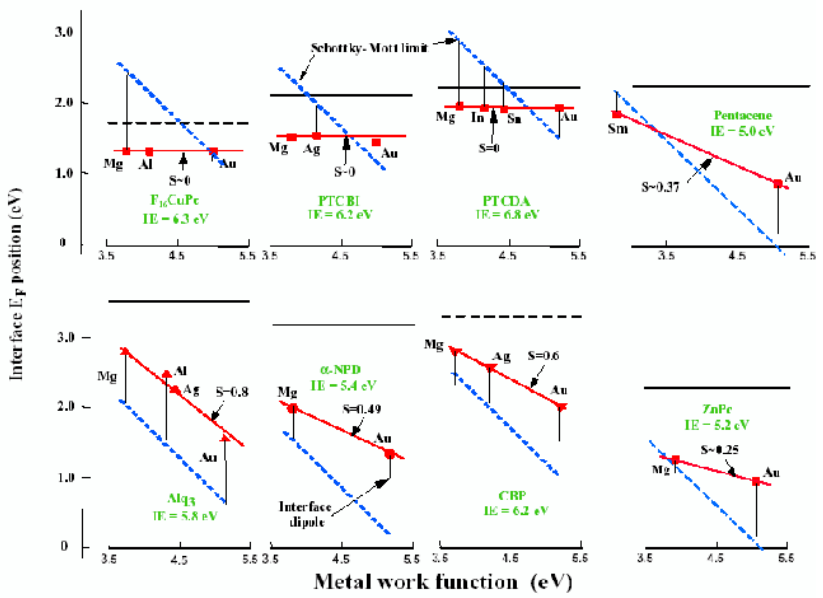

Figure 3.2.: Breakdown of the vacuum level rule. Experimental Fermi level position (red squares), and vacuum level rule prediction (blue dashed lines) for different metal/organic interfaces. The difference between the two is the magnitude of the interface dipole. Energies are expressed from the top of the HOMO. From Ref. [Shen01b].

interface dipoles. The fit to the experimental Fermi level positions gives the measured S parameter. In some cases, like F_{16}CuPc, PTCBI or PTCDA, $S \sim 0$ implies a Fermi level position independent of the metal work function, anchored or 'pinned' at a particular energy. In other cases, the Fermi level position is dependent on the metal work function, though not as much as predicted by the Schottky-Mott model. The failure of vacuum level alignment implies the existence of Fermi level pinning mechanisms, which give rise to the observed interface dipoles.

Several models have been proposed for the energy level alignment at metal/organic interfaces: metal-molecule chemical reaction and formation of gap states, compression of the metal electronic tail by the adsorbed molecules (the 'pillow' effect) and exchange interactions, charge transfer based on the relative values of the metal

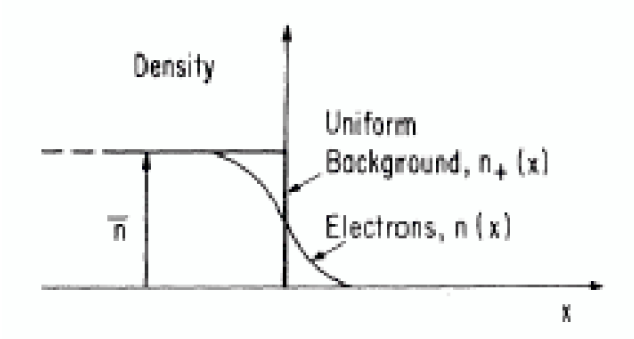

Figure 3.3.: Electron distribution at a metal surface (from Ref. [Lang70]).

work function and the organic ionization or affinity levels, energetically distributed valence states and band bending, and orientation of molecular permanent dipoles.

A brief survey of these mechanisms is presented below. Several review articles discussing these models exist [Knupfer05a, Kahn03, Shen01b, Ishii01], as well as the well-known and now classic paper by Ishii, Sugiyama, Ito and K. Seki [Ishii99].

3.2.1. Compression of metal electronic tail: 'pillow' effect

At a clean metal surface, the abrupt termination of the metal and of the attractive potential of the nuclei makes the electron wavefunctions 'spill out' into the vacuum. This causes clean metal surfaces to have a surface dipole layer, with a slight positive charge on the metal side, and a slight negative charge on the vacuum side (see Figs. 3.3 and 3.4).

When molecules are adsorbed on metal surfaces, the metal wavefunctions which are tailing into the vacuum overlap with the wavefunctions of the adsorbed molecule (the 'pillow' effect, see Fig. 3.5). To avoid this repulsion, the metal tails are pushed back into the metal. This rearrangement has the effect of reducing the surface component of the dipole, and therefore contributes in the dipole which is created at metal/organic interfaces.

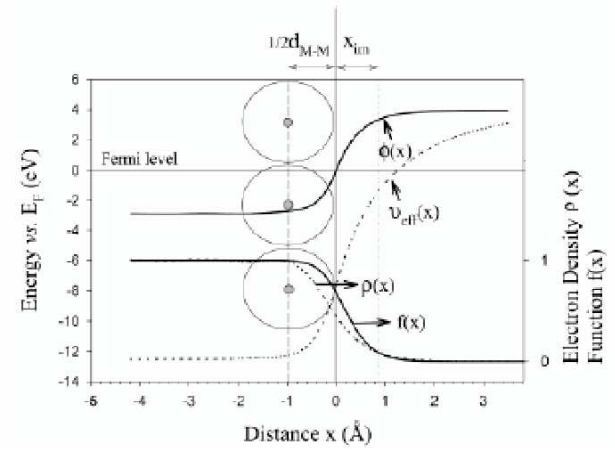

Figure 3.4.: Electron density ρ(x), effective potential v_{eff}(x) and electrostatic potential ϕ(x) across a metal/vacuum interface, from [Crispin02].

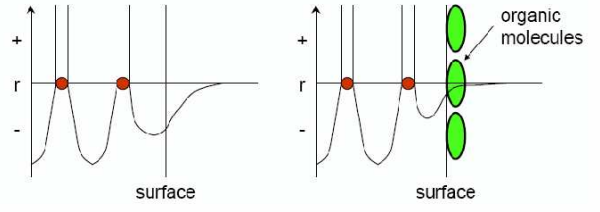

Figure 3.5.: Compression of the metal electronic tail ('pillow' effect), leading to a reduction in the metal work function, due to adsorbed organic molecules, from [Shen01b].

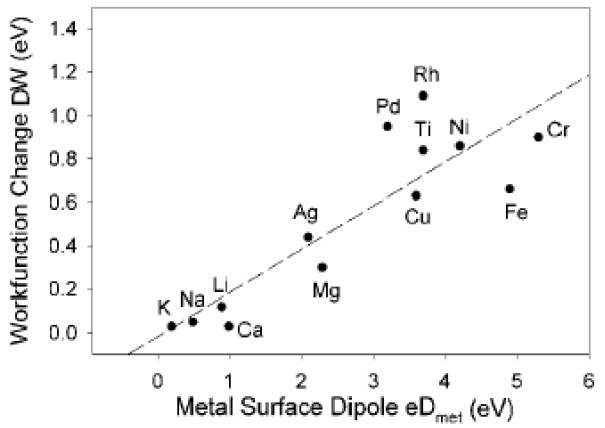

Figure 3.6.: Work function change upon adsorption of a Xe monolayer (data from Ref. [Lang81]) with respect to the metal surface dipole (data from Ref. [Wandelt84]). Figure taken from [Crispin02].

This has been analyzed theoretically by Crispin *et al.* [Crispin02,Crispin04]. Their work, focusing mainly on chemisorption, is carried out by performing DFT calculations of adsorbed molecules on metal clusters and computing the reduction in the metal work function.

Since many of their results deal with reactive interfaces, they will be discussed in Section 3.2.2; here we will focus on their results for physisorption.

Concerning physisorption, little theoretical work has been carried out explicitly on the adsorption of organic molecules on metals. Results for inorganic adsorbates on metals, calculated within the jellium approximation [Lang70, Lang81], are taken from the literature and expected to yield similar results for organic materials. Xe adsorbed on various metal surfaces, together with metal surface dipoles calculated within the jellium approximation, have yielded a linear relation (see Fig. 3.6) between the reduction of the metal work function, $\Delta\phi_M$, and the surface contribution to the work function D_{met} [Crispin02]:

$$\Delta\phi_M \simeq 0.2 e D_{met} \tag{3.1}$$

Therefore, both charge transfer through chemisorption (Crispin *et al.*, see Sec-

tion 3.2.2), as well as the reduction 3.1 of the metal work function observed for physisorbed noble gas atoms, are expected to operate at organic/metal interfaces.

Bagus *et al.* [Bagus02] have performed calculations on closed-shell species physisorbed on Cu surfaces and concluded that the changes in the interface dipole and metal work function stem from exchange-like effects (Pauli repulsion), rather than chemical or electrostatic interactions. Due to the failure of DFT where van der Waals interactions are important, their approach for Xe and cyclohexane (C_6H_{12}) on Cu is a wavefunction-based approach, computed at the Hartree-Fock level including van der Waals interactions as second-order perturbation theory.

The adsorbate is placed on the cluster which models the Cu(111) surface, while keeping both the adsorbate and cluster wavefunctions within the 'frozen orbital' approach. Then, either the adsorbate, or the metal wavefunctions are unconstrained and allowed to respond, or both simultaneously. In this way, chemical effects can be included in a controlled way. Their results show that the dominant contribution to the interface dipole is due to the first ('frozen orbital') step, which dominates over the other (chemical) contributions. This shows that the most important contributions to the interface dipole stem from a purely quantum-mechanical phenomenon such as the antisymmetrization of the full N-electron wavefunction. Since similar results are found for Xe and cyclohexane, the model is expected to have captured the essential ingredients at the interface.

The interaction between n-alkanes and metal surfaces has been studied theoretically by Morikawa, Ishii and Seki [Morikawa04]. Through DFT calculations making use of the GGA functional, the lowering of the work function upon n-alkane adsorption was calculated. The large ($\sim 3 - 4$ Å) metal-organic distance and the presumably important contribution of van der Waals forces (which are not discussed in the paper) yield a rather poor agreement of the physisorption energy with experiment, even though it is true that the small values which are typically found make this a difficult task. In spite of this, good agreement with experiment was obtained in the work function reduction upon alkane adsorption for a variety of metal substrates (which suggests that the poor agreement in physisorption energies comes from not taking van der Waals forces into account). The results show that the distance between the metal and the alkane (which is adsorbed lying down, with its C–C–C plane parallel to the surface) depends on the metal substrate. In turn, this distance largely determines the work function reduction upon adsorption (Fig. 3.7).

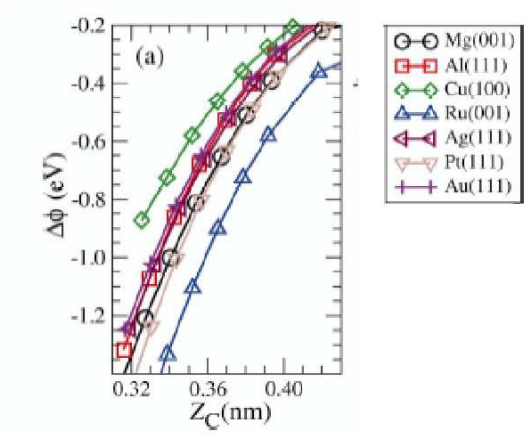

Figure 3.7.: Work function change calculated for polyethylene adsorbed on several surfaces (from Ref. [Morikawa04].

Experimentally, the reduction of the metal work function due to the compression of the metal electronic tail (the 'pillow' effect) has been demonstrated experimentally [Koch03] by comparing the energy level alignment and surface dipoles of several organic materials deposited on Au and on the conducting polymer mixture poly(3,4-ethylene dioxythiophene)/poly- (styrene sulfonate) (PEDOT:PSS). This polymer has good optical, electrical and processing characteristics and its work functions is approximately 5 eV, very close to that of Au. However, the contribution of the surface electron tail to the dipole is much smaller than in Au, since PEDOT:PSS is made of closed-shell moieties and has far fewer free electrons than a metal. Thus its wavefunction 'spills out' less than in the case of Au, and a smaller 'pillow' effect can be expected, as is observed experimentally, thus experimentally demonstrating the 'pillow' effect.

However, in other cases it is sometimes difficult to differentiate between the 'pillow' effect and other contributions (such as chemical reaction and formation of gap states) when several are operating simultaneously [Kahn03]. Theoretical calculations have been performed only for noble gas atoms or small molecules, with some exceptions [Morikawa04]. In addition, equation 3.1 suggests that it depends exclusively on the metal substrate, irrespective of the organic adsorbate. Though clearly

important, the lack of a systematic, quantitative understanding at a theoretical level beyond equation 3.1 hampers the evaluation of the achievements and predictions of the 'pillow' model.

3.2.2. Metal-molecule chemical reaction and formation of gap states

A large number of metal/organic interfaces exhibit chemical reaction and formation of new bonds at the interface. Many examples can be found in Refs. [Hill00d, Ishii99, Shen01a, Hill98b, Eremtchenko04, Crispin04, Morikawa04].

Frequently [Kahn03, Salaneck01], metal-on-organic interfaces are more reactive than those formed through the reverse deposition sequence. This is due to the diffusion of hot metal atoms into the organic material.

At metal-on-organic interfaces, metal atoms do not diffuse into the organic matrix, and the chemical reaction is limited to the first organic layer. Although some trends have been drawn [Knupfer05a, Knupfer05b], predictions about a particular chemical reaction are rather difficult to make. It seems, however, that the reactivity of the interface is related to the metal on which the organic material is deposited. Some metals, like Au, are almost non-reactive. Others, like Ag, exhibit a higher reactivity, whereas Al and Mg, for example, are highly reactive and tend to form bonds with many organic materials.

Chemical reactions are characterized by the formation of metal-molecule bonds, often through the re-hybridization of molecular orbitals, and accompanied by geometrical deformations of the organic molecule. The characteristic signature is the appearance of **chemistry-induced gap states** in the energy gap of the organic material. Gap states can be detected experimentally through UPS, STS, or core level spectroscopy, for instance. Evidence that this DOS comes from a chemical reaction can be provided by XPS (core level shifts), or from theoretical calculations. Chemistry-induced gap states reflect metal-molecular bonds and are derived from the combination of the orbitals of the metal and the molecule. As in inorganic semiconductors [Flores87, Mönch], they are very important since they can pin the Fermi level in the organic energy gap.

Chemisorption and charge transfer in metal/organic interfaces has been also studied theoretically by Crispin et al. [Crispin02, Crispin04] using metal cluster calculations. As stated by the authors, these calculations are intricate, since there is no two-dimensional periodicity and one is really working with cluster 'molecular orbitals', rather than wavefunctions with the appropriate two-dimensional period-

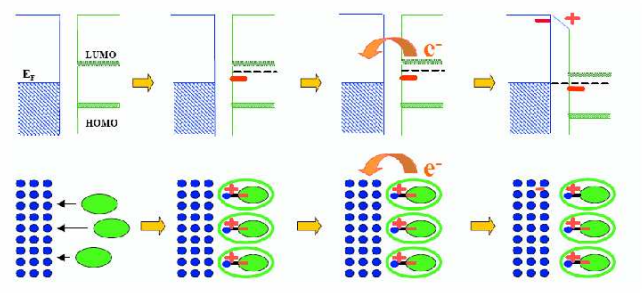

Figure 3.8.: Chemical reaction, charge transfer and formation of an interface dipole at the metal/organic interface (from Ref. [Shen01a]).

icity. Since the electronic structure of the metal cluster reflects its size and geometry, care must be taken that a particular wavefunction truly resembles that of the metal, and is not an 'artifact' of the cluster geometry. Having converged the cluster size, the results for PPDA (p-phenylenediamine, $C_6N_2H_8$) on $Ni_16(100)$ [Crispin04], as well as AN (acrylonitrile, C_3NH_3) on $Cu_9(100)$, $Ni_9(100)$, and $Fe_9(100)$ [Crispin02]are presented. The results yield adsorbate geometries with small molecule-metal distances, $\sim$ 2 Å. Charge transfer of 0.2–0.3 e from molecule to metal gives rise to a strong dipole at the interface. Experimental data, from XPS and UPS measurements, confirms the calculated binding geometry and charge transfer, and yields a $\sim$ 1.5 eV reduction of the metal work function upon chemisorption. The calculated charge transfer which comes from chemisorption contributes to the interface dipole, and is expected to be a significant contribution to the total $\sim$ 1.5 eV lowering of the metal work function.

The main difficulty when analyzing chemisorption in metal/organic interfaces is that the outcome of a particular chemical reaction is unpredictable, not being possible to know in advance the position at which the Fermi level will be pinned. Thus, each interface has to be considered separately, and progress is made in a 'one-at-a-time' fashion.

Chemical reaction at the interface, characterized by the formation of metal-molecule bonds and the appearance of gap states in the organic energy gap, is common in many metal/organic interfaces. It is an important mechanism governing the energy level alignment since the gap states that are created can pin the Fermi level in the organic energy gap. However, in most cases it is impossible to predict the Fermi level position. From a theoretical point of view, an advantage is that DFT methods can be straightforwardly applied since interface bonds have bonding distances of ($\sim$ 1 – 2 Å) and high electron density (this is not the case for physisorption or weakly-interacting interfaces, as will be discussed below). In spite of the applicability of DFT, a detailed knowledge of the interface structure is required, since the results are often very sensitive to the details of the interaction. Moreover, it is difficult to extrapolate the results to other cases, so that each interface requires a specific calculation. Thus, in spite of the relative ease with which theoretical calculations can be performed on these systems, the results cannot be extrapolated and knowledge of reactive interfaces advances in single steps.

3.2.3. Charge transfer based on the organic ionization or affinity levels

Charge transfer between the metal and the organic molecules is intuitively expected at interfaces having the combination **strong organic acceptor – low work function metal** or **strong organic donor – high work function metal** (see Fig. 3.9). Recently, the role of electron affinity in chemisorptive interfaces was discussed [Knupfer05b].

This has been observed experimentally for a large number of interfaces (TCNQ on Au and Al, Al/DP-NTCI, Au/TTN [Ishii99], PTCDA on Mg, In and Sn and Au/NPD [Hill98c]). It has been proposed [Ishii99] that this mechanism should be also operative at organic/organic interfaces for the combination of strong donor and acceptor organic materials. In some cases, charge transfer has been observed at interfaces displaying little chemical interaction, such as Au/PTCBI or Ag/PTCBI [Hill00d]. The small interaction at the interface is evidenced by the fact that the molecular levels are not disturbed.

In the case of Ag/PTCBI, the metal work function is smaller (less negative) than the organic electron affinity, and electrons are transferred from the metal to the LUMO of the molecule. This gives rise to an interface dipole which raises the organic levels with respect to the metal work function, a mechanism which prevents further electron transfer and thus stabilizes charge transfer at the interface. As evidenced by the attenuation of the photoemission signal upon further PTCBI

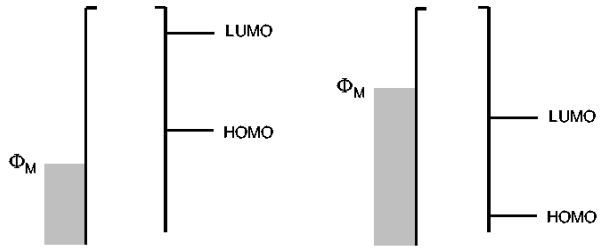

Figure 3.9.: Charge transfer can be expected when the difference between the metal Fermi level and the molecular HOMO or LUMO is high. In the left figure, electrons would flow from molecule to metal; in the figure on the right, charge would be transferred from metal to molecule.

deposition, the transferred charges are localized at the interface.

These charge excitations are known as polaron or bipolaron states [Hill00d] and are localized almost at individual molecules. The energy of the (singly occupied) polaron relaxes into the energy gap of the material, giving rise to gap states which are detected experimentally, and can pin the Fermi level in the gap of the organic material.

The use of the organic ionization energy, on the other hand, for understanding the energy level alignment is more troublesome. In some cases [Picozzi03] it smaller than the metal work function is (closer to the vacuum level), whereas the measured interface dipole is consistent with charge transfer **from** the molecule **to** the metal. In this respect, the calculation of the electronic structure **at the interface**, which has an induced DOS, will clarify this point.

3.2.4. Energetically distributed valence states and band bending

In organic molecular crystals, disorder on a molecular scale or contamination can give rise to a Gaussian or exponential energy distribution of the molecular states. That is, states which have a well-defined energy in a clean crystal exhibit an energy

distribution around these values due to disorder or contamination.

It has been shown through calculations of Poisson's equation for the potential drop at the interface [Paasch03] that this energy distribution of molecular states results results in band bending in the organic layer: for an exponential distribution of states whose widths are large compared to the thermal energy (ie. when the effects of disorder are large on the thermal energy scale), the magnitude of band bending which results from this distribution is of the order of the total interface dipole [Paasch03]. Since this might represent a significant contribution to the potential offset determined experimentally, it might be interpreted as a contribution to the interface dipole [Knupfer05a].

This mechanism depends on the amount of disorder or contamination at the interface, so that for a clean crystal of perfect crystallinity, it should not be operative.

3.2.5. Orientation of permanent molecular dipoles

Layers of polar organic molecules have been used to modify the energy level alignment at the metal/organic interface [Knupfer05a, Kera04]. The molecular dipole modifies the total interface dipole and can thus be used to tune the properties of the interface.

In a clear example [Kera04], the polar molecule OTiPc was used as an interlayer to modify the vacuum level (and thus interface energy level alignment) at the graphite/CuPc interface (see Fig. 3.10).

Another example is Alq_3, which has a large permanent dipole, and its interface with Al has been studied theoretically [Yanagisawa06]. In our formalism, described below, we have not taken into account the permanent dipole of Alq_3, so our analysis rests on the assumption that the deposition distribution of Alq_3 molecules is symmetrical, such that the overall dipole (when considering a large number of molecules) is zero.

The effect of a molecular permanent dipole D on the energy level alignment is to induce a potential shift ΔV given by (atomic units)

$$\Delta V = 4\pi \frac{D}{A} \tag{3.2}$$

where A is the area of the molecule and D is its permanent dipole.

The effect of monolayers of molecules exhibiting a permanent dipole on the interface dipole is clearly important, especially if the direction of the molecular dipole

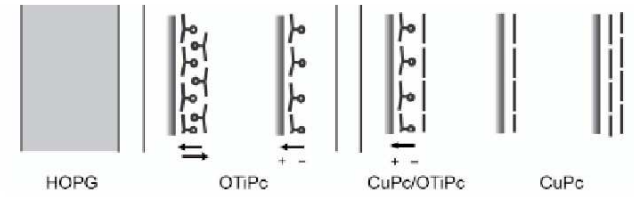

Figure 3.10.: The orientation of permanent molecular dipoles at the interface can change the interface dipole (figure from [Kera04]).

points towards the metal surface. In the case of planar molecules, the molecular dipoles (if present) is within the molecular plane, such as in PTCDA. Since planar molecules are frequently deposited flat on the metal surface, one can assume that the effect of the molecular dipoles will not be so important. On the other hand, one could think that the presence of in-plane molecular dipoles in these planar molecules could affect the adsorption geometry, inducing the molecule to tilt so that the dipoles interact more strongly with the substrate. However, until more theoretical and experimental work is carried out, this discussion is merely speculative.

Although the presence of electronegative atoms (such as oxygen) tends to favor charge transfer within the molecule and thus molecular dipoles, many organic materials do not exhibit permanent dipoles, so that the orientation of molecular dipoles is not a mechanism taking place in most metal/organic interfaces [Knupfer05a].

3.3. The Induced Density of States model

Recently [Vázquez04a,Vázquez04b,Vázquez05a], we proposed a more general mechanism based on the concepts of Induced Density of Interface States (IDIS) and Charge Neutrality Level (CNL), originally developed for the alignment at *inorganic*

semiconductor interfaces. The CNL acts as an effective Fermi level for the organic material. The metal-organic interaction induces a DOS in the organic energy gap and these induced states partially pin the Fermi level near the CNL of the organic material. As will be shown below, even for weakly-interacting metal/organic interfaces, this 'intrinsic' DOS can explain the interface dipoles and Fermi level pinning observed experimentally. The model is intuitive and its results for non-reactive interfaces show good agreement with experiment.

In fact, many of the mechanisms mentioned in the previous sections are described by or can be incorporated to our method. For instance, charge transfer based on the difference between ϕ_M and the ionization or affinity energies is naturally explained by our proposal: the values of IE and A enter our model through the description of the organic electronic structure, and determine the location and magnitude of the gap, and thus the position of the CNL, which then tends to align with the metal work function. Chemical reactive interfaces have not been considered in the present work, but there is no fundamental difference between these and the weakly-interacting interfaces we have studied. The metal-molecule interaction would be stronger in the former case, and the interface electronic structure would be different, but our formalism is adapted to automatically incorporate these changes with no need for $ad-hoc$ assumptions: the calculation of the interface electronic structure, in a way similar to the present work, would yield an induced DOS and a CNL position, such that the interface properties could be determined. Chemically reactive interfaces are equivalent to weakly-interacting interfaces, except in the details of the induced DOS. Other mechanisms, however, such as the inclusion of molecular permanent dipoles or the 'pillow' effect, cannot be included from first principles at present. In our analysis of molecules having permanent dipoles, our model relies on the assumption that the molecules are deposited in such a way that the average dipole is zero, since it is not taken into account in our analysis. As for the 'pillow' effect, it can be phenomenologically incorporated immediately into our formalism as a modification of the initial metal work function, as will be discussed below. In addition, we are currently working on introducing this effect from first principles by expanding the metal-molecule interactions in powers of the overlap between the metal and molecular orbitals.

We thus see that, even if this thesis deals with weakly-interacting interfaces only, our formulation is very general and allows for the description of most of the mechanisms listed above. Moreover, our model, as will be seen, can be applied to several of these interfaces, such as Au/organic and organic/organic interfaces.

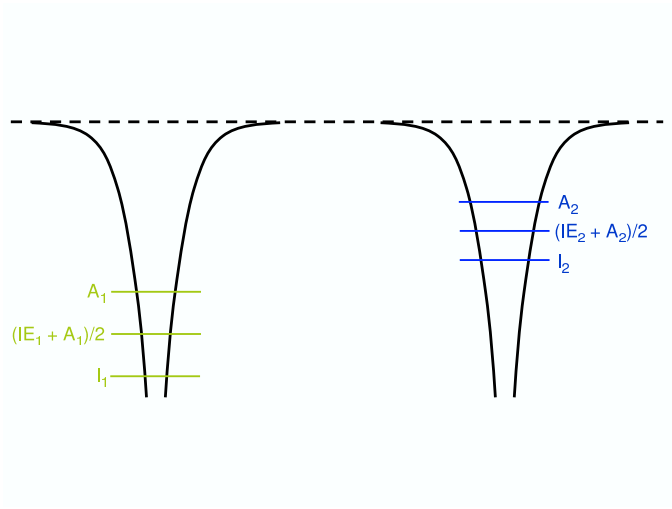

Figure 3.11.: Ionization (IE) and affinity (A) energies for two different atoms. The average $\frac{IE+A}{2}$ was used by Pauling to determine atom electronegativities.

In our approach, the CNL is the central quantity, whose alignment with the metal work function (in the case of metal/organic interfaces) or the CNL of the other material (at organic heterojunctions) determines the interface properties.

The advantage of this approach is that it provides, within its limitations, a level whose relative position to the metal work function largely determines the energy level alignment. The idea of trying to identify energy levels whose alignment determines the interface properties can be traced back as early as Pauling and Mülliken. Their work was mainly concerned with the quantum properties of atoms, such as explaining the periodic table properties, or the character of chemical bonds, from the quantum properties of the atoms. Consider two atoms, each with its Ionization and Affinity Levels, IE_1, A_1 and IE_2, A_2 (Fig. 3.11). Charge transfer from 1 to 2 depends on the difference IE_1-A_2 (since the electron is removed from IE_1 and placed at A_2). Charge transfer in the opposite direction depends on IE_2-A_1. The difference between the two yields IE_1+A_1 - (IE_2+A_2). Mülliken proposed to consider the average of the atomic Ionization and Affinity Levels, (IE+A)/2, as the quantity which determines the charge transfer to or from that atom. The atom with the higher value of (IE+A)/2 gains electronic charge from the one with the lower value. Pauling used this idea to determine atom electronegativities [Pauling60].

In the present case, considering all molecular states in addition to the HOMO and LUMO is crucial, since, due to the interaction at the interface, these states will have a lorentzian broadening, and several of them will contribute to the position of the CNL in the organic gap. For several organic materials, the CNL is located close to the LUMO [Vázquez04a, Vázquez04b, Vázquez05a] as the DOS is higher around the HOMO that around the LUMO: the tails of these states push the CNL upwards in the gap. The simple (IE+A)/2 average, on the other hand, predicts the CNL always at mid-gap. In semiconductors, our generalization of the (IE+A)/2 concept coincides with the average of optical gaps in the Brillouin zone, which is the CNL of the semiconductor. In inorganic semiconductors, the CNL was shown to determine the energy level alignment and dipole formation at metal-semiconductor and semiconductor-semiconductor interfaces [Tejedor77, Flores87]. By now, the CNL model in inorganic semiconductors is well established. In organic semiconductors, the idea of using the average (IE+A)/2 as the chemical potential of the organic material has been recently used by Crispin *et al.* [Crispin02, Crispin04] for a reactive MO interface. The value (IE+A)/2 was used to predict (correctly) the direction of charge transfer upon chemisorption. For fluorinated phthalocyanines on gold, Peisert *et al.* have also pointed out the coincidence of the Fermi level of the organic material with mid-gap, within $\sim$ 0.25 eV [Peisert03]. Alkauskas *et al.* have also used the average (IE+A)/2 to analyze the alignment at interfaces between copper-octaethylporphyrin (CuEOP) and noble metal surfaces [Alkauskas05].

In light of this, our approach for the calculation of the CNL can be viewed as a generalization of the previous (IE+A)/2 concept to the case of organic semiconductors, which includes a realistic representation of the molecular levels around the HOMO and the LUMO. Our results for metal/organic interfaces, as will be seen, yield results for Fermi level positions and interface dipoles in good agreement with experiment, suggesting that including the effect of many molecular levels is necessary for the calculation of the CNL.

The position of the CNL in the organic energy gap is determined by integrating the induced DOS. The statement that the electronic structure of the organic material **at the interface** is a continuum DOS (whose particular shape is determined by the details of the interaction) is in contrast with the usual assumption of discrete molecular levels like the HOMO and LUMO. The notion of a continuum DOS, reminiscent of Anderson's chemisorption model, provides a DOS to or from which electrons can be transferred: this induced DOS acts as a buffer for the transferred charge. In the case of Au/PTCDA, for example, where the HOMO is centered $\sim$ 2

eV below the gold work function, if the energy level alignment were interpreted in terms of charge transfer to and from the HOMO and LUMO, electrons would have to overcome this $\sim$ 2 eV energy barrier to be transferred to gold, as is observed. Similarly, it is difficult to understand charge transfer in the Ag/PTCDA case using the HOMO and LUMO, a problems which becomes especially acute when the DFT gap is used [Picozzi03], since the well-known underestimation of the gap directly affects the energy level diagram. Within our approach, a scheme for correcting this deficiency in the gap has been described (Section 2.8.6), while the concepts of a continuum DOS and a CNL rationalize charge transfer at the interface, aiding in the understanding of the energy level alignment.

Moreover, as will be seen, our results imply that in the case of unreactive interfaces, in addition to the van der Waals interaction (which has not been considered here but does not alter the conclusions), there is a 'chemical' one, coming from the interaction of the metal and the organic material. Notice that all other theoretical models applied to physisorptive systems explain the reduction of the metal work function in terms of a rearrangement or symmetrization of the metallic and organic wavefunctions (while charge transfer occurs only through chemisorption). This makes is difficult to understand the pinning of the Fermi level, as there is no DOS in the gap acting as a buffer to 'pin' it. In our approach, on the other hand, the dipole is created by **charge transfer** across the interface, as observed experimentally, providing a simultaneous explanation for the dipole and for the pinning of the Fermi level.

Nevertheless, since several alignment mechanisms are believed to be operating simultaneously at metal/organic interfaces and cannot be simply added up [Knupfer05a], our model does not aim at invalidating these alternative models, but rather to complement them from a perspective which had not been considered until now.

This state of things, with several mechanisms being proposed, is reminiscent of the situation which occurred some thirty years ago, when surface physics was focused on *inorganic* semiconductor interfaces. The theoretical model we propose is described below, with a brief introduction to its origins.

3.4. Origin of the IDIS model

This section presents a brief summary of the research done towards understanding the basic mechanisms operating at metal/*inorganic* semiconductor interfaces, focusing on the theoretical method on which our approach for *organic* semiconductors is based. For more details, see the paper [Flores87]. For a recent and thorough review on metal/inorganic interfaces, see Ref. [Tung01].

Understanding the details of what happens when a metal and a semiconductor are brought together has been the focus of considerable research in surface science for the second half of the 20^{th} century. When a metal and a semiconductor are in contact, their Fermi levels are, in general, different, so that an electric field exists between them and a flow of charge takes place. This flow of charge tends to reduce the difference in the potential of the electrons in the metal and the semiconductor, equalising them at the interface, as shown in Fig. 3.12.

The electric field which exists at the interface due to the difference in the metal and semiconductor Fermi levels, penetrates both the metal and the semiconductor, but a different amount, due to each material's characteristic screening length. These are the Thomas-Fermi and Debye lengths, for the metal and the semiconductor, respectively [Rhoderick88]. Typically, $\lambda_{metal} \sim 1$ Å or less, whereas the Debye length, which depends on the doping level of the semiconductor, is on the order of nanometers [Mönch]. Because the donor concentration in semiconductors is many orders of magnitude smaller than the electron concentration in metals, the uncompensated donors occupy a layer of appreciable thickness, which is known as band bending [Rhoderick88]. The region in the semiconductor near the interface where the energy levels are disturbed with respect to the bulk is the Interface Space Charge Region (ISCR).

The barrier height, which represents the minimum energy needed to transport charge across the interface, is the difference between the interface Fermi level and the edge of the majority carrier band: the valence band minimum for n-doped semiconductors (electron transport) and the conduction band maximum for p-doped semiconductors (hole transport).

The rectifying behaviour or many metal-semiconductor interfaces can be seen from Fig. 3.14. When the metal is at negative bias ($V_{metal} < 0$, top), electrons can flow easily from the semiconductor to the metal as a current (towards the left of Fig. 3.14). When the metal is at positive bias, on the other hand, ($V_{metal} > 0$, bottom),

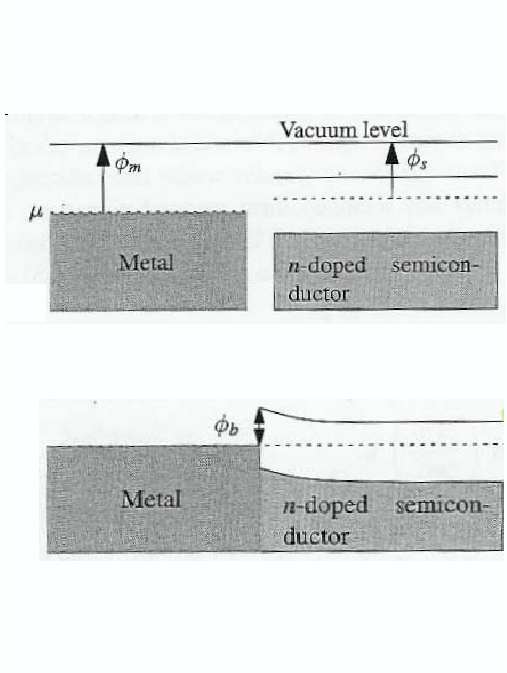

Figure 3.12.: Metal/inorganic semiconductor interface, showing the formation of the interface and band bending (from [Marder00]).

electrons must still overcome a barrier, so that conduction towards the right of Fig. 3.14, with electrons flowing into the semiconductor, is not possible.

Charge transport through the interface occurs primarily via thermionic emission over the Schottky barrier. Secondary mechanisms, such as tunnelling through the barrier, are only significant for semiconductors with a high degree of doping, where band bending is strong. In this way, the Schottky barrier height is the single most important parameter determining charge transport across the interface, and the mechanisms governing its formation become of interest.

3.4.1. Schottky-Mott rule

The earliest theoretical analysis of the origin of the Schottky barrier can be attributed to Walter Schottky and Sir Neville Mott. The characteristic feature of their approach is the assumption that the semiconductor has no surface states, and that

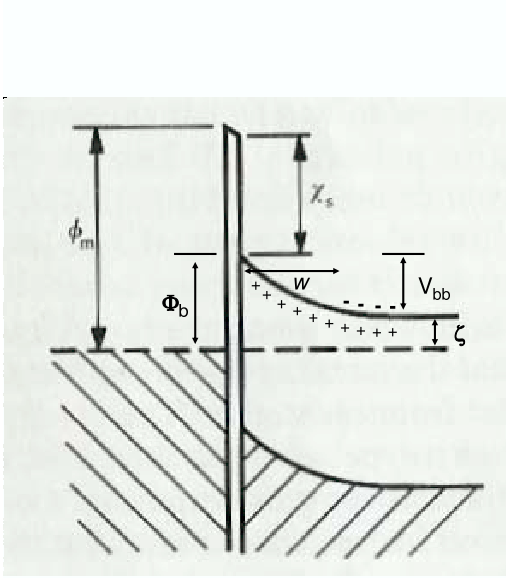

Figure 3.13.: Band bending is caused by the penetration of the electric field at the interface. Because the carrier concentration in the semiconductor is much smaller than in the metal, uncompensated donors occupy a region of appreciable thickness, w (from [Rhoderick88]).

the metal and semiconductor vacuum levels align. This situation is schematically represented in Fig. 3.15:

The injection barrier at the interface is given by the difference between the metal Fermi level and the electron affinity, χ_S, of the semiconductor. This is expressed by the famous Schottky-Mott equation:

$$\phi_{Bn} = \phi_M - \chi_S \tag{3.3}$$

Experimentally, barrier heights were seen to depend linearly on the metal work function, as described by equation 3.3, but with a slope $S = \frac{d\phi_{Bn}}{d\phi_M}$ different to 1, as is predicted by the Schottky-Mott rule.

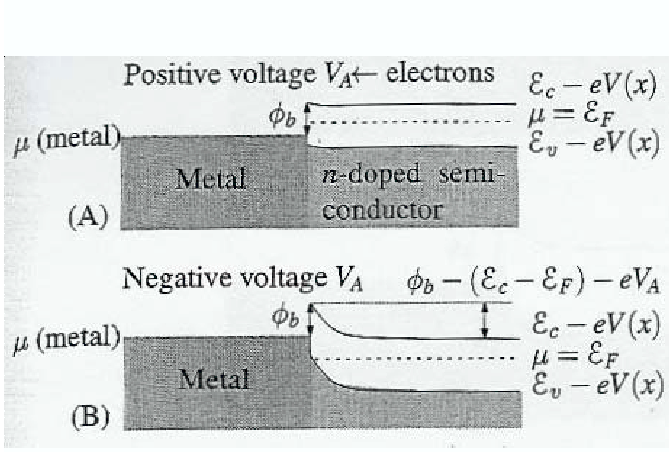

Figure 3.14.: Rectification at a metal/semiconductor interface: when the metal is at negative bias ($V_{metal} < 0$, top), electrons can flow easily from the semiconductor to the metal; when the metal is at positive bias, ($V_{metal} > 0$, bottom), electrons must still overcome a barrier, which is the injection or Schottky barrier (from [Marder00]).

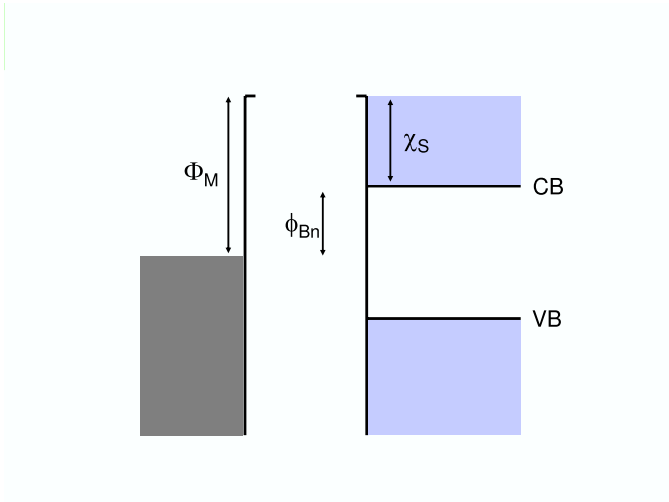

Figure 3.15.: Schottky-Mott rule at metal/semiconductor interfaces, consisting in the alignment of the vacuum levels (no band bending is shown for simplicity). The injection barrier ϕ_{Bn} is then simply the difference between ϕ_M and χ_S.

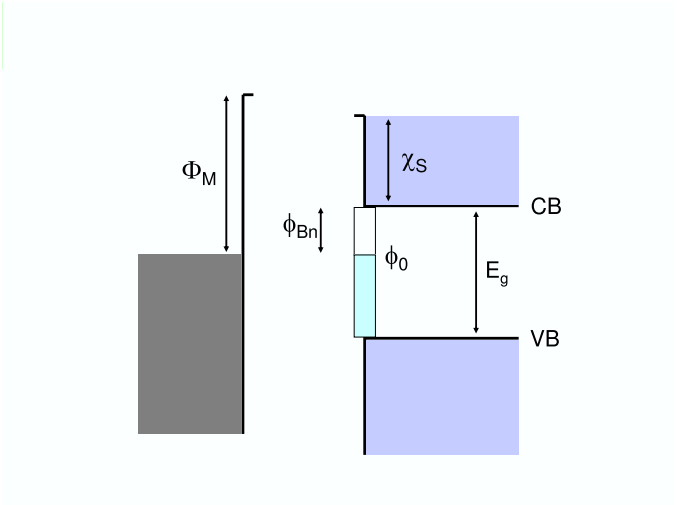

Figure 3.16.: In the Bardeen model, the semiconductor surface states, filled up to ϕ_0 completely screen the potential difference at the interface. This creates a dipole at the interface due to charge transfer and aligns ϕ_0 with ϕ_M. The barrier height is then E_g - ϕ_0 (again, no band bending is shown for simplicity).

3.4.2. The Bardeen model

Bardeen [Bardeen47] proposed that the surface states of the semiconductor were playing an important role and could account for the discrepancy in the slope parameter S between experiment and the theoretical predictions of equation 3.3.

Let us consider a situation as shown in Fig. 3.16, in which a density of semiconductor surface states is filled up to an energy ϕ_0. The total charge in the semiconductor must now include the charge in these surface states and in the interface space-charge region: $Q_{tot} = Q_{ISCR} + Q_{SS}$. If we denote by primes the semiconductor quantities *without* including the effect of the surface states (ie. the Schottky-Mott case), we have, $|Q_{ISCR}| < |Q'_{ISCR}|$, since part of the semiconductor charge is now on the surface states. Therefore, the extent of the space-charge region will now be smaller $(w < w')$, and so will band bending, V_{bb}. Since the barrier height can be written as (Fig. 3.13)

$$\phi_{Bn} = V_{bb} + \xi, \tag{3.4}$$

we can see how the surface states push ϕ_0 towards ϕ_M. For a large surface state

DOS, $CNL \simeq E_F$, and we have

$$\phi_{Bn} = E_g - \phi_0 \tag{3.5}$$

Equation 3.5 is known as the Bardeen limit. The barrier height is fixed, due to the pinning of the Fermi level by a high density of semiconductor surface states. These states screen the semiconductor from the electric field which exists at the interface, so that w and ϕ_B are independent of the metal work function.

Equations 3.3 and 3.5 are two limiting cases: for no interface states, the metal and semiconductor vacuum levels simply align, and, as the metal work function is changed, the barrier height simply follows the differences in ϕ_M. On the other hand, for a high density of surface states, the variation of ϕ_M is completely screened by these surface states, rendering the barrier height independent of the metal work function. The Fermi level is then said to be anchored or 'pinned' at this energy position.

3.4.3. Interface states

Cowley and Sze [Cowley65] followed on these ideas and included a phenomenological density of states in the semiconductor gap. They assumed this DOS to be constant throughout the gap and, which is filled up to an energy ϕ_0 (see Fig. 3.16).

Since the DOS is constant, the charge accumulated in the surface states is $Q_{SS} = -eD_{SS}(E_g - \phi_0 - \phi_B)$. At the same time, the charge in the space-charge region is $Q_{SC} = [2e\epsilon_S N_D(\phi_B + \xi - kT/e)]^{1/2}$ [Cowley65], where ϵ_S is the semiconductor dielectric constant, and N_D is the bulk donor density. Since charge has to be conserved at the interface, $Q_M = -Q_{SS} - Q_{SCR}$. By Gauss' law, the potential drop at the interface, for no applied bias, is $\Delta_0 = -\frac{\delta Q_M}{\epsilon_i}$, where δ is the width of the interfacial layer, and ϵ_i its dielectric constant. On the other hand, we have

$$\Delta_0 = \phi_M - \chi_S - \phi_{Bn} \tag{3.6}$$

Equating these two expressions of Δ_0, and substituting Q_M, we obtain

$$\phi_{Bn} = S(\phi_M - \chi_S) + (1 - S)(E_g - \phi_0), \tag{3.7}$$

where

$$S = \frac{1}{1 + \frac{eD_S\delta}{\epsilon_i}} \tag{3.8}$$

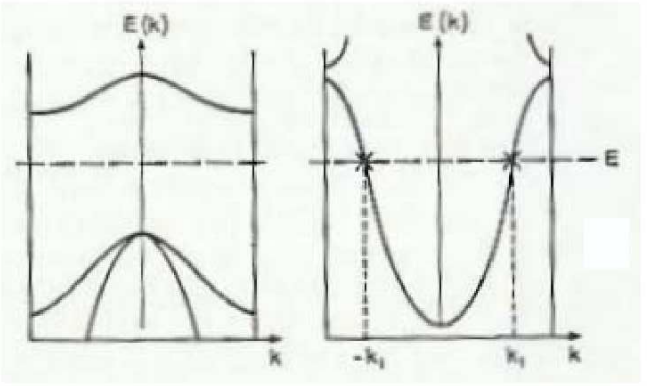

Figure 3.17.: Resonance of a semiconductor surface state with metal wavefunctions (with wavevectors $\pm$ k_1): at this energy there are actually no surface states (from [Heine65]).

The slope $S = \frac{d\phi_{Bn}}{d\phi_M}$ varies between 0 and 1 and is measures the degree of pinning at the interface: $S \rightarrow 0$ leads to the Bardeen case of complete pinning at the energy ϕ_0 due to the high D_S (Eqn. 3.8), whereas $S \rightarrow 1$ corresponds to no density of states in the gap (Eqn. 3.8), and the alignment of the vacuum levels of both systems.

An important step in understanding the *origin* of the density of states at the interface was done by Heine [Heine65] by pointing out that these states are not the semiconductor surface states, but virtual states of the semiconductor, which 'resonate' with the metal eigenfunctions tunnelling into the semiconductor, in the energy range of the semiconductor gap. These virtual states are the solutions of the Schrödinger equation in the semiconductor gap, and can be thought of Bloch waves with a complex wavevector, localized at the interface. In the semiconductor/vacuum interface, they decay into the semiconductor and into the vacuum; at a metal/semiconductor interface, however, they match metal Bloch waves, as shown in Fig 3.17.

The paper of Louie and Cohen [Louie76] illustrates this for the Al-Si case. The authors found that the nature of the electronic states was different depending on the energy range:

1. In the energy range which corresponds to both the metal and semiconductor

bands, the states are bulklike in both materials.

2. For energies in the semiconductor band, but where there is no metal density of states, the states are bulklike in the semiconductor, and decay into the metal.

3. Truly localized surface states, which decay into the metal and the semiconductor are observed at energies in the semiconductor gap, for which there are no metallic bands.

4. 'Gap' or 'interface' states, bulklike in the metal and decaying into the semiconductor, are found at energies where the semiconductor gap matches the metallic bands. It is these states that pin the Fermi level at the interface.

Moreover, by plotting the DOS in different spatial regions (well into the metal and into the semiconductor, and at the interface) their results show how the semiconductor gap is 'filled' with a DOS whose origin lies in the interaction of the virtual gap states with the metal.

The induced density of states and its role in the barrier height was analysed in detail by Flores and coworkers [Tejedor77, Flores87] in their Induced Density of Interface States (IDIS) model. By matching the wavefunctions of the metal and the semiconductor and using surface Green's function methods, the IDIS model shows how the density of states induced at the interface is related to a decrease in the DOS of the conduction and valence bands. The states induced in the bottom (top) of the gap are compensated by a decrease in the valence (conduction) bands, as shown in Fig 3.18. Since no new states can be *created* when the interface is formed, the density of states induced in the gap has to be compensated by a decrease in the DOS of the valence and conduction bands. It is the *semiconductor* DOS, and not that of the metal, which is rearranged, as the *semiconductor* virtual states are in resonance with the metal.

Central to the problem of interface states is the concept of the Charge Neutrality Level (CNL), ϕ_0, of the semiconductor. It represents the energy up to which the semiconductor states at the interface that are filled, and acts as the Fermi level of the semiconductor. If the Fermi level of the interface is above (below) the CNL, the semiconductor will be negatively (positively) charged.

The first calculations for the CNL of semiconductors [Tejedor77] were performed by matching the metal wavefunctions with the virtual gap states of the semicon-

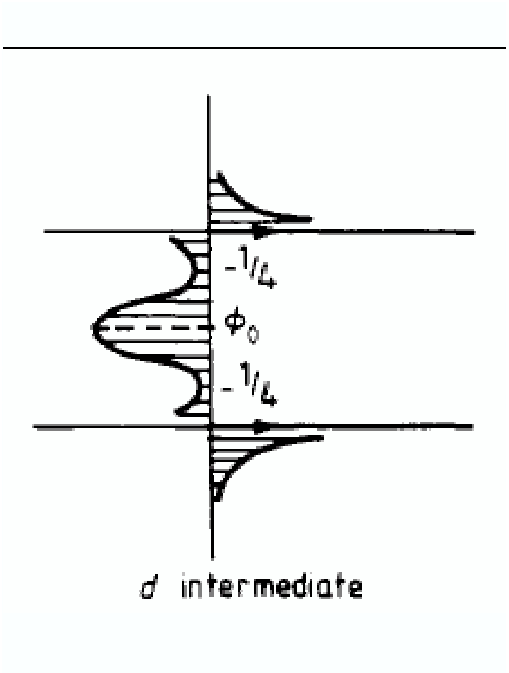

Figure 3.18.: The DOS induced in the metal (left) around its surface state is compensated by a similar decrease in the DOS of the conduction and valence bands of the semiconductor (right). Figure from [Flores87]

ductor. In a one-dimensional analysis, assuming a two-band model for the semiconductor, the induced DOS is symmetrical around midgap, and the CNL is located at midgap. The extension to three dimensions was done by considering points of high symmetry in the two-dimensional Brillouin zone, and averaging the results of the one-dimensional analyses at these points. Tersoff [Tersoff84] later extended the CNL to the branch point of the virtual gap states, where their character changes from valence-like to conduction-like.

The alignment of the semiconductor CNL with the metal work function, due to the interface states, gives rise to an additional contribution to the interface dipole [1]. This contribution can be written, in similarity to the phenomenological model of

[1] Notice that the interface dipole can have several contributions. Due to the potential difference in the solid and in vacuum, the metal wavefunctions 'spill out' of the solid, giving rise to a surface dipole. Reconstructions, or differences in the ionicity of the semiconductor constituents can create

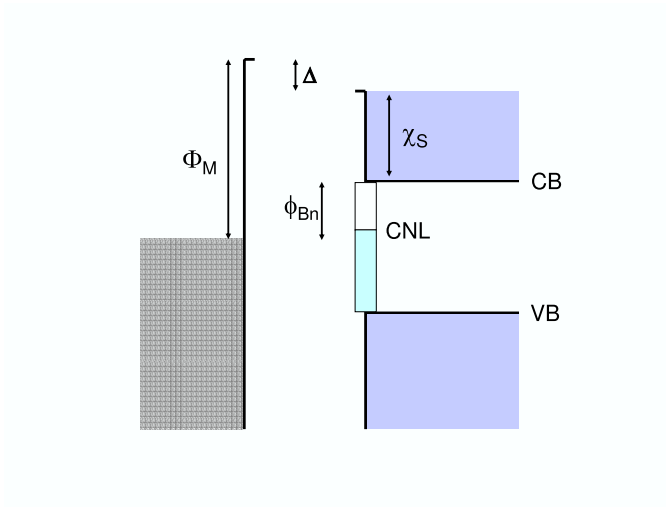

Figure 3.19.: Energy level diagram of a metal/semiconductor interface showing the induced dipole Δ due to charge transfer, and the small final CNL - ϕ_M offset due to efficient screening. Flat bands are shown for convenience. It is seen that ϕ_{Bn} = ϕ_M - χ_S + Δ.

Cowley and Sze, as:

$$\Delta_{is} = \alpha N_{is}\ (E_g - \phi_B - \phi_0) \tag{3.9}$$

where N_{is} is the semiconductor DOS per unit area induced in the gap, assumed to be constant over the energy interval $(E_g - \phi_{Bn} - \phi_0)$, and ϕ_0 is measured from the top of the valence band. α is a parameter related to the effectiveness of the screening by the semiconductor.

On the other hand, we have, from Fig. 3.19

$$\phi_{Bn} = \phi_M - \chi_S + \Delta \tag{3.10}$$

Substituting, and solving for ϕ_{Bn}, we have

$$\phi_{Bn} = \frac{1}{1 + \alpha N_{is}}\ [\phi_M - \chi_S + \Delta^0 + \alpha\ N_{is}\ (E_g - \phi_0)], \tag{3.11}$$

where Δ^0 is the dipole in the case where $\phi_M = \phi_0$. Notice that, since α, N_{is} and Δ^0

a dipole at the semiconductor surface. When both systems are brought together, an additional contribution due to charge transfer between them arises, which we now describe.

depend on the metal, the relation of the barrier height with ϕ_M is more complicated; its slope is given by $\frac{1}{1+\alpha N_{is}}$.

This analysis recovers the results of Cowley and Sze for the slope parameter, which had been obtained by assuming a phenomenological density of states in the gap. In the limit of a high density of interface states, $N_{is} \to \infty$, only the last term in Eqn. 3.11 survives and we have the Bardeen result: complete pinning, $S = 0$ and $\phi_B = (E_g - \phi_0)$. On the other hand, for no interface states, we have $N_{is} \to 0$ and, from Eqn. 3.11, $S = 1$ and $\phi_B = \phi_M - \chi_S + \Delta^0$, where the last term Δ^0, which is the dipole in the absence of charge transfer, was not included explicitly in the Schottky-Mott equation.

The IDIS model, therefore, allows Schottky barrier heights to be calculated in terms of the metal work function, the semiconductor electron affinity, the CNL, and a proportionality factor.

We have seen how a DOS in the semiconductor gap is crucial for explaining the energy level offset at metal-inorganic semiconductor interfaces, since these interface states make charge transfer across the interface possible. This gives rise to a dipole which tends to push the CNL towards ϕ_M

The CNL represents a Fermi level for the semiconductor, since it is the energy up to which the semiconductor levels at the interface are filled, and tends to align with the metal work function.

3.4.4. Inorganic semiconductor heterojunctions

At semiconductor heterojunctions, the main quantity of interest is the band offset which exists at the interface between the top of the valence (bottom of the conduction) bands, of both semiconductors, **once the junction is created**. Fig. 3.20 shows the energy level diagram after the interface is formed.

The calculation of the semiconductor band offsets within the IDIS model was first done by Tejedor and Flores [Tejedor78, Flores79]. By approximating the semiconductor wavefunctions with a two-band model, a similar approach as in metal-semiconductor interfaces was followed: the two-dimensional problem is spilt in several one-dimensional ones corresponding to k-points of high symmetry in the (two-dimensional) Brillouin zone. At each of these k-points, the corresponding one-dimensional wavefunction matching equations are solved and the DOS induced at the interface, as well as the position of the CNL, are calculated. Finally, the results are averaged over the number of k-points considered.

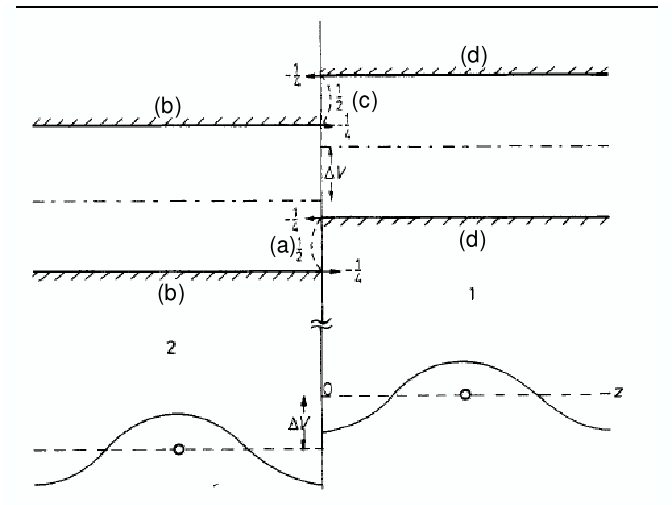

Figure 3.20.: In the regions where the gap of one semiconductor overlap with the bands of the other material ((a) and (c)), a DOS is induced, which is compensated by a corresponding decrease of the DOS of the valence and conduction bands of that semiconductor ((b) and (d)). Figure adapted from Ref. [Tejedor78]).

At heterojunctions, the interface states are similar to those formed at metal- semiconductor interfaces: bulk electronic states of one semiconductor tunnel into the gap and resonate with virtual states of the other semiconductor.

As before, a deficit of DOS appears near the valence band maxima and conduction band minima of each semiconductor, which is compensated by an induced DOS at the energy range where its energy gap coincides with the valence (VB) or conduction (CB) bands of the other semiconductor. This is shown schematically in Fig. 3.20.

Let us first consider the valence band region (Fig. 3.20): in the energy range where VB_1 overlaps gap_2, an induced DOS appears in $semiconductor_2$ (a). This is compensated by a decrease in the DOS of VB_2 and CB_2 (b). In the CB region, the opposite occurs: in the energy range between the bottom of CB_2 and that of CB_1, an induced DOS appears in $semiconductor_1$ (c). This induced DOS is draws from the VB and CB of $semiconductor_1$ (d).

At the heterojunction, charge flows from the semiconductor with the higher CNL (ie. closer to the vacuum) to the one with the lower one (more negative). The final band offsets, therefore, are determined by the (partial) alignment of the CNLs of

both semiconductors.

The valence band-edge discontinuity, ΔE_v, is (Fig. 3.20)

$$\Delta E_v = (\chi^2 + E_g^2) - (\chi^1 + E_g^1) - D_J - \alpha(\phi_0^2 - \phi_0^1) \tag{3.12}$$

where χ and E_g are the electron affinities and gaps of each of the semiconductors measured with respect to vacuum, D_J is the dipole at the interface *excluding* the effect due to charge transfer, and α is the parameter introduced before for metal-semiconductor interfaces, which was found to be constant for all semiconductors considered [Flores79].

At the same time, we can write (Fig. 3.20)

$$\phi_0^2 - \phi_0^1 = (\chi^2 + E_g^2 - \phi_0^2) - (\chi^1 + E_g^1 - \phi_0^1) - D_J - \alpha(\phi_0^2 - \phi_0^1) \tag{3.13}$$

so that, substituting, we get

$$\Delta E_v = \frac{1}{1+\alpha}[(\chi^2 + E_g^2) - (\chi^1 + E_g^1) - D_J + \alpha(\phi_0^2 - \phi_0^1)] \tag{3.14}$$

Equation 3.14 enables the band-edge discontinuity, ΔE_v, to be found from values of the gap, electron affinity and CNL of both semiconductors. Notice the similarity with equation 3.11 for metal/semiconductor contacts.

The driving mechanism at semiconductor heterojunctions is thus the tendency of the CNLs to align. This is made possible by the existence of interface states, which allows for charge transfer and a dipole at the interface. As pointer out by Tersoff [Tersoff84],the magnitude of the transferred charge need not be much, since a small deviation from the 'canonical' lineup (the alignment of CNLs, in the IDIS picture) gives rise to a large interface dipole, due to the dielectric screening at the interface.

Due to the rather strong screening at *inorganic* semiconductors, the Fermi level is strongly pinned near the CNL. This means that the induced dipole is such that the metal work function are almost completely aligned (in the case of metal-semiconductor interfaces), with values of the S parameter close to zero [Flores87]. At heterojunctions, the CNLs of both semiconductors align almost completely, a feature which proved very useful in analysing the transitivity rule [Katnani83].

3.4.5. The Defect Model

Parallel to the IDIS model, Spicer and collaborators developed the Unified Defect model [Spicer79] to explain the Fermi level pinning at semiconductor interfaces.

The pinning at very low ($\sim$ 0.1 ML), *before* a metallic layer was formed, put into question the IDIS model, since the metal would induce little or no DOS in the semiconductor gap. Moreover, the pinning position was the same regardless of whether the adatom was a metal or oxygen: the Fermi level was pinned at an energy characteristic of the semiconductor (near the top of the gap for InP, in the middle of the gap for GaAs, and near the bottom for GaSb [Spicer79]).

Spicer and collaborators suggested that the adatoms were creating defects in the semiconductor, (whose position in the gap would be characteristic of the semiconductor). A mechanism was tentatively proposed in which semiconductor atoms moved into the metal due to the energy released when the adatoms were adsorbed on the semiconductor surface. This would give rise to two discrete levels in the gap: one for the semiconductor anion and one for the cation.

The rather long-standing struggle between the IDIS and Defect models, which were seen to describe competing rather than complimentary mechanisms, was complicated by the fact that in many cases both yielded similar theoretical predictions [Flores87].

For low metallic coverages, the density of defects at the interface needed to pin the Fermi level can be expected to be present at any metal-semiconductor interface; for high metal coverages, on the other hand, the metallic screening of these defects makes the density of defects needed to pin the Fermi level very high. At semiconductor heterojunctions, the high quality of the interface makes defects less likely to be present.

In summary, it is now accepted that the low-coverage data for metal-semiconductor interfaces tends to support the Defect model, whereas high-coverage data ($\gtrsim$ 1 ML), as well as that for heterojunctions, favour the IDIS model.

3.5. Theoretical approach to metal/organic interfaces

3.5.1. Organic semiconductor interfaces

Films of organic semiconductors show that these materials are composed of individual, well differentiated molecules. The interaction between them is weak, as evi-

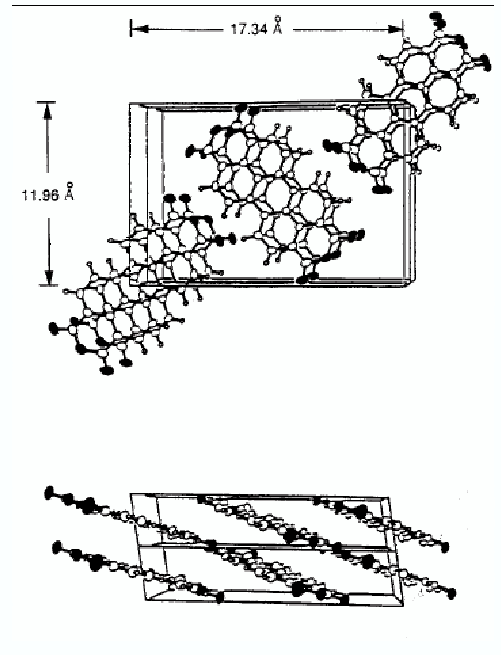

Figure 3.21.: PTCDA unit cell (from [Forrest97]).

denced by the almost flat bands. The geometrical structure of the organic molecules, often flat, is characterized by the presence of aromatic (benzene) rings, which is reflected in the highly anisotropic (in-plane and out-of-plane) growth, transport and optical properties [Forrest97] (see Fig. 3.21).

The bulk stacking distance in the growth direction, perpendicular to the molecular planes, is large: 3.21 Å for PTCDA and 3.45 Å for PTCBI [Forrest97]. Such large interplanar distances come from the nature of the organic material, which consists of individual molecules of closed-shell structure, with a weak interaction, as evidenced by almost flat bands, typically less than 0.1 eV for amorphous solids [Baldo01] and $\sim$ 0.1 – 0.4 eV for stacked organic materials [Forrest97].

The two-dimensional structure of polycyclic aromatic molecules on metal surfaces (see Figs. 3.22,3.23,3.24,3.25) reveals that the organic molecules are generally deposited flat on the metal substrate [Forrest97, Krause03, Schreiber04, Umbach96, Fenter95], so that films of organic material can be thought of being formed

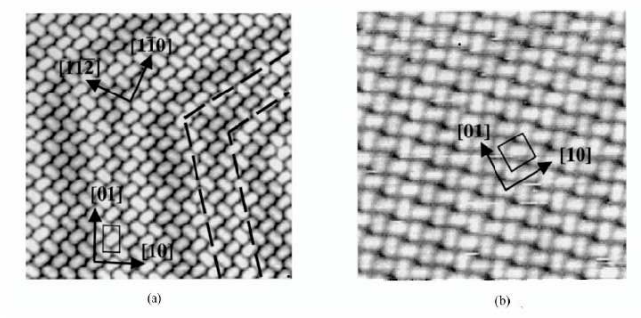

Figure 3.22.: STM images of a PTCDA monolayer on Au. The figures show the 'herringbone' (a) and 'square' (b) phases (from [Chizhov00]).

by the repetition of this molecular layer in the direction perpendicular to the surface.

Although metal-organic interfaces exhibit a wide range of reactivities [Ishii99, Ishii01, Shen01b, Schreiber04, Hill00d, Shen01a, Hill98b, Eremtchenko04], the closed-shell nature of the organic molecules makes the interaction with the metal weaker (weaker, for example, than 'small' chemisorbed species made up of the same atoms, like CO, CO_2, CH_3 or NH_3, for example), so that the metallic surface and the organic molecular plane are separated a distance $d \sim 3$ Å [Forrest97, Schreiber04]. Generally, the weaker the interaction, the larger the organic-metal distance: more reactive metals will tend to form bonds with the molecule, possibly with light (H) atoms or with the most electronegative ones (O, F). At the same time, this complicates the energy level alignment analysis, since the gap states have to be calculated for the specific metal/organic geometry and binding configuration. On the other hand, non-reactive interfaces, exhibiting physisorption, are more difficult to analyze theoretically since DFT cannot be used directly, as will be described below. However, at the same time results about 'intrinsic' properties of the interface can be drawn, which do not depend on the occurrence of a chemical reaction or defects to appear. Since there is evidence that metals other than Au are reactive

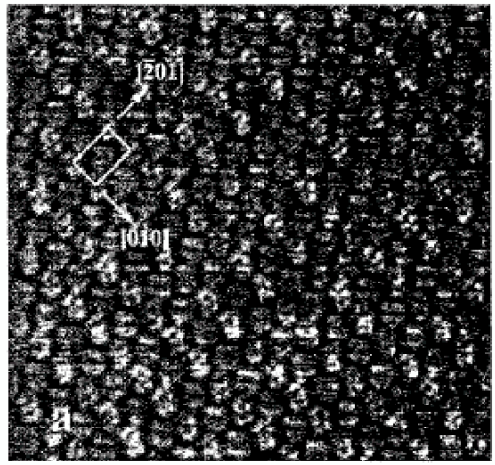

Figure 3.23.: STM image of a PTCDA monolayer adsorbed on HOPG (from [Kendrick96]).

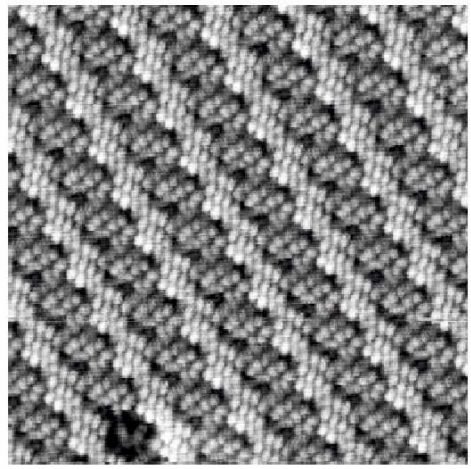

Figure 3.24.: STM image of a saturated monolayer of PTCDA on Ag(111). Inequivalent molecules per unit cell are distinguishable by their different intensities in the STM image (from [Umbach96]).

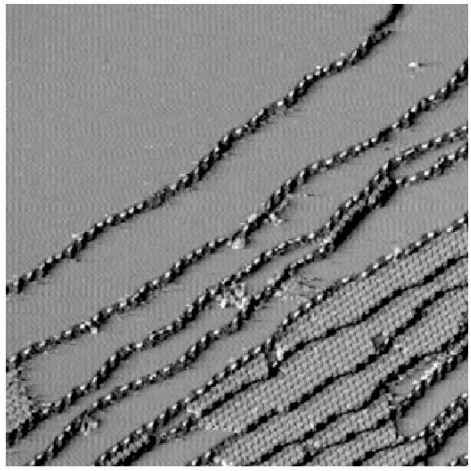

Figure 3.25.: STM image for submonolayer coverage of PTCDA on a stepped Ag(111) surface. Bright objects at step edges are PTCDA molecules (from [Tautz02]).

or interdiffusive [Salaneck01], we restrict our discussion to the case of interfaces between organic materials and Au: Au is non-reactive and the junctions formed with organic semiconductors are abrupt, resulting in almost ideal interfaces [Fenter95, Hill00d, Eremtchenko04, Peisert03, Schmitz-Hübsch96]. We therefore restrict our discussion to non-reactive metals, for which we take Au(111) as a prototype.

Despite its importance in determining the strength of the substrate-adsorbate interaction, the issue of the metal-molecule distance is still an open question at large. Only a few experimental measurements exist [Krause03, Schreiber04] for some molecular materials on certain metals, and the answer to this topic is far from complete. Krause *et al.* have determined, using X-ray diffraction, the distance between the first PTCDA layer and the Ag(111) surface to be 2.85 Å [Krause03]. For CuPc, the CuPc-metal distance is 2.6 – 2.9 Å on Cu(111) and 3.25 – 3.45 Å on Ag(111) [Gerlach05]. These values have an uncertainty no smaller than 0.1 Å.

For the case of the less reactive Au, one can expect a similar or slightly larger distance, $\gtrsim$ 3 Å, but there is very little experimental data so far ($d \simeq$ 3.4 Å [Umbach]). The lack of experimental information in this case arises from the position of the Au d-band, close to the Fermi level. Apparently, the large contribution of this band greatly reduces the contrast of X-ray diffraction measurements, so that, to our

knowledge, no experimental determination of non-reactive organic-Au distances exists to the present date.

From the theoretical point of view, the organic/metal distance is difficult to calculate. Due to the closed-shell nature of the adsorbate, and the electronic structure of noble metals, the metal-organic interaction has an important van der Waals (or dispersion forces) contribution. As is well known [Kohn98, Hult99, Lee02a, Lee02b, Das03, Basanta], DFT does not provide a good description of the van der Waals interaction. It adequately describes the chemical (covalent, ionic) bond, in regions where the wavefunction overlap, and therefore electron density is high, but not the present case of closed-shell molecules ~ 3 Å away from noble metal surfaces.

Thus, standard DFT calculations are not reliable for determining the organic-metal distance[2]. In our calculations, the distance d has been introduced as a fixed external parameter.

3.5.2. Single-molecule approach

Due to the closed-shell nature of molecular solids, In organic semiconductors, the **intermolecular** interaction is of van der Waals type [Forrest97]. It is rather weak, and it preserves the individuality of the organic molecules. Moreover, the effect of intermolecular interactions on the organic spectrum is to produce (small) shifts and broadening of the molecular levels, but it can be separated from the mechanisms described in the IDIS model in that it does not induce any DOS in the organic energy gap. Since the Fermi level pinning and energy level alignment depend on these interface states, we can safely neglect the effect of intermolecular interactions and restrict our analysis to a single molecule deposited flat, with its plane parallel to a metal surface, separated ~ 3 – 3.5 Å, as shown in Fig. 3.26.

3.5.3. Energy levels at the interface

A detailed knowledge of the energy levels at the metal/organic interface is needed for a good description of injection properties. For this, it is necessary in the first place to identify which electronic levels are relevant for charge injection to, and transport through, the interface. These are given by *uncorrelated* electron-hole pairs in the solid, whose energy is referred to as the **single-particle or transport gap**

[2]Recently, the implementation of van der Waals forces within a local-orbital approach has been developed [Basanta], and its application to the present problem is expected to aid the calculation of d.

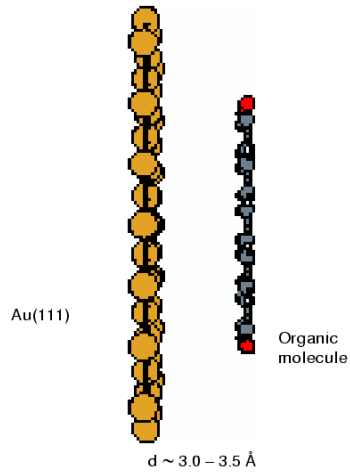

Figure 3.26.: Geometry for our Au/organic theoretical analysis. The metal-organic distance d is introduced in our calculations as a fixed external parameter.

(E^t) [Shen01b]. When the pair is *bound or correlated*, due to the interactions coming from the proximity of the electron and hole, the lowest absorption energy is given by the **optical gap (E^{opt})**. The difference between the two is the energy required to separate or 'uncorrelate' the electron-hole pair, and is the **exciton binding energy** (Fig. 3.27).

Here, an important difference arises with *inorganic* semiconductors, since in that case, one can think in terms of delocalized wavefunctions, extended throughout large distances [Forrest97]. Screening of charge excitations is efficient, and exciton binding energies are small, in the order of meV. The optical and transport gaps are therefore almost equal. Organic semiconductors, on the other hand, are composed of weakly-interacting molecules which retain their electronic structure and have small intermolecular overlap, and are therefore described in terms of localized wavefunctions. Charge excitations are localized to either the same or neighboring

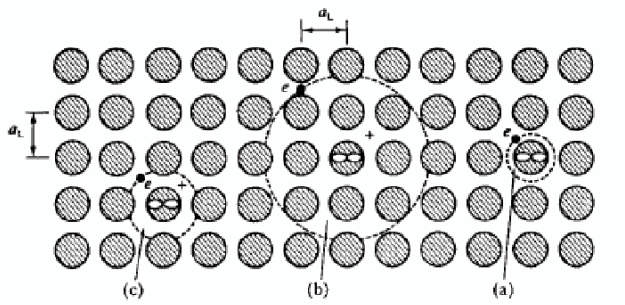

Figure 3.27.: Different types of charge excitations: (a) Small radius ($a \sim a_L$) Frenkel exciton, resembling molecular excitations, (b) Large radius ($a \gg a_L$) Wannier-Mott exciton, common in inorganic semiconductors, (c) Intermediate radius ($a > a_L$) charge-transfer exciton, proposed to be present in many organic molecular crystals (from [Forrest97]).

molecules [Forrest97], and the Coulomb energies between the electron and hole are large, $\sim$ 0.3 – 1eV [Hill00b]. The small intermolecular overlap and large polarizabilities results in rather poor screening. Exciton binding energies, which give the difference between the optical and transport gaps, are therefore large, of the order of several tenths of an eV (see Fig. 3.28).

Thus, unlike inorganic semiconductors, the optical and transport gaps do not coincide in organic materials, and E^t needs to be determined independently, which has been achieved experimentally through the combination of photoemission and inverse photoemission techniques [Salaneck01]. This difference between the transport and optical gaps complicates the analysis of organic semiconductor interfaces, since the optical gap is more accessible experimentally, but it is the transport gap which is relevant for charge transport properties.

3.5.4. Polarization at the interface

The discussion of our modification of 'Koopmans' theorem was concerned with the (correct) calculation of **gas-phase** Ionization an Affinity levels of organic molecules. The organic energy levels and transport gap **at the metal/organic interface** are

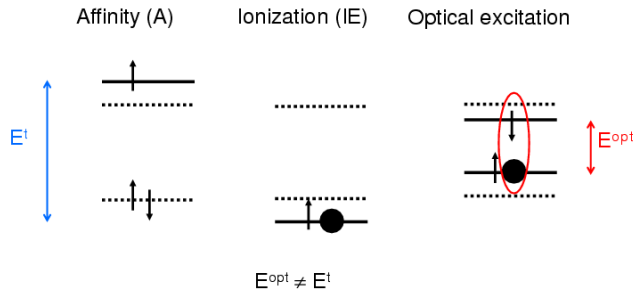

Figure 3.28.: In organic materials, the transport (left) and optical (right) gaps differ greatly, by several tenths of an eV. Notice how the DFT gap (dashed lines) equals neither E^t nor E^{opt}, but its value is closer to the latter.

modified with respect to their gas-phase or bulk values. This comes from to the change in polarization and screening due to the different chemical environments. Because the vacuum in not polarizable, the gas-phase transport gap has a larger value than in the bulk or at interfaces. The presence of neighboring molecules or a metal surface allows these media to be polarized. Polarization, or the rearrangement of charges in the surrounding media, has the result of screening charge excitations. Metals, with delocalized wavefunctions, can efficiently screen these charge excitations. In organic materials, with wavefunctions more localized on individual molecules, the medium is polarized to screen the additional electron or hole. Due to the higher localization, it is not as efficient as in metals, and typically extends through several layers [Forrest97].

At metal-organic interfaces, therefore, polarization of the surrounding media screens charge excitations. Its effect is to decrease the ionization energy and increase the electron affinity (i.e. to draw IE and A closer to each other, Fig 3.30), thereby reducing the transport gap at the interface with respect to the gas phase.

Tsiper *et al.* [Tsiper02, Tsiper03, Tsiper01] have analyzed polarization changes at several metal-organic interfaces. Their calculations use the atom-atom polarizability tensor, which is calculated within a semiempirical Hamiltonian. The organic ma-

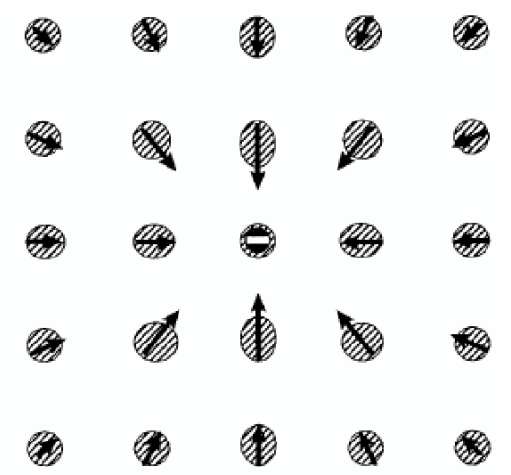

Figure 3.29.: Lattice polarization in an organic molecular crystal, showing the response of the surrounding media to an excess negative charge (Fig. from [Forrest97]).

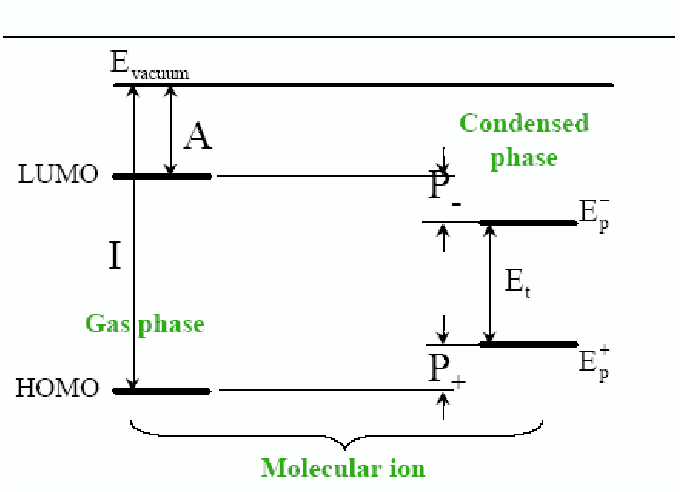

Figure 3.30.: The polarization of the surrounding (metal or organic) material screens charge excitations, decreasing the value of the transport gap at the interface ([Shen01b]).

terials are described out using the so-called sub-molecular approach, in which the charges of all individual atoms in the molecule are taken into account. This enables a good description of the polarizability of these materials, since some molecules (like PTCDA) have strong permanent dipoles for which a good description is needed. Self-consistent equations for the atomic charges are solved for clusters of molecules of mesoscopic ($\sim$100 Å or $\sim$ 2500 molecules) size, extrapolating to the macroscopic limit.

The papers discuss the polarization and transport gap at different positions in an organic film deposited on a metal surface. In the bulk of the material, with organic molecules surrounding the excited molecule, polarization reduces the transport gap by $\sim$1.8 and $\sim$ 2.0 eV (for PTCDA and Pentacene, respectively) with respect to the gas phase. This value is similar to that of a single organic monolayer deposited on the metal surface, the situation of interest for STM experiments. The lack of organic material on the vacuum side is compensated for by the higher polarizability of the metal. In organic-based devices, on the other hand, charge injection is determined by the layer next to the metal of a thick film of organic material. In this case, the organic molecules in the first monolayer have metal on one side and organic material on the other, and electronic polarization effects are larger, $\sim$ 2.2 eV for both PTCDA and Pentacene [Tsiper02, Tsiper03].

If polarization calculations are available, as is the case of PTCDA and Pentacene just mentioned, the change in polarization can be calculated and the gap at the **interface** can be determined numerically. Otherwise, combined UPS/IPES spectra of organic thin films yield the transport gap of the material. Since these are surface-sensitive techniques, the measurement correspond to the transport gap at the **surface** of the film, with vacuum (rather than the metal) on one side. The polarization at the metal/organic interface is then inferred, and the appropriate reduction of the gap is introduced.

In principle, this would enable the calculation of the transport gap at the interface, which is the relevant quantity in charge injection. However, electronic polarization energies, as described above, are known only for a few organic materials [Shen01b], and the approach for other materials, for which electronic polarization energies are unknown, must be different. As our general approach, we take the transport gap at the interface from optical gap measurements and calculations or estimations of the exciton binding energy. Calculations are used when these are available, but the optical gap is more accessible experimentally and its value is known for a large number of organic materials [Shen01b].

	E^{opt} (onset)	exciton binding energy	E^{t} (peak-to-peak)
PTCDA	2.2	0.6	3.2
PTCBI	2.0	0.7	3.1
CuPc	1.6	0.6	2.6
CBP	3.1	1.0	4.6
Pentacene	1.35	1.1	2.95

Table 3.1.: Onset of optical gaps, exciton binding energies and peak-to-peak transport gaps [Shen01b], as used in our calculations. Notice the $\sim$ 0.4–0.5 eV correction when passing from onset to center-to-center values.

We start with the optical gap, whose magnitude is taken from experiment. In most cases, the **onset** of photoemission is reported, which corresponds to optical transitions between the HOMO and LUMO **edges**. The maximum of optical absorption, corresponding to transitions between HOMO and LUMO peaks, is $\sim$ 0.5 eV larger. Since we are working with the peaks or centers of molecular states, it is this value we are interested in. This represents the energy needed to form a correlated electron-hole pair. By adding the exciton binding energy, the separation energy of an uncorrelated electron-hole pair is obtained, which is the magnitude of the transport gap. We have thus followed this procedure to obtain the following values (table 3.1).

Let us mention two comments as a word of caution. First, note the large ($\sim$ 0.4 eV) uncertainty in the experimental values for the transport gap, suggesting that further work, especially theoretical, is needed. Second, the figures for the exciton binding energies come from the comparison from values of E^{t} and E^{opt}. Using these binding energies to deduce E^{t} is a somewhat circular argument, but necessary for materials like PTCBI, CBP or CuPc, where neither experimental data nor theoretical calculations for exciton binding energies are available.

We have followed this procedure to obtain the transport gaps of the organic materials studied, as summarized in the right column of Table 3.1.

In the case of CBP, the lack of a clear understanding of the estimates for the exciton binding energy led us to the value of 5.1 eV for the gap [Vázquez04a], which was later corrected to 4.6 eV [Vázquez05b].

To summarize, several points must be considered when determining the organic energy levels and transport gap at metal-organic interfaces: first, the transport gap of the organic material does not coincide with its optical gap, and needs to be

determined independently. When this is done theoretically, the DFT gap cannot be used directly [Picozzi03] but needs to be corrected, to compensate for the systematic underestimation of the gap which is characteristic of DFT. We have developed a scheme, in the spirit of Koopmans' theorem, for calculating these corrections within a local-orbital formulation, as was described in Chapter 2.

In addition, the chemical environment at the interface, with polarization effects and screening of charge excitations, as well as other effects must be taken into account. These effects are large in organic materials, $\sim$ 2 eV, and result in a reduction of the transport gap at the interface with respect to gas-phase values. The calculation of these effects is incompatible with a first-principles calculation of the electronic structure of the organic molecule as it requires the simulation of organic films of mesoscopic dimensions. Since it falls beyond the scope of this thesis, we have included these effects by fitting the transport gap at the interface to experimental values reported in the literature [Shen01b]. It should be noted that the procedure of fitting the HOMO and LUMO to experimental values is common, since the level of detail provided by first-principles methods cannot be carried to large systems (of $\sim$ 2500 molecules), so that theoretical calculations are inevitably aimed at a proper description at either the (sub-)molecular or the mesoscopic level.

Having determined the transport gap, the initial position of the molecular levels with respect to the metal work function, we now turn to the organic-metal interaction and induced DOS.

3.6. Metal-adsorbate interaction: Self-energy

To address the problem of an organic molecule interacting with a metal surface, let us consider, following Zangwill [Zangwill88], a single, discrete level, ϵ_a, resonating with a continuum of metal states $|k\rangle$. This is almost identical to the problem of chemisorption, solved by Anderson and Newns [Newns69]. Here we will develop the theory for a general situation, with no *a priori* conditions on the strength of the metal-organic interaction. The term **adsorption** will be used in a general sense, without any implications about the degree of interaction (ie. chemisorption, physisorption...), whether or not bonds are formed between adsorbate and substrate. We will suppose, however, that the coupling is **not** strong enough to distort the electronic structure of each of the constituents, so that the metal and adsorbate retain their individual electronic structures. This situation is depicted in Fig. 3.31.

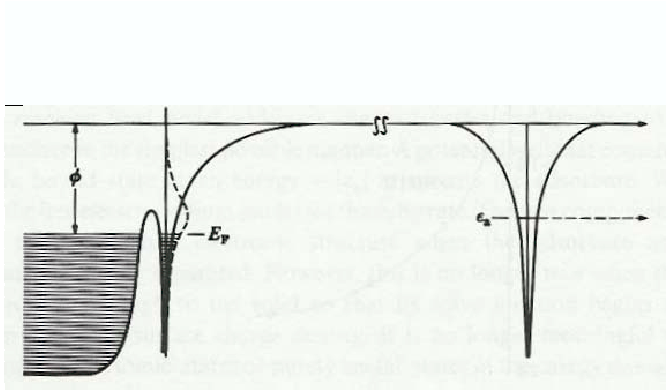

Figure 3.31.: Metal-adsorbate electronic structure for a weakly-interacting interface, where the electronic structure of the adsorbate (in this case, a single level) is not significantly distorted (from [Zangwill88]).

The Hamiltonian for the system, proposed by Anderson and Newns, can be written as

$$H_{tot} = \left(\begin{array}{c|cccc} \epsilon_a - E & T_{a,k_1} & T_{a,k_2} & T_{a,k_3} & \cdots \\ \hline T^*_{a,k_1} & \epsilon_{k_1} - E & 0 & \cdots & 0 \\ T^*_{a,k_2} & 0 & \epsilon_{k_2} - E & 0 & \vdots \\ T^*_{a,k_3} & \cdots & 0 & \epsilon_{k_3} - E & 0 \\ \vdots & 0 & \cdots & 0 & \ddots \end{array}\right). \tag{3.15}$$

where the diagonal elements show the molecular level and the metal eigenvalues ϵ_k. The interaction between metal and adsorbate is given by the off-diagonal elements T_{a,k_i}. The energy levels of the adsorbate-metal system follow from the diagonalization of Hamiltonian 3.15.

It is useful to include the interaction of the metal on the adsorbate using a self-energy [Newns69]. The effect of the metal on the adsorbate is given by the following self-energy, which acts on the adsorbate level ϵ_a:

$$\Sigma_a(E) = \Lambda(E) + i\Delta(E), \tag{3.16}$$

where the imaginary and real parts of the self-energy are given by:

$$\Delta(E) = \sum_k |T_{a,k}|^2 \, \delta(E - E_k), \tag{3.17}$$

$$\Lambda(E) = \frac{1}{\pi} \int \frac{\Delta(E)}{E - E'} \, dE' \tag{3.18}$$

or, in terms of the substrate Green's function,

$$\Sigma_a(E) = \sum_k |T_{a,k}|^2 \, G(E), \tag{3.19}$$

where the real and imaginary parts of the self-energy come from those of G. Thus, Hamiltonian 3.15 can be substituted by

$$\epsilon_a + \Sigma_a(E) \tag{3.20}$$

The LDOS corresponding to this state, coupled to the metal, is

$$rho_a(E) = -\frac{1}{\pi} Im\Big\{ \frac{1}{E - \epsilon_a - \Sigma_a(E)} \Big\} \tag{3.21}$$

The effect of the real and imaginary parts of the self-energy $\Sigma_a(E)$ can be seen in the LDOS at the adsorbate. This is [Newns69]

$$\rho_a(E) = \sum_a \delta(E - E_a) = \frac{1}{\pi} \frac{\Delta_a(E)}{[E - \epsilon_a - \Lambda_a(E)]^2 + \Delta_a^2(E)} \tag{3.22}$$

The imaginary part of the self-energy, $\Delta_a(E)$, broadens the adsorbate level, initially a delta function. The real part, $\Lambda_a(E)$, has the effect of shifting the adsorbate level from its initial value ϵ_a. For the simple case of an energy-independent self-energy, $\Lambda_a(E) = const. = \Lambda_a$, $\Delta_a(E) = const. = \Delta_a$, the LDOS is a Lorentzian function, centered not at ϵ_a but at $\epsilon_a + \Lambda_a$ and with a Half Width at Half Maximum (HWHM) of Δ_a:

$$\rho_a(E) = \frac{1}{\pi} \frac{\Delta_a}{[E - \epsilon_a - \Lambda_a]^2 + \Delta_a^2} \tag{3.23}$$

The above analysis can be applied to the different organic molecules under study. In these cases, there is not just a single adsorbate level ϵ_a, but several molecular levels ϵ_i, resonating with the Au bands. The adsorbate-metal Hamiltonian 3.15 has

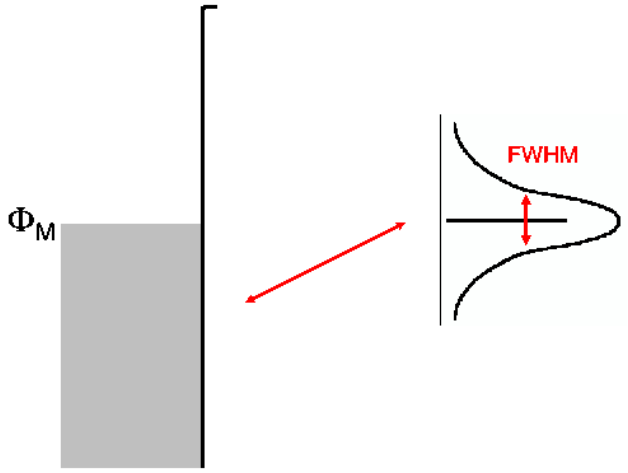

Figure 3.32.: For an energy-independent self-energy, the interaction with the metal substrate broadens each molecular state into a Lorentzian function.

now looks like

$$H_{tot} = \left(\begin{array}{ccc|ccc} \epsilon_1 - E & 0 & \cdots & T_{1,k_1} & \cdots & T_{1,k_{N_k}} \\ 0 & \ddots & 0 & \cdots & \ddots & \vdots \\ \vdots & 0 & \epsilon_N - E & T_{N,k_{N_k}} & \cdots & T_{N,k_{N_k}} \\ \hline T^*_{1,k_1} & \cdots & T^*_{1,k_{N_k}} & \epsilon_{k_1} - E & 0 & \cdots \\ \vdots & \ddots & \cdots & 0 & \ddots & 0 \\ T^*_{N,k_{N_k}} & \cdots & T^*_{N,k_{N_k}} & \cdots & 0 & \epsilon_{k_N} - E \end{array}\right) \tag{3.24}$$

The upper-left and bottom-right 'boxes' are diagonal and correspond to the molecular and metallic levels, respectively. The interaction between both systems is given by the off-diagonal 'boxes', where T_{i,k_j} is the hopping element between the

corresponding molecular eigenfunction and the metallic $|k\rangle$ state.

Similarly to what was described above, the application of the self-energy replaces Hamiltonian 3.24 by an **adsorbate** Hamiltonian plus a self-energy matrix $H_{tot} \rightarrow H_{ads} + \Sigma(E)$:

$$H_{ads} + \Sigma(E) = \begin{pmatrix} \epsilon_1 + \Sigma_{1,1}(E) - E & \Sigma_{1,2}(E) & \cdots & \Sigma_{1,N}(E) \\ \Sigma_{2,1}(E) & \epsilon_2 + \Sigma_{2,2}(E) - E & \cdots & \vdots \\ \vdots & \cdots & \ddots & \vdots \\ \Sigma_{N,1}(E) & \cdots & \cdots & \epsilon_N + \Sigma_{N,N}(E) - E \end{pmatrix} \tag{3.25}$$

The 'box' in 3.24 corresponding to the metal is substituted by the self-energy terms acting on the molecular Hamiltonian. This reduces enormously the dimension of 3.24 (from $(N + N_k)x(N + N_k)$ to (NxN)) at the expense of introducing an energy dependence through $\Sigma(E)$ on the matrix to be solved. Notice, in addition, that 3.25 is no longer diagonal as was the 'box' in Hamiltonian 3.24 for the organic molecule.

3.7. Calculation of self-energy terms

The generalization of 3.19 to the multilevel adsorbate case is straightforward:

$$\Sigma_{MO,MO'}(E) = \sum_{k,k'} T^*_{MO,k}\, G_{k,k'}(E)\, T_{k',MO'} \tag{3.26}$$

where subscripts MO and MO' label the molecular orbitals. It is useful to express relation 3.26 in a local-orbital basis. Expanding the molecular states in terms of the local-orbitals, we have $\psi_i = \sum_j c_{i,j}\phi_j$, so that 3.26 becomes

$$\Sigma_{MO,MO'}(E) = \sum_{ij,\alpha\beta} c^*_{MO,i}\, T^*_{i,\alpha}\, G_{\alpha,\beta}(E)\, T_{\beta,j}\, c_{j,MO'} \tag{3.27}$$

From expressions 3.27 (or 3.26), we see that the shift and broadening of the molecular levels, given by the real and imaginary parts of $\Sigma(E)$, depend on (i) the electronic structure of the substrate, through its Green's function $G_{\alpha,\beta}(E)$, (ii) that of the adsorbate, through the wavefunction coefficients, $c_{MO,i}$, and (iii) the interaction or coupling $T_{\alpha,i}$ between them.

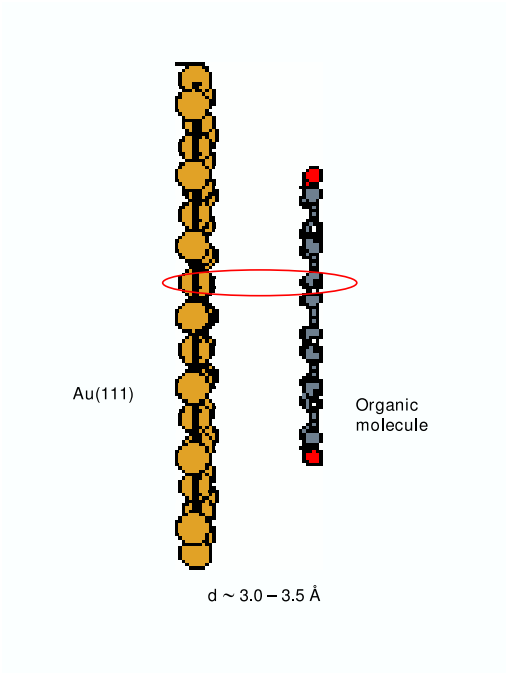

Figure 3.33.: The Au-organic interaction is calculated by computing the hopping elements between the orbitals of each metal-molecule atom pairs.

The calculation of (i) and (ii) using DFT techniques can be carried out using DFT-based methods. In the present case, we will adopt the simple case of neglecting the 5d shell and consider only the 6s orbitals of Au. The hopping elements (iii) between the organic molecule and the metal atoms are calculated for each pair of molecule-substrate atoms (Fig. 3.33).

The organic molecule is assumed to be deposited flat over the metal surface, at a distance d. The magnitude of the hopping elements as a function of this distance is shown in Fig. 3.34.

Although a full calculation, including the effect of other atoms on substrate-molecule pairs should, in principle, be carried out, its effect is small and will be neglected here on a first approximation. Moreover, since we are considering non-reactive interfaces, there are no atoms that, through chemical reactions or adsorbate-induced reconstructions, can move between the substrate-molecule pairs, rendering the hopping elements of Fig. 3.34 a good approximation.

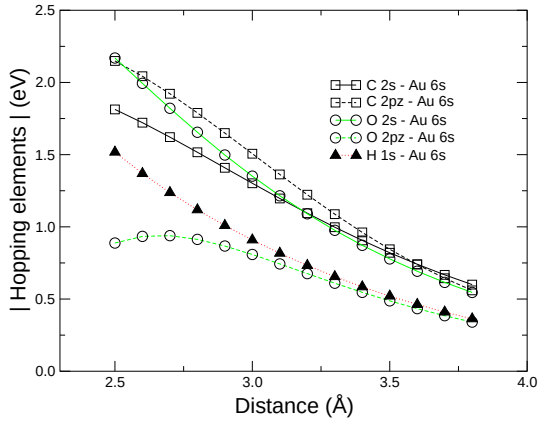

Figure 3.34.: C–, N–, O– and H–Au hopping elements as a function of distance.

From equation 3.27, the most important elements are the diagonal ones MO=MO'. Off-diagonal self-energy elements correspond to the coupling of different molecular orbitals through the substrate, greatly increase the computational cost and are not of great importance.

The main contributions to equation 3.27 come from the $i = j$ terms: the $i \neq j$ terms correspond to taking two different atoms in the molecule or, in the case of σ orbitals, two different orbitals of the same atom. In either case, their contribution is not as important as the diagonal $i = j$ terms and will not be included here.

With this, the expression for the self-energy acting on the molecular orbital MO finally reduces to the simple form

$$\Sigma_{MO}(E) = \sum_i |c_{MO,i}|^2 \, |T_{i,6s}|^2 \, G_{6s,6s}(E) \tag{3.28}$$

Here, MO refers to a particular molecular orbital, i labels an atomic orbital, and the Green's function $G_{6s,6s}$(E) provides information about the metal DOS through the relation

$$\rho_{6s}(E) = -\frac{1}{\pi} \, G_{6s,6s}(E) \tag{3.29}$$

Since we are interested in the LDOS in the molecular energy gap, close to the Fermi level, we can take $G_{6s,6s}(E) \simeq G_{6s,6s}(E_F)$. Using the data of Papaconstantopoulos ($\rho_{total}(E_F)$ = 0.147 eV^{-1}, $\rho_{6s}(E_F)$ = 0.036 eV^{-1} [Papaconstantopoulos86]),

d (Å)	Γ_i^π (eV)	Γ_i^σ (eV)
2.8	2.1	1.05
3.0	1.5	0.75
3.2	1.0	0.5
3.5	0.5	0.25

Table 3.2.: Molecular level widths (FWHM) for orbitals of π and σ symmetry as a function of the organic-Au distance d.

we obtain for the broadening of the molecular levels with respect to the metal-organic distance d (Table 3.2).

Notice that, due to the approximations made, the broadening of all molecular orbitals of π symmetry is the same, and the same happens for σ orbitals.

Though remarkably simple, equation 3.28 produces surprisingly good results. We have seen that the effect on the organic molecule of its interaction with the metal, described using a self-energy Σ, is to broaden the molecular levels. The initial delta-like[3] spectrum of the isolated molecule is transformed into a superposition of Lorentzian curves, each of which corresponds to a particular molecular orbital. This modifies completely the organic electronic structure. The broadening of the levels around the Fermi energy, especially the HOMO and LUMO, induce a LDOS in the former organic energy gap, which is 'filled' due to the interaction with the metal substrate (Fig. 3.35).

Where does this DOS come from? Like the case of inorganic semiconductors, where the increase in the induced DOS was derived from a similar decrease in the valence and conduction bands, here the induced DOS is compensated by an equal decrease in the DOS outside the gap.

It is important to notice that, the stronger the metal-organic interaction, the broader the Lorentzian DOS will be, but its integral, which gives the charge, always remains constant. This is illustrated in Fig. 3.36: no matter how broad or narrow the Lorentzian curve is, its integral always equals one, as corresponds to each MO accommodating one electron per spin.

The induced DOS is obtained by adding the contributions of the different MOs,

[3] The spectrum of the isolated molecule is of course not strictly δ-like, but rather has a Gaussian shape due to thermal broadening, and probably the (small) intermolecular interaction. However, these Gaussians are very narrow compared to the Lorentzian FWHM reported in Table 3.2, and certainly do not fill the gap as Lorentzians do, so that the comparison with δ functions remains valid.

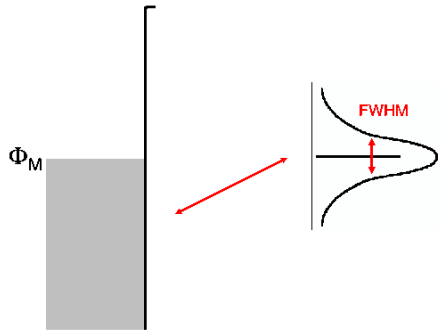

Figure 3.35.: The broadening of the molecular levels, especially the HOMO and LUMO, modified the electronic structure of the organic material, giving rise to a DOS in the former energy gap.

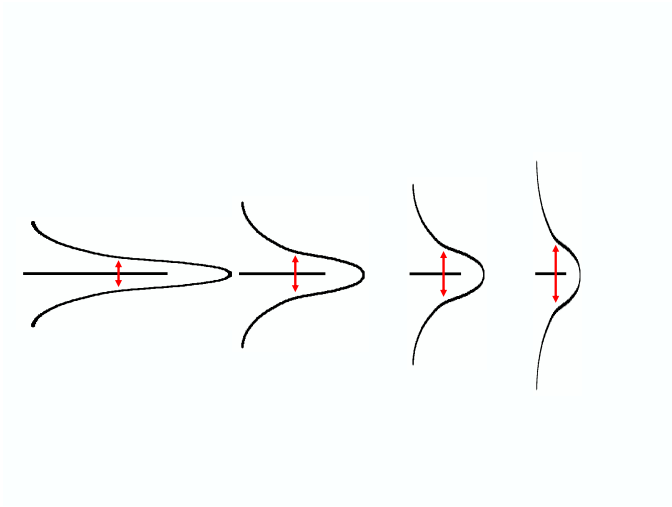

Figure 3.36.: A stronger interaction with the metal gives rise to a greater broadening of the molecular levels. Regardless of the broadening, however, the integrated charge is always equal to one electron per spin.

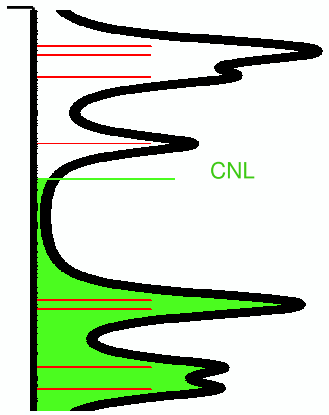

Figure 3.37.: The CNL position is determined by integrating the induced DOS up to the number of electrons in the isolated molecule.

each of which is a Lorentzian curve of width given by equation 3.23. The CNL position is obtained by integrating this DOS up to the number of electrons in the isolated molecule (Fig. 3.37):

$$\int_{-\infty}^{CNL} \rho_{IDIS}(E)\, dE = N \tag{3.30}$$

The CNL position indicates the energy at which the organic molecule **at the interface** is neutral.

The position of the CNL and the magnitude of the DOS induced in the former energy gap determines the strength of the Fermi level pinning at the interface. This is described by the S parameter introduced for inorganic semiconductors [Tejedor77]:

$$S = \frac{1}{1 + 4\pi e^2 D(E_F)\, d/A} \tag{3.31}$$

where all quantities are expressed in atomic units, $D(E_F)$ is the induced DOS at the Fermi level (almost the CNL), d is the metal-organic distance, and A is the area associated with each molecule.

From the theoretical values of S and the CNL, the position of the interface Fermi level at the metal-organic interface, E_F, can be calculated. As in inorganic semiconductors, it is given by

$$CNL - E_F = S\ (CNL - \phi_M) \tag{3.32}$$

where it has been assumed that the interface dipole acts on the metal, shifting its electronic spectrum, while the organic molecular levels are fixed. The dipole at the interface is given by

$$\Delta = (1 - S)\ (\phi_M - CNL) \tag{3.33}$$

The results for the induced DOS and energy level alignment for the different organic materials are analyzed below:

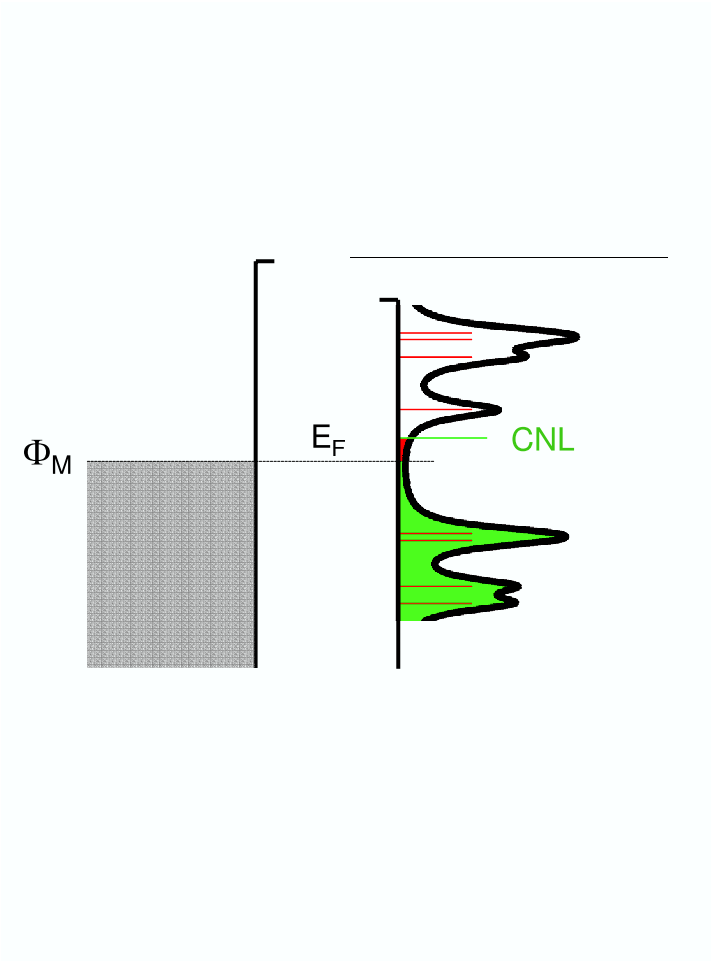

Figure 3.38.: The tendency of the CNL and ϕ_M to align gives rise to charge transfer between metal and molecule. In this case, electrons are transferred (shaded area) from the organic material to the metal.

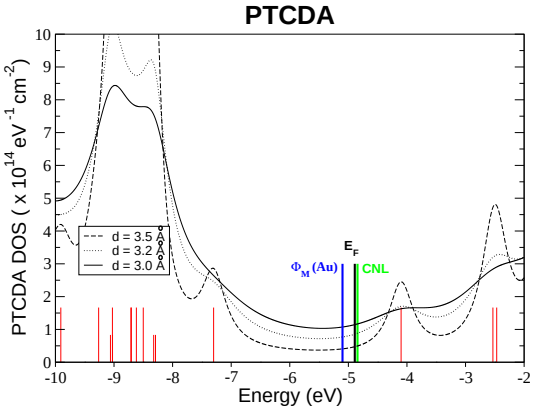

Figure 3.39.: PTCDA induced DOS for the Au/PTCDA interface calculated for d = 2.8 Å (dashed line), d = 3.0 Å (continuous line), and d = 3.2 Å (dotted line). Long (short) bars correspond to the π (σ) states neglecting the metal-molecule interaction. The position of the CNL, work function and interface Fermi level are also shown.

3.8. Au/PTCDA

The electronic structure of the Au/PTCDA interface within our approximation is shown in Fig. 3.39. The figure shows the induced DOS calculated for three organic-metal distances. The molecular levels of the PTCDA molecule are shown as vertical bars. Long (short) bars correspond to π (σ) orbitals neglecting molecular relaxation upon adsorption. The energy scale is referred to vacuum.

The calculated HOMO and LUMO have π symmetry, and their electron density, described in the previous chapter, are in agreement with STM measurements on weakly-reactive interfaces and previous theoretical calculations [Kendrick96]. The HOMO is separated $\sim$ 1 – 2 eV from other occupied states, where, in particular, the σ states are located on the oxygen atoms and are associated with O lone pairs. Above the LUMO are a group of orbitals of π symmetry, the σ states being found $\sim$ 10 eV above the LUMO position.

The most important characteristic of Fig. 3.39 is that the energy gap is filled with the 'tails' of the Lorentzians of occupied and empty states. These states, broadened due to their interaction with the metal, add up to yield a non-negligible DOS in the former energy gap. The figures shows this DOS calculated for three different metal-organic distances (d = 2.8, 3.0 and 3.2 Å). For these distances, the molecular levels are broadened by $\Gamma_i^\pi \simeq$ 2.1, 1.5 and 1.0 eV, and $\Gamma_i^\sigma \simeq$ 1.05, 0.75 and 0.5 eV,

d (Å)	2.8	3.0	3.2	3.5
S	0.12	0.13	0.16	0.23

Table 3.3.: Values for the S parameter for the Au/PTCDA interface for several metal-organic distances, *d*.

respectively. The position of the CNL, calculated from 3.30, is found in PTCDA at -4.8 eV with respect to vacuum, or 2.5 eV above the **center** of the HOMO peak.

The induced DOS at the CNL are 1.5, 1.2 and 0.9 $\times$ 10^{14} eV^{-1} cm^{-2} for these distances. Obviously, the larger the distance, the sharper the molecular states, and the lower their contribution to the DOS at the CNL.

An important result is that, even if the magnitude of the induced DOS, particularly around the CNL, depends rather strongly on the interaction strength, the position of the CNL remains unchanged: in the 2.8 – 3.2 Å range, the CNL position changes by less than 0.1 eV. This is an important result, showing that the CNL position is an intrinsic property of the organic material, and will be discussed later, in the context of the zeros of the real part of the molecular Green's function (Chapter 4).

This insensitivity of the CNL position to *d* is due to the slow decay of Lorentzian functions, and shows that the CNL position depends of the occupied and empty states around the energy gap. For instance, in the Au/PTCDA interface, the occupied states around $\sim$ -9 eV in Fig. 3.39, together with the well-separated states in the empty part of the spectrum, push the CNL upwards in the gap.

The theoretical values of the S parameter can be calculated from equation 3.31, for the organic-metal distances considered. $D(E_F)$ is the induced DOS, d is our fixed external parameter, and A = 120 $Å^2$ is the area per PTCDA molecule (it is not the area A of the molecule, as results from the molecular calculation, but from low-coverage STM measurements yielding the unit cell).

At variance with the CNL position, S depends rather strongly on the metal-organic distance. However, the low ($\sim$ 0.1 – 0.2) value of S indicates that the Fermi level is strongly pinned at the interface, due to the high DOS induced in the gap.

From the calculated value of S and the position of the CNL, the interface Fermi level can be obtained theoretically using equation 3.32. Taking a value of ϕ_M = -5.1 eV [Hill98c] yields E_F = -4.85 eV, or 2.45 eV above the HOMO peak. Because the

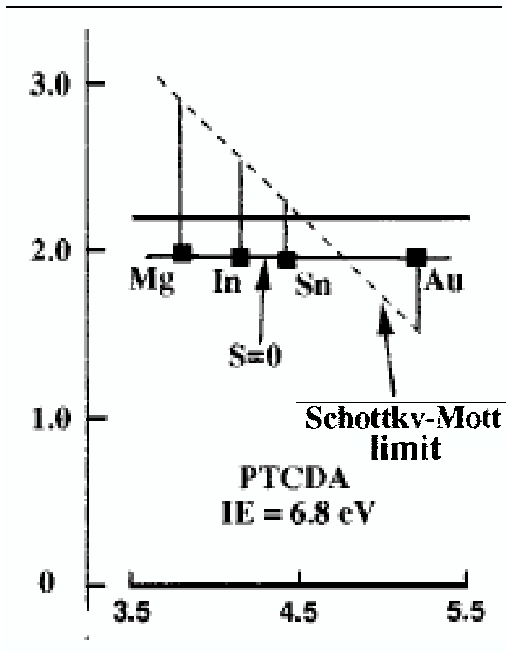

Figure 3.40.: Experimental Fermi level position (black squares) for PTCDA on different metals. The solid line is a least-squares fit, which yields the S parameter over these metals, while the dashed line shows the prediction of the Schottky-Mott model. The difference between E_F and the **top** of the HOMO (which sets the zero of the energy scale) is $\sim$ 2.0 eV. Notice that the LUMO position is deduced by adding the optical gap to the HOMO (from [Hill98c]).

initial difference ϕ_M - CNL = 0.3 eV is rather small, it makes little difference what value of S is used; we take S = 0.16 This is to be compared with the experimental value of 2.0 eV above the HOMO edge (see Fig. 3.40), or 2.5 above the HOMO center (since the HOMO and LUMO **edges** are measured experimentally, and 0.5 eV must be added to refer them to molecular level **peaks**).

The theoretical value of the interface dipole is 0.25 eV (calculated from equation 3.31), close to the experimental [Hill98c] value of 0.2 eV (Fig. 3.41) .

The Fermi level is strongly pinned near the CNL, as shown by the large dipole created, resulting in the relative shift of the molecular electronic spectrum, which brings the CNL and ϕ_M closer.

Notice how the initial ϕ_M - CNL = 0.3 eV is distributed: the low value of S results

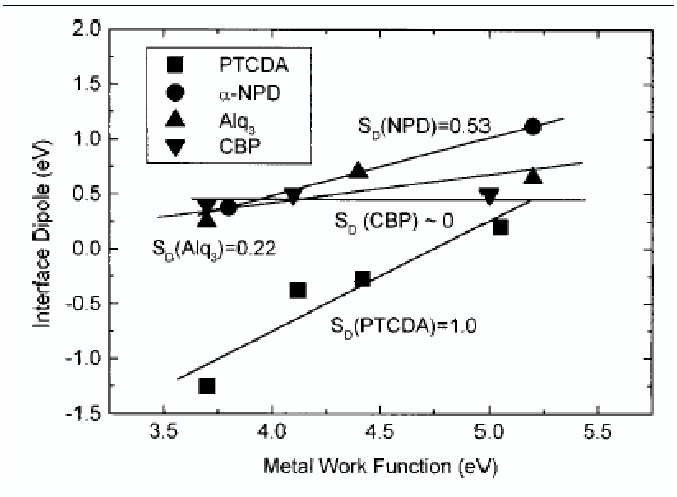

Figure 3.41.: Interface dipole as a function of the metal work function for several organic materials, determined experimentally. Notice that the value for Au/PTCDA is $\sim$ 0.2 eV (from [Hill98c]).

in a large (0.25 eV) interface dipole, and a remaining small (0.05 eV) difference between the interface Fermi level and the CNL. This is the consequence of the strong pinning at the Au/PTCDA interface, resulting from the high DOS induced in the organic energy gap.

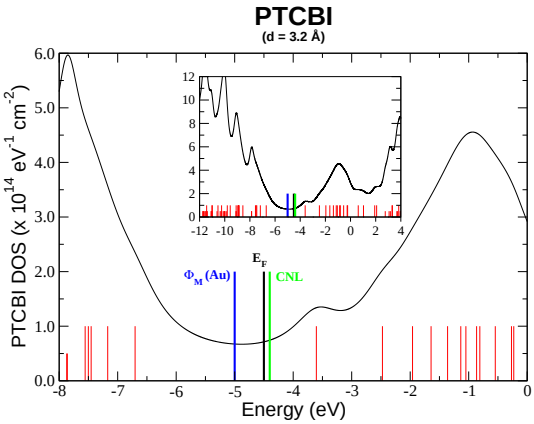

Figure 3.42.: PTCDA induced DOS for the Au/PTCBI interface calculated for d = 3.2 Å. Long (short) bars correspond to the π (σ) states neglecting the metal-molecule interaction. The position of the CNL, work function and interface Fermi level are also shown.

3.9. Au/PTCBI

The calculated induced DOS for PTCBI on Au is shown in Fig 3.42 for a metal-organic distance of 3.2 Å. In this case, the HOMO is not resolved due to other close-lying occupied π states. The LUMO is resolved and lies below a group of empty states, also of π symmetry, in the -2.5 – 0 eV range (with respect to vacuum).

The integration of the induced DOS yields a CNL position of -4.4 eV (with respect to vacuum). The values of D(E_F) = 0.71 and 0.36 $\times$ 10^{14} eV^{-1} cm^{-2} for 3.2 and 3.5 Å (here A = 191 $Å^2$) yield an S parameter for this interface of S $\sim$ 0.2 for this distance range: we have S = 0.16 for d = 3.2 Å and S = 0.28 for d = 3.5 Å. As in the case of PTCDA, the CNL position is changed by less than 0.1 eV for both cases. Notice, however, that the peaks are barely resolved for the shorter distance.

At this interface, a value of ϕ_M = -5.0 eV has been measured [Hill00d]. This gives a 0.6 eV initial difference between the CNL and the metal work function. Using S = 0.16, we obtain a Fermi level position of -4.50 eV with respect to vacuum, or 2.2 eV above the HOMO peak (-6.7 eV), and a calculated interface dipole of 0.50 eV. Experimentally [Hill00d], the Fermi level is measured 1.6 eV above the HOMO edge, or 2.1 eV above the HOMO center, and a downwards dipole of 0.4 eV is measured. This is shown in Fig. 3.44, where it should be noted that the PTCBI optical (rather than transport) gap is presented.

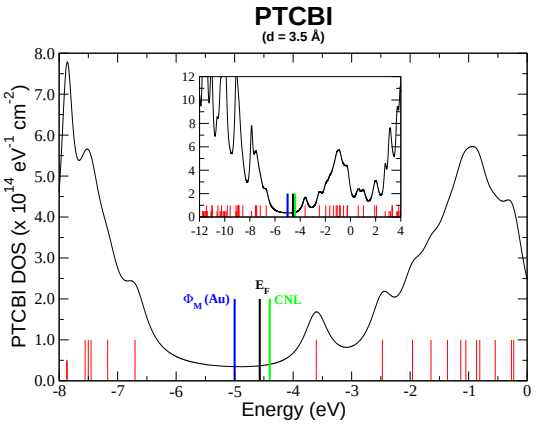

Figure 3.43.: PTCDA induced DOS for the Au/PTCBI interface calculated for d = 3.5 Å. Long (short) bars correspond to the π (σ) states neglecting the metal-molecule interaction. The position of the CNL, work function and interface Fermi level are also shown.

As in the case of PTCDA, this is a strongly pinning interface. This is reflected in the low value of S and how the initial ϕ_M - CNL difference is screened, resulting in a large interface dipole and a small offset between the interface E_F and the CNL.

The agreement with the experimental values is good: the difference in the Fermi level position and interface dipole is $\sim$ 0.1 eV, showing that the strongly pinning character of the interface is correctly described. For the slope parameter S, the agreement is reasonable; the theoretical results yield a low value, showing the pinning is strong, but, as in the case of PTCDA, still larger than the experimental value of S $\sim$ 0. This will be discussed below.

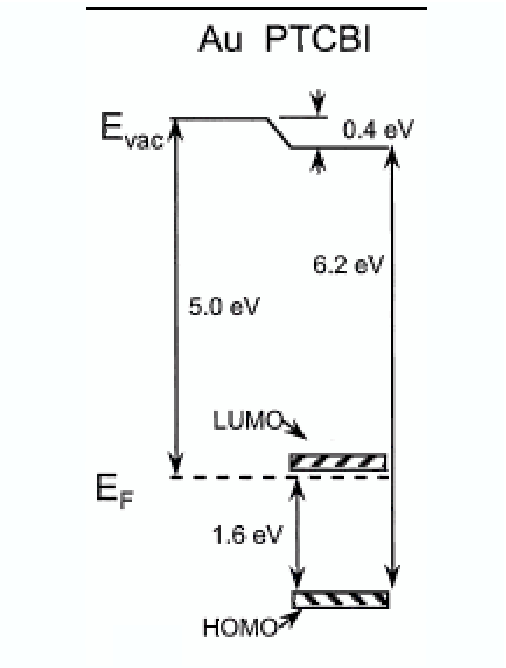

Figure 3.44.: Energy level diagram determined experimentally ([Hill00d]) for the Au/PTCBI interface. Notice that HOMO and LUMO **edges** are shown, and 0.5 eV have to be added in each case to translate to level centers.

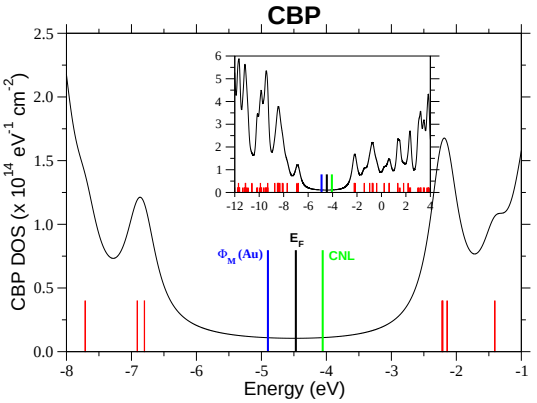

Figure 3.45.: PTCDA induced DOS for the Au/CBP interface calculated for d = 3.5 Å. Long (short) bars correspond to the π (σ) states neglecting the metal-molecule interaction. The position of the CNL, work function and interface Fermi level are also shown.

3.10. Au/CBP

The induced DOS for the Au/CBP interface is shown in Fig. 3.45, calculated for a metal-molecule distance of 3.5 Å. The large energy gap (4.6 eV) results in a smaller induced DOS in the gap. The presence of fewer molecular orbitals around the gap adds to this effect. These orbitals are distributed rather symmetrically around the gap, which results in the CNL closer to mid-gap. The DOS induced at the CNL is $\sim 0.1 \times 10^{14}$ eV^{-1} cm^{-2}, much smaller than in the previous cases.

For the case of CPB, the CNL position has been somewhat troublesome. First, an incorrect value for the peak-to-peak gap was taken (5.1 eV [Vázquez04a]) later, this gap was corrected to 4.6 eV [Vázquez05b]. After recalculating the Au/CBP interface, we have arrived at the CNL position of -4.05 eV. Given our previously reported value of -4.2 eV [Vázquez05b]PRB-OO, we consider this figure to have an uncertainty of $\pm$ 0.1 eV.

The value of CNL = -4.05 eV is a slightly more symmetric position in the gap than in the previous cases, and a theoretical value of the S parameter of S = 0.5 (taking A = 251 Å^2). Using the experimental value of ϕ_M = -4.9 eV (Fig. 3.46), the Fermi level position is calculated at E_F = -4.47 eV (2.33 above the HOMO center), and a dipole magnitude of 0.43 eV. Experimental data [Hill98b], shown in Fig. 3.46, report a dipole of 0.5 eV, and the Fermi level position 1.9 eV above the HOMO edge, or $\sim$ 2.4 eV above the HOMO peak (notice again that in Fig. 3.46, the optical gap is

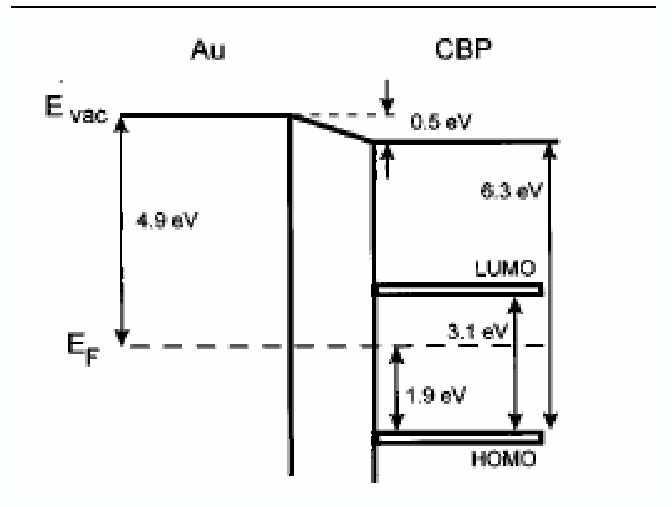

Figure 3.46.: Energy level diagram for the Au/CBP interface, showing the interface dipole and the Fermi level position. Notice that this is referred to HOMO and LUMO onsets (rather than centers). Figure from [Hill98b].

presented).

The larger value of S than the previous cases, which translates into a higher E_F - CNL difference, reflects the lower pinning behavior at the CBP/Au interface. This is due to the lower DOS induced in the gap, which allows the interface Fermi level to move more within the gap.

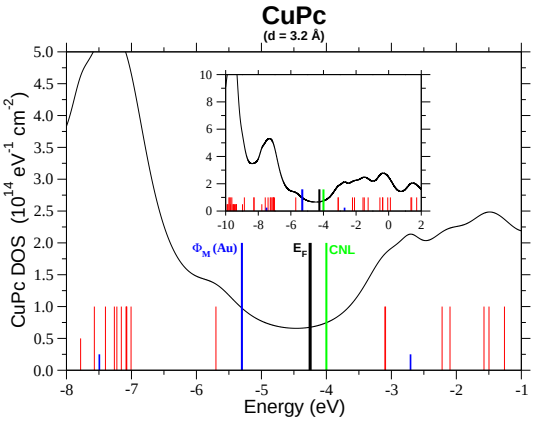

Figure 3.47.: PTCDA induced DOS for the Au/CuPc interface calculated for d = 3.2 Å. The rather strong metal-organic interaction results in the large broadening of the molecular states and in the pinning of the Fermi level close to the CNL.

3.11. Au/CuPc

When calculating the electronic structure of the Au/CuPc interface, the singly-occupied Cu-associated molecular orbital, which is the HOMO and LUMO at the same time, and which gives rise to two states within our Koopmans approach, is taken into account. For the sake of clarity, these states are shown as broader, shorter vertical bars in Figs. 3.47 and 3.50, to distinguish them from other molecular orbitals.

The comparison of our results [Vázquez05b] with experimental data has forced a reconsideration of the metal-organic distance, d.

Fig. 3.47 shows the induced DOS and CNL for d = 3.2 Å. The main feature is the relatively high DOS induced in the gap, created mostly by the rather small (2.6 eV) energy gap. This gives rise to values of $D(E_F) \simeq 0.65 \times 10^14$ eV^{-1} cm^{-2}. Taking d = 3.2 Å results in a value of S = 0.19, indicative of a rather strongly pinning interface.

The CNL is located 1.7 eV above the HOMO peak, or at CNL = -4.0 eV from the vacuum level. Inserting ϕ_M = -5.3 eV [Peisert02] in equation 3.32 yields an interface dipole of Δ = 1.05 eV and a Fermi level located 1.45 eV above the HOMO peak (E_F = -4.25 eV with respect to vacuum).

Experimentally, CuPc interfaces have been extensively analyzed. Experiments [Peisert02] report a large vacuum level drop (of which $\sim$ 0.8 – 0.9 eV is attributed to the surface dipole), and a Fermi level position $\sim$ 1.4 eV above the HOMO center.

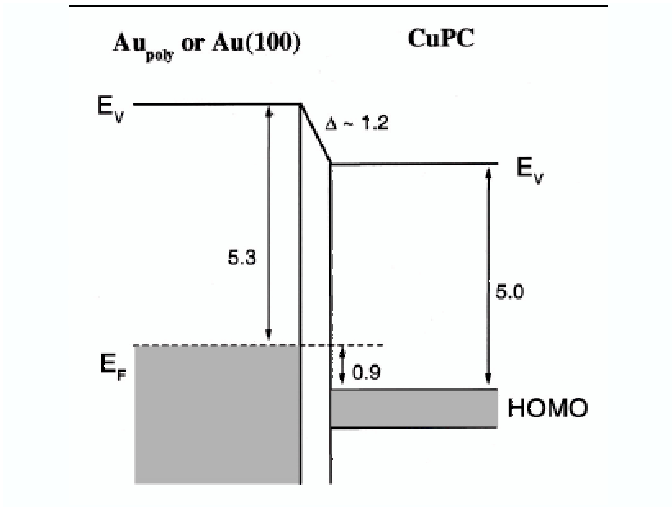

Figure 3.48.: Energy level diagram for Au/CuPc interfaces as determined from photoemission measurements. Notice that no differences are found between single-crystal and polycrystalline Au substrates (from [Peisert02]).

While the Au-CuPc distance has not been determined, other evidence points in the direction of little metal/CuPc interaction. Although the details about adsorption mechanisms on the metal surface are missing, CuPc molecules can adopt flat-lying or upright configurations [Schreiber04, Peisert02], and the reported values of Fermi level position relative to the HOMO and interface dipole are similar in both cases (see Fig. 3.48). The evolution of photoemission spectra is consistent with the interaction of neighboring CuPc molecules, and the results seem to be insensitive to the interaction with the gold substrate.

In addition, STM data [Xu02] do not measure significant DOS induced in the gap (Fig. 3.49). The STM resolution in this experiment is clearly not at its best, making the interpretation of Fig. 3.49 difficult. A detailed analysis shows that possibly the tip is scanning the second CuPc layer.

Our results of Fig. 3.47 indicate a rather strong influence of the gold substrate, contrary to what is observed experimentally. After an evaluation of the data [Peisert02, Knupfer], we consider the possibility that the metal-molecule distance is larger, around $d \sim 3.7$ Å. In this way, the metal/CuPc interaction would be smaller. The calculated DOS for this distance is shown in Fig. 3.50.

The broadening of the molecular orbitals is smaller, due to the larger Au-CuPc

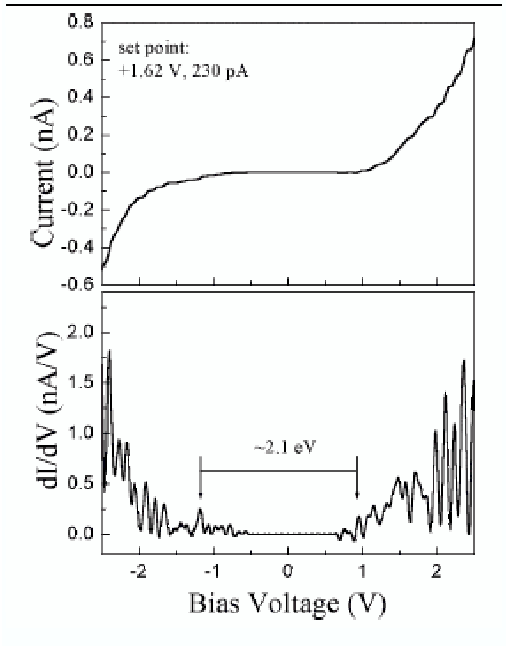

Figure 3.49.: I/V and di/dV curves for ultrathin films of CuPc deposited on Au(111) (from [Xu02]).

distance, resulting in the weaker metal-molecule interaction. Remarkably, the position of the CNL is almost unaffected, changing by less than 0.1 eV. The S parameter, on the other hand, reflects the change in d more strongly, resulting in the value S = 0.39.

The use of this value for S in equation 3.32 results in a lower pinning behavior, yielding a smaller dipole magnitude Δ = 0.8 eV and a Fermi level closer to the HOMO center (E_F - HOMO = 1.19 eV, or E_F = -4.51 eV from vacuum). Since the interface is less pinning, the Fermi level can more freely within the gap, giving rise to a lower E_F - HOMO offset. The lower screening at the interface also results in a lower induced dipole. The experimental Fermi level position, however, points in the direction of stronger pinning closer to the CNL, yielding larger E_F - HOMO offsets.

The results for Au/CuPc interfaces are puzzling, since, on one hand, experiments

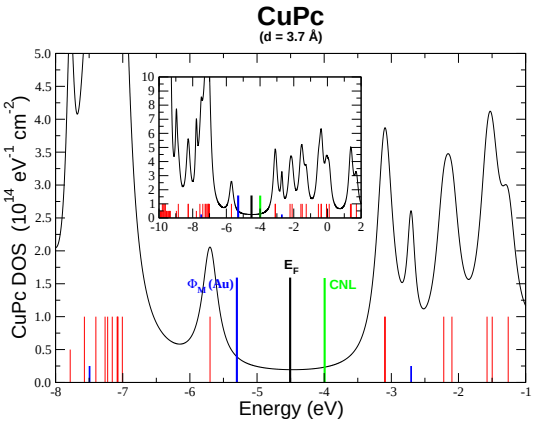

Figure 3.50.: Same as Fig. 3.47 for d = 3.7 Å. The weaker interaction with the substrate is shown in the well-defined peaks. The CNL position, remarkably, is almost unchanged, while the weaker pinning results in a Fermi level position further away from the CNL.

seem to indicate little interaction with the metal substrate, while our results for large (d = 3.7 Å) distances yield a better agreement in the dipole (which increases with a smaller S) but 'underpin' the Fermi level. A 'compromise value' of d $\sim$ 3.6 Å is taken, as will be commented on below, but in any case further theoretical work is needed.

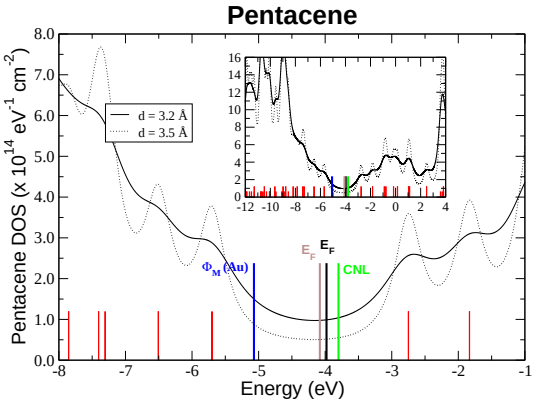

Figure 3.51.: Induced DOS for the Au/Pentacene interface calculated for two metal-organic distances, d. Also shown are the CNL position, work function (taken from Ref. [Schroeder02] and Fermi level position for 3.2 Å (black) and 3.5 Å (grey) distances.

3.12. Au/Pentacene

Pentacene is a widely-studied molecular solid and several experimental studies have been carried out. We have carried out calculations for the Au/Pentacene interface for two different distances d, 3.2 Å and 3.5 Å. Fig. 3.51 shows the electronic structure of the interface for both distances. The integration of this induced DOS yields a CNL position of CNL = -3.8 eV (the difference between both CNL positions is 0.02 eV). The calculation of the S parameter, using the area A = 84.04 Å^2 from Ref. [Schroeder02], gives the theoretical values of S = 0.14 for d = 3.2 Å and S = 0.22 for d = 3.5 Å.

Experimentally, since the adsorption geometry depends strongly on the growth conditions, Pentacene has been reported to lie flat at the surface [Schroeder02] or to be deposited almost vertically on the metal surface [Tsiper03]. In our calculations, we are considering the molecules to be deposited parallel to the metal surface. Thus, comparison with experiment can be obscured by the particular adsorption geometry, which is not known. The comparison of our results with experiment must take into account the particular value of ϕ_M and organic ionization energy (IE) that is measured experimentally. These typically vary by a few tenths of an eV due to growth conditions. In the case of the metal work function, the figures depend on the face of the metal or whether the substrate is polycrystalline, and on

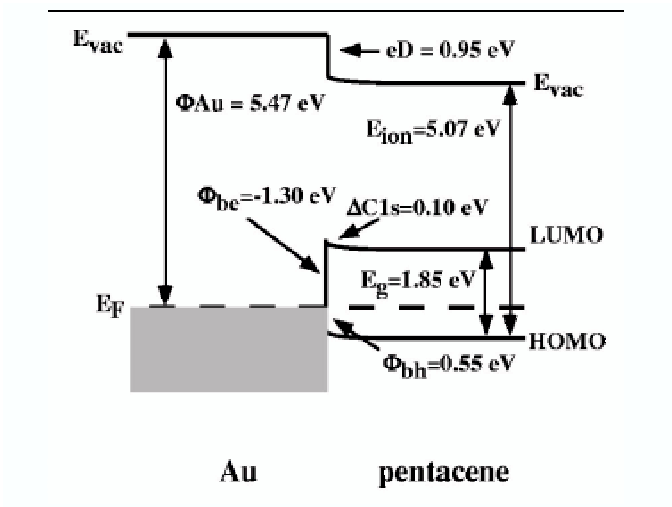

Figure 3.52.: Energy levels for the Au/Pentacene interface, showing a large interface dipole. Figure from Ref. [Schroeder02].

possible contamination.

We first compare with the results reported in Ref. [Schroeder02], where the values of ϕ_M = -5.47 eV and an ionization energy for Pentacene of IE = -5.07 eV. Our calculations yield a hole injection barrier of ϕ_{Bh} = 1.04 eV for d = 3.2 Å and ϕ_{Bh} = 0.90 eV for d = 3.5 Å, corresponding to Fermi level positions of E_F = -4.03 and -4.17 eV, respectively. Experimentally, a value of ϕ_{Bh} = 1.05 eV with respect to the HOMO center is reported (Fig. 3.52). For the interface dipole, we obtain Δ_{th} = 1.44 and 1.30 eV for d = 3.2 and 3.5 Å respectively, larger than the measured value of Δ_{exp} = 0.95 eV.

Gao and coworkers [Watkins02] reported an energy level diagram as shown in Fig. 3.53, where the relevant interface is the one on the left, which corresponds to the deposition of Pentacene on Au (the right-hand interface is for Au on Pentacene). The values for the Au work function and ionization energy are ϕ_M = -5.4 eV and IE = -4.9 eV. Using these values results in a Fermi level position and hole injection barriers of E_F = -4.02 eV and ϕ_{Bh} = 1.34 eV for the closest distance, and E_F = -4.15 eV and ϕ_{Bh} = 1.25 eV for d = 3.5 Å. This is to be compared to ϕ_{Bh}(exp) $\simeq$ 1.0 eV (with respect to the HOMO center). As for the interface dipole, our calculations yield Δ_{th} = 0.88 and 1.25 eV for d = 3.2 and 3.5 Å respectively, while the measured value is

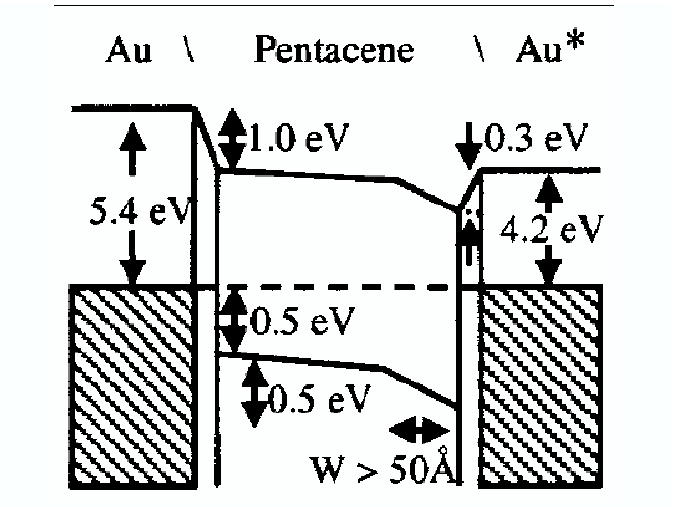

Figure 3.53.: Energy level diagram for the Au/Pentacene interface. The left interface corresponds to Pentacene on Au and is the one used for comparison. The Au-on-Pentacene interface (right) yields slightly different values but is more troublesome to interpret due to interdiffusion and band bending. Figure from Ref. [Watkins02].

Δ_{exp} = 1.0 eV.

Koch *et al.* [Koch03] have reported results with a similar value for the dipole, but with a higher hole injection barrier (Fig. 3.54). Their values of ϕ_M = -5.4 eV and IE = -5.7 eV (much higher than the value reported in Ref. [Watkins02]), together with our calculated values of the CNL and S, yield a Fermi level position of E_F = -4.02 eV and E_F = -4.15 eV for 3.2 and 3.5 Å respectively, as before. However, the different ionization energy results in higher hole injection barriers, ϕ_{Bh} = 1.68 eV and 1.55 eV for the shorter and larger distance, to be compared with the reported experimental value of ϕ_{Bh} (exp) = 1.35 eV. The theoretical interface dipole overestimates the experimental value, since our calculations yield Δ_{th} = 1.38 and 1.25 eV for d = 3.2 and 3.5 Å respectively, whereas the experimental value is Δ_{exp} = 1.05 eV.

A recent study of the Au/Pentacene interface [Amy05] reports smaller values both for the hole injection barrier and for the interface dipole (Fig. 3.55). The authors' careful analysis of the energy levels, both in the bulk and at the interface, reveals that the gap is somewhat smaller than previously reported [Shen01b]. In principle, this would imply a stronger pinning within our model, with a larger value for the dipole. Instead, the reported values of Δ_{exp} = 0.6 eV and ϕ_{Bh} (exp) =

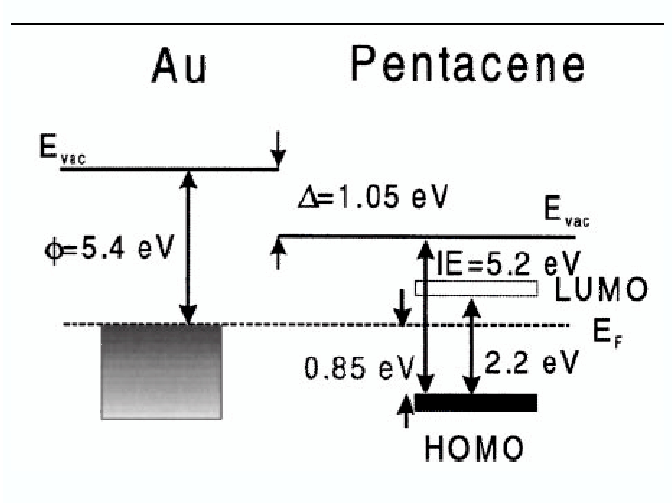

Figure 3.54.: Experimental energy level diagram for the Au/Pentacene interface determined from UPS measurements (from Ref. [Koch03]). Notice that the values refer to HOMO and LUMO edges.

0.97 eV are somewhat puzzling. Our calculations, using the measured values ϕ_M = -5.05 eV and IE = -5.5 eV, yield hole injection barriers of ϕ_{Bh} = 1.53 and 1.43 eV for d = 3.2 and 3.5 Å respectively, much larger than experiment. Concerning the dipole, our values of Δ_{th} = 1.08 and 0.98 eV (d = 3.2 and 3.5 Å) are in both cases much larger than the experimental value. In fact, our calculated results seem to be consistent with a shift of the Pentacene spectrum, since a $\sim$ 0.4 eV shift of the experimental levels towards the vacuum level would result in a similar increase both in ϕ_{Bh} and Δ, in almost perfect match with our results. However, the experimental results are what they are, and the agreement with our results is unfortunately not too good.

The above results are summarized in Table 3.4, which takes into account the different values of the metal work function and organic ionization affinity that have been measured experimentally.

Table 3.4 shows that an analysis of the results for the Au/Pentacene is not simple. In the first case of Table 3.4, the hole injection barrier is in good agreement with experiment, but the dipole is overestimated. For the other cases, our results would improve with a greater metal-Pentacene distance (both ϕ_{Bh} and Δ would decrease).

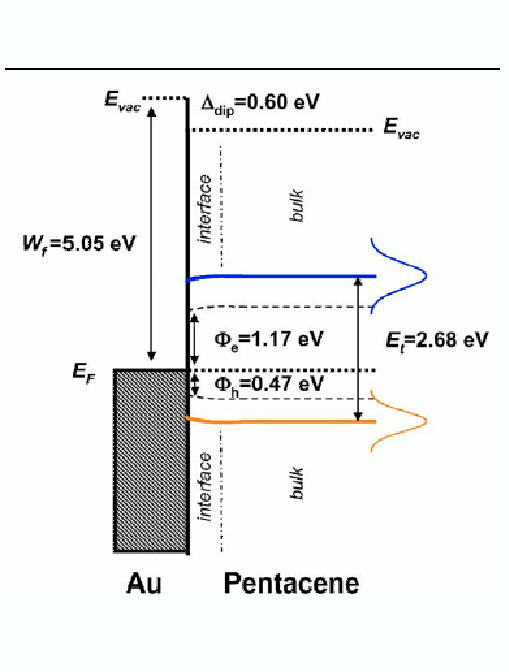

Figure 3.55.: UPS/IPES-derived energy level diagram, from Ref. [Amy05]. Notice the closing of the gap at the interface due to increased polarization effects, and the small values for the interface dipole and hole injection barrier.

In addition, the rather large dispersion found in the experimental values of ϕ_{Bh} and IE suggest that the energy level alignment is quite sensitive to the morphology of the interface, which in turn depends on the growth conditions. It has been proposed [Watkins02] that the adsorption geometry of Pentacene of gold is not flat, but with the short axis tilted $\sim$ 13 degrees with respect to the substrate, while keeping its long axis parallel to the surface.

This tilted geometry can be understood since possible geometrical deformations can disrupt the backbone of π orbital, becoming energetically 'costly'. Instead, the whole molecule is tilted (for instance, so as to maximize the interaction with a stepped metal substrate) while keeping the π molecular orbitals undisturbed. In any case, it seems clear from the numerous experimental studies that the details of the interface morphology affect quite substantially the energy level alignment.

In summary, our results for Au/Pentacene show a reasonable general agreement

	d = 3.2 Å	d = 3.5 Å	Exp.
ϕ_{Bh}	1.04	0.90	1.05 [Schroeder02]
Δ	1.44	1.30	0.95 [Schroeder02]
ϕ_{Bh}	1.38	1.25	1.0 [Watkins02]
Δ	1.38	1.25	1.0 [Watkins02]
ϕ_{Bh}	1.68	1.55	1.35 [Koch03]
Δ	1.38	1.25	1.05 [Koch03]
ϕ_{Bh}	1.53	1.43	0.97 [Amy05]
Δ	1.08	0.98	0.60 [Amy05]

Table 3.4.: Comparison between theoretical and experimental hole injection barrier and interface dipoles. In each case, the corresponding values of the metal work function and organic ionization energy have been used in the calculations.

with experiment, but without the lack of a detailed knowledge of the geometry of the interface as input to our calculations limits the accuracy of our results.

3.13. Molecular distortions

In our discussion, we have assumed the molecule to present no geometrical distortion when deposited flat on the metal. Recent DFT calculations for organic molecules adsorbed on metals [Öström03] show non-negligible bond-length changes (e.g., the C–C bond in an octane molecule adsorbed on Cu(110) is shortened by $\sim$ 0.04 Å. In addition, geometrical deformations have been measured experimentally for F_{16}CuPc molecules on Ag(111) and Cu(111) surfaces [Gerlach05]. In these cases, the electronegative F atoms move away and the molecule 'bends' away from the metal surface. It can be argued that, given the linear geometry of the alkanes, their geometrical distortions are probably larger than the ones in PTCDA on Au(111). For the F_{16}CuPc case, the phthalocyanine carbon 'backbone' is not significantly disrupted, making it difficult to judge whether changes in the molecular orbitals near the gap will be affected.

Nevertheless, we explored the sensitivity of our results to geometrical distortions by changing some of the molecular bond lengths. We analyzed how the deformation of the molecular C–C and C–O bonds modify the position of the CNL and the LDOS. Our calculations indicate that the CNL shifts by 0.1 eV for a change of 0.1 Å of the carboxyl C–C bonds and by $\sim$ 0.07 for a 0.1 Å change in the C–O bonds, while in all cases the LDOS around the CNL is practically unaltered. Thus,

we conclude that the CNL undergoes only minor changes due to the molecular deformation, and that the LDOS is not significantly modified. The CNL shift due to molecular distortions can be estimated by realizing that the weaker single C–C bonds are probably going to suffer the largest deformation. In the case of the alkanes, these distortions are $\sim$ 0.05 Å [Öström03]. This suggests that the accuracy in our calculated CNL, neglecting molecular deformations, is better than 0.1 eV.

3.14. Summary

The above results for the different interfaces can be summarized in the following tables, where a comparison with experimental data is presented. Some of these results have been slightly modified with respect to previously published values in light of new data [Wan05, Gao03a, Knupfer]. Moreover, given the good agreement found with experiment, and the similar agreement found for organic/organic interfaces (as will be seen in the next chapter), we consider them to be the most robust and 'up to date' values.

We have taken S = 0.16 for Au/PTCDA and Au/PTCBI, as result from our calculations for a metal-organic distance d of 3.2 Å, and S = 0.5 for Au/CBP, which results from our model for d = 3.5 Å. For CuPc/Au, our choice of S = 0.3 ($d \sim$ 3.6 Å) needs to be commented on. Experimental studies [Peisert02, Knupfer] seem to indicate that the molecular level broadening stems from intermolecular interactions, and that the interaction with the Au substrate is weaker than predicted by our model [Vázquez05b] (where a value d = 3.2 Å was taken), which would result in narrower CuPc peaks at the interface, and a larger value of S (and possibly d). Considering all this information, we have taken a larger value of S, S = 0.3, which is in better agreement with the reported experimental findings. Finally, for Au/Pentacene, although the details of the interface have not been properly take into account, as described above, the value of S = 0.22, which corresponds to a weaker interaction with the substrate, gives a better agreement with experiment. It must be stressed that these values for the S parameter for the interface with Au, S_{Au}, are similar, but not exactly equal, to those determined experimentally by fitting the Fermi level positions over a range of different metals (see Fig. 3.2). Interestingly, we find $S_{Au} \lesssim S_{MO}$, where the latter value is this fit over several reactive and unreactive interfaces, although the reasons for this are unclear at the moment. However, notice that the tendency, or relative values between S_{Au} and S (over different metals) is maintained.

	-CNL	-IE	$-\phi_M$	S_{Au} (th.)
PTCDA	4.8	7.3 (6.8)	5.1	0.16
PTCBI	4.4	6.7 (6.2)	5.0	0.16
CBP	4.05	6.8 (6.3)	4.9	0.50
CuPc	4.0	5.7 (5.2)	5.3	0.30
Pentacene	3.8	5.07 (4.57)	5.47	0.22
	3.8	5.4 (4.9)	5.4	0.22
	3.8	5.7 (5.2)	5.4	0.22
	3.8	5.5 (5.0)	5.05	0.22

Table 3.5.: CNL position, HOMO center (edge) and metal work function in eV ([Hill98c, Hill00d, Hill98b, Peisert02, Schroeder02, Watkins02, Koch03, Amy05]), with respect to the vacuum level, as well as theoretical values of the S_{Au} parameter used in the calculations.

Table 3.5 shows CNLs and S parameters for the organic materials considered, while 3.6 compares the theoretical and experimental values of the interface dipole Δ and hole injection barrier ϕ_{Bh} using these values. Notice the good agreement with experiment, except perhaps for Au/Pentacene, of the theoretical values, calculated with no aid from external parameters. The agreement in Δ and ϕ_{Bh} is in most cases within 0.1 eV, and the calculated S_{Au} are not necessarily equal though certainly compatible with experimental values derived from a range of several reactive and non-reactive interfaces (Fig. 3.2).

	Δ (th.)	Δ (exp.)	ϕ_{Bh} (th.)	ϕ_{Bh} (exp.)
PTCDA	0.25	0.2	2.45	2.40
PTCBI	0.50	0.4	2.20	2.10
CBP	0.43	0.5	2.33	2.40
CuPc	0.91	1.2	1.31	1.60
Pentacene	0.90	1.05	1.30	0.95
	1.25	1.0	1.25	1.0
	1.55	1.35	1.25	1.05
	1.43	0.97	0.98	0.60

Table 3.6.: Comparison between theoretical and experimental ([Hill98c, Hill00d, Hill98b, Peisert02, Schroeder02, Watkins02, Koch03, Amy05]) interface dipoles and hole injection barriers are given using the data shown in Table 3.5. All energies are given in eV.

	S_{Au} (th.)	S (exp.) [Shen01b]
Au/PTCDA	0.16	0.0
Au/PTCBI	0.16	0.0
Au/CBP	0.50	0.6
Au/CuPc	0.33	0.25
Au/Pentacene	0.22	0.37

Table 3.7.: Comparison between the theoretical S parameters used in the calculations for the interfaces with gold, S_{Au}, and the values determined experimentally from a fit over several reactive and unreactive interfaces.

Notice that for the first three interfaces the agreement in both the dipole and injection barrier is very good, within the experimental uncertainty of ~ 0.1 eV, while for the last two interfaces, the lack of a detailed description of the interface results in a greater discrepancy with experiment. This suggests that, while the pinning behaviour is correctly described in all cases, more theoretical work or more experimental input, currently unavailable, is needed for a better quantitative agreement.

In addition, note the scatter in the work function determined experimentally: values ranging from -4.9 eV to -5.4 eV have been reported, as quoted above. Issues such as the face of the metal, the crystallinity of the substrate clearly affect the measured values of ϕ_M and thus affect the comparison with our theoretical results. Recently, the effect of contamination of the metal surface was investigated [Wan05]. It was found that contamination by C and O can profundly affect the energy level diagram: the value of ϕ_M is reduced by 0.7 eV, the hole injection barrier can vary in ~ 0.4 eV, and the induced dipole can change by as much as 1 eV. This effect, not discussed explicitly in the experimental works quoted above, can be present and can therefore obscure the comparison of theoretical and experimental results.

Concerning the values used for the S parameter, S_{Au}, these are specific for the case of gold and are similar, though not equal, to those obtained experimentally from a fit of the Fermi level position over a range of several reactive and unreactive metals [Shen01b]. This is summarized in Table 3.7. As mentioned before, we find $S_{Au} \lesssim S$, where the latter is the experimental fit. This suggests, perhaps counterintuitively, that chemical reactions ultimately result in a larger Fermi level movement in the gap and thus a larger value of S, although in lack of any detailed information about the details of the interface this is highly speculative and the reasons for this relation are unclear at the moment.

	S_{Au}	Δ (th.)	Δ (exp.)	ϕ_{Bh} (th.)	ϕ_{Bh} (exp.)
α-NPD	0.33	0.70	0.86	1.31	1.74
Alq_3	0.58	0.65	0.68	1.75	1.75
BCP	0.42	—	—	—	—

Table 3.8.: Theoretical and experimental interface dipoles and hole injection barriers for Au/organic interfaces, for those materials for which their CNL position is deduced, as discussed in the text (all energies in eV).

In addition, we include here the CNL of several organic materials whose interfaces with Au have not been calculated, but which will appear in Chapter 4 when dealing with organic/organic interfaces. The CNL of these materials was obtained from a fit to experimental data [Hill00c], once the calculated CNLs of PTCDA, PTCBI, CBP and CuPc were fixed. The resulting CNL positions and S parameters enable the calculation of the corresponding interface dipoles and injection barriers in their interface with Au, as results from the **fitted** CNL positions. The results, summarized in Table 3.8, show that the calculated induced dipoles and hole injection barriers are in good agreement with metal/organic data. Thus, not only the fitted values, as expected, yield good agreement with experiment but so do the theoretical ones, calculated with no aid from external parameters.

At this point it is worth mentioning that the CNL position can be calculated using Greens' functions for the isolated molecule. This will be shown in Section 4.4, but suggests in any case that the CNL positions are almost intrinsic to the organic material, so that the fit of the CNL of these materials is likely to be very close to the calculated value, if this was done for the Au/organic case.

It is interesting to compare the values for S for metal/organic interfaces with those found at metal/*inorganic* semiconductor interfaces. Those materials with the lowest S_{Au} values (like PTCDA) have high induced DOS in the gap (the values for Au/PTCDA are $\sim 2 \times 10^{14}$ eV^{-1} cm^{-2}, comparable to IDIS calculated for *inorganic* semiconductors like Si or GaAs [Flores87]. On the other hand, materials exhibiting a less pinning behaviour like CBP have a lower induced DOS ($\sim 0.1 \times 10^{14}$ eV^{-1} cm^{-2}), as reflected in the larger value of S. Since the area A per associated with each molecule is 120 and 251 $Å^2$ for PTCDA and CBP, respectively, the DOS induced by each molecule (regardless of their area) is ~ 2.4 eV^{-1} for PTCDA and ~ 0.251 eV^{-1} for CBP, almost ten times less. This way, the pinning ability of the different organic

materials is clearly seen: each PTCDA induces a DOS which is much larger than than of CBP. If we consider that the area associated with each CBP molecule is twice that of PTCDA, the $D(E_F)/A$ ratio is clearly different for both materials. Since this quotient directly enters the definition of S (equation 3.31), it is easy to see how the induced DOS and pinning ability of both materials result in such different values of the S parameter. Of course, the induced DOS depends on the magnitude of the gap, which is smaller for PTCDA (3.2 eV) than for CBP (4.6 eV), since the closer the HOMO and LUMO are, the larger the DOS in the gap when these states are broadened. In addition, the metal-organic distance d also enters the definition of S and, though by no means negligible, it does not affect the final value of S so much.

In summary, while, in general, the values of S in metal/organic interfaces are larger than for *inorganic* semiconductors and their pinning of the Fermi level is weaker, the organic materials with the highest pinning behaviour have induced DOS and values of S comparable to the inorganics.

3.15. Conclusions

To summarize, we have analyzed the energy level alignment at several metal/organic interfaces by calculating the DOS that is induced in the organic energy gap. This induced DOS enables the calculation of a CNL, which we propose acts as an effective Fermi level for the organic material. Its partial alignment with the metal work function gives rise to charge transfer between both systems, which induces a dipole at the interface, tending to align the CNL and the metal work function.

Theoretical results for the slope parameter, induced dipole and interface Fermi level are in good agreement with experimental data for non-reactive interfaces, and the pinning behavior of the different interfaces has been discussed and correctly described. The direction of the dipole is always correct: since Au has a large work function ϕ_M = -4.9 – -5.5 eV, charge is transferred from the organic molecule to the metal, while the magnitude of the interface dipole is in good agreement with experiment. Hole injection barriers, too, are found to agree well with experimental findings.

After the discussion of S_{Au} and its relation to the values determined experimentally from a fit over various reactive and unreactive interfaces, it is clear that, while S depends rather strongly on the metal-organic distance, one of the main assumptions in our model, this is not the case for the CNL. The position of the CNL in the gap is almost unchanged with respect to substrate-induced molecular deforma-

tions or with respect to the interaction strength. Our calculations indicate that the CNL position does not change by more than 0.1 eV for strong bond deformations, and variations in the molecular level broadenings leave the CNL position almost unchanged. This shows that the CNL is a robust quantity, nearly independent on the details of the interaction.

Our model analyzes the energy level alignment in terms of the DOS induced at the interface and the (stronger or weaker) pinning of the Fermi level near the CNL. The central quantity in our approach is, clearly, the CNL. Beyond the limitations of our calculation of the CNL (such as the assumptions in the model, or that the CNL position ultimately depends on values for the ionization energy that have an experimental uncertainty [Tadayyon04]), the position of the CNL is an absolute quantity. It acts as an effective Fermi level for the organic material, determining whether and in which direction charge will be transferred at the interface, making the model **predictive**.

Since it is likely that several mechanisms are operating simultaneously at the interface, it is interesting to see how these can be incorporated into our formalism. In the case of the reduction of the metal work function by the adsorbed molecules (the 'pillow' effect), this can be introduced (at least phenomenologically) as a reduction in the initial value of ϕ_M. Concerning chemisorption, the results presented here apply to non-reactive interfaces, but the approach for reactive ones is similar: the calculation of the interface electronic structure yields charge transfer and gap states (in this case, chemistry-induced), which are responsible of the pinning of the Fermi level. Thus, the formulation of our model is general and can incorporate or describe these other mechanisms.

At reactive metal-organic interfaces, where the interaction is strong, the states induced in the organic gap should be calculated for each particular interface. But even though the results presented here, such as CNL positions, are not strictly applicable in those cases, the fact that the Fermi level is completely pinned for PTCDA or PTCBI on **all** metals **at the same energy position** suggests a preferred energy position, characteristic of the organic material, and that the particular shape of the induced DOS does not greatly affect the position of the CNL. Thus, for these materials, there is already a high 'intrinsic' pinning at the unreactive interface, and the existence of defects or chemical reaction does not greatly modify this behaviour. For other materials, like CBP, the 'intrinsic' pinning is weaker, and other mechanisms,

if present, will have a greater effect on the energy level alignment.

To summarize, while chemical reaction or interdiffusion are present in many interfaces and their importance is obvious, their often complex behaviour can, in fact, obscure the understanding of the mechanisms taking place. Our aim has been to focus on the **opposite** class of interfaces: free of the complexity of chemical reaction or defects, the study of unreactive, 'ideal' junctions focuses on a more fundamental behaviour, present in all interfaces, and can unveil, in a consistent and predictive manner, the basic mechanisms governing the Schottky barrier formation and the energy level alignment.

CHAPTER 4

Organic/organic interfaces

Who are you going to believe,
me or your own eyes?

(Groucho Marx)

4.1. Introduction to Organic/Organic interfaces.

The efficiency of organic-based devices is often determined by the performance at the interface. Thus, organic heterojunctions have become the focus of considerable attention in recent years. In these devices, electron-hole recombination or separation takes place at or near interfaces between electron and hole transport layers. Creating structures with the desired electron and hole injection barriers is necessary for maximizing the performance of the device, such as confining electrons or holes to particular layers, or enhancing recombination, for instance. All of these depend on the molecular level offsets when the interface is formed.

A detailed understanding of the energy level alignment at these heterojunctions is thus essential for the control and optimization of these organic-based devices, as well as from a fundamental point of view.

4.2. Organic heterojunctions

In order to determine molecular level offsets and injection barriers, a study of the energy level alignment at organic/organic interfaces is necessary.

Experimental studies [Hill00c, Hill98a, Rajagopal98] reveal a somewhat contradictory situation: **in most cases**, the vacuum level rule is followed within experimental resolution, by which the vacuum levels of the two organic materials simply align at the interface. In some cases, however, **a significant dipole** (up to 0.5 eV) is observed at the interface. In addition, a series of recent experiments [Gao01,Gao03b,Gao02,Kahn06] when one of the materials is p-doped have revealed the appearance of a large (0.5 – 0.9 eV) interface dipoles upon doping. Up to now, no consistent explanation of these data has been put forward, and the energy level alignment at organic/organic interfaces remains an open problem.

Let us first restrict our analysis to the case of undoped organic heterojunctions. The experimental situation is summarized in Fig. 4.1.

As has been mentioned, most interfaces exhibit little or no interface dipoles, following the vacuum level rule. This is perhaps not too surprising, considering that both semiconductors are made up of closed-shell molecules, and chemical reaction or indeed a strong chemical interaction between them is not expected.

At the same time, notable exceptions to this rule exist, such as the CuPc/PTCDA (Δ=0.4 eV), PTCDA/Alq_3 (Δ=-0.5 eV) or BCP/PTCBI (Δ=0.4 eV) interfaces (Fig. 4.1). The reasons for the appearance of such large dipoles are unclear. It has been

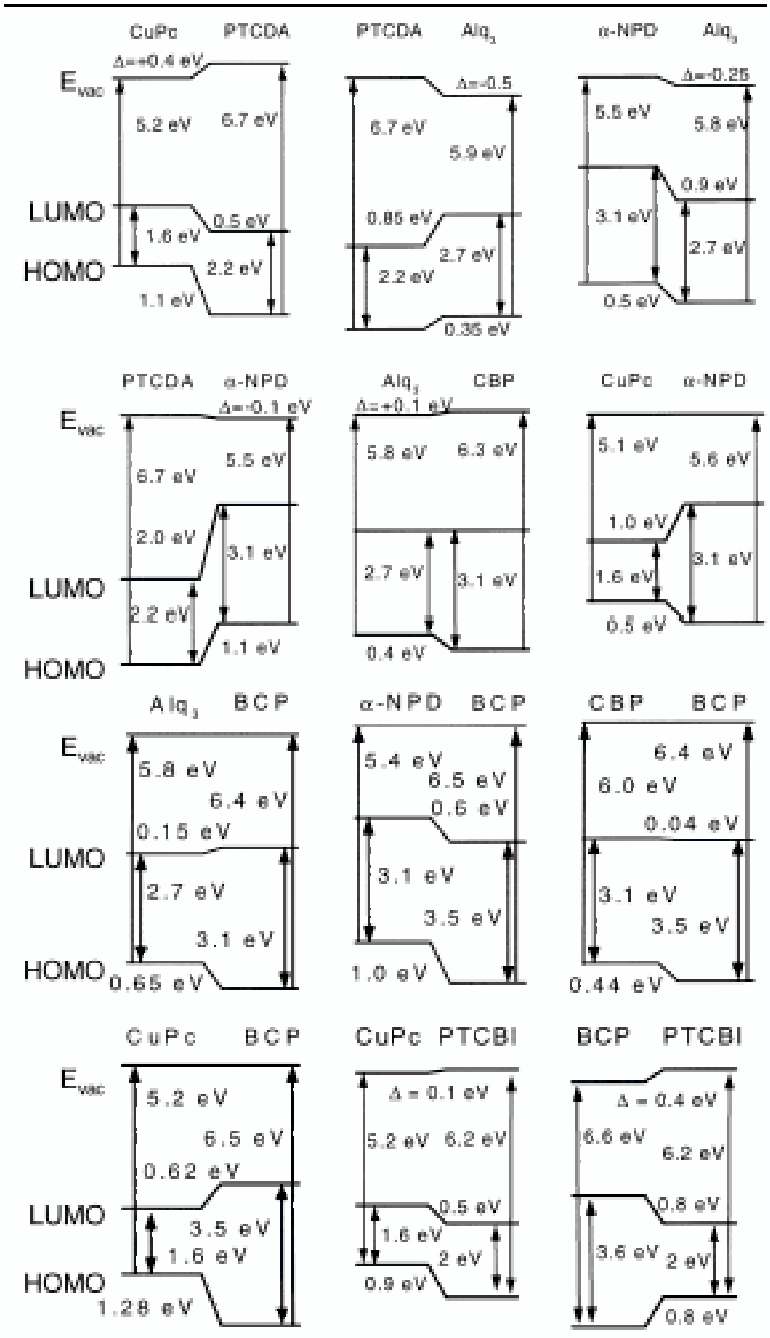

Figure 4.1.: Experimental energy level diagram and molecular band offsets at several organic heterojunctions, from Ref. [Hill00c]. Notice that the LUMO positions are derived by adding the optical gaps to the HOMO energies.

suggested [Ishii99] that the appearance of dipoles is to be expected at interfaces between donor and acceptor materials, as in the CuPc/PTCDA or PTCDA/Alq_3 interfaces. However, this argument, as pointed out by the authors, would predict a dipole at the PTCDA/α-NPD interface, whereas a small Δ = -0.1 eV value is observed.

Clearly, the large negative values for the PTCDA HOMO and LUMO make this material an electron acceptor, but this distinction is not straightforward for other semiconductors. From the HOMO and LUMO positions of the materials shown in Fig. 4.1 it is not easy to predict the direction of charge transfer.

It is not straightforward to correlate the sign or magnitude of the observed dipoles with the relative positions of the HOMOs of the materials shown in Fig. 4.1. Large differences in the HOMO positions before the interface is formed could give rise to dipoles at the interface. The material with the lower (more negative) HOMO position could be considered as the electron acceptor, thereby raising its vacuum level with respect to the other material, as is the case of PTCDA in the CuPc/PTCDA or PTCDA/Alq_3 interfaces, or Alq_3 in the α-NPD/Alq_3 case. But this argument breaks down in the many cases where initial HOMO offsets are large, but zero or negligible dipoles are detected (α-NPD/BCP, CuPc/BCP or, notably, PTCDA/α-NPD). In addition, the opposite of the above argument's prediction is observed at the BCP/PTCBI interface, where the vacuum level of the material with the most negative initial HOMO position (BCP) is lowered, not raised.

If Fig. 4.1 is analyzed from the point of view of considering the initial differences between the HOMO of one material and the LUMO of the other one, then large barriers are found, like 0.7, 1.4, 3.4 or 1.0 eV for the CuPc/PTCDA, PTCDA/Alq_3, α-NPD/Alq_3 and PTCDA/α-NPD interfaces, respectively.

4.3. Charge Neutrality Levels

The previous analysis suggests that the molecular level offset at organic heterojunctions is not easily predicted from the relative positions of the HOMO or LUMO of the organic materials. How, then, can the energetics of organic heterojunctions be understood?

Since the energy level alignment at non-reactive metal/organic interfaces can be successfully described within the induced DOS and CNL scenario, and given the weak interaction at organic heterojunctions, we extend our analysis to organic/organic interfaces.

Our model for organic heterojunctions [Vázquez05b] extends our previous arguments and proposes to consider the CNLs as the organic 'effective' Fermi or electronegativity levels. This implies that the CNLs, calculated for metal/organic interfaces, are an **intrinsic** property of the organic material and can be used to analyze organic heterojunctions. Although, strictly speaking, this should be confirmed by specific calculations of the different organic/organic interfaces, the validity of this assumption in our model is supported by the insensitivity of the CNL at metal/organic interfaces, together with the good agreement of our results with experiment.

We propose that the energy level alignment at organic heterojunctions is governed by the partial alignment of the CNLs of the two organic materials: the initial relative position of the CNLs of the two organic materials determines how charge is transferred between them. This energy difference gives rise to charge transfer between the two organic semiconductors. This creates an interface dipole, which tends to reduce the initial CNL difference.

The position of the CNL of several organic materials is shown in Fig. 4.2 and Table 4.1. As was mentioned in Section 3.14, whereas the values for the first four organic materials was calculated as described in the previous chapter, the latter three were deduced from the best fit to experimental data ([Hill00c], Fig. 4.1), once the calculated CNLs of PTCDA, PTCBI, CBP and CuPc are fixed. For these materials, their CNL positions result in good agreement with experiment when their interfaces with Au, using the fitted CNLs, are considered. In addition, the results of the following Section (4.4) show that the dependence of the CNL position on the details of the interaction is very weak, so that the CNL depends, on these weakly-interacting interfaces, almost solely on the molecular electronic structure. In light of the good agreement with experiment, this suggests that the fitted CNLs for these materials is probably very close to true value is this was calculated.

Within our model, therefore, the energy level offset is determined by the tendency of the CNLs of the organic materials to align.

4.4. Charge Neutrality Levels and branch points

So far, the CNLs have been calculated by integrating the induced DOS obtained by the broadening of the molecular levels due to the interaction with the metal surface.

In search of a definition of the CNL as an **intrinsic** property of the organic material, however, the property that the CNL coincides with the branch point of the

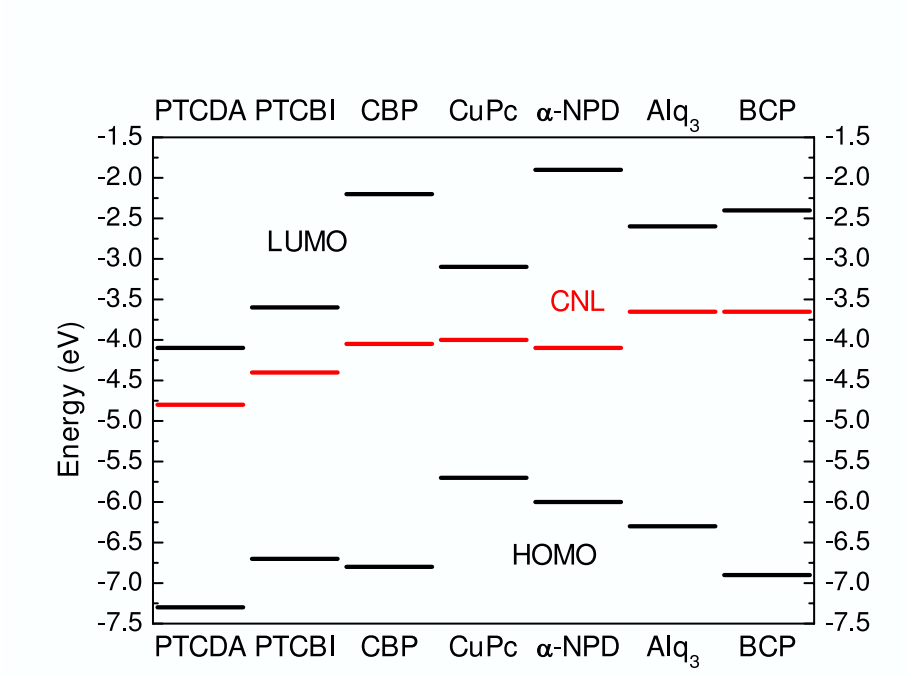

Figure 4.2.: HOMO, LUMO and CNL (grey) positions for the organic materials considered in this section. The values for the latter three materials have been fitted to experiment, as discussed in the text.

	-CNL (eV)	-IE (eV)	CNL-IE (eV)
PTCDA	4.8	7.3 (6.8)	2.5
PTCBI	4.4	6.7 (6.2)	2.3
CBP	4.05	6.8 (6.3)	2.75
CuPc	4.0	5.7 (5.2)	1.7
α-NPD	4.1	6.0 (5.5)	1.9
BCP	3.65	6.9 (6.4)	3.25
Alq_3	3.65	6.3 (5.8)	2.65

Table 4.1.: Charge Neutrality Level (CNL) (with respect to the vacuum level), and ionization energy (IE) center (peak) positions for various organic materials. The CNLs of the bottom three compounds are deduced, as discussed in the text.

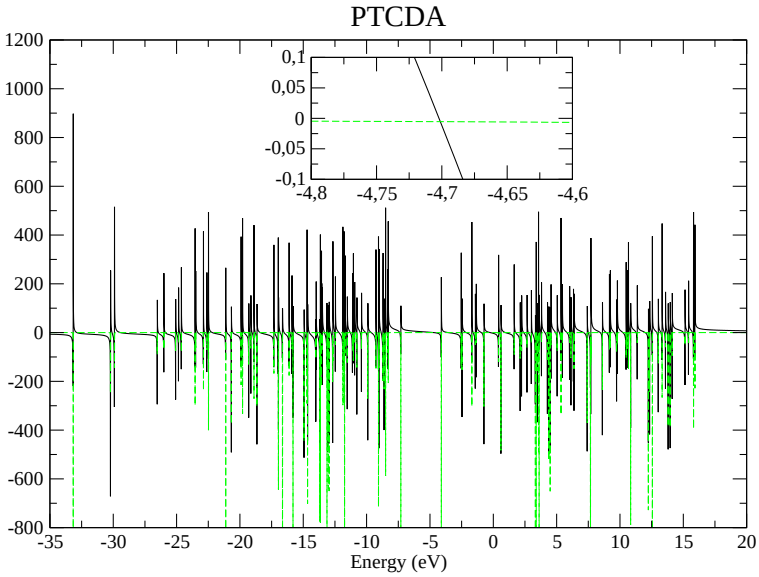

Figure 4.3.: Real (black, continuous line) and imaginary (grey, dashed line) parts of the molecular Green's function for PTCDA. The inset shows the point at which Re (G) = 0 within the gap, which coincides with the CNL of the material.

material's Green's function [Tersoff84] is useful.

The calculation of the molecular Green's function is straightforward, since their electronic spectrum has already been calculated using DFT-based methods. Thus, in the basis of the molecular eigenstates, the molecular Hamiltonian is diagonal and the Green's function is simply

$$G(E) = \frac{1}{E - H + i\eta} = \sum_i \frac{1}{E - E_i + i\eta}, \tag{4.1}$$

where E_i are the molecular levels or eigenvalues.

Since the real part of the Green's function becomes zero at these branch points, by plotting the real and imaginary part of G for the different molecules, the CNL can be determined. It is important to mention that the Hamiltonian used here is not the DFT Hamiltonian, since this yields a very small gap, as noted before, but the spectrum with the appropriate value for the gap, with the value at the interface.

This is shown in Fig. 4.3 for the case of PTCDA.

The figure, as well as those for the other materials, shown the real part (black,

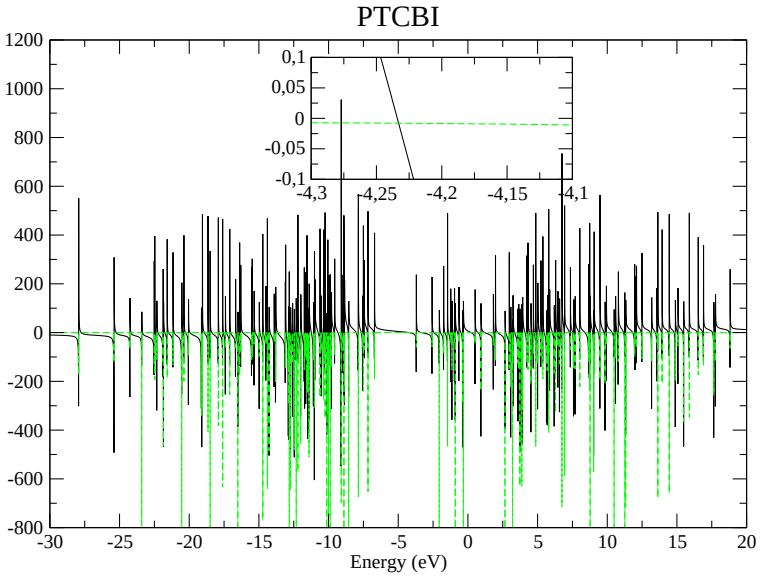

Figure 4.4.: Real (black, continuous line) and imaginary (grey, dashed line) parts of the molecular Green's function for PTCBI. The inset shows the point at which Re (G) = 0 within the gap, which coincides with the CNL of the material.

continuous line) crossing the axis many times. The imaginary part (grey, dashed line) is always negative and its absolute value becomes very large when E = E_i; that is, at the zeros (poles) of the molecular Hamiltonian, when the energy coincides with that of a molecular level. The inset shows in detail the region in the gap where the real part of G becomes zero.

In our calculation of the Green's functions of the different materials, an energy step of 0.01 eV, and the value taken for η was 0.001. Notice that Im (G) is composed of the sum of the different contributions of the molecular levels. Each of these is a (very narrow) lorentzian function of width η, close to a delta function. The negative sign of the imaginary part ensures that the DOS is positive:

$$\rho(E) = -\frac{1}{\pi} Im[G(E)] \tag{4.2}$$

Notice that the values given by this calculation are slightly smaller (less negative) than the ones reported in the metal/organic case. For instance, in PTCDA the branch point is situated at -4.7 eV (Fig. 4.3), while for PTCBI is at -4.25 eV (Fig. 4.4) and $\sim$ 4 eV for CBP (Fig. 4.5). In the case of CuPc, the branch point is located near

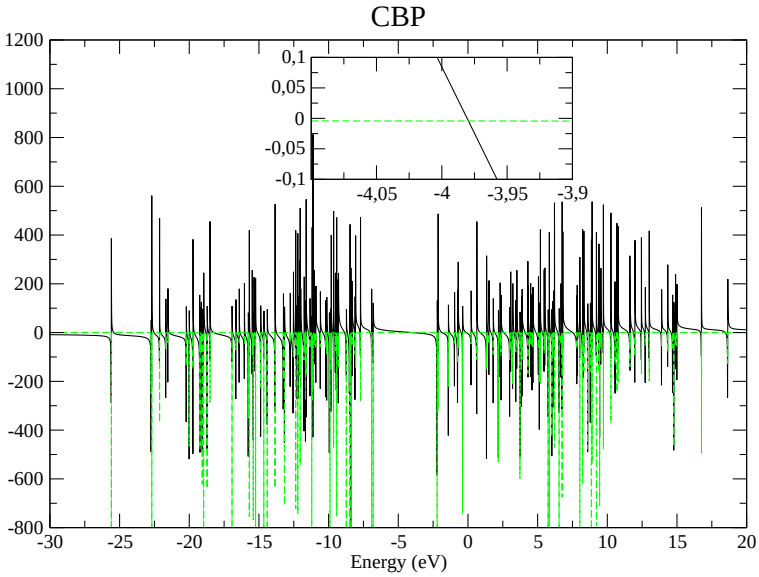

Figure 4.5.: Real (black, continuous line) and imaginary (grey, dashed line) parts of the molecular Green's function for CBP. The inset shows the point at which Re (G) = 0 within the gap, which coincides with the CNL of the material.

-3.85 eV (Fig. 4.6) and close to -3.65 for Pentacene (Fig. 4.7).

Since the offsets between the CNL positions calculated from the branch point and from the Au/organic interface are almost the same for all molecules, these offsets will have little effect on organic/organic interfaces, as they are mere shifts of similar quantities of both molecular spectra. When comparing with metal/organic interfaces, however, small differences may arise.

The comparison of these values with those derived from metal/organic interfaces shows a systematic difference: the CNLs obtained as branch points are always $\sim$ 0.1 – 0.2 eV less negative than the metal/organic ones. A reason for this can be the use of a minimal basis set for the description of the molecular electronic properties. The fact that a minimal basis set is used means that the Hilbert space is truncated early on, and that a large number of empty molecular states are neglected. We speculate that the inclusion of these states would push the CNL towards more negative energies. However, it is difficult to see why this effect is not seen in the Au/organic cases, while a more negative CNL position is obtained. Nevertheless, the good agreement between the CNLs calculated in these two different approaches shows the robustness of the results. Due to the use of a minimal basis, the CNL

values presented here should therefore be regarded as an upper bound, since the inclusion of additional basis functions would shift the CNLs towards more negative values, as commented above. Thus, it can be safely concluded the CNL positions are given by the values quoted in Chapter 3, while the ones presented here can be regarded both as an upper bound and as an indication of the accuracy of our approac

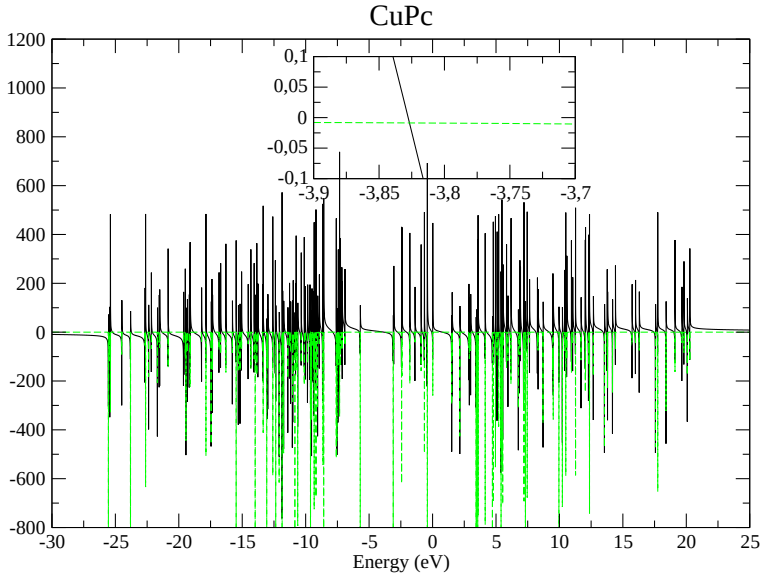

Figure 4.6.: Real (black, continuous line) and imaginary (grey, dashed line) parts of the molecular Green's function for CuPc. The inset shows the point at which Re (G) = 0 within the gap, which coincides with the CNL of the material.

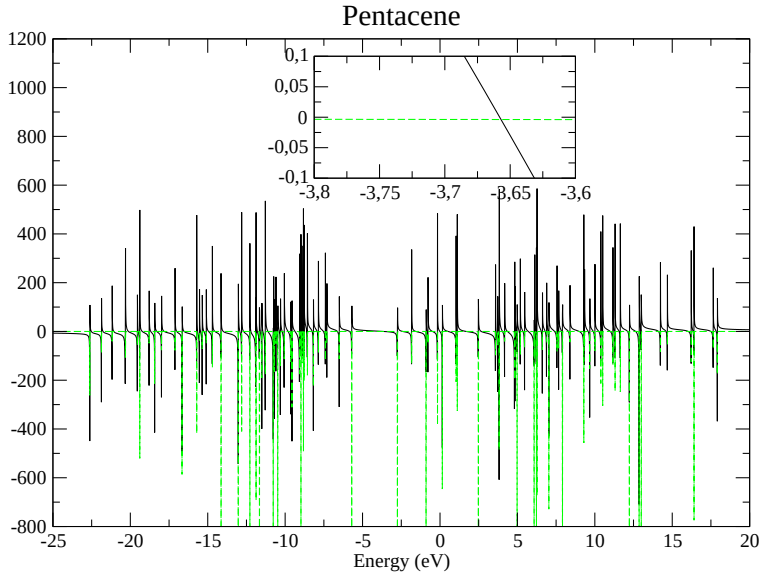

Figure 4.7.: Real (black, continuous line) and imaginary (grey, dashed line) parts of the molecular Green's function for Pentacene. The inset shows the point at which Re (G) = 0 within the gap, which coincides with the CNL of the material.

4.5. Screening at the interface

The initial CNL difference is partially screened at the interface when this is formed. This screening reflects the ability of the interface to 'equalize' the potentials given by the CNLs of both organic materials. To quantify these ideas, an interface screening parameter, S_{OO}, can be introduced. This is similar, though not equal, to the one used in metal/organic interfaces.

In principle, the screening ability of an organic material at the junction is described by its static dielectric function in the direction perpendicular to the interface, ϵ. The S parameter at organic heterojunctions therefore depends on the values of ϵ of its constituents. For metal/organic interfaces, S varies between 0 and $1/\epsilon$, depending on whether the screening takes place in the metal ($\epsilon_{metal} \rightarrow \infty$, $S \simeq 0$), or in the semiconductor ($S \simeq 1/\epsilon$) [Tersoff85]. For organic heterojunctions, a simple electrostatic argument, assuming that the potential offset is equally screened by each organic material, yields [Tersoff85]

$$S_{OO} = \frac{1}{2}\left(\frac{1}{\epsilon_1} + \frac{1}{\epsilon_2}\right). \tag{4.3}$$

The problem with the application of equation 4.3 is the lack of experimental data for ϵ_i. It is known that $\epsilon_{\perp}(PTCDA) \simeq 1.9$ [Shen97, Forrest97], but, to our knowledge, the values for other organic materials have not been measured. There are, however, ways to estimate or make an 'educated guess' of the values of ϵ in materials other than PTCDA.

We know, for instance, that (ϵ - 1) is inversely proportional to the square of the energy gap of the material [Ziman]:

$$\epsilon - 1 \sim \frac{1}{E_g^2}, \tag{4.4}$$

This suggests estimating ϵ_i using equation 4.4, by comparing the gaps of the organic materials relative to that of PTCDA.

Similarly, Mönch long ago verified the relation [Mönch96]:

$$\left(\frac{1}{S_{Au}} - 1\right) \sim (\epsilon - 1)^2, \tag{4.5}$$

where S_{Au} is the S parameter of the corresponding organic material in its interface with gold, described in the previous chapter.

	ϵ (E^{opt})	ϵ (E^{t})	ϵ (S_{Au})	E^{opt} (eV)	E^{t} (eV)	S_{Au}
PTCDA	1.9 [Shen97]	1.9 [Shen97]	1.9 [Shen97]	2.6	3.2	0.16
PTCBI	1.97	1.96	1.90	2.5	3.1	0.16
CBP	1.50	1.44	1.39	3.5	4.6	0.50
CuPc	2.52	2.36	1.60	2.0	2.6	0.30
α-NPD	1.50	1.46	1.56	3.5	4.5	0.33
BCP	1.40	1.38	1.46	3.9	4.9	0.42
Alq_3	1.63	1.44	1.33	3.1	4.6	0.58

Table 4.2.: Estimated values of ϵ for the different organic materials obtained using equation 4.4 with the peak-to-peak optical [Hill00c] and transport gaps, or using equation 4.5, relative to that of PTCDA.

Both equation 4.4 and 4.5 enable the calculation of ϵ for other materials relative to that of PTCDA. This is illustrated in Table 4.2.

The values of ϵ are given here with two decimal places in parentheses not to reflect the accuracy of the figure (which is of course smaller, since these values are **estimated** from equations 4.4 and 4.5), but to show that using E^{opt} or E^{t} yields very similar values of ϵ (equation 4.5, with its values of S_{Au}, yields slightly different results in some cases). Since the measured value of ϵ has one decimal, the accuracy of our estimated values is of course not greater than this.

With these values of ϵ, the S_{OO} parameters for the organic/organic interfaces considered in Fig. 4.1 can be calculated from equation 4.3 and are given in Table 4.3.

Again, the values calculated using the different values of ϵ yield very similar results for the S_{OO} parameter. It is interesting to look at the range of values of S_{OO} for the interfaces considered: the figures vary between 0.45 and 0.73. This is in contrast to *inorganic* semiconductor heterojunctions, where the delocalized nature of the semiconductor wavefunctions results in typical values of $S \sim 0.1$ [Flores87]. This means that screening at organic/organic interfaces is much weaker than in their inorganic counterparts: the large values of S, typically around 0.6, indicate that initial potential (CNL) offsets at organic heterojunctions will not be completely screened and that significant final CNL offsets will be found, in contrast with the inorganic case.

	S (E^{opt})	S (E^{t})	S (S_{Au})
CuPc/PTCDA	0.46	0.48	0.58
CuPc/PTCBI	0.45	0.47	0.58
CuPc/CBP	0.53	0.56	0.67
CuPc/α-NPD	0.53	0.55	0.63
PTCDA/Alq_3	0.57	0.61	0.64
PTCDA/α-NPD	0.60	0.61	0.58
BCP/Alq_3	0.66	0.71	0.72
BCP/CBP	0.69	0.71	0.70
BCP/PTCBI	0.61	0.62	0.61
BCP/α-NPD	0.69	0.70	0.66
Alq_3/α-NPD	0.64	0.69	0.70
Alq_3/CBP	0.64	0.69	0.73

Table 4.3.: Calculated values of the S_{OO} parameter using the values of ϵ estimated with the optical (left column) or transport (middle column) gaps, or from the values of S_{Au} (right column).

4.6. Partial CNL alignment

The theoretical values for the S_{OO} parameters enable the quantitative evaluation of the energy level alignment at the heterojunctions. Having determined the screening parameter, the CNL offset after the interface is formed is given by

$$(CNL_1 - CNL_2)_f = S_{OO}\ (CNL_1 - CNL_2)_i, \tag{4.6}$$

and the dipole induced at the interface is

$$\Delta = (1 - S_{OO})\ (CNL_1 - CNL_2)_i, \tag{4.7}$$

where subscripts i and f refer to initial and final conditions of the interface formation.

The energy level offset at the interface, in which the CNLs of both materials tend to align, is shown in Figure 4.8.

The initial CNL offset gives rise to charge being transferred when the interface is formed: the material with the higher (less negative) CNL donates electrons to the other material, thereby giving rise to a dipole at the interface. This dipole shifts

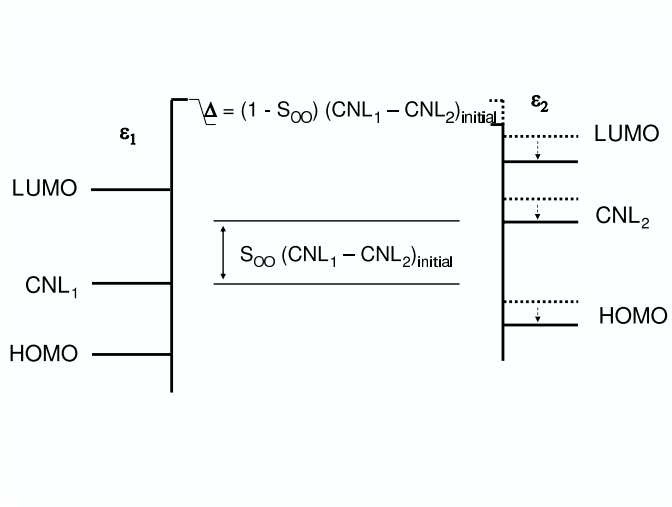

Figure 4.8.: Energy level alignment at organic heterojunctions: the initial CNL offset is screened according to S_{OO}. Charge is transferred and a dipole Δ is induced, while the weaker screening results in a significant final CNL difference.

the whole electronic spectrum, including its vacuum level, of one semiconductor relative to the other one. In Fig. 4.8, for example, the electronic spectrum of $Organic_2$ is lowered with respect to that of $Organic_1$, a process which tends to align the CNLs of both materials. The low screening ability of organic heterojunctions results in the fact that the initial CNL difference is not completely screened, and a significant CNL offset is present after the interface is formed.

In the case of the CuPc/PTCDA interface (Fig. 4.1), for instance, the initial 0.8 eV CNL difference is reduced by the induced dipole $\Delta = (1 - S_{OO})\ (CNL_{CuPc} - CNL_{PTCDA})$ = 0.34 eV, which shifts the PTCDA levels upwards (since it CNL is more negative) or, equivalently, those of CuPc downwards, by this quantity, and a final CNL offset of $S_{OO}\ (CNL_{CuPc} - CNL_{PTCDA})$ = 0.46 eV remains. Experimentally [Flores87], an interface dipole of +0.4 eV raising the PTCDA spectrum is observed.

The sign and magnitude of the dipole can be calculated for the different interfaces considered and compared with experiment. The results are shown in Table 4.4 and Fig. 4.9. In the calculation of Δ, the values of S_{OO} resulting from ϵ_i estimated from S_{Au} through equation 4.5 have been used, although the difference with the dipoles obtained when using the the optical [Hill00c] or transport gap is very small. In Ref. [Vázquez05b], the values using the optical gaps were used. As stated

	Δ (theory)	Δ (exp.)
CuPc/PTCDA	0.34	0.4
CuPc/PTCBI	0.17	0.1
CuPc/CBP	0.02	0.0
CuPc/α-NPD	0.04	0.0
PTCDA/Alq_3	-0.42	-0.5
PTCDA/α-NPD	-0.29	-0.1
BCP/Alq_3	0.00	0.0
BCP/CBP	0.12	0.0
BCP/PTCBI	0.30	0.4
BCP/α-NPD	0.15	0.0
Alq_3/α-NPD	0.14	0.25
Alq_3/CBP	0.11	0.1

Table 4.4.: Calculated and experimental [Hill00c] interface dipoles (in eV) for different organic heterojunctions, as shown in Fig. 4.9.

before, the difference with the values using E^t are very small and the optical gap is more accessible experimentally and is thus more reliable. In any case, small differences with our calculated values of S will be found if the dielectric constants of the materials, ϵ_i, are different from our estimated values, but this will not alter the results in the interface dipoles, which depend predominantly on the positions of the CNLs.

Comparing the calculated and experimental interface dipoles (Table 4.4, Fig. 4.9), it can be seen that the signs always agree, and that the agreement in the magnitude is good, the largest difference being around 0.2 eV for the PTCDA/α-NPD interface, close to the experimental error of ~ 0.1 eV.

As in the case of metal/organic interfaces, the large permanent dipole of Alq_3 is not taken into account, so it must be assumed that the molecules are deposited in such a way that the total net dipole is zero.

The comparative analysis between the calculated and experimental interface dipoles thus provides a quantitative evaluation of our model for organic heterojunctions.

4.7. Transitivity in organic heterojunctions

Our model can be used to analyze the validity of the transitivity rule in organic heterojunctions: this rule states that the molecular level offset between two organic

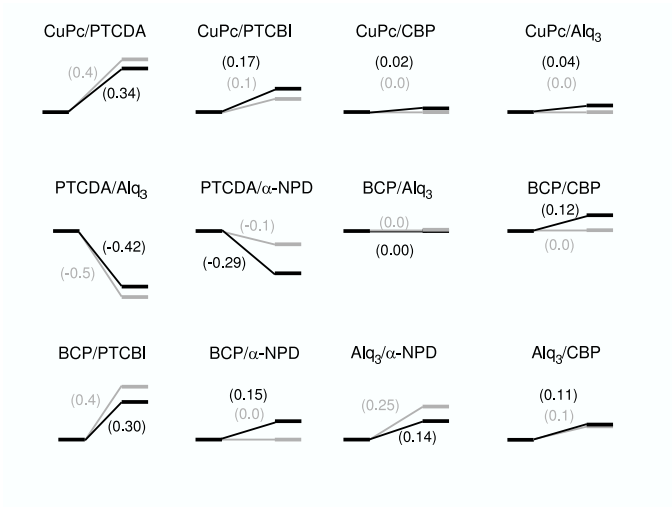

Figure 4.9.: Schematic representation of theoretical (black) and experimental (grey, [Hill00c]) induced dipoles, for the organic/organic interfaces considered.

semiconductors can be obtained by aligning each one of them with a third organic material. Within our model,

$$\begin{aligned}(CNL_1 - CNL_2)_f &= S_{1,2}\,(CNL_1 - CNL_2)_i \\ (CNL_2 - CNL_3)_f &= S_{2,3}\,(CNL_2 - CNL_3)_i,\end{aligned} \tag{4.8}$$

so that the offset between the CNLs of semiconductors 1 and 3 is given, on one hand, by a similar equation for that interface,

$$(CNL_1 - CNL_3)_f = S_{1,3}\,(CNL_1 - CNL_3)_i, \tag{4.9}$$

and, at the same time, by the addition of equations 4.8:

$$(CNL_1 - CNL_3)_f = S_{1,2}\,CNL_{1,i} + (S_{2,3} - S_{1,2})\,CNL_{2,i} - S_{2,3}\,CNL_{3,i}. \tag{4.10}$$

It is easy to see that if the screening parameters $S_{i,j}$ were the same for the three interfaces, $S_{1,2} = S_{2,3} = S_{1,3}$, the transitivity rule would be satisfied within our model, since in all three cases, the same factor would be screening the difference between the CNLs.

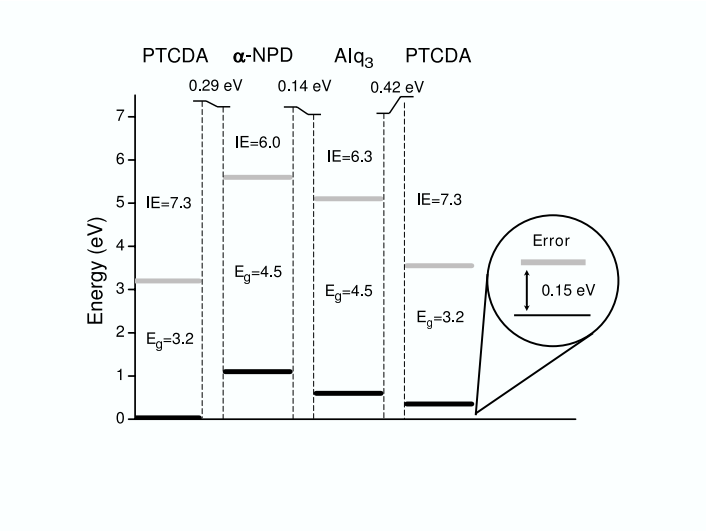

Figure 4.10.: Transitivity in organic heterojunctions: experimental results (adapted from Ref. [Rajagopal98]. HOMO and LUMO are represented by black and grey bars, respectively. Interface dipoles, ionization energies and peak-to-peak transport gaps and shown.

Small differences among the screening parameters $S_{i,j}$ introduce some inaccuracies in the transitivity rule. Since the values of $S_{i,j}$ are all very similar (Table 4.3), the transitivity rule 'almost holds' at organic/organic interfaces.

Let us consider the particular case of the PTCDA/α-NPD/Alq_3/PTCDA interface, which has been analyzed experimentally [Rajagopal98]. The transitivity rule would imply that the PTCDA levels in the initial and final deposition are aligned, and that the sum of the interface dipoles is zero.

From the theoretical values given in Table 4.4, we find the following interface dipoles:

$$\begin{aligned} \Delta(PTCDA/\alpha - NPD) &\simeq -0.29eV \\ \Delta(\alpha - NPD/Alq_3) &\simeq -0.14eV \\ \Delta(Alq_3/PTCDA) &\simeq 0.42eV \end{aligned} \tag{4.11}$$

The experimental situation is depicted graphically in Fig. 4.10 (note in passing that transport gaps are represented).

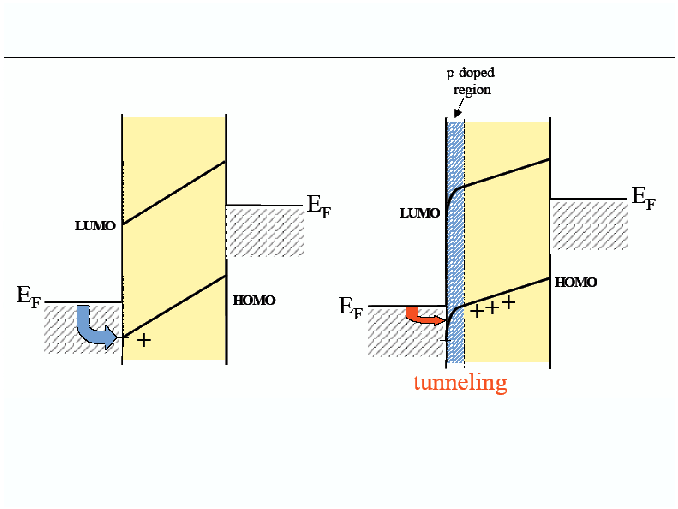

Figure 4.11.: At metal/organic interfaces, doping of the organic material leads to band bending and the formation of a space-charge region near the interface, which enhances current injection due to tunneling (Fig. from [Shen01b]).

Comparing the sums of the calculated and experimental dipoles induced at the different interfaces, a good agreement is found. The sum of the theoretical values (-0.01 eV) shows that the transitivity rule for these organic materials is almost satisfied within our model, due to the slightly different values of S at the different interfaces. This is consistent with the experimental data, shown in Figure 4.10.

4.8. Doped organic heterojunctions

Our model has been applied to study the puzzling change in the molecular level alignment at organic/organic interfaces when one of the materials is p-doped.

Doping of organic semiconductors is an efficient way of improving conductivity and injection properties at organic semiconductor interfaces. At metal/organic junctions, doping leads to the formation of a space-charge region at the interface (see Fig. 4.11) and an increase in charge injection of several orders of magnitude through tunneling has been observed [Gao01,Shen01b]. At organic heterojunctions, the movement of the Fermi level induced by doping opens the possibility of controlling molecular level offsets at the interface.

Doping is carried out by co-evaporation of the host and dopant materials (Fig.

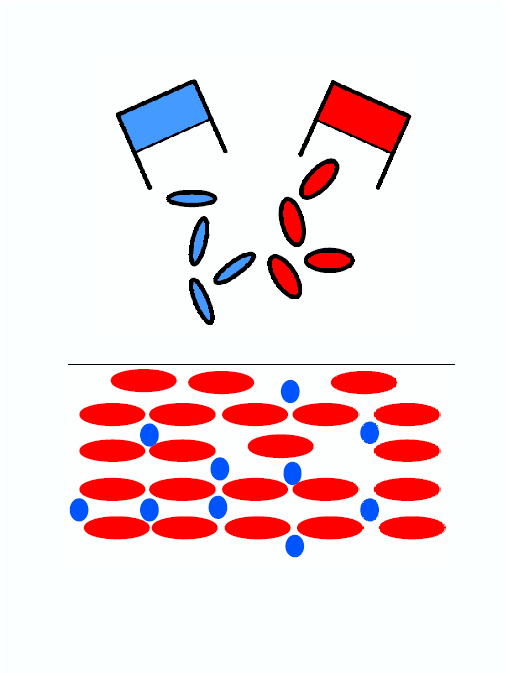

Figure 4.12.: Doping in organic materials is done by co-evaporation of host and dopant. The doping concentration is typically $\sim$ 0.1 to $\sim$ 5 %, much larger than in inorganic semiconductors.

4.12). The dopant concentration in organic materials ranges from $\sim$ 0.1 to $\sim$ 5 % [Gao03b], which is much larger than in standard inorganic semiconductors (typically $10^{-4} - 10^{-3}$ %). These large concentrations in inorganic semiconductors would lead to conditions beyond degenerate doping and associated with the formation of an alloy or doping-induced bands. In the case of organic materials, the weakly-interacting molecules, where the overlap and interaction between them is small, is associated with high carrier localization. Thus, in spite of the large concentrations of dopants compared to the inorganic case, it is accepted that the notion of doping in organic semiconductors remains valid.

We analyze how p-doping of one of the materials at an organic/organic interface gives rise to the formation of a large interface dipole, as well as the modification of the molecular offsets at the interface.

In particular, we have analyzed interfaces involving the electron-transport mate-

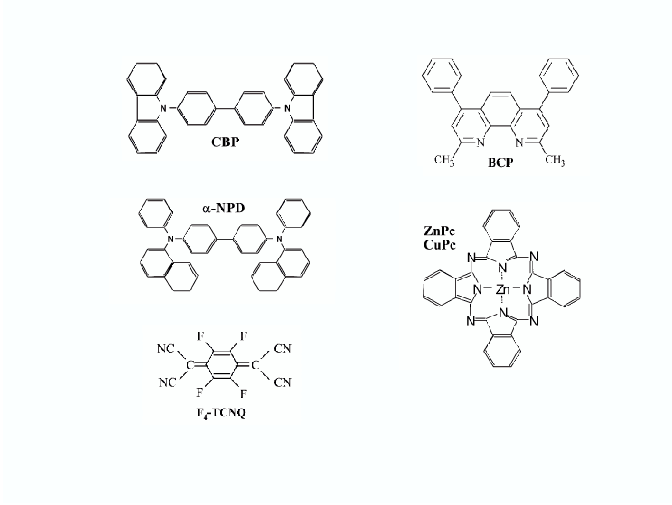

Figure 4.13.: Organic materials considered in this study of doped organic heterojunctions: electron transport materials (CBP and BCP), hole transport materials (α-NPD and ZnPc), as well as the dopant F_4-TCNQ.

rials CBP or BCP, on doped or undoped hole-transport materials (α-NPD or ZnPc). In both cases, the dopant material was F_4-TCNQ (see Fig. 4.13).

Doping in these systems is done by direct charge transfer between host and dopant. p-doping of α-NPD or ZnPc by F_4-TCNQ is so efficient because of the energy position of the host and dopant molecular levels: the HOMO (or ionization energy) of α-NPD or ZnPc is $\sim$ -5.7 – -6.0 eV, very close to the position of the LUMO of F_4-TCNQ (-5.8 eV), all referred to vacuum level [Gao02]. This excellent energy match (see Fig. 4.14) favours charge transfer, resulting in very efficient p-doping [Gao02, Gao02, Kahn06].

The effect of doping on the energy level alignment is dramatic: large dipoles are induced at the interface, and the Fermi level position at the undoped material is fixed, irrespective of the doped material on which it is deposited. This is illustrated in Fig. 4.15.

Notice, first of all, that none of the four *undoped* interfaces exhibits a significant interface dipole. The values measured experimentally are negligible, while those calculated within our model are small (see Table 4.4), within experimental error.

Upon doping, large interface dipoles are induced in three of the four cases: -0.6

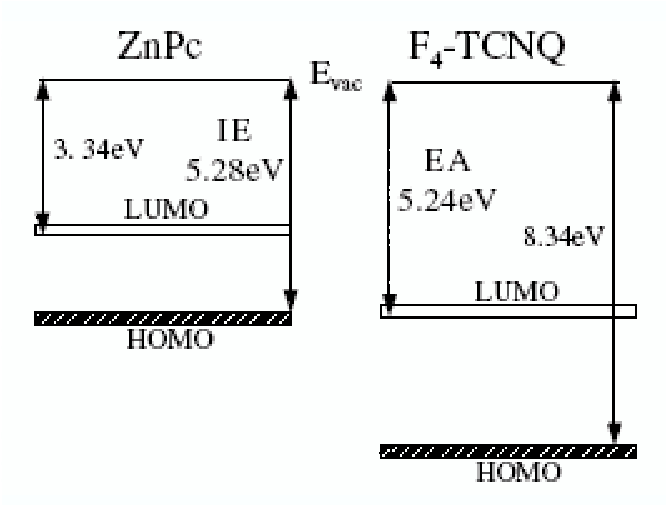

Figure 4.14.: Ionization and affinity levels of ZnPc and F_4-TCNQ as deduced from direct and inverse photoemission measurements (from [Gao02]).

eV in the case of 0.5% α-NPD/BCP, -0.9 eV for 3% ZnPc/BCP, and -0.5 eV for the 3% ZnPc/CBP interface. The other (0.5% α-NPD/CBP) interface exhibits a small -0.08 eV dipole.

Importantly, these interface dipoles are not induced by a movement of the Fermi level only. It could be possible that Fermi level shift induced in the host through doping could be responsible for the observed dipoles at the doped heterojunctions. However, this is disproved by the fact that when the Fermi level in the organic material is changed (by modifying the work function of the metal on which it is deposited), the dipole remains unchanged (see Fig. 4.17). A shift in the Fermi level position, therefore, does not necessarily induce an interface dipole. Thus, while the Fermi level position in the (bulk) organic material can be determined by doping, the dipoles appearing at the organic heterojunction are a consequence of interface, and not bulk, mechanisms. This is confirmed by reversing the deposition sequence, where the same offsets and dipoles are observed, which means that they are specific of the heterojunction, characteristic of the electronic structure at the interface, and not due to shifts of the Fermi level or artifacts of fabrication.

Notice in Fig. 4.15 that the position of the Fermi level in the gap of the **undoped** material remains fixed, irrespective of the doped material on which it is deposited.

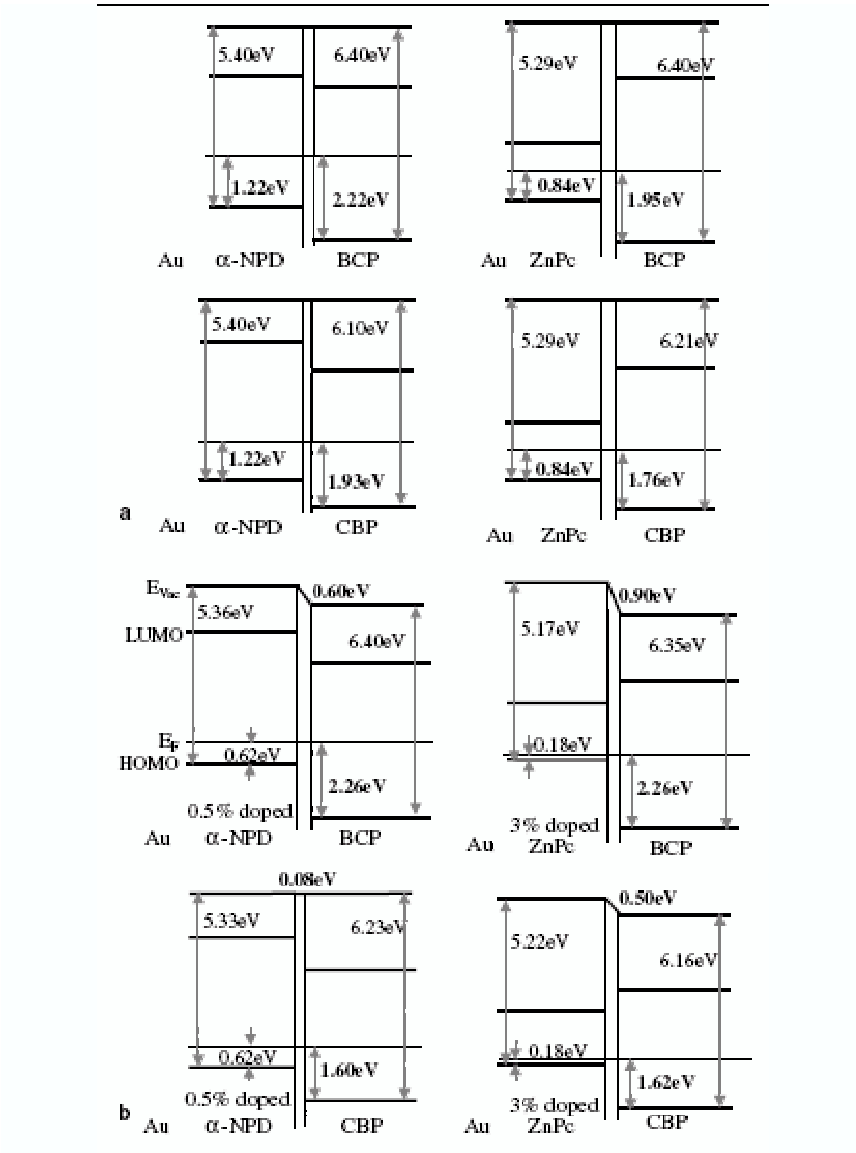

Figure 4.15.: Energy level diagram of the four organic heterojunctions where the hole transport material is undoped (a) and doped (b). Figure from [Kahn06].

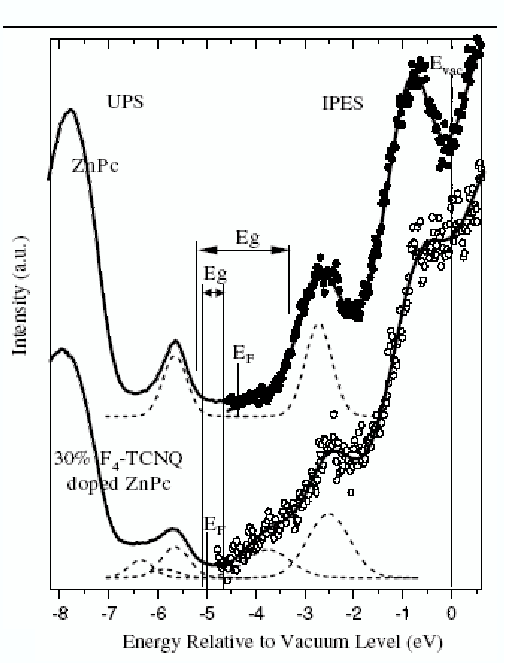

Figure 4.16.: UPS/IPES spectra of undoped (bottom) and 30% doped ZnPc films (from [Kahn06]). Notice the reduction of the energy gap due to the large dopant DOS.

The E_F-to-HOMO-edge for BCP is 2.26 eV and $\sim$ 1.6 eV for CBP, whether they are deposited on doped α-NPD or on doped ZnPc. It therefore seems that the doped organic 'pins' the Fermi level at a characteristic position in the undoped material, a situation reminiscent of metal/organic interfaces which suggests that the pinning behaviour of the doped organic material resembles that of a metal.

We interpret these changes within the induced DOS and CNL model as a shift of the CNL upon doping. To rationalize this, consider the molecular levels of the host and dopant presented in Fig. 4.14. Even though only the HOMO and LUMO of both materials are presented, it suggests that the empty states of the dopant are overlapping with at least the upper half of the gap of the host material. Thus, especially at high doping concentrations, the electronic structure of the dopant has the effect of effectively reducing the gap of the doped material. This is clearly seen in the extreme case of 30% doped ZnPc (Fig. 4.16), where inverse photoemission is able to pick up the large dopant DOS. The overlap of host and dopant DOS leads

to a reduction of the effective gap. Thus, the CNL of the doped material is clearly much closer to the HOMO of the undoped organic. Although the doping concentration of 30% presented above is clearly an extreme case, it nevertheless illustrates a mechanism (the lowering of the CNL upon p-doping due to the reduction of the host-dopant energy gap) that is expected to take place in less doped materials. This is schematically illustrated in Fig. 4.18

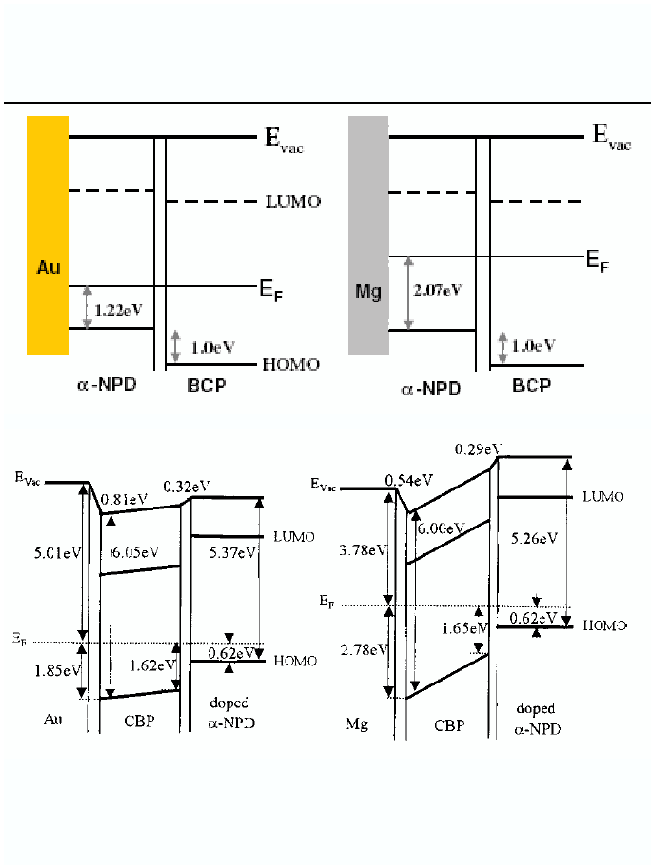

Figure 4.17.: Energy level diagram of undoped [Kahn06] (top) and doped [Gao03b] (bottom) organic/organic interfaces, deposited on Mg and Au. Notice that the change in the interface dipole change is not caused by a movement of the Fermi level.

Moreover, if the charge transferred per host molecule δq, is large, it could be argued that the CNL position should be such that the integrated DOS was N - δq.

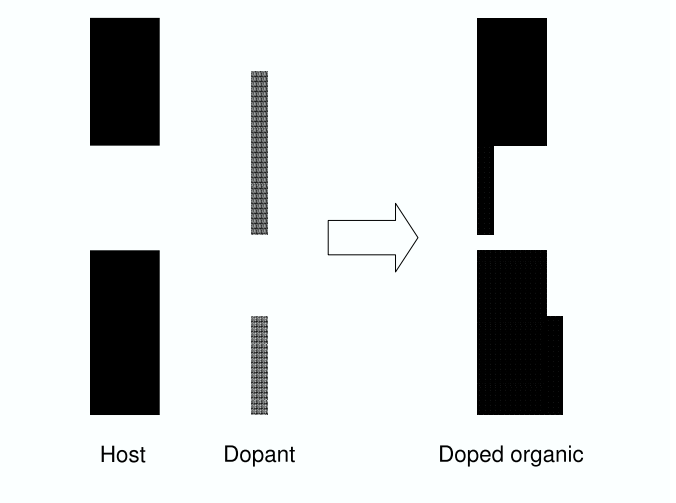

Figure 4.18.: Schematic representation of the reduction in the effective gap of the host and dopant due to the contributions of both DOS. This leads to a shift in the CNL of the doped organic towards the HOMO of the undoped material.

In the case of p-doping, all the above arguments suggest that the CNL position is bound to be lowered to more negative energies.

To quantify our analysis of the doped organic heterojunctions, let us first consider the charges at the metal/organic interface induced upon doping, a situation shown in Fig. 4.19. p-doping results in the formation of a depletion region at the interface and the reduction of the interface dipole. Similar results have been observed for doped ZnPc/metal interfaces [Gao02] (since ZnPc and CuPc have similar energy gaps, ionization and affinity energies, and presumably similar electronic structures, we estimate the CNL of ZnPc as that of CuPc). Within our model, this change in the dipole $\delta(\Delta)$ is related to a shift in the CNL position $\delta(CNL)$ via

$$\delta(CNL) \sim \frac{\delta(\Delta)}{(1 - S_{MO})}, \tag{4.12}$$

where the S parameter for the metal/organic interface (which changes only slightly in the low doping limit) should be used. The data shown in Fig. 4.19 yield $\delta(\Delta) \simeq 0.08$ eV, and $S_{MO} \simeq 0.6$, which gives a downwards shift in the CNL position of ~ 0.2 eV (using the S parameter, calculated for the finite differences shown in

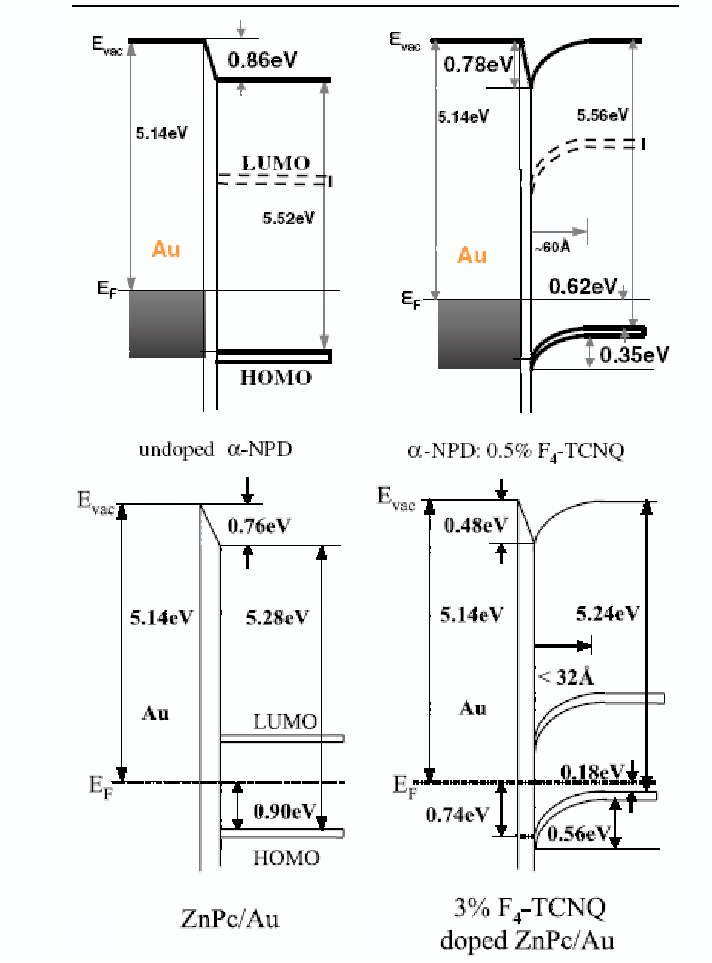

Figure 4.19.: Energy level diagram for doped and undoped α-NPD/Au (top) and ZnPc/Au (bottom) interfaces.

Fig. 4.17, for the doped or undoped case makes little difference).

The CNL of α-NPD thus shifts from -4.1 to -4.3 eV upon doping. In addition, its dielectric constant is seen to increase when the material is doped [Kahn06]. Since it is large compared to that of the undoped organic, we can neglect it in equation 4.3, so that the screening parameter for the **doped** organic heterojunctions is given by

	Δ theory (eV)	Δ exp. (eV)
0.5% doped α-NPD/BCP	-0.42	-0.6
0.5% doped α-NPD/CBP	-0.16	-0.1
3% doped ZnPc/BCP	-0.56	-0.9
3% doped ZnPc/CBP	-0.26	-0.5

Table 4.5.: Calculated and experimental interface dipoles for the doped organic/organic interfaces considered.

$$S_{dOO} \simeq \frac{1}{2} \frac{1}{\epsilon_{undoped}}, \tag{4.13}$$

where the subscript *dOO* labels the doped organic/organic interface. Using the values for the dielectric constants given in Table 4.2, we take $S_{dOO} \simeq 0.35$ (S_{dOO} = 0.34 for the doped α-NPD/BCP interface, while S_{dOO} = 0.36 for the doped α-NPD/CBP one). The dipole at the doped organic/organic interface is then given by equation 4.7, substituting S_{OO} by S_{dOO}. For ZnPc, the above analysis results in a downward shift of the CNL of 0.4 eV, from -4.0 to -4.4 eV where a value of $S_{dOO} \simeq$ 0.25 for the doped ZnPc interfaces is taken, smaller than in the case of 0.5% doped α-NPD as higher doping presumably leads to a stronger interface screening. We must mention, however, that these values of S_{dOO} can have a large uncertainty as errors (especially in the case of the highly reactive Mg) in its calculation might add up. The results for the different doped organic heterojunctions using these values are summarized in Table 4.5.

These values are slightly different to those published in Ref. [Kahn06]. The reason, as was the case for metal/organic interfaces, is the slight modification of the CNL values, which have recently been changed [Vázquez] in light of new data. These CNL values, slightly different to previously reported ones for some materials make minor modifications to the calculated values of Δ, but do not, nevertheless, alter the general trends and conclusions, which of course remain valid.

The agreement with experiment is fairly good in the case of 0.5% doped α-NPD. The results are not as accurate for the 3% doped ZnPc, since, although the calculated values show the correct tendency and correctly predict the dipole sign, its magnitude is smaller than observed. The poorer agreement in this case is presumably due to an underestimation of the CNL shift in the highly doped (3%) material: it is likely that such high doping deeply affects the electronic structure [Kahn06] in

a way that our model has not described correctly. If we assume that in the case of the highly doped 3% ZnPc, the CNL after doping is only slightly above the Fermi level (-5.0 eV), at CNL_{doped} = -4.9 eV, the interface dipoles are, using the same values of S_{dOO},

$$\Delta(3\%\ doped\ ZnPc/BCP) = -0.83eV$$

$$\Delta(3\%\ doped\ ZnPc/CBP) = -0.53eV$$

These results are in much better agreement with experiment. Although this CNL shift is of course speculative and has not been justified, its importance is that it suggests that the model presented in this section, whose results are shown in Table 4.5, applies to a 'low-doping limit', yielding better agreement for the less doped (0.5%) material. Doping ratios of 3% thus seem to correspond to a 'high-doping limit', where the effective CNL of the doped material has shifted greatly from its undoped value, and where a specific calculation of its electronic structure (possibly resembling that of an alloy, and where the presence of dopants at the interface can be significant) is therefore essential.

To summarize, we have applied our model for the energy level alignment at organic heterojunctions to study the striking realignment of molecular levels induced when one of the materials is p-doped. Although the small number of cases considered hinders the analysis of the general trends, we interpret this realignment in terms of a shift in the CNL of the doped material. The magnitude of this shift is extracted from data of metal/organic interfaces and are independent of the heterojunctions analyzed here. It is then applied to describe the behavior at the doped organic/organic interfaces, explaining in a consistent manner the appearance of interface dipoles. The better agreement obtained from the less doped material suggests that our model is valid in the 'low doping limit', and that the electronic structure can be significantly modified at high doping concentrations.

4.9. Summary and Conclusions

We have presented an extension of our model to analyze the molecular level offset at organic/organic interfaces, in which we propose that the energy level alignment is driven by the tendency of the CNLs of both materials to align. The initial CNL difference determines whether and in which direction charge will be trans-

ferred between both materials: this creates an interface dipole which tends to align both CNLs. Screening at organic/organic interfaces is rather weak: the S parameter, which we have estimated from the values of the static dielectric constant of the organic materials, is typically around 0.6, in contrast to the case of inorganic semiconductors, where $S \sim 0.1$. Thus, the initial CNL offset is not completely screened. The dipoles induced at the interface are calculated and found to be in good agreement with experiment: the sign is always correct and the magnitude is in most cases within the experimental error of 0.1 eV.

We have then applied our approach to study transitivity in organic heterojunctions, to find that the transitivity rule 'almost holds' at these interfaces. Small differences in the screening parameters introduce some inaccuracies to this rule.

In addition, we have presented an *ad-hoc* extension of our model to explain the puzzling behavior observed at organic/organic interfaces when one of the materials is p-doped. Large dipoles appear and the Fermi level is pinned at a specific position in the gap of the undoped organic, independent of the doped material on which it is deposited. This is interpreted in terms of a shift in the CNL of the host material upon doping, and calculated interface dipoles are presented. The agreement with experiment is fairly good for the less doped material, suggesting that the electronic structure at high doping concentrations needs to be calculated in detail. Nevertheless, our approach reproduces in a consistent way the trends observed experimentally.

In summary, we have considered several instances of (doped or undoped) organic heterojunctions where the driving mechanism when determining band offsets is the tendency of the CNLs to align. This makes our model **predictive**, where the CNL is the central quantity in our approach, and opens a new way of analyzing organic heterojunctions. Notice that all CNLs for the organic materials of Table 4.1 are within 3.8 ± 0.2 eV, except for PTCDA and PTCBI. This implies that large interface dipoles will be observed only at interfaces with these two materials. The other cases correspond to small interface dipoles, close to the experimental resolution of photoemission spectroscopy. This is an important effect that has obscured the physics behind the behavior of these interfaces, suggesting (wrongly) that the vacuum level alignment rule would be an appropriate way of determining all organic/organic molecular level offsets.

CHAPTER 5

Conclusions

Instinct, intuition, or insight is what first leads to the beliefs which subsequent reason confirms or confutes; but the confirmation, where it is possible, consists, in the last analysis, of agreement with other beliefs no less instinctive. Reason is a harmonising, controlling force rather than a creative one. Even in the most purely logical realms, it is insight that first arrives at what is new.

(Bertrand Russell)

There are more thing on heaven and earth than are dreamt of in your philosophy.

(William Shakespeare (Hamlet))

In this thesis, we have studied the electronic structure of weakly-interacting organic semiconductor interfaces.

First, the electronic properties of small and π-conjugated molecules has been studied using DFT-based methods. Two different approaches, conventional LDA and the Orbital-Occupancy method, have been used to calculate the electronic properties of small organic molecules. Results for these molecules have been compared and discussed in light of the different exchange-correlation functionals and basis sets used. Then, the electronic structure of large, π-conjugated molecules was calculated, with particular attention to the nature and symmetry of molecular orbitals, as well as the position of the electronic levels. Since DFT severely underestimates the molecular gap and the DFT spectrum is therefore completely unreliable, a scheme to correct for this deficiency has been developed. The 'Koopmans' energy shifts, which were checked in several systems to be in good agreement with exact results, enable an accurate calculation of the 'true' single-particle gap, an issue of prime importance for the molecular level alignment at interfaces.

In a second step, the model for the energy level alignment has been introduced for metal/organic interfaces. Since chemical reactions can complicate the analysis, we have restricted our discussion to weakly-interacting junctions. Within our model, the Schottky barrier formation is governed by the tendency of the organic CNL and the metal work function to align, with the CNL acting as the central quantity in our analysis. Its calculation is carried out in several steps: first, the electronic structure of the metal and the organic material are determined separately. Then, the interaction between them is calculated, which has the effect of broadening the molecular levels. By adding up the contributions of all molecular orbitals, where the 'Koopmans' approach is necessary for the molecular level positions, a non-negligible DOS is induced in the former energy gap. This induced DOS is generally weaker than in inorganic materials, although the more pinning organic semiconductors exhibit values comparable to traditional inorganic ones. By integrating the induced DOS up to the charge of the isolated molecule, the position of the CNL is determined.

The CNL position of several organic materials has been calculated: PTCDA, PTCBI, CBP, CuPc and Pentacene. The electronic properties of interfaces of these materials with Au has been determined, which depend on the relative position

of the metal work function and the organic CNL, as well as on the screening at the interface. This is described through the S parameter, which has been determined theoretically and found in good agreement with experimental results. Using the calculated values of the CNL and S, and the experimentally measured metal work function as input, interface properties such as interface dipoles and hole injection barriers have been obtained with the organic-metal distance as the sole external parameter. Theoretical results have been found to be in good agreement with experiment, since the direction of the interface dipole is always correct and the quantitative agreement in dipoles and injection barriers is in most cases within experimental uncertainty. Importantly, the pinning behaviour of these interfaces, reflected too in the values of S, is always correctly described: our model predicts stronger or weaker pinning in accordance with what is found experimentally.

Our model implies that physisorptive interfaces, where it was commonly assumed that the interaction is purely van der Waals and that the vacuum level rule holds, show a chemical interaction that is strong enough to induce a DOS in the organic material that can pin the Fermi level. This results, firstly, from claiming that the Au/organic interaction induces a continuum DOS in the organic energy gap that acts as a buffer for the transferred charge. Secondly, it results from the robustness of the CNL position, which is almost insensitivity to the metal-organic distance d, one of the main assumptions in our model. Finally, the screening at the interface, too, influences the interface properties, but much more weakly than changes in the CNL.

The result that CNL positions depend very weakly on the details of the interaction and are thus almost intrinsic to the organic material enables the extension of the model to organic/organic interfaces. We interpret the energy level alignment at organic heterojunctions through the partial alignment of the CNLs of both organic materials. The initial CNL difference determines the direction of charge transfer and thus the sign of the interface dipole. The final molecular level offset depends on this initial CNL difference and on the screening at the interface, described through a similar parameter S. This screening parameter is similar to the one introduced for metal/organic interfaces and depends on the static dielectric functions of both materials. Since these have not been determined either theoretically or experimentally in most cases, they are estimated in our model in different ways: through the relative values of the molecular gap, and using the relative S parameters at the corresponding metal/organic interfaces. The results for S are very similar using these

approaches, and we find that typically S $\sim$ 0.6, indicative of rather weak screening. These large values of S mean that the initial CNL differences are not completely screened, so that organic heterojunctions exhibit significant final CNL offsets. This result is important since it differs from inorganic semiconductors, where S is almost zero and the final CNL positions are almost completely aligned. In spite of the different approaches to estimate S at organic heterojunctions, our results depend rather weakly on S, and are governed mainly by the initial CNL offsets.

Our approach for organic heterojunctions has used the CNL positions calculated for metal/organic interfaces, together with fits of the CNL of three materials whose interfaces with Au had not been studied theoretically. These CNL values, together with the interfaces S parameters, enable the calculation of the interface properties of organic/organic interfaces. These heterojunctions were not fully understood: the vacuum level rule was followed in most cases but large dipoles were observed in some interfaces. While previous mechanisms had not been able to rationalize this behaviour, our model provided a consistent approach where good qualitative and quantitative agreement with experiment was found: the sign of the predicted dipole was always correct and the values for the dipoles were in good agreement with experiment, in most cases within experimental uncertainty. The model has been used to explain transitivity in organic heterojunctions, where is was found that the transitivity rule 'almost holds' at these interfaces due to small differences in the screening parameters.

Finally, an *ad-hoc* extension of the model was carried out to understand the behaviour of organic heterojunctions when one of the materials is p-doped. The large interface dipoles and fixed molecular level offsets were rationalized in terms of a shift of the CNL upon doping. Fair agreement was found for the less doped material, suggesting that a careful calculation is necessary for highly-doped materials, but providing at the same time a consistent explanation for the results observed at these interfaces.

In summary, we have presented our model for the energy level alignment for weakly-interacting organic semiconductor interfaces. In the model, the central quantity is, clearly, the CNL, whose alignment with the metal work function (in the case of metal/organic interfaces) or the CNL of the organic material (at organic heterojunctions) largely determines properties such as interface dipoles or injection barriers. The model has been successfully applied to a range of weakly-interacting interfaces: metal/organic, organic/organic and doped organic heterojunctions. Al-

though the good agreement found in these cases show the validity of the model, this is by no means complete and there are many issues which would be interesting to consider. These are either the focus of current research, or will be in the near future.

5.1. Future work

The first of these issues deals with the inclusion of off-diagonal elements and an energy dependence in the self-energy in equation 3.27 of Section 3.7. The implies relaxing the simplification made in equation 3.28 and considering $\Sigma_{ij}(E)$ for all molecular orbitals i and j over a range of energies.

Concerning the simplification of considering just diagonal self-energy elements we have found, to our surprise, that π orbitals couple quite strongly through the substrate and that off-diagonal self-energy elements are significant and have to be taken into account. This does not occur, however, for σ (in-plane) molecular orbitals, whose interaction with the metal substrate is weaker, resulting in negligible off-diagonal elements. Thus $\Sigma_{ij}(E)$ elements have to be considered when i and j have π symmetry, but not when they exhibit σ in-plane character. Thus, the self-energy matrix contains only diagonal elements for σ molecular orbitals and both diagonal and off-diagonal ones for π states. In practice, this means that while σ self-energies can be computed quite rapidly, it is necessary to invert the 'boxes' corresponding to π states for each energy step, which is more costly computationally.

As for the energy dependence, let us mention, first of all, that the approximation $\Sigma_i(E) \simeq \Sigma_i(E_F)$ made in Section 3.7 is not at all unreasonable: those molecular orbitals near the gap will exhibit $\Sigma_i(E) \simeq \Sigma_i(E_F)$, while the approximation will break down for those states further away from the gap, which do not contribute significantly to the induced DOS anyway. The extension proposed here is just the generalization of the self-energy for all pairs i, j and to include the energy dependence. The inclusion of the energy dependence, which comes through the substrate Greens' function $G_{\alpha\beta}(E)$ gives rise to self-energy elements whose variation with respect to E depends on the energy of the molecular state, the coupling of that state to the substrate (the hopping elements) and the metal Greens' function.

This work has already been carried out, including Au 5d orbitals (which have a small but significant effect) but our calculations show that a detailed integration of the charges (the diagonal elements of $\rho_{ij} = -\frac{1}{\pi}\frac{1}{E-H-\Sigma_{ij}(E)}$) is essential. We have found that small error in the integrated charge of each molecular orbital ac-

cumulate rapidly when considering the large (~ 100) molecular states, yielding an uncertainty in the CNL position of a few tenths of an eV.

Thus, since these issues are not completely resolved at present but have proven quite troublesome for over a year, the corresponding results have not been included in this work and will be published in due time.

Another extension of our model, which is being carried out in our group, involves what could be called an *ab-initio* description of the 'pillow' effect, not phenomenologically through a modification of ϕ_M (see Section 3.3) but from first principles. This is done by considering the overlap between metal and molecular orbitals, and expanding the interaction terms between the metal and the molecule in powers of the overlap up to second order. Similar work has been done for inorganic substrate-adsorbate systems and the results would enable a clear understanding of the 'pillow' effect, not just through a final value of the dipole shift, but with the contributions of the different interaction terms between the metal and the molecule. Organic heterojunctions, on the other hand, are not affected by the 'pillow' effect since organic wavefunctions are more localized, so this is a mechanism dealing with metal/organic interfaces only. Thus, this mechanism, which we believe to be important at metal/organic interfaces, will be better understood with this approach.

Finally, since only weakly-interacting interfaces have been considered, the model can be extended in an obvious way by studying reactive metal/organic interfaces. As has been mentioned, the formulation of our method is adapted to the description of these junctions, since there are no qualitative differences between both sets of interfaces. The values for the hopping elements would be different since the metal-organic interaction would be much stronger, and the molecular level broadenings would differ too from the weakly-interacting case, but this would only result in a different induced DOS in the gap. This would be specific to the metal/organic molecule system which is being studied, and it would thus seem that the CNL position could, in principle, be quite different from the values quoted in this work. However, experimental results over a wide range of reactive and unreactive metals show that in some organic materials the Fermi level is completely pinned at a specific position in the molecular energy gap: this suggests a preferred energy position specific to the organic material, and that the exact shape of the induced DOS is not too important. Since this pinning position is the same for strongly- and weakly-interacting interfaces, the 'intrinsic' degree of pinning proposed by our model must

be dominant. In other materials, however, the Fermi level position changes significantly with the metal work function, indicating that the 'intrinsic' pinning ability of this material is smaller and that details of the metal-molecule interaction will affect the energy level alignment more strongly. In all cases, and particularly the latter, a detailed study of reactive interfaces is of obvious importance and will both enrich the model and contribute to the understanding of these interfaces.

5.2. Summary

Despite the limitations and approximations that the preceding section has made evident, our model in its present stage has yielded results in surprisingly good results: results for metal/organic interfaces are well described and experimental trends in the pinning behaviour of different organic materials are reproduced. At organic heterojunctions, our scenario of partial CNL alignment has provided a consistent view of the previously not understood behaviour, as well as yielding results in good agreement with experiment, and an (admittedly *ad-hoc*) extension of the model has been made for doped organic heterojunctions.

It is important to notice that our approach stresses the differences between the DFT and the transport gap: as has been commented on, DFT greatly underestimates the molecular gap, so that the value of the transport gap at the interface differs significantly from the DFT result. Although the use of the DFT gap can be seen in the literature, our approach, on the other hand, includes a scheme to correct this value through the 'Koopmans' energy shifts and polarization corrections at the interface. Since molecular level positions are of obvious importance in the energy level alignment, we believe a correction to the molecular DFT spectrum, not included in other theoretical approaches, is essential.

An important result of our approach is the idea that weakly-interacting physisorptive interfaces can exhibit an interaction that is strong enough to govern the energy level alignment properties. Traditionally, physisorptive interfaces had been considered inert and the vacuum level alignment rule had been implicitly assumed, since 'nothing happens' at these interfaces except for van der Waals interactions. Thus, interface dipoles and Fermi level pinning were not completely understood. Our model, on the other hand, shows that, in addition to this, there is a chemical interaction that is strong enough to induce a DOS in the organic energy gap that largely determines the interface properties.

At the heart of our results lies the concept of the CNL, which has been seen to be very robust, almost intrinsic to the organic material. Notice that metal/organic and organic/organic interfaces depend, though rather weakly, on the screening parameters and the distance d. At the same time, in the metal/organic calculations where the distance d has been changed, the CNL position is practically unaltered. This, together with the zeros of the Greens' function results of the organic molecules, indicates that CNL positions are apparently intrinsic to the organic material to within ~ 0.1 eV. This is an important result, since it implies that, even though the CNL depends on the position of the HOMO and LUMO, which are ultimately taken from experiment and are subject to experimental accuracy, the position of the CNL is an **absolute** quantity, whose position can be used to calculate and predict interface properties.

Thus, while our model is restricted to the limit of weak interaction, it represents and intuitive yet general and, for the first time, **predictive** analysis of the energy level alignment at organic semiconductor interfaces.

APPENDIX A

Molecular spectra of small and π-conjugated molecules

In this section, we present the molecular spectrum of the molecules studied in this work: from the small molecules to the larger π-conjugated ones that are the focus of this thesis.

A.1. CO

The electronic spectrum of CO is shown in the following Table.

In this case, σ symmetry means along the molecular axis, whereas π orbitals are situated in the plane perpendicular to this axis.

MO	Energy (eV)	Symmetry
1	-32.58	σ
2	-12.79	σ
3	-10.64	π
4	-10.64	π
5	-6.69	σ
6	-0.58	π
7	-0.58	π
8	11.44	σ

Table A.1.: Molecular spectrum for CO.

A.2. CO_2

MO	Energy (eV)	Symmetry
1	-29.36	σ
2	-27.72	σ
3	-10.73	σ
4	-9.30	π
5	-9.30	π
6	-7.43	σ
7	-4.95	π
8	-4.95	π
9	3.29	π
10	3.29	π
11	5.92	σ
12	22.78	σ

Table A.2.: Molecular spectrum for CO_2.

As before, σ symmetry means along the molecular axis, whereas π orbitals are situated in the plane perpendicular to this axis.

A.3. CH_4

MO	Energy (eV)	Symmetry
1	-17.57	sp^3
2	-7.96	sp^3
3	-7.96	sp^3
4	-7.96	sp^3
5	10.81	sp^3
6	11.40	sp^3
7	11.40	sp^3
8	11.40	sp^3

Table A.3.: Molecular spectrum for CH_4.

In the case of the CH_4 molecule, all states are sp^3 hybrids.

A.4. C_2H_4

MO	Energy (eV)	Symmetry
1	-20.16	σ
2	-14.37	σ
3	-10.29	σ
4	-8.69	σ
5	-7.26	σ
6	-5.18	π
7	1.95	π
8	10.12	σ
9	10.54	σ
10	11.81	σ
11	15.49	σ
12	18.04	σ

Table A.4.: Molecular spectrum for C_2H_4.

As in other cases, σ symmetry means along the molecular axis, whereas π orbitals are situated in the plane perpendicular to this axis.

A.5. Benzene C_6H_6

MO	Energy (eV)	Symmetry
1	-22.66	σ
2	-19.48	σ
3	-19.46	σ
4	-14.64	σ
5	-14.60	σ
6	-11.73	σ
7	-10.57	σ
8	-9.54	σ
9	-9.08	σ
10	-9.04	σ
11	-7.98	π
12	-6.90	σ
13	-6.86	σ
14	-4.86	π
15	-4.83	π
16	1.63	π
17	1.67	π
18	6.03	π
19	6.41	σ
20	7.30	σ
21	7.81	σ
22	7.97	σ
23	8.43	σ
24	8.50	σ
25	13.12	σ
26	13.25	σ
27	13.28	σ
28	13.53	σ
29	17.48	σ
30	18.68	σ

Table A.5.: Molecular spectrum for Benzene.

In the case of benzene, σ symmetry means that the orbitals are contained within the molecular plane, while π orbitals are the resonant, out-of-plane states.

A.6. PTCDA

In the following cases, we present the molecular spectrum as results from the DFT calculation. Notice the small (underestimated) gap, as well as the values corresponding to the interface, after the 'Koopmans' and polarization corrections have been taken into account. For PTCDA, the data are presented in Table A.6, and for the sake of clarity, we mention that the HOMO corresponds to molecular orbital 70.

MO	Symmetry	DFT (eV)	Interface (eV)
1	σ	-29.24	-33.16
2	σ	-29.24	-33.16
3	σ	-26.30	-30.22
4	σ	-26.30	-30.22
5	σ	-25.99	-29.90
6	σ	-25.99	-29.90
7	σ	-22.61	-26.53
8	σ	-22.09	-26.00
9	σ	-21.16	-25.08
10	σ	-20.93	-24.84
11	σ	-20.71	-24.62
12	σ	-19.63	-23.54
13	σ	-19.58	-23.49
14	σ	-18.97	-22.88
15	σ	-18.70	-22.61
16	σ	-18.57	-22.48
17	σ	-17.20	-21.12
18	σ	-16.76	-20.68
19	σ	-16.00	-19.91
20	σ	-15.88	-19.79
21	σ	-15.39	-19.31
22	σ	-15.22	-19.14
23	σ	-14.98	-18.89
24	σ	-14.74	-18.66
25	σ	-13.41	-17.32

Table A.6.: Molecular spectrum for PTCDA, showing the results from the DFT calculation (third column), and the values at the interface (right).

MO	Symmetry	DFT (eV)	Interface (eV)
26	σ	-13.06	-16.97
27	σ	-13.04	-16.96
28	σ	-12.72	-16.64
29	σ	-12.21	-16.12
30	σ	-11.98	-15.89
31	σ	-11.89	-15.81
32	σ	-11.02	-14.94
33	σ	-10.79	-14.70
34	σ	-10.74	-14.66
35	π	-10.31	-13.65
36	π	-10.21	-13.55
37	σ	-10.09	-14.01
38	σ	-10.07	-13.99
39	σ	-9.78	-13.70
40	σ	-9.65	-13.56
41	σ	-9.58	-13.50
42	π	-9.34	-12.68
43	σ	-9.21	-13.13
44	σ	-9.17	-13.09
45	σ	-9.11	-13.03
46	σ	-9.04	-12.96
47	σ	-8.75	-12.66
48	σ	-8.55	-12.46
49	π	-8.40	-11.74
50	π	-8.37	-11.70
51	π	-8.19	-11.53
52	σ	-7.96	-11.87
53	σ	-7.86	-11.77
54	π	-7.43	-10.77
55	σ	-7.20	-11.11
56	σ	-7.13	-11.04
57	π	-7.07	-10.41
58	σ	-7.03	-10.94
59	π	-6.57	-9.91
60	π	-5.93	-9.26

Table A.7.: Molecular spectrum for PTCDA (continued).

MO	Symmetry	DFT (eV)	Interface (eV)
61	π	-5.69	-9.03
62	π	-5.38	-8.71
63	π	-5.37	-8.70
64	π	-5.28	-8.62
65	π	-5.16	-8.50
66	σ	-5.14	-9.06
67	σ	-5.11	-9.03
68	σ	-4.41	-8.32
69	σ	-4.38	-8.29
70	π	-3.96	-7.30
71	π	-2.38	-4.10
72	π	-0.81	-2.53
73	π	-0.74	-2.47
74	π	0.03	-1.69
75	π	0.31	-1.42
76	π	0.38	-1.35
77	π	0.99	-0.74
78	π	2.14	0.42
79	π	2.33	0.60
80	π	3.37	1.65
81	π	3.85	2.12
82	π	3.96	2.23
83	σ	4.11	2.66
84	σ	4.45	3.00
85	σ	4.77	3.32
86	σ	4.84	3.39
87	σ	4.93	3.48
88	σ	5.02	3.57
89	σ	5.07	3.62
90	π	5.53	3.81
91	σ	5.72	4.27
92	σ	5.83	4.38
93	σ	5.94	4.49
94	π	6.28	4.55
95	σ	6.49	5.04
96	σ	6.80	5.35
97	σ	6.90	5.45
98	σ	7.47	6.03
99	σ	7.58	6.13
100	σ	7.77	6.32

Table A.8.: Molecular spectrum for PTCDA (continued).

MO	Symmetry	DFT (eV)	Interface (eV)
101	σ	7.82	6.37
102	σ	8.86	7.41
103	σ	9.12	7.67
104	σ	9.14	7.69
105	σ	9.15	7.71
106	σ	10.06	8.61
107	σ	10.61	9.17
108	σ	10.68	9.24
109	σ	11.18	9.73
110	σ	11.24	9.80
111	σ	11.93	10.49
112	σ	12.00	10.56
113	σ	12.11	10.67
114	σ	12.29	10.84
115	σ	12.81	11.36
116	σ	13.69	12.24
117	σ	13.79	12.34
118	σ	14.01	12.56
119	σ	14.47	13.02
120	σ	14.78	13.33
121	σ	15.04	13.59
122	σ	15.25	13.80
123	σ	15.41	13.96
124	σ	15.57	14.12
125	σ	16.58	15.13
126	σ	16.86	15.42
127	σ	17.26	15.81
128	σ	17.37	15.92

Table A.9.: Molecular spectrum for PTCDA (continued).

A.7. PTCBI

For PTCBI, the HOMO is number 96.

MO	Symmetry	DFT (eV)	Interface (eV)
1	σ	-25.49	-27.93
2	σ	-25.49	-27.93
3	σ	-24.31	-25.39
4	σ	-24.31	-25.39
5	σ	-22.74	-24.25
6	σ	-22.21	-23.41
7	σ	-21.58	-22.51
8	σ	-21.58	-22.47
9	σ	-21.28	-22.33
10	σ	-21.14	-21.87
11	σ	-20.81	-21.58
12	σ	-20.76	-21.85
13	σ	-20.54	-21.16
14	σ	-19.57	-20.54
15	σ	-19.41	-20.54
16	σ	-19.18	-20.38
17	σ	-18.90	-20.05
18	σ	-18.47	-19.05
19	σ	-18.41	-19.10
20	σ	-18.33	-19.12
21	σ	-17.97	-18.65
22	σ	-17.88	-18.50
23	σ	-16.97	-17.91
24	σ	-16.63	-17.40
25	σ	-16.41	-17.60

Table A.10.: Molecular spectrum for PTCBI, showing the results from the DFT calculation (third column), and the values at the interface (right).

MO	Symmetry	DFT (eV)	Interface (eV)
26	σ	-16.18	-17.09
27	σ	-15.98	-16.67
28	σ	-15.54	-16.38
29	σ	-15.52	-16.51
30	σ	-15.43	-16.30
31	σ	-14.86	-15.52
32	σ	-14.83	-15.48
33	σ	-14.64	-15.34
34	σ	-14.37	-14.97
35	σ	-13.91	-14.72
36	σ	-13.84	-14.49
37	σ	-13.57	-14.39
38	σ	-13.24	-13.90
39	σ	-13.20	-14.27
40	σ	-13.09	-13.80
41	σ	-12.77	-13.80
42	σ	-12.52	-13.10
43	σ	-12.51	-13.08
44	σ	-12.26	-12.87
45	σ	-12.07	-12.59
46	σ	-12.00	-12.73
47	σ	-11.72	-12.32
48	π	-11.66	-12.82
49	π	-11.62	-12.89
50	σ	-11.44	-12.00
51	σ	-11.35	-12.20
52	σ	-11.34	-12.00
53	σ	-11.12	-11.69
54	σ	-11.10	-11.63
55	σ	-11.07	-11.71
56	σ	-11.01	-11.74
57	π	-10.95	-12.46
58	σ	-10.91	-11.55
59	σ	-10.81	-11.40
60	σ	-10.65	-11.41

Table A.11.: Molecular spectrum for PTCBI (continued).

MO	Symmetry	DFT (eV)	Interface (eV)
61	σ	-10.60	-11.50
62	σ	-10.47	-11.08
63	σ	-10.44	-11.01
64	π	-10.35	-11.44
65	σ	-10.10	-11.07
66	π	-9.99	-11.02
67	σ	-9.99	-10.61
68	π	-9.97	-10.98
69	σ	-9.62	-10.29
70	σ	-9.54	-10.36
71	π	-9.43	-10.53
72	σ	-9.39	-10.13
73	π	-9.31	-10.25
74	σ	-9.30	-9.88
75	σ	-9.23	-10.03
76	σ	-9.22	-10.01
77	σ	-8.96	-10.05
78	σ	-8.89	-9.98
79	π	-8.80	-9.56
80	π	-8.78	-9.80
81	π	-8.47	-9.09
82	π	-8.03	-8.90
83	σ	-7.95	-9.09
84	σ	-7.95	-9.09
85	π	-7.93	-8.90
86	π	-7.68	-8.56
87	π	-7.58	-8.86
88	π	-7.52	-8.96
89	π	-7.45	-8.89
90	σ	-6.89	-7.87
91	σ	-6.89	-7.86
92	π	-6.76	-7.45
93	π	-6.55	-7.50
94	π	-6.55	-7.55
95	π	-6.33	-7.17
96	π	-5.98	-6.70
97	π	-4.77	-3.60
98	π	-3.59	-2.47
99	π	-3.22	-1.96
100	π	-2.80	-1.13

Table A.12.: Molecular spectrum for PTCBI (continued).

MO	Symmetry	DFT (eV)	Interface (eV)
101	π	-2.68	-1.04
102	π	-2.53	-1.64
103	π	-2.41	-1.36
104	π	-1.96	-0.86
105	π	-1.71	-0.81
106	π	-1.55	-0.54
107	π	-1.38	-0.26
108	π	-1.11	-0.23
109	π	-0.56	0.62
110	π	-0.22	1.04
111	π	0.38	1.93
112	π	0.72	2.08
113	π	1.87	3.30
114	π	1.87	3.34
115	σ	1.97	2.76
116	σ	2.16	3.07
117	π	2.29	3.83
118	σ	2.48	3.18
119	σ	2.49	3.69
120	σ	2.92	3.75
121	σ	2.95	3.95
122	π	3.21	5.11
123	σ	3.26	4.03
124	σ	3.26	3.97
125	σ	3.59	4.33
126	σ	3.68	4.41
127	σ	3.91	4.63
128	σ	4.02	4.80
129	σ	4.11	4.97
130	σ	4.26	5.12
131	σ	4.35	5.34
132	σ	4.47	5.48
133	σ	4.70	5.90
134	σ	4.78	5.83
135	σ	4.96	5.75
136	σ	5.00	5.80
137	σ	5.08	6.40
138	σ	5.23	5.97
139	σ	5.48	6.85
140	σ	5.50	6.30

Table A.13.: Molecular spectrum for PTCBI (continued).

MO	Symmetry	DFT (eV)	Interface (eV)
141	σ	5.65	6.39
142	σ	5.76	6.56
143	σ	5.92	6.68
144	σ	5.94	6.85
145	σ	6.09	6.84
146	σ	6.19	7.04
147	σ	6.49	7.46
148	σ	6.60	7.80
149	σ	6.72	7.69
150	σ	6.95	8.13
151	σ	7.98	8.77
152	σ	8.00	8.82
153	σ	8.05	8.84
154	σ	8.09	8.87
155	σ	8.30	9.16
156	σ	8.32	9.12
157	σ	8.76	9.58
158	σ	8.76	9.58
159	σ	8.95	9.95
160	σ	9.15	10.04
161	σ	9.48	10.70
162	σ	9.72	10.59
163	σ	9.78	10.90
164	σ	9.95	10.89
165	σ	10.40	11.42
166	σ	10.41	11.36
167	σ	10.96	12.07
168	σ	11.02	12.12
169	σ	11.22	12.20
170	σ	11.32	12.59
171	σ	12.22	13.29
172	σ	12.49	13.67
173	σ	12.59	13.73
174	σ	12.81	14.04
175	σ	13.18	14.55
176	σ	13.73	14.99
177	σ	13.85	15.18
178	σ	14.39	15.59
179	σ	14.68	15.99
180	σ	15.50	16.63

Table A.14.: Molecular spectrum for PTCBI (continued).

MO	Symmetry	DFT (eV)	Interface (eV)
181	σ	15.75	17.01
182	σ	16.30	17.75
183	σ	16.50	17.87
184	σ	17.36	18.92

Table A.15.: Molecular spectrum for PTCBI (continued).

A.8. CBP

The HOMO is molecular orbital 89 in this case.

MO	Symmetry	DFT (eV)	Interface (eV)
1	σ	-23.25	-25.59
2	σ	-23.25	-25.59
3	σ	-21.42	-22.74
4	σ	-21.21	-22.13
5	σ	-20.82	-21.69
6	σ	-20.79	-22.69
7	σ	-20.79	-22.69
8	σ	-20.49	-21.54
9	σ	-19.40	-20.22
10	σ	-19.18	-20.01
11	σ	-18.87	-19.73
12	σ	-18.54	-19.74
13	σ	-18.47	-19.25
14	σ	-18.33	-19.14
15	σ	-18.31	-19.07
16	σ	-18.17	-19.23
17	σ	-17.91	-18.72
18	σ	-17.62	-18.97
19	σ	-17.61	-18.97
20	σ	-17.40	-18.51
21	σ	-15.81	-16.66
22	σ	-15.56	-16.42
23	σ	-15.42	-16.93
24	σ	-15.23	-16.04
25	σ	-14.94	-15.77

Table A.16.: Molecular spectrum for CBP, showing the results from the DFT calculation (third column), and the values at the interface (right).

MO	Symmetry	DFT (eV)	Interface (eV)
26	σ	-14.80	-15.69
27	σ	-14.53	-15.35
28	σ	-14.53	-15.41
29	σ	-14.45	-15.24
30	σ	-14.23	-15.48
31	σ	-14.05	-14.88
32	σ	-13.86	-14.65
33	σ	-13.28	-14.41
34	σ	-13.07	-13.86
35	σ	-13.06	-13.84
36	σ	-12.51	-13.26
37	σ	-12.49	-13.25
38	σ	-12.43	-13.17
39	σ	-11.96	-12.76
40	σ	-11.60	-12.36
41	σ	-11.59	-12.55
42	σ	-11.50	-12.26
43	σ	-11.45	-12.18
44	σ	-11.42	-12.21
45	σ	-11.27	-12.01
46	σ	-11.21	-12.06
47	σ	-10.95	-11.66
48	σ	-10.86	-12.04
49	σ	-10.80	-11.62
50	π	-10.67	-12.53
51	π	-10.66	-12.53
52	σ	-10.55	-11.61
53	σ	-10.52	-11.34
54	σ	-10.41	-11.12
55	σ	-10.40	-11.18
56	σ	-10.40	-11.21
57	σ	-10.17	-11.77
58	σ	-10.17	-11.75
59	σ	-9.95	-10.92
60	π	-9.87	-11.70

Table A.17.: Molecular spectrum for CBP (continued).

MO	Symmetry	DFT (eV)	Interface (eV)
61	σ	-9.72	-11.02
62	σ	-9.53	-10.20
63	σ	-9.41	-10.14
64	π	-9.36	-10.60
65	σ	-9.28	-9.95
66	σ	-9.13	-9.81
67	σ	-9.11	-9.84
68	π	-8.99	-11.12
69	π	-8.99	-11.12
70	σ	-8.94	-9.64
71	π	-8.81	-9.90
72	σ	-8.74	-9.51
73	σ	-8.59	-9.30
74	σ	-8.55	-9.42
75	σ	-8.45	-9.33
76	σ	-8.37	-9.45
77	π	-8.31	-9.31
78	π	-7.59	-8.46
79	π	-7.48	-8.51
80	π	-7.34	-8.32
81	π	-6.91	-8.06
82	π	-6.91	-8.11
83	π	-6.82	-8.48
84	π	-6.77	-8.73
85	π	-6.71	-7.71
86	π	-6.14	-8.41
87	π	-6.14	-8.41
88	π	-5.94	-6.91
89	π	-5.59	-6.80
90	π	-2.80	-2.20
91	π	-2.60	-2.13
92	π	-2.52	-2.21
93	π	-2.07	-0.73
94	π	-1.97	-0.74
95	π	-1.94	-0.69
96	π	-1.94	-0.38
97	π	-1.76	-1.40
98	π	-1.33	-0.96
99	π	-1.00	0.65
100	π	-1.00	0.65

Table A.18.: Molecular spectrum for CBP (continued).

MO	Symmetry	DFT (eV)	Interface (eV)
101	π	-0.64	0.23
102	σ	0.80	1.34
103	π	0.91	1.34
104	σ	0.97	1.52
105	π	1.39	1.82
106	π	1.61	2.19
107	σ	2.08	2.32
108	σ	2.14	2.38
109	π	2.40	4.61
110	π	2.46	4.67
111	π	2.46	4.32
112	σ	2.75	3.22
113	σ	2.84	3.44
114	σ	2.85	3.00
115	σ	2.99	3.08
116	σ	3.12	3.22
117	σ	3.16	3.52
118	σ	3.33	3.74
119	σ	3.34	3.83
120	σ	3.71	3.85
121	σ	3.75	3.89
122	σ	3.89	4.51
123	σ	4.10	4.31
124	σ	4.34	5.21
125	σ	4.92	5.07
126	σ	4.97	5.13
127	σ	5.07	5.48
128	σ	5.07	5.53
129	σ	5.57	5.76
130	σ	5.64	6.03
131	σ	5.67	5.85
132	σ	5.89	6.15
133	σ	5.92	6.10
134	σ	6.03	6.22
135	σ	6.06	6.75
136	σ	6.27	6.55
137	σ	6.42	6.69
138	σ	6.44	6.82
139	σ	6.50	6.77
140	σ	7.26	7.83

Table A.19.: Molecular spectrum for CBP (continued).

MO	Symmetry	DFT (eV)	Interface (eV)
141	σ	7.26	7.84
142	σ	7.27	8.04
143	σ	7.67	8.24
144	σ	7.97	8.27
145	σ	8.01	8.33
146	σ	8.03	8.28
147	σ	8.34	8.60
148	σ	8.57	8.79
149	σ	8.58	8.87
150	σ	8.63	8.92
151	σ	8.72	9.23
152	σ	9.10	9.41
153	σ	9.19	9.46
154	σ	9.23	9.55
155	σ	9.23	9.73
156	σ	9.42	10.27
157	σ	9.95	10.57
158	σ	9.95	10.56
159	σ	10.41	10.70
160	σ	10.50	10.79
161	σ	10.69	11.63
162	σ	11.08	11.65
163	σ	11.72	11.99
164	σ	11.73	12.00
165	σ	12.11	12.46
166	σ	12.32	12.73
167	σ	12.48	13.02
168	σ	13.31	13.90
169	σ	13.62	14.35
170	σ	14.10	14.69
171	σ	14.31	14.78
172	σ	14.51	14.91
173	σ	14.60	15.00
174	σ	15.33	16.77
175	σ	16.86	18.65
176	σ	16.86	18.64

Table A.20.: Molecular spectrum for CBP (continued).

A.9. CuPc

In CuPc, the singly-occupied molecular orbital 98 is the DFT HOMO **and** LUMO. It is strongly localized in the Cu and neighbouring N atoms. The LUMO associated with this state is shown in Table A.21 as molecular orbital 186. Notice that due to the 'Koopmans' and polarization corrections, there is a crossing of molecular levels so that the HOMO **at the interface** is of π symmetry, as the Cu-related states have been displaced away from the gap.

MO	Symmetry	DFT (eV)	Interface (eV)
1	σ	-23.69	-25.43
2	σ	-23.36	-25.27
3	σ	-23.35	-25.26
4	σ	-22.78	-24.43
5	σ	-22.07	-23.82
6	σ	-21.21	-22.68
7	σ	-21.21	-22.71
8	σ	-20.77	-21.82
9	σ	-20.66	-21.88
10	σ	-20.61	-21.75
11	σ	-20.58	-22.27
12	σ	-20.34	-22.05
13	σ	-18.82	-19.76
14	σ	-18.62	-20.62
15	σ	-18.59	-19.49
16	σ	-18.55	-19.62
17	σ	-18.49	-19.52
18	σ	-18.48	-19.45
19	σ	-18.45	-19.75
20	σ	-18.42	-19.70
21	σ	-17.20	-18.14
22	σ	-16.49	-17.63
23	σ	-16.48	-17.62
24	σ	-15.43	-17.21
25	σ	-15.37	-16.80

Table A.21.: Molecular spectrum for CuPc, showing the results from the DFT calculation (third column), and the values at the interface (right).

MO	Symmetry	DFT (eV)	Interface (eV)
26	σ	-15.31	-17.15
27	σ	-15.29	-16.81
28	σ	-15.27	-16.11
29	σ	-14.50	-15.65
30	σ	-14.32	-15.40
31	σ	-14.28	-15.32
32	σ	-14.10	-14.91
33	σ	-13.98	-15.37
34	σ	-13.08	-14.09
35	σ	-12.97	-14.12
36	σ	-12.95	-13.99
37	σ	-12.19	-13.46
38	σ	-12.18	-13.50
39	σ	-12.15	-13.24
40	σ	-11.94	-12.72
41	σ	-11.43	-12.24
42	σ	-11.42	-12.23
43	σ	-11.36	-12.25
44	σ	-11.28	-12.67
45	σ	-11.18	-12.56
46	σ	-11.13	-12.94
47	σ	-11.11	-12.91
48	σ	-10.95	-11.77
49	σ	-10.64	-11.48
50	π	-10.50	-11.75
51	σ	-10.42	-11.58
52	σ	-10.41	-11.30
53	σ	-10.35	-11.50
54	π	-10.21	-11.42
55	π	-10.21	-11.44
56	σ	-10.08	-10.97
57	σ	-9.94	-10.92
58	σ	-9.92	-10.74
59	σ	-9.89	-11.10
60	π	-9.73	-10.67

Table A.22.: Molecular spectrum for CuPc (continued).

MO	Symmetry	DFT (eV)	Interface (eV)
61	σ	-9.43	-10.93
62	σ	-9.02	-10.11
63	σ	-8.91	-9.87
64	σ	-8.81	-9.91
65	σ	-8.77	-9.86
66	π	-8.68	-9.80
67	π	-8.66	-9.75
68	π	-8.62	-9.69
69	π	-8.58	-9.62
70	σ	-8.58	-9.34
71	σ	-8.51	-9.42
72	σ	-8.43	-9.54
73	σ	-8.41	-9.46
74	π	-8.19	-8.85
75	σ	-8.11	-8.97
76	σ	-8.00	-9.34
77	σ	-7.97	-9.37
78	π	-7.95	-10.42
79	π	-7.94	-10.45
80	σ	-7.79	-10.30
81	σ	-7.74	-9.71
82	σ	-7.42	-11.27
83	π	-7.38	-8.27
84	π	-7.38	-8.26
85	π	-6.89	-7.57
86	σ	-6.85	-9.55
87	σ	-6.84	-9.52
88	π	-6.48	-7.40
89	σ	-6.42	-7.78
90	π	-6.42	-7.26
91	π	-6.41	-7.16
92	π	-6.38	-7.22
93	π	-6.24	-7.01
94	π	-6.10	-7.08
95	π	-6.09	-7.07
96	π	-5.94	-7.08
97	π	-4.90	-5.70
98	σ	-4.65	-7.49
99	π	-3.58	-3.10
100	π	-3.58	-3.09

Table A.23.: Molecular spectrum for CuPc (continued).

MO	Symmetry	DFT (eV)	Interface (eV)
101	π	-2.43	-2.22
102	π	-2.23	-2.10
103	π	-1.93	-1.50
104	π	-1.89	-1.57
105	π	-1.86	-1.26
106	π	-0.84	-0.54
107	π	-0.75	-0.36
108	π	-0.72	-0.38
109	π	-0.32	0.10
110	π	-0.15	-0.06
111	π	0.77	1.41
112	π	0.79	1.37
113	π	0.98	1.72
114	π	2.41	2.92
115	π	2.54	2.93
116	π	2.59	2.98
117	π	2.67	3.31
118	σ	3.01	4.30
119	σ	3.41	4.32
120	σ	3.45	4.03
121	σ	3.48	4.02
122	σ	3.54	4.00
123	π	3.89	5.04
124	σ	4.23	5.22
125	σ	4.29	5.26
126	σ	4.58	5.63
127	σ	4.63	5.18
128	σ	4.69	5.35
129	σ	4.74	5.73
130	σ	4.78	5.78
131	σ	5.31	5.54
132	σ	5.40	6.36
133	σ	5.44	6.22
134	σ	5.50	6.27
135	σ	5.53	5.91
136	σ	5.63	5.82
137	σ	5.66	5.95
138	σ	6.05	6.22
139	σ	6.40	7.02
140	σ	6.53	7.51

Table A.24.: Molecular spectrum for CuPc (continued).

MO	Symmetry	DFT (eV)	Interface (eV)
141	σ	6.59	7.23
142	σ	6.60	7.40
143	σ	6.65	7.17
144	σ	6.89	7.38
145	σ	7.11	7.58
146	σ	7.12	7.60
147	σ	7.25	7.81
148	σ	7.68	8.10
149	σ	8.24	8.68
150	σ	8.29	8.74
151	σ	8.72	9.15
152	σ	9.35	9.88
153	σ	9.36	9.89
154	σ	9.40	9.87
155	σ	9.72	10.64
156	σ	9.77	10.72
157	σ	9.79	10.61
158	σ	9.87	10.36
159	σ	10.37	10.72
160	σ	10.62	11.04
161	σ	10.94	11.43
162	σ	10.97	11.39
163	σ	11.43	11.84
164	σ	11.62	12.39
165	σ	11.75	12.66
166	σ	11.89	12.24
167	σ	12.08	12.49
168	σ	12.10	12.51
169	σ	12.45	12.84
170	σ	13.29	14.41
171	σ	13.34	14.21
172	σ	13.41	14.20
173	σ	13.44	14.02
174	σ	14.15	14.73
175	σ	14.89	16.05
176	σ	15.00	16.22
177	σ	15.06	15.87
178	σ	16.23	17.73
179	σ	16.31	17.66
180	σ	16.37	18.14

Table A.25.: Molecular spectrum for CuPc (continued).

MO	Symmetry	DFT (eV)	Interface (eV)
181	σ	16.43	18.63
182	σ	17.06	19.33
183	σ	17.13	19.41
184	σ	17.18	19.56
185	σ	17.25	19.70
186	σ	-4.65	-2.71

Table A.26.: Molecular spectrum for CuPc (continued).

For the following organic molecules (except Pentacene), due to lack of experimental information, no analysis of the interface properties has been carried out, and thus only the DFT spectrum is shown.

A.10. Anthracene

In this case, the HOMO corresponds to molecular orbital 33.

MO	Symmetry	DFT (eV)
1	σ	-21.70
2	σ	-20.84
3	σ	-19.63
4	σ	-19.32
5	σ	-18.45
6	σ	-18.13
7	σ	-17.21
8	σ	-15.69
9	σ	-15.03
10	σ	-14.87
11	σ	-14.44
12	σ	-13.13
13	σ	-12.90
14	σ	-12.39
15	σ	-11.48
16	σ	-11.46
17	σ	-11.39
18	σ	-10.86
19	σ	-10.68
20	σ	-10.36
21	π	-10.03
22	σ	-9.85
23	σ	-9.64
24	σ	-9.55
25	π	-9.12

Table A.27.: Molecular DFT spectrum for Anthracene.

MO	Symmetry	DFT (eV)
26	σ	-8.86
27	σ	-8.59
28	σ	-8.36
29	π	-7.85
30	π	-7.79
31	π	-6.91
32	π	-6.72
33	π	-5.64
34	π	-3.38
35	π	-2.09
36	π	-1.87
37	π	-0.78
38	π	-0.60
39	π	1.36
40	σ	2.79
41	π	2.98
42	σ	3.03
43	σ	3.15
44	σ	3.87
45	σ	4.06
46	σ	4.89
47	σ	4.98
48	σ	5.34
49	σ	5.46
50	σ	5.90
51	σ	5.93
52	σ	5.97
53	σ	6.25
54	σ	7.77
55	σ	8.17
56	σ	8.67
57	σ	8.75
58	σ	9.40
59	σ	10.46
60	σ	10.58

Table A.28.: Molecular DFT spectrum for Anthracene (continued).

MO	Symmetry	DFT (eV))
61	σ	10.70
62	σ	11.03
63	σ	12.93
64	σ	13.45
65	σ	15.49
66	σ	15.95

Table A.29.: Molecular DFT spectrum for Anthracene (continued).

A.11. Tetracene

For this material, the HOMO corresponds to orbital 42.

MO	Symmetry	DFT (eV)
1	σ	-21.80
2	σ	-21.25
3	σ	-20.40
4	σ	-19.47
5	σ	-19.33
6	σ	-18.90
7	σ	-18.12
8	σ	-18.03
9	σ	-16.96
10	σ	-16.03
11	σ	-15.11
12	σ	-14.97
13	σ	-14.69
14	σ	-14.53
15	σ	-13.57
16	σ	-12.96
17	σ	-12.31
18	σ	-12.19
19	σ	-12.10
20	σ	-11.55
21	σ	-11.30
22	σ	-10.92
23	σ	-10.87
24	σ	-10.60
25	σ	-10.40

Table A.30.: Molecular DFT spectrum for Tetracene.

MO	Symmetry	DFT (eV)
26	σ	-10.27
27	π	-10.15
28	σ	-9.93
29	σ	-9.70
30	π	-9.55
31	σ	-9.17
32	σ	-9.16
33	σ	-8.72
34	π	-8.64
35	σ	-8.58
36	σ	-8.27
37	π	-7.93
38	π	-7.56
39	π	-7.35
40	π	-6.71
41	π	-6.45
42	π	-5.35
43	π	-3.71
44	π	-2.45
45	π	-2.12
46	π	-1.36
47	π	-1.01
48	π	-0.63
49	π	0.56
50	π	2.08
51	σ	2.83
52	σ	2.97
53	σ	3.02
54	π	3.18
55	σ	3.70
56	σ	3.80
57	σ	3.93
58	σ	4.44
59	σ	5.03
60	σ	5.16

Table A.31.: Molecular DFT spectrum for Tetracene.

MO	Symmetry	DFT (eV)
61	σ	5.33
62	σ	5.46
63	σ	5.62
64	σ	5.65
65	σ	6.00
66	σ	6.22
67	σ	6.51
68	σ	7.21
69	σ	7.60
70	σ	8.54
71	σ	8.75
72	σ	9.17
73	σ	9.30
74	σ	9.73
75	σ	10.11
76	σ	10.50
77	σ	11.22
78	σ	11.28
79	σ	11.92
80	σ	12.41
81	σ	14.35
82	σ	14.47
83	σ	15.92
84	σ	16.20

Table A.32.: Molecular DFT spectrum for Tetracene.

A.12. Pentacene

In Pentacene, the HOMO corresponds to molecular orbital 51. The spectra of DFT calculations and at the interface are shown below:

MO	Symmetry	DFT (eV)	Interface (eV)
1	σ	-21.86	-22.62
2	σ	-21.47	-21.87
3	σ	-20.86	-21.17
4	σ	-20.07	-20.32
5	σ	-19.56	-20.31
6	σ	-19.16	-19.55
7	σ	-19.12	-19.39
8	σ	-18.53	-18.79
9	σ	-18.11	-18.43
10	σ	-17.72	-17.99
11	σ	-16.78	-17.11
12	σ	-16.28	-16.66
13	σ	-15.17	-15.54
14	σ	-15.06	-15.36
15	σ	-15.02	-15.71
16	σ	-14.69	-15.10
17	σ	-14.39	-14.70
18	σ	-13.89	-14.14
19	σ	-12.83	-13.03
20	σ	-12.80	-13.03
21	σ	-12.61	-12.81
22	σ	-12.06	-12.28
23	σ	-11.73	-11.90
24	σ	-11.62	-11.88
25	σ	-11.48	-11.66

Table A.33.: Molecular spectrum for Pentacene, showing the results from the DFT calculation (third column), and the values at the interface (right).

MO	Symmetry	DFT (eV)	Interface (eV)
26	σ	-11.38	-11.51
27	σ	-10.97	-11.28
28	σ	-10.70	-10.77
29	σ	-10.52	-10.74
30	σ	-10.52	-10.59
31	σ	-10.27	-10.69
32	π	-10.21	-11.28
33	σ	-10.13	-10.31
34	σ	-9.92	-10.06
35	π	-9.80	-10.48
36	σ	-9.60	-10.06
37	σ	-9.42	-9.56
38	π	-9.14	-9.64
39	σ	-8.93	-9.06
40	σ	-8.91	-9.07
41	σ	-8.67	-8.82
42	σ	-8.58	-8.92
43	π	-8.30	-8.77
44	σ	-8.21	-8.56
45	π	-8.02	-8.98
46	π	-7.60	-8.18
47	π	-7.37	-7.85
48	π	-6.95	-7.40
49	π	-6.71	-7.31
50	π	-6.11	-6.51
51	π	-5.16	-5.70
52	π	-3.93	-2.75
53	π	-2.87	-1.83
54	π	-2.14	-0.90
55	π	-1.87	-0.77
56	π	-1.29	-0.16
57	π	-1.06	0.15
58	π	-0.55	1.04
59	π	0.00	1.12
60	π	1.34	2.48

Table A.34.: Molecular spectrum for Pentacene (continued).

MO	Symmetry	DFT (eV)	Interface (eV)
61	π	2.50	3.82
62	σ	2.85	3.59
63	σ	2.93	3.83
64	σ	2.94	3.72
65	π	3.28	4.98
66	σ	3.47	4.18
67	σ	3.79	4.81
68	σ	3.87	4.84
69	σ	3.96	5.19
70	σ	4.10	4.83
71	σ	4.66	5.46
72	σ	5.10	6.08
73	σ	5.29	6.12
74	σ	5.37	6.23
75	σ	5.38	6.27
76	σ	5.46	6.26
77	σ	5.64	6.61
78	σ	5.93	6.89
79	σ	6.02	7.03
80	σ	6.57	7.91
81	σ	6.59	7.66
82	σ	6.65	7.56
83	σ	7.42	8.39
84	σ	8.30	9.34
85	σ	8.37	9.29
86	σ	8.70	9.67
87	σ	9.10	10.01
88	σ	9.45	10.39
89	σ	9.56	10.51
90	σ	10.10	11.17
91	σ	10.33	11.31
92	σ	10.52	11.65
93	σ	11.10	12.23
94	σ	11.42	12.86
95	σ	11.51	12.86
96	σ	11.98	13.00
97	σ	13.13	14.24
98	σ	13.61	14.69
99	σ	15.07	16.23
100	σ	15.09	16.41

Table A.35.: Molecular spectrum for Pentacene (continued).

MO	Symmetry	DFT (eV)	Interface (eV)
101	σ	16.12	17.65
102	σ	16.33	17.91

Table A.36.: Molecular spectrum for Pentacene (continued).

A.13. Hexacene

For this material, the HOMO is molecular orbital 61.

MO	Symmetry	DFT (eV)
1	σ	-21.89
2	σ	-21.61
3	σ	-21.16
4	σ	-20.55
5	σ	-19.81
6	σ	-19.61
7	σ	-19.31
8	σ	-18.97
9	σ	-18.84
10	σ	-18.22
11	σ	-18.12
12	σ	-17.48
13	σ	-16.64
14	σ	-16.47
15	σ	-15.39
16	σ	-15.21
17	σ	-15.06
18	σ	-14.80
19	σ	-14.51
20	σ	-14.47
21	σ	-14.12
22	σ	-13.01
23	σ	-12.99
24	σ	-12.64
25	σ	-12.38

Table A.37.: Molecular DFT spectrum for Hexacene.

MO	Symmetry	DFT (eV)
26	σ	-11.96
27	σ	-11.94
28	σ	-11.63
29	σ	-11.45
30	σ	-11.31
31	σ	-11.30
32	σ	-11.01
33	σ	-10.66
34	σ	-10.51
35	σ	-10.40
36	σ	-10.29
37	σ	-10.28
38	π	-10.25
39	σ	-10.24
40	π	-9.94
41	σ	-9.64
42	σ	-9.58
43	σ	-9.54
44	π	-9.45
45	σ	-9.13
46	σ	-8.81
47	π	-8.80
48	σ	-8.74
49	σ	-8.63
50	σ	-8.58
51	σ	-8.17
52	π	-8.07
53	π	-8.04
54	π	-7.75
55	π	-7.27
56	π	-7.24
57	π	-6.72
58	π	-6.62
59	π	-5.85
60	π	-5.02

Table A.38.: Molecular DFT spectrum for Hexacene.

MO	Symmetry	DFT (eV)
61	π	-4.10
62	π	-3.19
63	π	-2.29
64	π	-2.16
65	π	-1.49
66	π	-1.48
67	π	-0.88
68	π	-0.50
69	π	-0.40
70	π	0.76
71	π	1.86
72	π	2.76
73	σ	2.86
74	σ	2.88
75	σ	2.91
76	σ	3.31
77	π	3.34
78	σ	3.76
79	σ	3.86
80	σ	3.87
81	σ	3.90
82	σ	3.98
83	σ	4.37
84	σ	4.80
85	σ	5.16
86	σ	5.34
87	σ	5.37
88	σ	5.38
89	σ	5.40
90	σ	5.57
91	σ	5.91
92	σ	6.02
93	σ	6.13
94	σ	6.24
95	σ	6.64
96	σ	6.83
97	σ	7.29
98	σ	7.57
99	σ	8.07
100	σ	8.81

Table A.39.: Molecular DFT spectrum for Hexacene.

MO	Symmetry	DFT (eV)
101	σ	8.95
102	σ	8.98
103	σ	9.14
104	σ	9.79
105	σ	9.79
106	σ	9.93
107	σ	10.61
108	σ	10.79
109	σ	10.94
110	σ	11.30
111	σ	11.51
112	σ	11.65
113	σ	12.53
114	σ	12.88
115	σ	13.97
116	σ	14.39
117	σ	15.45
118	σ	15.50
119	σ	16.24
120	σ	16.39

Table A.40.: Molecular DFT spectrum for Hexacene.

Conclusiones

En la presente tesis se ha estudiado el alineamiento de niveles en interfases de semiconductores orgánicos, a traves de un modelo propuesto para el régimen de interacción débil.

En primer lugar, se han estudiado, usando métodos basados en la Teoría del Funcional de la Densidad, las propiedades electrónicas de moléculas pequeñas y moléculas orgánicas con enlaces aromáticos π. Se han descrito y comparado distintas aproximaciones para el canje y la correlación y la aplicación de éstas a estos sistemas ha sido discutida. Los resultados permiten conocer la estructura electrónica de estas moléculas. En particular, y dada la subestimación del gap por parte de DFT, se ha desarrollado un método para corregir esta deficiencia, lo que permite calcular el espectro molecular de forma precisa. Estas correcciones son esenciales para el posterior estudio de las interfases de estos metariales.

En segundo lugar, se ha introducido el modelo en uniones metal/orgánico con interacción débil. Tras describir la manera de calcular la posición del Nivel de Neutralidad de Carga del material, éste ha sido hallado para diversos semiconductores orgánicos, así como una descripción del apantallamiento en la interfase. A partir de estos resultados, las propiedades más importantes de las interfases, tales como dipolos inducidos, barreras Schottky o posición del nivel de Fermi, han sido calculadas, en buen acuerdo con los valores experimentales.

Finalmente, se ha desarrollado una extensión del modelo a heterouniones de materiales orgánicos, en la que el mecanismo principal es el alineamiento parcial de los Niveles de Neutralidad de Carga de ambos semiconductores. Además de un

buen acuerdo con los valores experimentales, el modelo desarrollado ha permitido, por primera vez, entender el comportamiento de estas interfases de una manera unificada. Se ha estudiado además el caso de heterouniones dopadas, donde los resultados experimentales son explicados por primera vez, en términos de una modificación del Nivel de Neutralidad de Carga del material dopado y del subsiguiente alineamiento.

Del trabajo realizado cabe destacar el método desarrollado para corregir los gaps moleculares que, junto con la polarización en la interfase, modifica de manera significativa la posición de los niveles. A pesar de ser de gran importancia la interfase, esto no ha sido tenido en cuenta otros métodos en la literatura, donde se usa el gap DFT a pesar de que este subestima de forma notable el gap y dar lugar a una posición incorrecta de los niveles moleculares. Del presente trabajo se deduce que es necesario corregir de manera adecuada la posición de los niveles y el gap de la molécula.

También cabe destacar que, en contra de la opinión generalizada de que las interfases con fisisorción 'no ocurre nada' y que todo se reduce a la interacción van der Waals, nuestro enfoque supone una **interacción química**. Los resultados demuestran que esta es lo suficientemente intensa como para inducir una densidad de estados significativa, que domina el alineamiento de niveles. Se trata, por tanto, de un mecanismo general de importancia en estas interfases.

En resumen, el buen acuerdo alcanzado en las distintas interfases de materiales orgánicos supone la validación del modelo: a pesar del trabajo existente en este campo, nuestro modelo explica, por primera vez, de una manera intuitiva, global y unificada, el alineamiento de niveles en estas interfases.

References

[Alkauskas05] A. Alkauskas, L. Ramoino, S. Schintke, M. von Arx, A. Baratoff, H.-J. Gu1ntherodt and T. A. Jung. Energy Level Alignment at Metal-Octaethylporphyrin Interfaces. *J. Phys. Chem. B* **109** 23558 (2005).

[Amy05] F. Amy, C. Chan and A. Kahn. Polarization at the gold/pentacene interface. *Org. Electron.* **6** 85 (2005).

[Anderson98] J. D. Anderson and et al. Electrochemistry and Electrogenerated Chemiluminescence Processes of the Components of Aluminum Quinolate/Triarylamine and Related Organic Light-Emitting Diodes. *J. Am. Chem. Soc.* **120** 9646 (1998).

[Andrzejak00] M. Andrzejak, G. Mazur and P. Petelenz. Quantum chemical results as input for solid state calculations: charge transfer states in molecular crystals. *J. Mol. Struct. (Theochem)* **527** 91 (2000).

[Bagus02] P. S. Bagus, V. Staemmler and C. Wöll. Exchangelike Effects for Closed-Shell Adsorbates: Interface Dipole and Work Function. *Phys. Rev. Lett.* **89** 096104 (2002).

[Baldo01] M. Baldo. *The Electronic And Optical Properties Of Amorphous Organic Semiconductors*. Ph.D. thesis, Princeton University, Princeton, NJ (2001).

[Bardeen47] J. Bardeen. Surface States and Rectification at a Metal Semi-Conductor Contact. *Phys. Rev.* **71** 63 (1947).

[Basanta] M. A. Basanta, Y. J. Dappe, J. Ortega and F. Flores. Van derWaals forces in the Local-Orbital-Density-Functional Theory. *Europhys. Lett.* **(accepted)**.

[Binnig83] G. Binnig, H. Rohrer, C. Gerber and E. Weibel. 7 x 7 Reconstruction on Si(111) Resolved in Real Space. *Phys. Rev. Lett.* **50** 120 (1983).

[Binning82a] G. Binning, H. Rohrer, C. Gerber and E. Weibel. Surface Studies by Scanning Tunneling Microscopy. *PRL* **49** 57 (1982).

[Binning82b] G. Binning, H. Rohrer, C. Gerber and E. Weibel. Tunneling through a controllable vacuum gap. *Appl. Phys. Lett.* **40** 178 (1982).

[Cahen03] D. Cahen and A. Kahn. Electron Energetics at Surfaces and Interfaces: Concepts and Experiments. *Adv. Mater. (Weinheim, Ger.)* **15** 271 (2003).

[Chizhov00] I. Chizhov, A. Kahn and G. Scoles. Initial growth of 3,4,9,10-perylenetetracarboxylic-dianhydride (PTCDA) on Au(111): a scanning tunneling microscopy study. *J. Crystal Growth* **208** 449 (2000).

[Clementi74] E. Clementi and C. Roetti. *At. Data Nucl. Data Tables* **14** 177 (1974).

[Clementi90] E. Clementi. *Modern Techniques in Computational Chemistry: MOTECC-90* (ESCOM, Leiden, 1990).

[Cowley65] A. M. Cowley and S. M. Sze. Surface States and Barrier Height of Metal-Semiconductor Systems. *J. Appl. Phys.* **36** 3212 (1965).

[Crispin02] X. Crispin, V. Geskin, A. Crispin, J. Cornil, R. Lazzaroni, W. R. Salaneck and J.-L. Brédas. Characterization

of the Interface Dipole at Organic/Metal Interfaces. *J. Am. Chem. Soc.* **124** 8131 (2002).

[Crispin04] X. Crispin. Interface dipole at organic/metal interfaces and organic solar cells. *Solar Energy Mat. Solar Cells* **83** 147 (2004).

[Das03] A. Das, C. K. Nandi and T. Chakraborty. Structure and electronic spectroscopy of naphthalene-acenaphthene van der Waals dimer: Hole-burning, dispersed fluorescence, and quantum chemistry calculations. *J. Chem. Phys.* **118** 9589 (2003).

[Demkov95] A. Demkov, J. Ortega, O. F. Sankey and M. P. Grumbach. Electronic structure approach for complex silicas. *Phys. Rev. B* **52** 1618 (1995).

[Dimitrakopoulos01] C. D. Dimitrakopoulos and D. J. Mascaro. Organic thin-film transistors: A review of recent advances. *IBM J. Res. & Dev.* **45** 11 (2001).

[Eremtchenko04] M. Eremtchenko, D. Bauer, J. A. Schaefer and F. S. Tautz. Polycyclic aromates on close-packed metal surfaces: functionalization, molecular chemisorption and organic epitaxy. *New Journal of Physics* **4** 6 (2004).

[Fenter95] P. Fenter, P. Burrows, P. Eisenberger and S. R. Forrest. Layer-by-layer quasi-epitaxial growth of a crystalline organic thin film. *J. Crystal Growth* **152** 62 (1995).

[Flores79] F. Flores and C. Tejedor. Energy barriers and interface states at heterojunctions. *J. Phys. C: Solid State Phys.* **12** 731 (1979).

[Flores87] F. Flores and C. Tejedor. On the formation of semiconductor interfaces. *J. Phys. C: Solid State Phys.* **20** 145 (1987).

[Forrest84] S. R. Forrest, M. L. Kaplan and P. H. Schmidt. Organic-on-inorganic semiconductor contact barrier diodes. II.

Dependence on organic film and metal contact properties. *J. Appl. Phys.* **56** 543 (1984).

[Forrest97] S. R. Forrest. Ultrathin Organic Films Grown by Organic Molecular Beam Deposition and Related Techniques. *Chem. Rev.* **97** 1793 (1997).

[Forrest04] S. R. Forrest. The path to ubiquitous and low-cost organic electronic appliances on plastic. *Nature* **428** 911 (2004).

[Frisch] M. J. Frisch and et al. Gaussian 98, Revision A.11.3. Gaussian, Inc., Pittsburgh, PA, 2001.

[Gao01] W. Gao and A. Kahn. Controlled p-doping of zinc phthalocyanine by coevaporation with tetrafluorotetracyanoquinodimethane: A direct and inverse photoemission study. *Appl. Phys. Lett.* **79** 4040 (2001).

[Gao02] W. Gao and A. Kahn. Electronic structure and current injection in zinc phthalocyanine doped with tetrafluorotetracyanoquinodimethane: Interface versus bulk effects. *Org. Electron.* **3** 53 (2002).

[Gao03a] W. Gao and A. Kahn. Controlled p doping of the hole-transport molecular material N,N′-diphenyl-N,N′-bis(1-naphthyl)-1,1′-biphenyl-4,4′-diamine with tetrafluorotetracyanoquinodimethane. *J. Appl. Phys.* **94** 359 (2003).

[Gao03b] W. Gao and A. Kahn. Effect of electrical doping on molecular level alignment at organic-organic heterojunctions. *Appl. Phys. Lett.* **82** 4815 (2003).

[Gao04] W. Gao. *Electrical Doping of Organic Molecular Semiconductors*. Ph.D. thesis, Princeton University, Princeton, NJ (2004).

[Gerlach05] A. Gerlach, F. Schreiber, S. Sellner, H. Dosch, I. A. Vartanyants, B. C. C. Cowie, T.-L. Lee and J. Zegenhagen. Adsorption-induced distortion of F_{16}CuPc on Cu(111)

and Ag(111): An x-ray standing wave study. *Phys. Rev. B* **71** 205425 (2005).

[Granström98] M. Granström, K. P. andA. C. Arias, A. Lux, M. R. Andersson and R. H. Friend. Laminated fabrication of polymeric photovoltaic diodes. *Nature* **395** 257 (1998).

[Gundlach97] D. J. Gundlach, Y. Y. Lin and T. N. Jackson. Pentacene organic thin film transistors-molecular ordering and mobility. *IEEE Electron. Dev. Lett.* **18** 87 (1997).

[Gutmann67] F. Gutmann and L. E. Lyons. *Organic Semiconductors* (Wiley, New York, 1967).

[Hamers96] R. J. Hamers. Scanned Probe Microscopies in Chemistry. *J. Phys. Chem.* **100** 13103 (1996).

[Harris85] J. Harris. Simplified method for calculating the energy of weakly interacting fragments. *Phys. Rev. B* **31** 1770 (1985).

[Heine65] V. Heine. Theory of Surface States. *Phys. Rev.* **138** A1689 (1965).

[Hill98a] I. G. Hill, and A. Kahn. Energy level alignment at interfaces of organic semiconductor heterostructures. *J. Appl. Phys.* **84** 5583 (1998).

[Hill98b] I. G. Hill, A. Rajagopal and A. Kahn. Energy-level alignment at interfaces between metals and the organic semiconductor 4,4'- N, N'- dicarbazolyl-biphenyl. *J. Appl. Phys.* **84** 3236 (1998).

[Hill98c] I. G. Hill, A. Rajagopal, A. Kahn and Y. Hu. Molecular level alignment at organic semiconductor-metal interfaces. *Appl. Phys. Lett.* **73** 662 (1998).

[Hill00a] I. G. Hill, A. Kahn, J. Cornil, D. A. dos Santos and J. Brédas. Occupied and unoccupied electronic levels in organic π-conjugated molecules: comparison between experiment and theory. *Chem. Phys. Lett.* **317** 444 (2000).

[Hill00b] I. G. Hill, A. Kahn, Z. G. Soos and R. A. Pascal Jr. Charge-separation energy in films of π-conjugated organic molecules. *Chem. Phys. Lett.* **327** 181 (2000).

[Hill00c] I. G. Hill, D. Milliron, J. Schwartz and A. Kahn. Organic semiconductor interfaces: electronic structure and transport properties. *Appl. Surf. Sci.* **166** 354 (2000).

[Hill00d] I. G. Hill, J. Schwartz and A. Kahn. Metal-dependent charge transfer and chemical interaction at interfaces between 3,4,9,10-perylenetetracarboxylic bisimidazole and gold, silver and magnesium. *Org. Electron.* **1** 5 (2000).

[Hipps05] K. W. Hipps. *Scanning Tunneling Spectroscopy*. Handbook of Applied Solid State Spectroscopy (Kluer Scientific, 2005).

[Hohenberg64] P. Hohenberg and W. Kohn. Inhomogeneous Electron Gas. *Phys. Rev.* **136** B864 (1964).

[Hult99] E. Hult, H. Rydberg and B. I. Lundqvist. Unified treatment of asymptotic van der Waals forces. *Phys. Rev. Lett.* **59** 4708 (1999).

[Hummer05a] K. Hummer and C. Ambrosch-Draxl. Electronic properties of oligoacenes from first principles. *Phys. Rev. B* **72** 205205 (2005).

[Hummer05b] K. Hummer and C. Ambrosch-Draxl. Oligoacene exciton binding energies: Their dependence on molecular size. *Phys. Rev. B* **71** 081202(R) (2005).

[Ishii99] H. Ishii, K. Sugiyama, E. Ito and K. Seki. Energy Level Alignment and Interfacial Electronic Structures at Organic/Metal and Organic/Organic Interfaces. *Adv. Mater. (Weinheim, Ger.)* **11** 605 (1999).

[Ishii01] H. Ishii and K. Seki. *Energy Level Alignment at Organic-Metal Interfaces*. Conjugated Polymer and Molecular Interfaces (Marcel Dekker, New York, 2001).

[Jelínek05] P. Jelínek, H. Wang, J. P. Lewis, O. F. Sankey and J. Ortega. Multicenter approach to the exchange-correlation interactions in ab initio tight-binding methods. *Phys. Rev. B* **71** 235101 (2005).

[Jones89] R. O. Jones and O. Gunnarsson. The density functional formalism, its applications and prospects. *Rev. Mod. Phys.* **61** 689 (1989).

[Kahn03] A. Kahn, N. Koch and W. Gao. Electronic Structure and Electrical Properties of Interfaces between Metals and π-Conjugated Molecular Films. *J. Polym. Sci.* **41** 2529 (2003).

[Kahn06] A. Kahn, W. Zhao, W. Gao, H. Vázquez and F. Flores. Mechanism for doping-induced realignment of molecular levels at organic-organic heterojunctions. *Chem. Phys.* **325** 129 (2006).

[Kao81] K. C. Kao and W. Hwang. *Electrical Transport in Solids* (Pergamon, Oxford, 1981).

[Karl89] N. Karl. Studies of organic semiconductors for 40 years. III. *Mol. Cryst. Liq. Cryst.* **171** 31 (1989).

[Karl99] N. Karl, K. H. Kraft, J. Marktanner, M. Münch, F. Schatz, R. Stehle and H. M. Uhde. Fast electronic transport in organic molecular solids? *Journal of Vacuum Science and Technology A* **17** 2318 (1999).

[Katnani83] A. D. Katnani and G. Margaritondo. Microscopic study of semiconductor heterojunctions: Photoemission measurement of the valance-band discontinuity and of the potential barriers. *Phys. Rev. B* **28** 1944 (1983).

[Kendrick96] C. Kendrick, A. Kahn and S. R. Forrest. STM study of the organic semiconductor PTCDA on highly-oriented pyrolytic graphite. *Appl. Surf. Sci.* **104** 586 (1996).

[Kera04] S. Kera, Y. Yabuuchi, H. Yamane, H. Setoyama, K. K. Okudaira, A. Kahn and N. Ueno. Impact of an interface dipole layer on molecular level alignment at an organic-conductor interface studied by ultraviolet photoemission spectroscopy. *Phys. Rev. B* **70** 085304 (2004).

[Kittel87] C. Kittel. *Quantum Theory of Solids* (Wiley, New York, 1987), 2^{nd} edition.

[Knupfer] M. Knupfer. (private communication).

[Knupfer05a] M. Knupfer and G. Paasch. Origin of the interface dipole at interfaces between undoped organic semiconductors and metals. *J. Vac. Sci. Technol. A* **23** 1072 (2005).

[Knupfer05b] M. Knupfer and T. Schwieger. Chemisorption at interfaces between organic semiconductors and metals: role of the electron affinity. *Appl. Surf. Sci.* **252** 77 (2005).

[Koch00] W. Koch and M. C. Holthausen. *A Chemist's Guide to Density Functional Theory* (Wiley, Wienheim, 2000).

[Koch03] N. Koch, A. Kahn, J. Ghijsen, J.-J. Pireaux, J. Schwartz, R. L. Johnson and A. Elschner. Conjugated organic molecules on metal versus polymer electrodes: Demonstration of a key energy level alignment mechanism. *Appl. Phys. Lett.* **82** 70 (2003).

[Kohn65] W. Kohn and L. J. Sham. Self-Consistent Equations Including Exchange and Correlation Effects. *Phys. Rev.* **140** A1133 (1965).

[Kohn98] W. Kohn, Y. Meir and D. E. Makarov. van der Waals Energies in Density Functional Theory. *Phys. Rev. B* **80** 4153 (1998).

[Kohn99] W. Kohn. Nobel Lecture: Electronic structure of matter-wave functions and density functionals. *Rev. Mod. Phys.* **71** 1253 (1999).

[Koopmans33] T. Koopmans. Ordering of Wave Functions and Eigenenergies to the Individual Electrons of an Atom. *Physica* **1** 104 (1933).

[Krause03] B. Krause, A. C. Dürr, F. Schreiber, H. Dosch and O. H. Seeck. Thermal stability and partial dewetting of crystalline organic thin films: 3,4,9,10-perylenetetracarboxylic dianhydride on Ag(111). *J. Chem. Phys.* **119** 3429 (2003).

[Lang70] N. D. Lang and W. Kohn. Theory of Metal Surfaces: Change Density and Surface Energy. *Phys. Rev. B* **1** 4555 (1970).

[Lang81] N. D. Lang. Interaction between closed-shell systems and metal surfaces. *Phys. Rev. Lett.* **46** 842 (1981).

[Lee02a] N. K. Lee, S. Park and S. K. Kim. Ab initio studies on the van der Waals complexes of polycyclic aromatic hydrocarbons. I. Benzene-naphthalene complex. *J. Chem. Phys.* **116** 7902 (2002).

[Lee02b] N. K. Lee, S. Park and S. K. Kim. Ab initio studies on the van der Waals complexes of polycyclic aromatic hydrocarbons. II. Naphthalene dimer and naphthalene-anthracene complex. *J. Chem. Phys.* **116** 7910 (2002).

[Lewis01] J. P. Lewis, G. A. V. Kurt R. Glaesemann and, J. Fritsch, A. A. Demkov, J. Ortega and O. F. Sankey. Further developments in the local-orbital density-functional-theory tight-binding method. *Phys. Rev. B* **64** 195103 (2001).

[Lide98] D. R. Lide. *Handbook of Chemistry and Physics* (Boca Raton, FL: Chemical Rubber Company Press, 1998).

[Lödin50] P.-O. Lödin. On the Non-Orthogonality Problem Connected with the Use of Atomic Wave Functions in the Theory of Molecules and Crystals. *J. Chem. Phys.* **18** 365 (1950).

[Louie76] S. G. Louie and M. L. Cohen. Electronic structure of a metal-semiconductor interface. *Phys. Rev. B* **13** 2461 (1976).

[Marder00] M. P. Marder. *Condensed matter physics* (John Wiley, New York, 2000).

[Mönch] W. Mönch. *Electronic Structure of Metal-Semiconductor Contacts* (Jaca Books, Milan).

[Mönch96] W. Mönch. Chemical trends of barrier heights in metal-semiconductor contacts: on the theory of the slope parameter. *Appl. Surf. Sci.* **92** 367 (1996).

[Morikawa04] Y. Morikawa, H. Ishii and K. Seki. Theoretical study of n-alkane adsorption on metal surfaces. *Phys. Rev. B* **69** 041403(R) (2004).

[Narioka95] S. Narioka, H. Ishii, D. Yoshimura, M. Sei, Y. Ouchi, K. Seki, S. Hasegawa, T. Miyazaki, Y. Harima and K. Yamashita. The electronic structure and energy level alignment of porphyrin/metal interfaces studied by ultraviolet photoelectron spectroscopy. *Appl. Phys. Lett.* **67** 13 (1995).

[Nenner75] I. Nenner and G. J. Schulz. Temporary negative ions and electron affinities of benzene and N-heterocyclic molecules: pyridine, pyridazine, pyrimidine, pyrazine and s-triazine. *J. Chem. Phys.* **62** 1747 (1975).

[Newns69] D. M. Newns. Self-Consistent Model of Hydrogen Chemisorption. *Phys. Rev.* **178** 1123 (1969).

[Niehaus05] T. A. Niehaus, M. Rohlfing, F. D. Sala, A. D. Carlo and T. Frauenheim. Quasiparticle energies for large molecules: A tight-binding-based Green's-function approach. *Phys. Rev. B* **71** 022508 (2005).

[Öström03] H. Öström, L. Triguero, K. Weiss, H. Ogasawara, M. G. Garnier, D. Nordlund, M. Nyberg, L. G. M. Pettersson

and A. Nilsson. Orbital rehybridization in n-octane adsorbed on Cu(110). *J. Chem. Phys.* **118** 3782 (2003).

[Oszwaldowski03] R. Oszwaldowski, H. Vázquez, P. Pou, J. Ortega, R. Pérez and F. Flores. Exchange-correlation energy in the orbital occupancy method: electronic structure of organic molecules. *J. Phys.: Condens. Matter* **15** S2665 (2003).

[Paasch03] G. Paasch, H. Peisert, M. Knupfer, J. Fink and S. Scheinert. Mixing of interface dipole and band bending at organic/metal interfaces in the case of exponentially distributed transport states. *J. Appl. Phys.* **93** 6084 (2003).

[Papaconstantopoulos86] D. A. Papaconstantopoulos. *Handbook of The Band Structure of Elemental Solids* (Plenum Press, New York, 1986).

[Pauling60] L. Pauling. *The Nature of the Chemical Bond* (Cornell University Press, Ithaca, NY, 1960), 3 rd edition.

[Payne92] M. C. Payne, M. P. Teter, D. C. Allan, T. A. Arias and J. D. Joannopoulos. Iterative minimization techniques for ab initio total-energy calculations: molecular dynamics and conjugate gradients. *Rev. Mod. Phys.* **64** 1045 (1992).

[Peisert02] H. Peisert, M. Knupfer, T. Schwieger, J. M. Auerhammer, M. S. Golden and J. Fink. Full characterization of the interface between the organic semiconductor copper phthalocyanine and gold. *J. Appl. Phys.* **91** 4872 (2002).

[Peisert03] H. Peisert, M. Knupfer, T. Schwieger, G. G. Fuentes, D. Olligs, J. Fink and T. Schmidt. Fluorination of copper phthalocyanines: Electronic structure and interface properties. *J. Appl. Phys.* **93** 9683 (2003).

[Peumans00a] P. Peumans, V. Bulovic and S. R. Forrest. Efficient, high-bandwidth organic multilayer photodetectors. *Appl. Phys. Lett.* **76** 3855 (2000).

[Peumans00b] P. Peumans, V. Bulovic and S. R. Forrest. Efficient photon harvesting at high optical intensities in ultrathin organic

double-heterostructure photovoltaic diodes. *Appl. Phys. Lett.* **76** 2650 (2000).

[Peumans01] P. Peumans and S. R. Forrest. Very high efficiency double heterostructure copper phthalocyanine/C_{60} photovoltaic cells. *Appl. Phys. Lett.* **79** 126 (2001).

[Peumans03] P. Peumans, S. Uchida and S. R. Forrest. Efficient bulk heterojunction photovoltaic cells based on small molecular weight organic thin films. *Nature* **425** 158 (2003).

[Picozzi03] S. Picozzi, A. Pecchia, M. Gheorghe, A. D. Carlo, P. Lugli, B. Delley and M. Elstner. Schottky barrier height at an organic/metal junction: A first-principles study of PTCDA/X (X=Al,Ag) contacts. *Phys. Rev. B* **68** 195309 (2003).

[Pou98] P. Pou, R. Pérez, J. Ortega and F. Flores. Ab-initio multicenter tight-binding model for molecular-dynamics simulations and other applications in covalent systems. *Mater. Res. Soc. Symp. Proc.* **491** 45 (1998).

[Pou00] P. Pou, R. Pérez, F. Flores, A. L. Yeyati, A. Martín-Rodero, J. M. Blanco, F. J. García-Vidal, and J. Ortega. Local-density approach and quasiparticle levels for generalized Hubbard Hamiltonians. *Phys. Rev. B* **62** 4309 (2000).

[Pou01] P. Pou. *Energía de canje y correlación como función de los números de ocupación: Cálculo de energías totales y cuasi-partículas*. Ph.D. thesis, Dept. de Física Teórica de la Materia Condensada, UAM, Madrid (2001).

[Pou02] P. Pou, R. Oszwaldowski, H. Vázquez, R. Pérez, F. Flores and J. Ortega. Exchange Correlation Energy as a Function of the Orbital Occupancies: Implementation on First Principles Local Orbital Methods. *Int. J. Quantum Chem.* **91** 151 (2002).

[Proehl01] H. Proehl, M. Toerker, F. Sellam, T. Fritz and K. Leo. Comparison of ultraviolet photoelectron spectroscopy and scanning tunneling spectroscopy measurements on highly ordered ultrathin films of hexa-perihexabenzocoronene on Au(111). *Phys. Rev. B* **63** 205409 (2001).

[Rajagopal98] A. Rajagopal, C. I. Wu and A. Kahn. Energy level offset at organic semiconductor heterojunctions. *J. Appl. Phys.* **83** 2649 (1998).

[Rhoderick88] E. H. Rhoderick and R. H. Williams. *Metal-Semiconductor Contacts* (Oxford University Press, Oxford, 1988), second edition edition.

[Salaneck01] W. R. Salaneck, K. Seki, A. Kahn and J. J. Pireaux. *Conjugated Polymer and Molecular Interfaces: Science and Technology for Photonic and Optoelectronic Applications* (Marcel Dekker, New York, 2001).

[Sankey89] O. F. Sankey and D. J. Niklewski. Ab-initio multicenter tight-binding model for molecular-dynamics simulations and other applications in covalent systems. *Phys. Rev. B* **40** 3979 (1989).

[Schmitz-Hübsch96] T. Schmitz-Hübsch, T. Fritz, F. Sellam, R. Staub and K. Leo. Epitaxial growth of 3,4,9,10-perylene-tetracarboxylic-dianhydride on Au(111): A STM and RHEED study. *Phys. Rev. B* **55** 7972 (1996).

[Schön00] J. H. Schön, C. Kloc and B. Batlogg. Fractional Quantum Hall Effect in Organic Molecular Semiconductors. *Science* **288** 2338 (2000).

[Schreiber04] F. Schreiber. Organic molecular beam deposition: Growth studies beyond the first monolayer. *Phys. Stat. Sol. (a)* **201** 1037 (2004).

[Schroeder02] P. G. Schroeder, C. B. France, J. B. Park and B. A. Parkinson. Energy level alignment and two-dimensional structure of pentacene on Au(111) surfaces. *J. Appl. Phys.* **91** 3010 (2002).

[Scott03] J. C. Scott. Metal-organic interface and charge injection in organic electronic devices. *J. Vac. Sci. Technol. A* **21** 521 (2003).

[Shaheen01] S. E. Shaheen, C. J. Brabec, N. S. Sariciftci, F. Padinger, T. Fromherz and J. C. Hummelen. 2.5% efficient organic plastic solar cells. *Appl. Phys. Lett.* **78** 841 (2001).

[Sharp53] R. T. Sharp and G. K. Horton. A Variational Approach to the Unipotential Many-Electron Problem. *Phys. Rev.* **90** 317 (1953).

[Shen97] Z. Shen and S. R. Forrest. Quantum size effects of charge-transfer excitons in nonpolar molecular organic thin films. *Phys. Rev. B* **55** 10578 (1997).

[Shen01a] C. Shen and A. Kahn. The role of interface states in controlling the electronic structure of Alq_3/reactive metal contacts. *Org. Electron.* **2** 89 (2001).

[Shen01b] C. Shen, A. Kahn and I. G. Hill. *Organic Molecular Interfaces: Investigations of Electronic Structure, Chemistry and Carrier Injection Properties*. Conjugated Polymer and Molecular Interfaces (Marcel Dekker, New York, 2001).

[Shen04] Y. Shen, A. R. Hosseini, M. H. Wong and G. G. Malliaras. Ohmic contacts to organic semiconductors. *ChemPhysChem* **5** 16 (2004).

[Shtein02] M. Shtein, J. Mapel, J. B. Benziger and S. R. Forrest. Effects of film morphology and gate dielectric surface preparation on the electrical characteristics of organic vapor phase deposited pentacene thin-film transistors. *Appl. Phys. Lett.* **81** 268 (2002).

[Silinsh94] E. A. Silinsh and V. Čápek. *Organic Molecular Crystals* (AIP Press, New York, 1994).

[Spicer79] W. E. Spicer, P. W. Chye, P. R. Skeath, C. Y. Su and I. Lindau. New and unified model for Schottky barrier and III-V insulator interface states formation. *J. Vac. Sci. Technol.* **16** 1422 (1979).

[Stephens94] P. J. Stephens, F. J. Devlin, C. F. Chabalowski, and M. J. Frisch. Ab Initio Calculation of Vibrational Absorption and Circular Dichroism Spectra Using Density Functional Force Fields. *J. Phys. Chem.* **98** 11623 (1994).

[Sze81] S. M. Sze. *Physics of Semiconductor Devices* (John Wiley, New York, 1981).

[Tadayyon04] S. M. Tadayyon, H. M. Grandin, K. Griffiths, L. L. Coatsworth, P. R. Norton, H. Aziz and Z. Popovic. Reliable and reproducible determination of work function and ionization potentials of layers and surfaces relevant to organic light emitting diodes. *Org. Electron.* **5** 199 (2004).

[Tautz02] F. S. Tautz, M. Eremtchenko, J. A. Schaefer, M. Sokolowski, V. Shklover, K. Glöckler and E. Umbach. A comparison of the chemisorption behaviour of PTCDA on different Ag surfaces. *Surf. Sci.* **502** 176 (2002).

[Tejedor77] C. Tejedor, F. Flores and E. Louis. The metal-semiconductor interface: Si (111) and zincblende (110) junctions. *J. Phys. C: Solid State Phys.* **10** 2163 (1977).

[Tejedor78] C. Tejedor and F. Flores. A simple approach to heterojunctions. *J. Phys. C: Solid State Phys.* **11** L19 (1978).

[Tersoff84] J. Tersoff. Theory of semiconductor heterojunctions: The role of quantum dipoles. *Phys. Rev. B* **30** 4874 (1984).

[Tersoff85] J. Tersoff. Schottky barriers and semiconductor band offsets. *Phys. Rev. B* **32** 6968 (1985).

[Toerker01] M. Toerker, T. Fritz, H. Proehl, F. Sellam and K. Leo. Tunneling spectroscopy study of 3,4,9,10-perylenetetracarboxylic dianhydride on Au(100). *Surf. Sci.* **491** 255 (2001).

[Tsiper01] E. V. Tsiper and Z. G. Soos. Charge redistribution and polarization energy of organic molecular crystals. *Phys. Rev. B* **64** 195124 (2001).

[Tsiper02] E. V. Tsiper, Z. G. Soos, W. Gao and A. Kahn. Electronic polarization at surfaces and thin films of organic molecular crystals: PTCDA. *Chem. Phys. Lett.* **360** 47 (2002).

[Tsiper03] E. V. Tsiper and Z. G. Soos. Electronic polarization in pentacene crystals and thin films. *Phys. Rev. B* **68** 085301 (2003).

[Tung01] R. T. Tung. Recent advances in Schottky barrier concepts. *Mat. Sci. Eng. R* **35** 1 (2001).

[Ullrich95] C. A. Ullrich, U. J. Gossmann and E. K. U. Gross. Time-Dependent Optimized Effective Potential. *Phys. Rev. Lett.* **74** 872 (1995).

[Umbach] E. Umbach. (private communication).

[Umbach96] E. Umbach, M. Sokolowski and R. Fink. Substrate-interaction, long-range order, and epitaxy of large organic adsorbates. *Appl. Phys. A* **63** 565 (1996).

[Vaeth03] K. M. Vaeth. OLED-display technology. *Inform. Display* **19** 12 (2003).

[van Hutten01] P. van Hutten, V. Krasnikov and G. Hadziioannou. *Role of Interfaces in Semiconducting Polymer Optoelectronic Devices*. Conjugated Polymer and Molecular Interfaces (Marcel Dekker, New York, 2001).

[Vázquez] H. Vázquez, F. Flores and A. Kahn. Induced Density of States model for weakly-interacting organic semiconductor interfaces. *Org. Electron. (Special Issue)* **(accepted)**.

[Vázquez04a] H. Vázquez, F. Flores, R. Oszwaldowski, J. Ortega, R. Pérez and A. Kahn. Barrier formation at metal/organic interfaces: dipole formation and the Charge Neutrality Level. *Appl. Surf. Sci.* **234** 107 (2004).

[Vázquez04b] H. Vázquez, R. Oszwaldowski, P. Pou, J. Ortega, R. Pérez, F. Flores and A. Kahn. Dipole Formation at metal/PTCDA interfaces: role of the Charge Neutrality Level. *Europhys. Lett.* **65** 802 (2004).

[Vázquez05a] H. Vázquez, F. Flores and A. Kahn. Role of the Charge Neutrality Level at Metal/Organic and Organic/Organic Interfaces. *Proc. Int. Symp. Super-Functionality Organic Devices, IPAP Conf. Series* **6** 1 (2005).

[Vázquez05b] H. Vázquez, W. Gao, F. Flores and A. Kahn. Energy level alignment at organic heterojunctions: Role of the charge neutrality level. *Phys. Rev. B* **71** 041306(R) (2005).

[Wan05] A. Wan, J. Hwang, F. Amy and A. Kahn. Impact of electrode contamination on the α-NPD/Au hole injection barrier. *Org. Electron.* **6** 47 (2005).

[Wandelt84] K. Wandelt and J. E. Hulse. Xenon adsorption on palladium. I. The homogeneous (110), (100), and (111) surfaces. *J. Chem. Phys.* **80** 1340 (1984).

[Warta85a] W. Warta and N. Karl. Hot holes in naphthalene: High, electric-field-dependent mobilites. *Phys. Rev. B* **32** 1172 (1985).

[Warta85b] W. Warta, R. Stehle and N. Karl. Ultrapure, high mobility organic photoconductors. *Appl. Phys. A* **36** 163 (1985).

[Watkins02] N. J. Watkins, L. Yan and Y. Gao. Electronic structure symmetry of interfaces between pentacene and metals. *Appl. Phys. Lett.* **80** 4384 (2002).

[Xu02] M. S. Xu, J. B. Xu, K. Xue, J. An, J. Z. He and I. H. Wilson. Variable-Temperature Scanning Tunneling Mi-

croscopy and Scanning Tunneling Spectroscopy Study on Copper Phthalocyanine Ultrathin Films on a Au(111) Surface. *J. Nanosci. Nanotech.* **2** 139 (2002).

[Yanagisawa06] S. Yanagisawa and Y. Morikawa. Important role of molecular permanent dipoles of the Alq_3/Al interface studied from first-principles. *Chem. Phys. Lett.* **420** 523 (2006).

[Zangwill88] A. Zangwill. *Physics at Surfaces* (Cambridge University Press, 1988).

[Zhao05] A. Zhao, Q. Li, L. Chen, H. Xiang, W. Wang, S. Pan, B. Wang, X. Xiao, J. Yang, J. G. Hou and Q. Zhu. Controlling the Kondo Effect of an Adsorbed Magnetic Ion Through Its Chemical Bonding. *Science* **309** 1542 (2005).

[Ziman] J. M. Ziman. *Principles of the Theory of Solids* (Cambridge University Press, 1964).

Publications

Part of the work described in this thesis has given rise to the following publications:

• *(Invited paper)* H. Vázquez, F. Flores and A. Kahn, Induced Density of States model for weakly-interacting organic semiconductor interfaces, *Org. Electron. (Special Issue)* (accepted).

• A. Kahn, W. Zhao, W. Gao, H. Vázquez and F. Flores, Mechanism for doping-induced realignment of molecular levels at organic-organic heterojunctions, *Chem. Phys.* **325** 129 (2006).

• *(Invited paper)* H. Vázquez, F. Flores and A. Kahn, Role of the Charge Neutrality Level at Metal/Organic and Organic/Organic Interfaces, *Proc. Int. Symp. Super-Functionality Organic Devices, IPAP Conf. Series* **6** 1 (2005).

• H. Vázquez, W. Gao, F. Flores and A. Kahn, Energy level alignment at organic heterojunctions: Role of the charge neutrality level, *Phys. Rev. B* **71** 041306(R) (2005).

• H. Vázquez, F. Flores, R. Oszwaldowski, J. Ortega, R. Pérez and A. Kahn, Barrier formation at metal/organic interfaces: dipole formation and the Charge Neutrality Level, *Appl. Surf. Sci.* **234** 107 (2004).

• H. Vázquez, R. Oszwaldowski, P. Pou, J. Ortega, R. Pérez, F. Flores and A. Kahn, Dipole Formation at metal/PTCDA interfaces: role of the Charge Neutrality Level, *Europhys. Lett.* **65** 802 (2004).

• R. Oszwaldowski, H. Vázquez, P. Pou, J. Ortega, R. Pérez and F. Flores, Exchange-Correlation Energy in the Orbital Occupancy method: electronic structure of Organic Molecules, *J. Phys.: Condens. Matter* **15** S2665 (2003).

• P. Pou, R. Oszwaldowski, H. Vázquez, R. Pérez, F. Flores and J. Ortega, Exchange-Correlation Energy as a Function of the Orbital Occupancies: Implementation on First Principles Local Orbital Methods, *Int. J. Quantum Chem.* **91** 151 (2002).